

**Light, Unstable Sterile Neutrinos:
Phenomenology, a Search in the IceCube
Experiment, and a Global Picture**

by

Marjon H. Moulai

B.A., University of California, Berkeley (2009)

Submitted to the Department of Physics
in partial fulfillment of the requirements for the degree of

Doctor of Philosophy

at the

MASSACHUSETTS INSTITUTE OF TECHNOLOGY

June 2021

© Massachusetts Institute of Technology 2021. All rights reserved.

Author

Department of Physics

April 23, 2021

Certified by

Janet M. Conrad

Professor

Thesis Supervisor

Accepted by

Deepto Chakrabarty

Associate Department Head of Physics

Light, Unstable Sterile Neutrinos: Phenomenology, a Search in the IceCube Experiment, and a Global Picture

by

Marjon H. Moulai

Submitted to the Department of Physics
on April 23, 2021, in partial fulfillment of the
requirements for the degree of
Doctor of Philosophy

Abstract

Longstanding anomalies in neutrino oscillation experiments point to the existence of a fourth, hypothetical neutrino: the sterile neutrino. Global fits to a sterile neutrino model find a strong preference for such a model over the massive neutrino Standard Model. However, the fit results suffer from inconsistencies between datasets, referred to as tension. This motivates more complicated models for new physics. This thesis considers a model of unstable sterile neutrinos, where the heaviest mass state can decay. First, the phenomenology of unstable sterile neutrinos is explored in the IceCube experiment, a gigaton neutrino detector located at the South Pole. Second, global fits to traditional and unstable sterile neutrino models are combined with one year of data from IceCube. A preference for the unstable sterile neutrino model is found, as well as a reduction in tension. Lastly, a high statistics search for unstable sterile neutrinos is performed in IceCube. The Standard Model is rejected with a p -value of 2.8% and the traditional sterile neutrino model is rejected with a p -value of 4.9%. The best-fit point is $\Delta m_{41}^2 = 6.7_{-2.5}^{+3.9} \text{ eV}^2$, $\sin^2 2\theta_{24} = 0.33_{-0.17}^{+0.20}$, and $g^2 = 2.5\pi \pm 1.5\pi$, where g is the coupling that mediates the neutrino decay. The best-fit corresponds to a lifetime of the heaviest neutrino of $\tau_4/m_4 = 6 \times 10^{-16} \text{ s/eV}$. A Bayesian analysis finds a best model with similar sterile parameters.

Thesis Supervisor: Janet M. Conrad
Title: Professor

Acknowledgments

First and foremost, I would like to thank my advisor, Janet Conrad. After several years away from academia, Janet gave me the opportunity to return, which had felt unlikely, if not impossible. She offered me a position in her research group and guided me into graduate school. Throughout graduate school, she believed in me. She shared interesting research projects with me and always had ideas for solving problems. I may not have gotten a graduate degree without her.

This thesis was made possible by collaborative work done by many people. In the IceCube Collaboration, I especially would like to thank Carlos Argüelles, Spencer Axani, Alex Diaz, Ben Jones, Grant Parker, Austin Schneider, Ben Smithers, David Vannerom, Blake Watson, and Philip Weigel for their efforts and assistance. I thank Jason Koskinen and Klaus Helbing for their review of the analysis, Anna Pollman, Juanan Aguilar, and Ignacio Taboada for their help in getting the box opened, and Tom Gaisser for useful discussion.

For the phenomenology work in this thesis, I extend my thanks to my collaborators Zander Moss, Gabriel Collin, and Mike Shaevitz. I also thank my DCTPC/MITPC collaborators: Josh Spitz, Allie Hexley, Anna Jungbluth, Adrien Hourlier, and Jaime Dawson.

I would not have made it through graduate school without the friends I made at MIT, including Christina Ignarra, John Hardin, Alex Leder, Cheko Cantu, Axel Schmidt, and Lauren Yates, to name a few. Similarly, I am grateful for the friends I made at WIPAC, which include Logan Wille, Josh Wood, Ali Kheirandish, Sarah Mancina, Matt Meehan, Jeff Lazar, Ibrahim Safa, and Donglian Xu.

I would like to acknowledge Cathy Modica, Sydney Miller, Nicole Laraia, Kim Krieger, and Tina Chorlton for their administrative assistance. I thank the rest of my thesis committee: Joe Formaggio and Claude Canizares.

Lastly, I am grateful for my parents, Ellie Golestani and Javad Moulai, and my sister, Maryam Moulai, for their love and support.

Contents

1	Introduction	17
1.1	Neutrino oscillations in vacuum	17
1.2	Anomalies	21
1.3	Traditional 3+1 model	26
1.4	Tension in the 3+1 fits	28
2	Status of 3+1 sterile neutrinos in IceCube	31
2.1	Neutrino oscillations in matter	31
2.2	Brief description of IceCube	35
2.3	Eight-year search results	36
2.4	Jumping off point for the work in this thesis	39
3	Phenomenology of unstable sterile neutrinos in IceCube	41
3.1	Unstable sterile neutrino model in IceCube	41
	<i>Publication: Exploring a nonminimal sterile neutrino model involving</i>	
	<i>decay at IceCube</i>	41
3.2	Incorporating IceCube data into global fits	54
	<i>Publication: Combining sterile neutrino fits to short-baseline data with</i>	
	<i>IceCube data</i>	54
3.3	More on the phenomenology of unstable sterile neutrinos in IceCube .	66
4	The IceCube neutrino detector	71
4.1	The IceCube Neutrino Observatory	71

4.2	IceCube in-ice array	72
4.3	Digital Optical Module	73
4.4	The ice	74
4.5	Data acquisition	77
4.6	Description of neutrino interaction	79
4.7	Muon reconstruction	86
5	Atmospheric neutrino fluxes	89
5.1	The coupled cascade equations	89
5.2	Cosmic ray and hadronic interaction models	92
5.3	Barr scheme for hadronic interaction uncertainties	94
5.4	Atmospheric flux uncertainty treatment	96
5.5	Neutrino flux at detector	104
6	Search for unstable sterile neutrinos	107
6.1	Data selection	107
6.2	Systematic uncertainties	110
6.2.1	Nuisance parameters	110
6.2.2	Minor systematic improvements from traditional 3+1 search .	115
6.2.3	The Antarctic bedrock	115
6.3	Oscillograms and expected event distributions	118
6.4	Likelihood function	121
6.5	Parameter scan	122
6.6	Frequentist analysis and Asimov sensitivity	122
6.7	Bayesian analysis	124
7	Results	125
7.1	Discussion	138
8	Future prospects and conclusions	141
A	Specific contributions	143

B	Supplementary figures	145
B.0.1	Data and systematic pulls	145
B.0.2	Fit systematic values	147
C	MITPC	165
	<i>Publication: Demonstrating a directional detector based on neon for</i>	
	<i>characterizing high energy neutrons</i>	165
	Bibliography	188

List of Figures

1-1	Feynman vertices for charged current neutrino interactions	17
1-2	Schematic illustration of the Normal Ordering	18
1-3	Neutrino oscillation probabilities for 1 GeV neutrinos	20
1-4	LSND anomaly	23
1-5	MiniBooNE anomaly	24
1-6	Reactor Antineutrino Anomaly	25
1-7	Schematic illustration of a 3+1 sterile neutrino model	27
2-1	Traditional 3+1 oscillation probabilities versus baseline along Earth's diameter	34
2-2	Traditional 3+1 oscillation probabilities versus energy for neutrinos traversing the Earth	34
2-3	Predicted atmospheric and astrophysical event distribution	35
2-4	Frequentist, traditional 3+1, eight-year result	37
2-5	Bayesian, traditional 3+1, eight-year result	38
3-1	Transition probabilities versus baseline along Earth's diameter for 3+1+de- cay	68
3-2	Transition probabilities versus energy for antineutrinos traversing the Earth for 3+1+decay	69
3-3	Transition probabilities versus energy for neutrinos traversing the Earth for 3+1+decay	70
4-1	Schematic illustration of IceCube Neutrino Observatory	72

4-2	IceCube digital optical module	73
4-3	Ice model scattering and absorption coefficients	76
4-4	Data flow from PMT to central DAQ	77
4-5	Feynman diagram for deep inelastic scattering	79
4-6	Charged-current cross sections	80
4-7	Mean inelasticity versus neutrino energy	80
4-8	Depth distribution of interactions from simulation	81
4-9	Muon range in ice	82
4-10	Muon energy losses in ice and secondary spectra	83
4-11	Event display for a 5.2 TeV muon	84
4-12	Event display for a 7.0 TeV muon	85
4-13	Reconstructed muon energy versus true neutrino energy	87
4-14	True neutrino energy versus reconstructed muon energy	87
5-1	Schematic illustration of a cosmic ray air shower	90
5-2	Energy spectra of atmospheric muon neutrinos and their various constituents	92
5-3	All-particle cosmic ray spectrum	93
5-4	Energy spectrum band from Barr scheme	98
5-5	Angular distribution spanned by Barr scheme at 90 GeV	99
5-6	Angular distribution spanned by Barr scheme at 900 GeV	100
5-7	Angular distribution spanned by Barr scheme at 9 TeV	101
5-8	Angular distribution spanned by Barr scheme at 90 TeV	102
5-9	Ratio of antineutrinos to neutrinos spanned by Barr scheme	103
6-1	Event selection energy and angular distribution from simulation	109
6-2	Effect of 1σ change in nuisance parameters	113
6-3	Effect of 1σ change in nuisance parameters	114
6-4	Fraction of events that originate in the bedrock	116
6-5	Effect of 50 m change in bedrock depth	117
6-6	Expected fractional statistical uncertainty	118

6-7	Oscillograms for antineutrinos	119
6-8	Oscillograms for neutrinos	119
6-9	Expected event distributions compared to three-neutrino model . . .	120
6-10	Expected event distributions compared to traditional 3+1 model . . .	120
6-11	Asimov sensitivity	123
7-1	Projected energy and angular distribution of the data	125
7-2	Data distribution	126
7-3	Result of the frequentist analysis	128
7-4	Result of the frequentist analysis	129
7-5	Oscillogram for best-fit point	130
7-6	Comparison of best-fit expectation and data to reference model . . .	131
7-7	Systematic and data pulls at best-fit point	132
7-8	Result of the Bayesian analysis	133
7-9	Posterior distributions of the nuisance parameters for the best model.	135
7-10	Correlation between the nuisance parameters.	136
7-11	$-2\Delta\text{LLH}$ and $\log_{10}(\text{Baye's factor})$ versus g^2	137
7-12	Change in pulls by best-fit point	139
7-13	The $g^2 = 3\pi$ panel from the frequentist result.	140
B-1	Systematic and data pulls assuming three neutrinos	146
B-2	Systematic and data pulls for the best traditional 3+1 point	146
B-3	The fit values of the DOM efficiency	147
B-4	The fit values of Ice Gradient 0	148
B-5	The fit values of Ice Gradient 1	149
B-6	The fit values of Hole Ice	150
B-7	The fit values of conventional normalization	151
B-8	The fit values of the cosmic ray spectral tilt	152
B-9	The fit values of the atmospheric density shift	153
B-10	The fit values of Barr WM	154
B-11	The fit values of Barr WP	155

B-12 The fit values of Barr YM	156
B-13 The fit values of Barr YP	157
B-14 The fit values of Barr ZM	158
B-15 The fit values of Barr ZP	159
B-16 The fit values of the astrophysical normalization	160
B-17 The fit values of the astrophysical spectral tilt	161
B-18 The fit values of the neutrino cross section	162
B-19 The fit values of the antineutrino cross section	163
B-20 The fit values of the kaon-nucleus cross section	164

List of Tables

1.1	Oscillation amplitudes for 3+1 model	28
5.1	Estimated uncertainties in the production of charged kaons and pions	95
6.1	Expected contributions to the event selection	108
6.2	Nuisance parameter central values, priors and boundaries	112
6.3	Critical values of the χ^2 test statistic	123
6.4	Strength of evidence determined from the Bayes factor.	124
7.1	Best-fit physics and nuisance parameter values.	127

Chapter 1

Introduction

1.1 Neutrino oscillations in vacuum

In the Standard Model of particle physics, there exist three neutrino flavor states: electron neutrino (ν_e), muon neutrino (ν_μ), and tau neutrino (ν_τ) [1–4]. The flavor of a neutrino can only be determined in charged current interactions, which involve the exchange of a W^\pm boson, and when the charged lepton that is produced can be identified. In these interactions, an incoming electron neutrino will produce an outgoing electron (e^-); a muon neutrino, a muon (μ^-); and a tau neutrino, a tau (τ^-), as shown in Fig 1-1. In the charged current interactions of antineutrinos, the corresponding positively charged lepton will be produced.

In the massive neutrino Standard Model, there exist three neutrino mass states

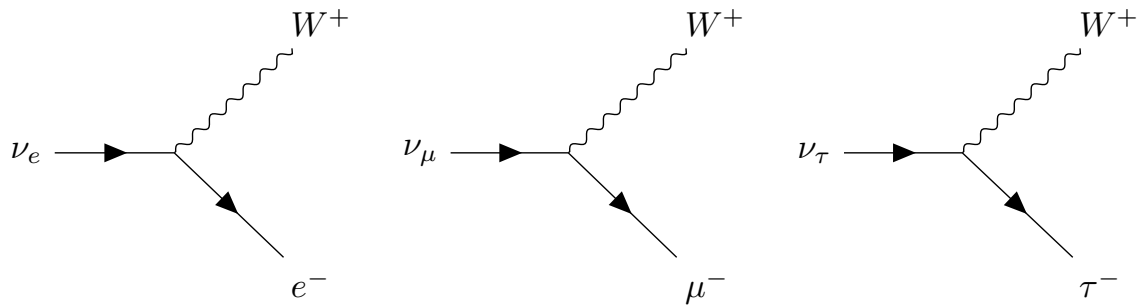


Figure 1-1: Feynman vertices for charged current neutrino interactions. Figure produced with TikZ-Feynman [5].

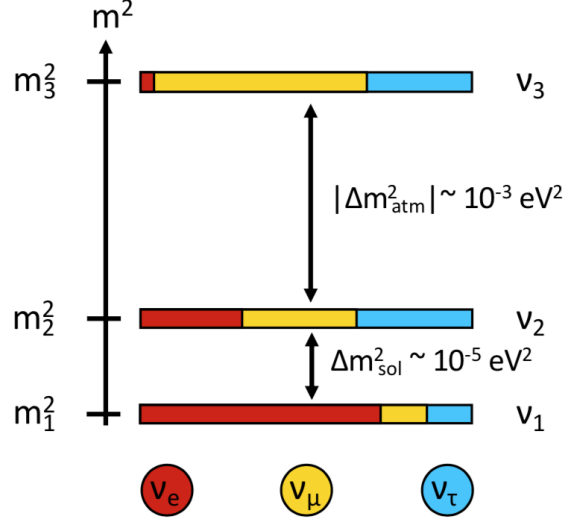


Figure 1-2: Schematic of the Normal Ordering, with approximate neutrino flavor contributions to each neutrino mass state.

$(\nu_1, \nu_2, \text{ and } \nu_3)$ that are distinct from the flavor states. The flavor and mass states mix via a unitary mixing matrix, the Pontecorvo-Maki-Nakagawa-Sakata (PMNS) matrix, U :

$$\begin{pmatrix} \nu_e \\ \nu_\mu \\ \nu_\tau \end{pmatrix} = \begin{pmatrix} U_{e1} & U_{e2} & U_{e3} \\ U_{\mu 1} & U_{\mu 2} & U_{\mu 3} \\ U_{\tau 1} & U_{\tau 2} & U_{\tau 3} \end{pmatrix} \begin{pmatrix} \nu_1 \\ \nu_2 \\ \nu_3 \end{pmatrix}. \quad (1.1)$$

This is equivalent to

$$|\nu_\alpha\rangle = \sum_{i=1}^3 U_{\alpha i}^* |\nu_i\rangle, \quad (1.2)$$

which follows the notation in [3,4]. This is illustrated schematically in Fig. 1-2. The mass states, $|\nu_i\rangle$, are eigenstates of the Hamiltonian. Assuming that the neutrino is a plane wave, the time evolution of the mass states is

$$|\nu_i(t)\rangle = e^{-iE_i t} |\nu_i\rangle, \quad (1.3)$$

and therefore, the time evolution of the flavor states is

$$|\nu_\alpha(t)\rangle = \sum_{i=1}^3 U_{\alpha i}^* e^{-iE_i t} |\nu_i\rangle, \quad (1.4)$$

where E_i is the energy of the i^{th} mass state and t is time. The neutrino mass states have three distinct masses, m_i . The mass-squared splittings are

$$\Delta m_{ij}^2 \equiv m_i^2 - m_j^2. \quad (1.5)$$

Neutrinos are highly relativistic particles, which means

$$E_i = \sqrt{p^2 + m_i^2} \simeq p + \frac{m_i^2}{2E_i} \quad (1.6)$$

$$t = L.$$

Here it is assumed that all mass states have the same momentum, p , and L is the baseline the neutrino has traveled, using natural units. All this together gives rise to the phenomenon of neutrino oscillation, where a neutrino born in one flavor state, ν_α , has an oscillatory probability of transforming into another state ν_β , as it travels through space. This oscillation probability is given by

$$P(\nu_\alpha \rightarrow \nu_\beta) = |\langle \nu_\beta | \nu_\alpha(t) \rangle|^2 \simeq \sum_{\substack{k,j \in [1,2,3] \\ k \neq j}} U_{\alpha k}^* U_{\beta k} U_{\alpha j} U_{\beta j}^* \exp\left(\frac{-i \Delta m_{kj}^2 L}{2E}\right) \quad (1.7)$$

where E is the energy of the neutrino. This formula is applicable if one can assume that the difference in energies of the various mass eigenstates can be neglected. A review on neutrino oscillation that explores the assumptions that were made here is in [6]. The oscillation of 1 GeV neutrinos born in the muon flavor is shown in Fig. 1-3. The observation of neutrino oscillation is the reason neutrinos are known to have mass, since nonzero Δm^2 requires at least one nonzero mass state [4, 7–9].

Like any unitary matrix, the PMNS matrix may be decomposed as the product of rotation matrices. A convenient representation is:

$$U = \begin{pmatrix} 1 & 0 & 0 \\ 0 & \cos \theta_{23} & \sin \theta_{23} \\ 0 & -\sin \theta_{23} & \cos \theta_{23} \end{pmatrix} \begin{pmatrix} \cos \theta_{13} & 0 & \sin \theta_{13} e^{i\delta_{\text{CP}}} \\ 0 & 1 & 0 \\ -\sin \theta_{13} e^{-i\delta_{\text{CP}}} & 0 & \cos \theta_{13} \end{pmatrix} \begin{pmatrix} \cos \theta_{12} & \sin \theta_{12} & 0 \\ -\sin \theta_{12} & \cos \theta_{12} & 0 \\ 0 & 0 & 1 \end{pmatrix}. \quad (1.8)$$

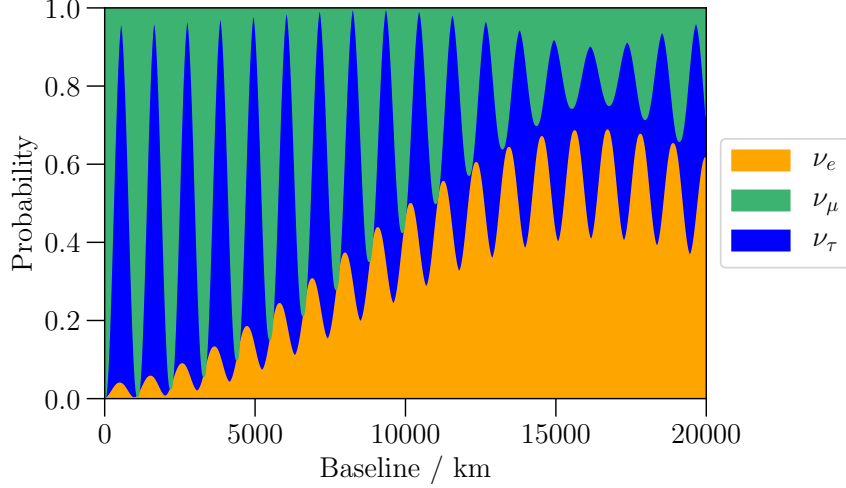


Figure 1-3: Neutrino oscillation probabilities for 1 GeV neutrinos born in the muon flavor, shown as a function of distance from the point of creation, or baseline. The oscillation probability of $\nu_\mu \rightarrow \nu_e$ is shown in yellow. The survival probability of $\nu_\mu \rightarrow \nu_\mu$ is shown in green. The oscillation probability of $\nu_\mu \rightarrow \nu_\tau$ is shown in blue. Probabilities were calculated with nuSQuIDS [10, 11].

In Eq. 1.8, it is assumed that neutrinos are Dirac and not Majorana, which is equivalent to assuming that neutrinos are not their own antiparticles. If neutrinos are Majorana, the representation of the PMNS matrix in Eq. 1.8 would need to be modified by a fourth factor, a complex matrix, at the far right-hand-side. The Majorana nature of neutrinos is largely irrelevant to this thesis.

The phase angle δ_{CP} in Eq. 1.8 represents violation of charge conjugation parity (CP) symmetry. A value of δ_{CP} that is neither 0° nor 180° would mean that neutrinos and antineutrinos have different oscillation probabilities. The global best-fit value of δ_{CP} is consistent with 180° [7, 8]. The work in this thesis is largely insensitive to CP violation. For simplicity, δ_{CP} is assumed to be 0 in this work; equivalently, neutrinos and antineutrinos are assumed to have identical oscillation probabilities.

Another unknown is the neutrino mass ordering, that is, the order of m_1 , m_2 , and m_3 . Solar neutrino experiments have determined that m_2 is greater than m_1 , with $\Delta m_{21}^2 \approx 7 \times 10^{-5} \text{ eV}^2$ [4]. Atmospheric neutrino experiments have determined that $|\Delta m_{31}|^2$ is much greater than $|\Delta m_{21}|^2$, with $|\Delta m_{31}|^2 \approx 2 \times 10^{-3} \text{ eV}^2$. The Normal Ordering refers to the scenario where m_3 is larger than m_1 , as depicted in Fig. 1-2, and

the Inverted Ordering is the alternative. The work in this thesis is largely insensitive to the ordering of the masses for the three known neutrinos. The Normal Ordering is assumed.

In the approximation of two neutrino flavors and two neutrino mass states, there is only one rotation angle, θ , and one mass-squared splitting, Δm^2 . In this scenario, the probability for a ν_α to oscillate to ν_β is given by Eq. 1.9 and the survival probability is for ν_α to remain ν_α is given by Eq. 1.10. The amplitude of oscillation is set by the mixing angle, θ , and the frequency is set by Δm^2 :

$$P(\nu_\alpha \rightarrow \nu_\beta) = \sin^2(2\theta) \sin^2\left(\frac{\Delta m^2 L}{4E}\right) \quad (1.9)$$

$$P(\nu_\alpha \rightarrow \nu_\alpha) = 1 - \sin^2(2\theta) \sin^2\left(\frac{\Delta m^2 L}{4E}\right) \quad (1.10)$$

1.2 Anomalies

Some long-standing neutrino experimental results do not fit within the three-neutrino oscillation framework [12]. Two of the most significant of these are the Liquid Scintillator Neutrino Experiment (LSND) and MiniBooNE. While inconsistent with the massive neutrino Standard Model, these results are consistent with each other, motivating searches for new physics, including the work in this thesis. These experiments are reviewed below and a more detailed review can be found in [12].

LSND ran at the Los Alamos National Laboratory LAMPF/LANSCE accelerator during 1993-1998 [13,14]. A 798 MeV proton beam struck a target, producing charged pions (π^\pm) and muons that came to rest in the beam dump. Stopped negatively charged pions would undergo nuclear capture, while stopped positively charged pions would undergo the decay chain

$$\begin{aligned} \pi^+ &\rightarrow \nu_\mu \mu^+ \\ \mu^+ &\rightarrow \bar{\nu}_\mu \nu_e e^+, \end{aligned} \quad (1.11)$$

where the muon also comes to rest before it decays. This produced a beam containing muon antineutrinos, muon neutrinos and electron neutrinos, with electron antineutrino contamination at the level of approximately 10^{-4} of the muon antineutrino flux in the relevant energy range [12, 15, 16]. The detector was a tank filled with mineral oil doped with scintillator and was instrumented with photomultiplier tubes. The center of the detector was 30 m away from the beam stop. In the detector, electron antineutrinos would interact via inverse beta decay,

$$\bar{\nu}_e p \rightarrow e^+ n, \quad (1.12)$$

while electron neutrinos would interact by scattering off carbon,

$$\nu_e + {}^{12}\text{C} \rightarrow {}^{12}\text{N}_{\text{ground state}} + e^-. \quad (1.13)$$

These two interactions were distinguishable, as the electron antineutrino signal had two features, annihilation of the positron (e^+) and a 2.2 MeV gamma from neutron capture, while the electron neutrino signal had one, the electron.

LSND observed an excess of electron antineutrino events [14]. The LSND result is shown in Fig. 1-4. Data are shown as black points. The purple and red stacked histograms are the expected background contributions. The beam-off backgrounds have been subtracted, which can explain the negative data point. The significance of the LSND anomaly is 3.8σ .

The MiniBooNE experiment was designed to probe the LSND anomaly [17, 18]. MiniBooNE ran at Fermi National Accelerator Laboratory during 2002 - 2019. MiniBooNE used the Booster Neutrino Beamline, created from 8 GeV protons hitting a target. Charged mesons, namely, pions and kaons were produced, and the polarity of the magnetic focusing horn would select for either positively or negatively charged mesons. These mesons would decay in flight to produce a muon neutrino or muon antineutrino beam. The MiniBooNE detector sat 541 m downstream of the target and was composed of a large tank filled with mineral oil and instrumented with photomultiplier tubes.

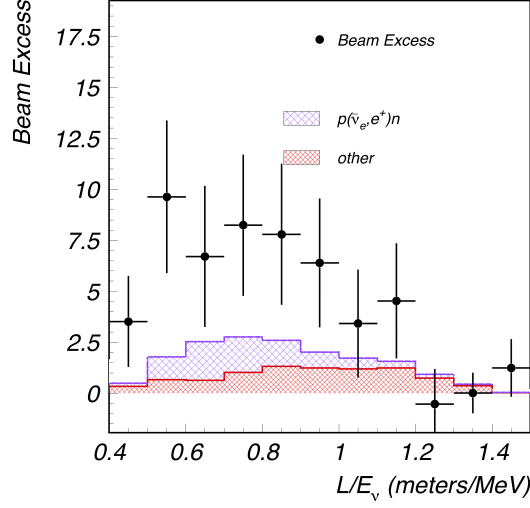


Figure 1-4: Distribution of LSND beam-on events as a function of baseline/energy. Figure adapted from [14].

MiniBooNE observed an excess of electron-like events in both the muon neutrino beam and muon antineutrino beam, shown in Fig. 1-5. The data are shown as black points and the expected backgrounds are shown as stacked histograms. At lower energies, the data sits above the background expectation. This is known as the MiniBooNE anomaly, or MiniBooNE low-energy excess. The significance of the MiniBooNE anomaly is 4.8σ .

If the appearance of electron-like events in MiniBooNE and LSND is interpreted as a $\nu_\mu \rightarrow \nu_e$ or $\bar{\nu}_\mu \rightarrow \bar{\nu}_e$ oscillation within a two-flavor model, then using Eq. 1.9 the data point to value a Δm^2 larger than 10^{-2} eV^{-2} . This cannot be accommodated with the three-neutrino framework, because the two known $|\Delta m_{ij}^2|$ do not add to a large enough value. Curiously, while the LSND and MiniBooNE experiments had significant systematic differences, such as a factor of ten in energy and different types of beams (decay-at-rest vs. decay-in-flight), the allowed regions of $[\Delta m^2, \sin^2 2\theta]$ in the oscillation interpretations of LSND and MiniBooNE are highly compatible [18]. The combined LSND and MiniBooNE excesses have a significance of 6.1σ .

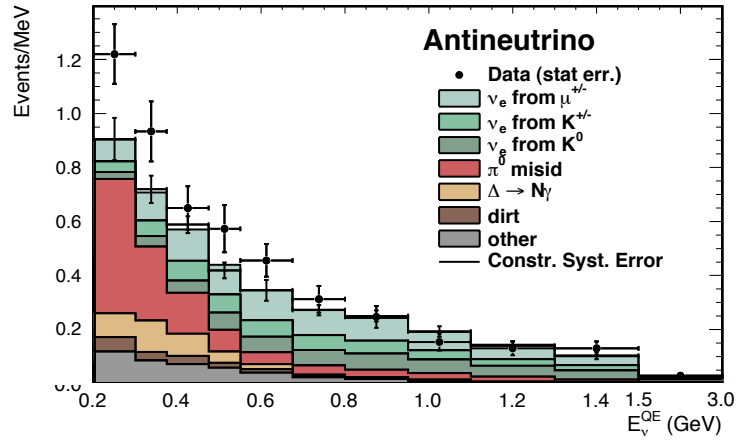
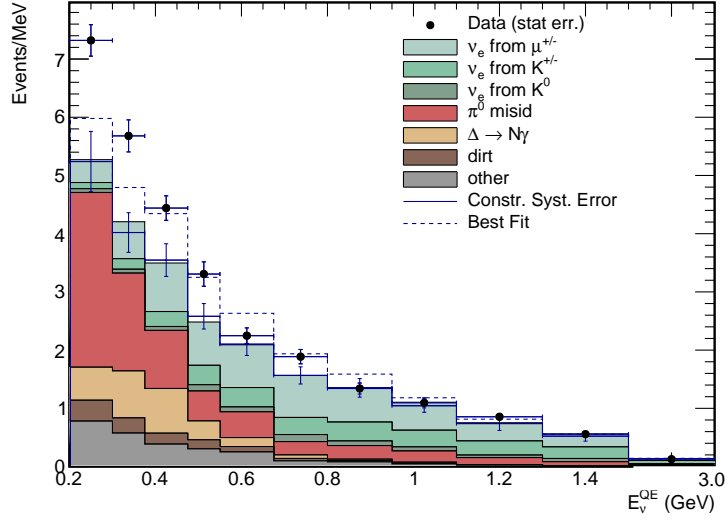


Figure 1-5: (Top) MiniBooNE anomaly in neutrino mode. Figure from [18]. (Bottom) MiniBooNE anomaly in antineutrino mode. Figure adapted from [17].

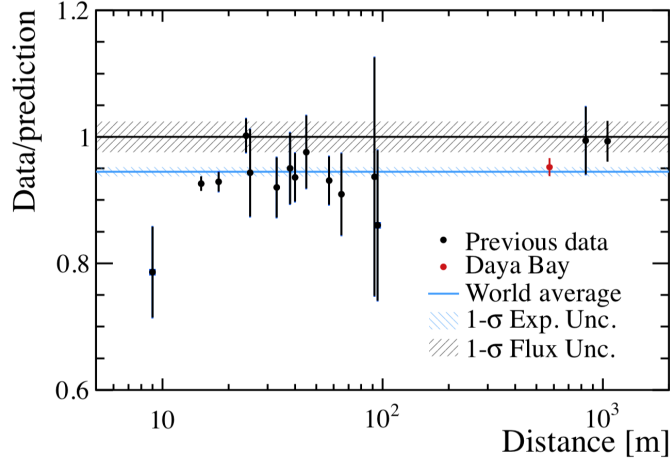


Figure 1-6: Ratio of reactor antineutrino flux measurement to prediction as a function of distance from the reactor core for Daya Bay and prior experiments. Figure from [19].

While LSND and MiniBooNE both observed anomalies in muon (anti)neutrino beams, anomalous results have also been observed in electron (anti)neutrino beams. These include the reactor anomalies and the gallium anomaly. The reactor antineutrino anomaly is a deficit in the flux of electron antineutrinos emerging from nuclear reactors as compared to theoretical predictions [20–23]. This anomaly has been observed in a number of experiments at various baselines from the reactor cores. A recent precision measurement from the experiment Daya Bay, as well as measurements from prior experiments, is shown in Fig. 1-6 [19]. The measurements are normalized to theoretical predictions, accounting for the effects of oscillations. The world average measurement sits significantly below the prediction. Ratios of measurements at different baselines from reactors have found small signals, at the level of $1 - 2\sigma$ [24, 25]. Finally, several experiments have observed a “5 MeV bump,” an unexpected feature in the antineutrino spectra with a magnitude of about 10% [26].

Lastly, the gallium anomaly is a deficit of electron neutrinos observed in the electron-capture decays of ^{37}Ar and ^{51}Cr by the GALLEX and SAGE experiments [27–33]. These were gallium-based experiments designed to measure the solar neutrino flux and which used ^{37}Ar and ^{51}Cr for calibration. These are electron neutrino emitting radioactive sources. These experiments observed a 2.3σ deficit in electron neu-

trinos from these radioactive sources [34].

1.3 Traditional 3+1 model

One model that has been put forth to account for the anomalies previously described is a 3+1 sterile neutrino model [25, 35, 36]. A sterile neutrino, ν_s , is a hypothetical flavor of neutrino which does not interact via the weak nuclear force. A 3+1 model is schematically depicted in Fig. 1-7, for the case of the normal ordering ($m_3 > m_2$). In a 3+1 model, a fourth, heavier mass state, ν_4 is introduced. This mass state is mostly comprised of the sterile flavor, ν_s . The three lighter mass states include a small sterile component. If the fourth mass state is heavy enough, the three lighter masses become degenerate.

In a 3+1 sterile neutrino model, the three-flavor mixing matrix, that is, the PMNS matrix, given in Eq. 1.1, is expanded by one column, to account for the fourth mass state, and one row, to account for the sterile flavor. This expanded, four-flavor mixing matrix is shown in Eq. 1.14:

$$\begin{pmatrix} \nu_e \\ \nu_\mu \\ \nu_\tau \\ \nu_s \end{pmatrix} = \begin{pmatrix} U_{e1} & U_{e2} & U_{e3} & U_{e4} \\ U_{\mu1} & U_{\mu2} & U_{\mu3} & U_{\mu4} \\ U_{\tau1} & U_{\tau2} & U_{\tau3} & U_{\tau4} \\ U_{s1} & U_{s2} & U_{s3} & U_{s4} \end{pmatrix} \begin{pmatrix} \nu_1 \\ \nu_2 \\ \nu_3 \\ \nu_4 \end{pmatrix} \quad (1.14)$$

The representation of the mixing matrix as the product of rotation matrices, given for three-flavor case in Eq. 1.8, requires equivalent modification. Following [37], the four-flavor mixing matrix can be written as

$$U = R_{34} \tilde{R}_{24} \tilde{R}_{14} R_{23} \tilde{R}_{13} R_{12} P, \quad (1.15)$$

where R_{ij} and \tilde{R}_{ij} are, respectively, real and complex rotation matrices in ij space.

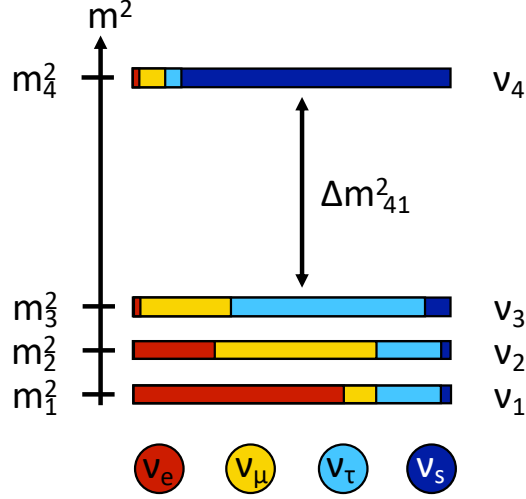


Figure 1-7: Schematic illustration of a 3+1 sterile neutrino model, assuming the normal neutrino ordering. The various components of the mass states, as well as the differences in the masses, are not to scale. This figure is for illustrative purposes only.

For example,

$$R_{34} \equiv \begin{pmatrix} 1 & 0 & 0 & 0 \\ 0 & 1 & 0 & 0 \\ 0 & 0 & \cos \theta_{34} & \sin \theta_{34} \\ 0 & 0 & -\sin \theta_{34} & \cos \theta_{34} \end{pmatrix} \text{ and } \tilde{R}_{14} \equiv \begin{pmatrix} \cos \theta_{14} & 0 & 0 & \sin \theta_{14} e^{-i\delta_{14}} \\ 0 & 1 & 0 & 0 \\ 0 & 0 & 1 & 0 \\ -\sin \theta_{14} e^{i\delta_{14}} & 0 & 0 & \cos \theta_{14} \end{pmatrix}. \quad (1.16)$$

The factor P is the diagonal Matrix:

$$P = \text{diag}(1, e^{i\alpha/2}, e^{i(\beta/2+\delta_{13})}, e^{(\gamma/2+\delta_{14})}), \quad (1.17)$$

where α , β and γ are the Majorana phases. These phases are only nonzero if neutrinos are Majorana particles, i.e. they are their own antiparticles.

In a 3+1 model, neutrinos oscillate between all four flavors. This could account for electron neutrinos appearing in a muon neutrino beam, as seen by LSND and MiniBooNE, as well as a disappearance of electron neutrinos from an electron neutrino

beam, as seen in the reactor and gallium experiments. The oscillation amplitudes for oscillation channels relevant to this thesis, and assuming a two-flavor approximation, are given in Table 1.1. These amplitudes are parameterized in three ways: in terms of the mixing matrix elements, $U_{\alpha i}$, which are the physical parameters; in terms of effective mixing angles, $\theta_{\alpha\beta}$; and in terms of rotation angles, θ_{ij} . In this thesis, plots and discussion related to global fits will use oscillation amplitudes given in terms the effective angles. Plots and discussion related only to the experiment IceCube will use oscillation amplitudes given in terms of rotation angles.

Channel	Mixing matrix elements	Effective mixing angles	Rotation angles
$\nu_e \rightarrow \nu_e$	$4(1 - U_{e4} ^2) U_{e4} ^2$	$\sin^2 2\theta_{ee}$	$\sin^2 2\theta_{14}$
$\nu_\mu \rightarrow \nu_\mu$	$4(1 - U_{\mu 4} ^2) U_{\mu 4} ^2$	$\sin^2 2\theta_{\mu\mu}$	$4 \cos^2 \theta_{14} \sin^2 \theta_{24} (1 - \cos^2 \theta_{14} \sin^2 \theta_{24})$
$\nu_\mu \rightarrow \nu_e$	$4 U_{e4} ^2 U_{\mu 4} ^2$	$\sin^2 2\theta_{\mu e}$	$\sin^2 2\theta_{14} \sin^2 \theta_{24}$

Table 1.1: Oscillation amplitudes for three neutrino oscillation channels given in terms of the mixing matrix elements, the effective mixing angles, and rotation angles. Note that $\sin^2 2\theta_{24} = \sin^2 2\theta_{\mu\mu}$ for $\theta_{14} = 0$.

1.4 Tension in the 3+1 fits

The oscillation amplitudes for the three channels shown in Table 1.1, which are $\nu_e \rightarrow \nu_e$, $\nu_\mu \rightarrow \nu_\mu$ and $\nu_\mu \rightarrow \nu_e$, depend on only two mixing matrix elements: U_{e4} and $U_{\mu 4}$. This means that these two parameters are over-constrained by experimental data spanning the three distinct channels. Global fits spanning these channels have been performed by several groups, and they find similar allowed regions, with Δm_{41}^2 around 1 eV^2 [25, 38, 39]. The most recent global fit finds a 5σ improvement over the null hypothesis, i.e. only three neutrinos [25]. Nevertheless, all three fitting groups find a similar problem in the fits: inconsistency between subgroups of the data.

One natural way to split up the data is into “appearance” and “disappearance” experiments. Appearance experiments are those in the $\nu_\mu \rightarrow \nu_e$ channel, while disappearance experiments are those in the $\nu_e \rightarrow \nu_e$ and $\nu_\mu \rightarrow \nu_\mu$ channels. One method of characterizing consistency between subgroups of data is the *parameter goodness-of-fit*

(PG) [40, 41]. One performs three separate fits: one on the appearance experiments, one on the disappearance experiments, and one on all the datasets. An effective χ^2 is defined [25]:

$$\chi_{\text{PG}}^2 = \chi_{\text{global}}^2 - (\chi_{\text{appearance}}^2 + \chi_{\text{disappearance}}^2). \quad (1.18)$$

The effective number of degrees of freedom is:

$$N_{\text{PG}} = (N_{\text{appearance}} + N_{\text{disappearance}}) - N_{\text{global}}. \quad (1.19)$$

The χ_{PG}^2 is then interpreted as a χ^2 with N_{PG} degrees of freedom and a probability (p -value) is calculated. A recent fit to short-baseline experiments found the p -value for the PG test to be 4E-6, which has a significance of 4.5σ [25]. This means that the appearance datasets and the disappearance datasets are highly inconsistent. This is referred to as tension in the fits. This motivates the consideration of models beyond a traditional 3+1 sterile neutrino model that could relieve this tension.

Chapter 2

Status of 3+1 sterile neutrinos in IceCube

2.1 Neutrino oscillations in matter

The experiment described in this thesis, IceCube, is uniquely capable of searching for a signature of sterile neutrinos that involves matter effects in oscillations. Neutrinos traversing matter experience different oscillation probabilities than those traversing vacuum [42–45]. This is because the different neutrino flavors undergo different interactions with matter, therefore experiencing different potentials, modifying the Hamiltonian. In fact, oscillations in matter may have a larger amplitude than oscillations in vacuum.

Following [46], the Schrödinger equation for a two-flavor approximation in vacuum can be written as

$$i \frac{d}{dt} \begin{pmatrix} \nu_\mu \\ \nu_s \end{pmatrix} = \begin{pmatrix} -\frac{\Delta m^2}{4E} \cos 2\theta_0 & \frac{\Delta m^2}{4E} \sin 2\theta_0 \\ \frac{\Delta m^2}{4E} \sin 2\theta_0 & \frac{\Delta m^2}{4E} \cos 2\theta_0 \end{pmatrix} \begin{pmatrix} \nu_\mu \\ \nu_s \end{pmatrix}, \quad (2.1)$$

where $\sin^2 2\theta_0$ is the oscillation amplitude in vacuum. In the case of oscillations in matter, the ν_μ state experiences a potential due to neutral current (NC) interactions

off quarks, while the ν_s state does not. This potential is

$$V_{\text{NC}} = \mp \frac{\sqrt{2}}{2} G_F N_n, \quad (2.2)$$

where $-(+)$ corresponds to $\nu_\mu(\bar{\nu}_\mu)$, G_F is the Fermi constant and N_n is the neutron number density. Adding this potential to the effective Hamiltonian,

$$i \frac{d}{dt} \begin{pmatrix} \nu_\mu \\ \nu_s \end{pmatrix} = \begin{pmatrix} -\frac{\Delta m^2}{4E} \cos 2\theta_0 \mp \frac{\sqrt{2}}{2} G_F N_n & \frac{\Delta m^2}{4E} \sin 2\theta_0 \\ \frac{\Delta m^2}{4E} \sin 2\theta_0 & \frac{\Delta m^2}{4E} \cos 2\theta_0 \end{pmatrix} \begin{pmatrix} \nu_\mu \\ \nu_s \end{pmatrix}, \quad (2.3)$$

and assuming constant matter density, one can diagonalize the effective Hamiltonian to find the oscillation amplitude in matter:

$$\sin^2 2\theta_{\text{matter}} = \frac{\left(\frac{\Delta m^2}{2E}\right)^2 \sin^2 2\theta_0}{\left(\frac{\Delta m^2}{2E} \cos 2\theta_0 \pm \frac{\sqrt{2}}{2} G_F N_n\right)^2 + \left(\frac{\Delta m^2}{2E}\right)^2 \sin^2 2\theta_0}. \quad (2.4)$$

The eigenstates in matter are a linear combination of the flavor eigenstates. A critical energy exists where regardless of the magnitude of the oscillation amplitude in vacuum, the oscillation amplitude in matter becomes unity either for neutrinos or antineutrinos. This critical energy is

$$E_{\text{critical}} = \mp \frac{\Delta m^2 \cos 2\theta_0}{\sqrt{2} G_F N_n}. \quad (2.5)$$

If Δm^2 is positive and the mixing angle is relatively small, that is, $|\theta_0| < \frac{\pi}{4}$, the resonance occurs for antineutrinos rather than neutrinos. For the following values,

$$\begin{aligned} \Delta m_{41}^2 &\approx 1 \text{ eV}^2 \\ \cos 2\theta_0 &\approx 1 \\ \rho_{\text{Earth}} &\approx 6 \text{ g/cm}^3, \end{aligned} \quad (2.6)$$

where ρ_{Earth} is the average density of the Earth, and with the approximation that half of the Earth's mass is from neutrons, one finds the critical energy to be about 3 TeV. This suggests that for sterile parameter values consistent with global fit find-

ings, a resonant transition would occur for antineutrinos traversing the Earth at TeV energies [47–49].

This derivation made two simplifying assumptions: constant density and two-flavor oscillations. Reality is more complicated. Oscillation probabilities for neutrinos traversing the diameter of the Earth, accounting for both the radially varying Earth density and a full four-neutrino oscillation framework, are calculated with `nuSQuIDS` and shown in the Figs. 2-1 and 2-2. In these calculations, the sterile parameters are

$$\begin{aligned}\Delta m^2 &= 1 \text{ eV}^2 \\ \sin^2 2\theta_{24} &= 0.1,\end{aligned}\tag{2.7}$$

and all other sterile mixing angles and CP-violating angles are zero. The neutrinos are born in the muon flavor. In Fig. 2-1, the oscillation probabilities for neutrinos and antineutrinos are shown as a function of baseline across the diameter of the Earth, for the energy 2.3 TeV. At this energy, the probability of oscillating from the muon flavor into either the electron or tau flavors is minuscule. The left panel corresponds to neutrinos; only small oscillations from the muon to sterile flavor are observed, shown in magenta. The right panel corresponds to antineutrinos; a resonant oscillation into the sterile flavor is observed. The magnitude of this conversion is much greater than 0.1 which is the value of $\sin^2 \theta_{\mu\mu}$, and would be the amplitude of the oscillation in vacuum.

Figure 2-2 shows the same phenomenon, over the energy range between 100 GeV and 100 TeV. This figure only shows the final oscillation probabilities across the diameter of the Earth. The thick magenta line shows the probability of a muon antineutrino oscillating into the sterile flavor, and the peak of the resonance is found at 2.3 TeV, corresponding to the scenario shown in Fig. 2-1. The thick green line shows the probability of such a muon antineutrino remaining in the muon flavor. The thin lines show the corresponding probabilities for neutrinos, rather than antineutrinos. At the lowest energies, oscillation into the electron and tau flavors is non-negligible, which accounts for the shown probabilities not adding up to unity.

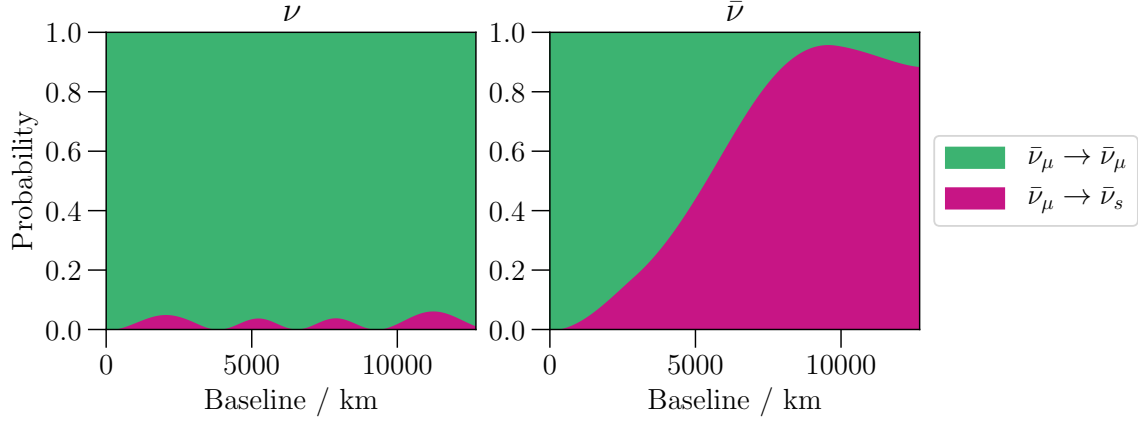


Figure 2-1: Oscillation probabilities as a function of baseline for a muon neutrino (left) and a muon antineutrino (right) traversing the diameter of the Earth for $\Delta m_{41}^2 = 1 \text{ eV}^2$, $\sin^2 2\theta_{24} = 0.1$, and 2.3 TeV of energy. Probabilities are calculated with nuSQuIDS [11].

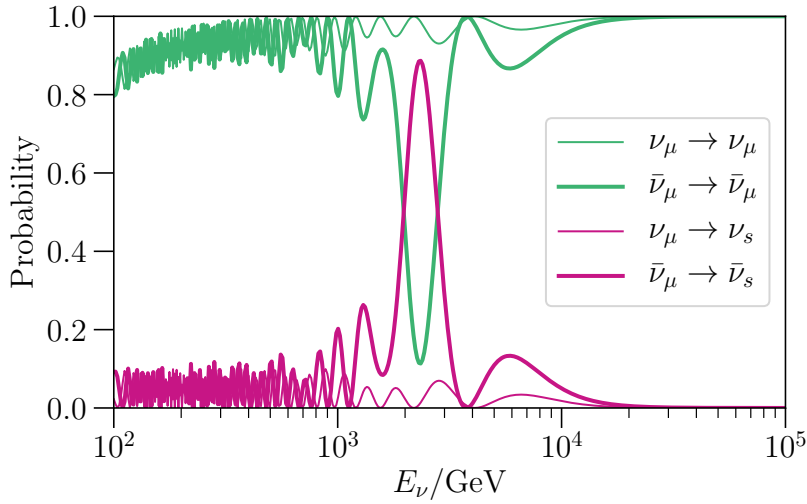


Figure 2-2: Oscillation probabilities as a function of energy for muon neutrinos (thin lines) and muon antineutrinos (thick lines) after having traversed the diameter of the Earth, for $\Delta m_{41}^2 = 1 \text{ eV}^2$ and $\sin^2 2\theta_{24} = 0.1$. The probability of remaining in the muon flavor is shown in green. The probability of oscillating into the sterile flavor is shown as magenta.

2.2 Brief description of IceCube

IceCube is a neutrino detector that can observe TeV neutrinos originating from across the Earth, allowing for a unique search for sterile neutrinos that makes use of the matter effect parametric resonance discussed previously. A brief description of IceCube is given here to facilitate understanding of the rest of this chapter and the following one. A longer description is given in Chapter 4. IceCube is a gigaton ice-Cherenkov neutrino detector located deep in the ice at the South Pole. Over 5000 optical sensors are deployed in the ice to observe light produced in neutrino interactions. IceCube observes atmospheric and astrophysical neutrinos coming from all directions, although the work in this thesis uses upward-going neutrinos, that is, those originating from below the horizon. IceCube detects neutrinos with energies above 100 GeV, and as high as several PeV. The atmospheric and astrophysical neutrino fluxes fall steeply with energy, while the efficiency of the detector increases with energy. This results in a peak of events near one TeV [50], which is shown in Fig. 2-3.

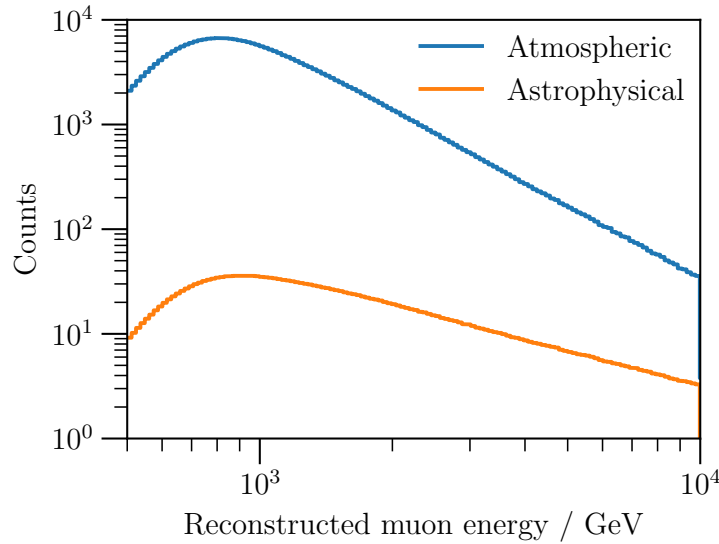


Figure 2-3: Predicted event distribution of muons associated with atmospheric and astrophysical neutrinos. This prediction corresponds to a livetime of 7.6 years. These events originate below the horizon.

2.3 Eight-year search results

A one-year search for an eV-scale sterile neutrino at TeV-energies was performed in 2015 in IceCube and found no evidence for them [51–53]. A subsequent eight-year search, with a fifteen-fold increase in statistics, was performed [54–56]. This search made use of the atmospheric neutrino flux systematic treatment described in Chapter 5. Both a frequentist analysis and a Bayesian analysis were performed. The result of the frequentist analysis is shown in Fig. 2-4 and the result of the Bayesian analysis is shown in Fig. 2-5. The frequentist analysis found a best-fit point at $\Delta m_{41}^2 = 4.5 \text{ eV}^2$ and $\sin^2 2\theta_{24} = 0.10$, and found that the null hypothesis was rejected with a p -value of 8%. The Bayesian analysis found a best-model location with approximately the same sterile parameter values, and found that model to be strongly preferred, by a factor of about 10, to the null hypothesis, that is, no sterile neutrino.

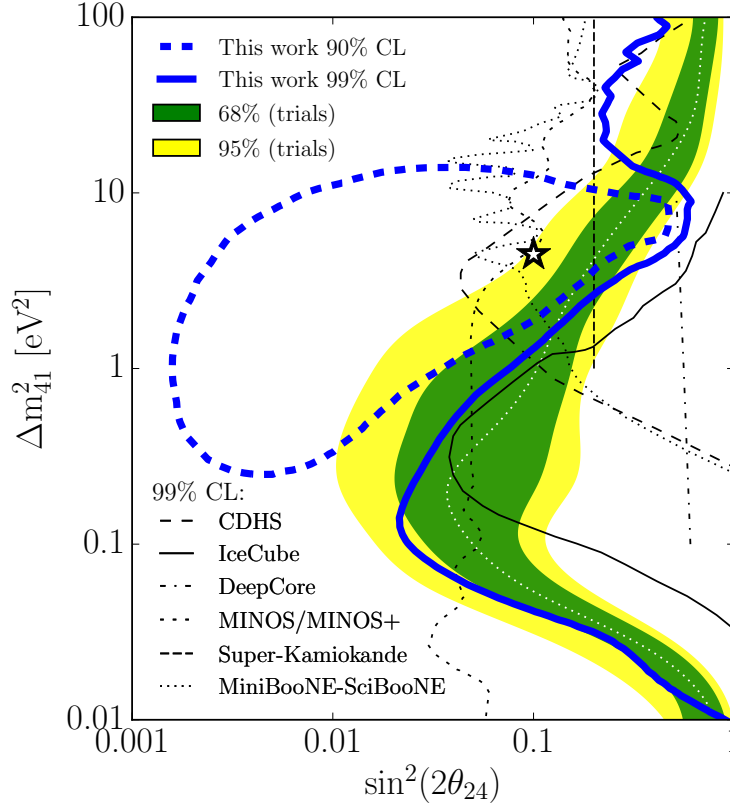


Figure 2-4: Frequentist result from an eight-year search for sterile neutrinos in IceCube. The best-fit point is marked with a star. The confidence level contours are found assuming Wilks' theorem, and are shown at 90% and 99% in dashed and solid blue curves, respectively. The median sensitivity at 99% confidence level is found from pseudoexperiments, and is shown as a thin dashed white curve. The 1σ and 2σ ranges of the sensitivity are shown in green and yellow bands, respectively. Results from other experiments are shown as black curves, and they reject the region to their right. Figure from [55].

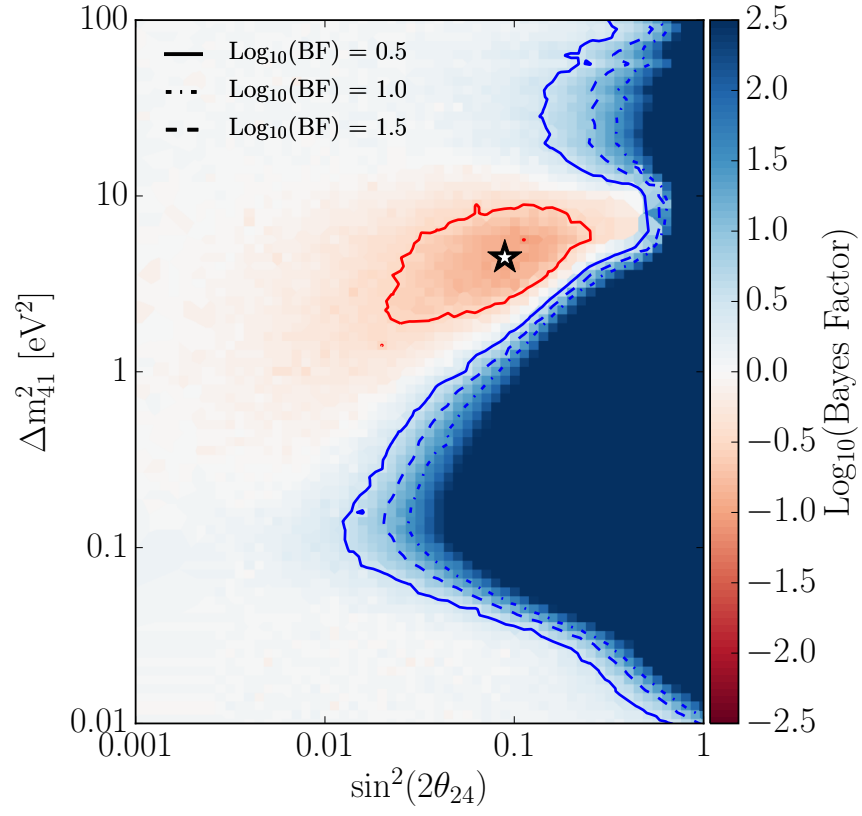


Figure 2-5: Bayesian result from an eight-year search for sterile neutrinos in IceCube. The logarithm of the Bayes factor [57] for a particular sterile model relative to the null hypothesis is shown. The best-model point is marked with a star. Figure from [55].

2.4 Jumping off point for the work in this thesis

The result of the eight-year search for sterile neutrinos in IceCube is intriguing. The best-fit point and the point corresponding to the best-model are in the region of interest from global fits. This result is likely to modify the global fit results. Nevertheless, the result is not very statistically significant and tension is likely to remain in the global fits. An alternative model that could resolve the tension is motivated. The rest of this thesis describes such a sterile neutrino model and a search for it in the IceCube experiment.

Chapter 3

Phenomenology of unstable sterile neutrinos in IceCube

3.1 Unstable sterile neutrino model in IceCube

In the Standard Model of Particle Physics, stable particles are those that are protected by a fundamental symmetry. Others decay. There is no fundamental symmetry that protects neutrinos. In the massive neutrino Standard Model, the heavier two of the three mass states can decay radiatively. Two processes for a heavier mass state, ν_i , to decay to a lighter mass state, ν_j , are

$$\begin{aligned}\nu_i &\rightarrow \nu_j + \gamma && \text{with lifetime } \tau \simeq 10^{36}(m_i/\text{eV})^{-5} \text{ years} \\ \nu_i &\rightarrow \nu_j + \gamma + \gamma && \text{with lifetime } \tau \simeq 10^{67}(m_i/\text{eV})^{-9} \text{ years,}\end{aligned}\tag{3.1}$$

where γ is a photon [25,58,59]. These decays are slow; for the neutrinos of the massive neutrino Standard Model, the lifetimes are many times longer the age of the Universe.

If there is a fourth mass state, it may decay. The decay of a heavy, fourth mass state, in the range 1 keV - 1 MeV was previously considered to explain the LSND anomaly [60,61]. In the following publication [62], a model involving oscillations and decay for eV-scale neutrinos was developed and applied to the IceCube detector. This used the open dataset from the one-year high-energy sterile neutrino search [53].

Exploring a nonminimal sterile neutrino model involving decay at IceCube

Z. Moss,^{*} M. H. Moulai,[†] C. A. Argüelles,[‡] and J. M. Conrad[§]

*Department of Physics, Massachusetts Institute of Technology,
Cambridge, Massachusetts 02139, USA*



(Received 26 November 2017; published 12 March 2018)

We study the phenomenology of neutrino decay together with neutrino oscillations in the context of eV-scale sterile neutrinos. We review the formalism of visible neutrino decay in which one of the decay products is a neutrino that potentially can be observed. We apply the formalism developed for decay to the recent sterile neutrino search performed by IceCube with TeV neutrinos. We show that for a ν_4 lifetime $\tau_4/m_4 \lesssim 10^{-16}$ eV⁻¹ s, the interpretation of the high-energy IceCube analysis can be significantly changed.

DOI: [10.1103/PhysRevD.97.055017](https://doi.org/10.1103/PhysRevD.97.055017)

I. INTRODUCTION

Oscillations between the three active flavors of neutrinos, ν_e , ν_μ , and ν_τ , have been definitively observed [1,2]. The mixing angles and mass-squared differences that describe these oscillations have been well measured [3], but the CP -violating phase value remains unknown. Nevertheless, there remain anomalies in accelerator [4–6], reactor [7], and radioactive source [8] experiments that do not fit this model well. These anomalies are often explained by introducing a new neutrino state, ν_s , that does not participate in the Standard Model (SM) weak interactions, hence the name sterile neutrino. As among the active neutrinos, mass mixing induces new flavor transitions between the sterile and the active neutrino flavors. The mass spectrum of the minimal sterile neutrino model contains three mostly active, light neutrinos, ν_1 , ν_2 , and ν_3 , and one mostly sterile neutrino, ν_4 . In the minimal 3 + 1 sterile neutrino model, ν_4 is much heavier than the other mass eigenstates.

Searches for sterile neutrinos performed by the IceCube [9,10], MINOS [11], Super-Kamiokande [12], KARMEN [13], MiniBooNE/SciBooNE [14], and CDHS [15] collaborations have found null results. This has produced increasing tension between the favored regions of parameter space found in global fits to short-baseline data and null results [16–19]. This tension has led to the consideration of more complicated new physics scenarios. These

include a keV fourth neutrino with decay [20–24], three and four neutrinos with CPT violation [25–31], five-neutrino oscillation [32], quantum decoherence [31,33], Lorentz violation [30,34], sterile neutrinos in extra dimensions [35–37], neutrinos with varying mass [38–40], muon decay with lepton number violation [41–43], three twin-neutrinos [44], neutrino-antineutrino oscillations [45], neutrino decay in the unparticle scenario [46], CP violation from neutral heavy leptons [47], and nonstandard interactions [48–50]. Here, we consider in detail the interplay of neutrino oscillation and neutrino decay in a 3 + 1 sterile neutrino model.

Neutrino decay is predicted by the SM, but the rate is too small to be detected by present experimental searches. Neutrino decay via some new physics process may be important and has previously been considered in the context of solar neutrinos [51–56], atmospheric neutrinos [57–62], accelerator neutrinos [60,63–65], supernova neutrinos [66–69], cosmology [70,71], and high-energy astrophysical neutrinos [72–74]. Although neutrino decay is an interesting theoretical proposition, it has not been observed and is very constrained for active neutrinos [52,71,75,76]. However, as we will discuss in detail in this work, constraints on the mostly sterile neutrino lifetime are weaker, and the IceCube results can be significantly altered, as we show in our main result.

The outline of this paper is as follows. In Sec. II we introduce the neutrino decay model. In Sec. III we develop our framework for models of neutrino oscillation with neutrino decay for two scenarios. First we consider the case where the neutrino daughters are all beyond the Standard Model particles, which we term “invisible decay.” Second, we consider the case where one neutrino daughter is a lighter SM neutrino, which we refer to as “visible decay.” In Sec. IV we illustrate our model in the IceCube experiment using atmospheric neutrino data. Finally, in Sec. V, we provide concluding remarks.

^{*}zander@caltech.edu

[†]marjon@mit.edu

[‡]caad@mit.edu

[§]conrad@mit.edu

II. NEUTRINO DECAY MODELS

In this paper, we are interested in neutrino decay via new interactions. The simplest cases are those in which the neutrino decays into two particles. These are expected to be dominant over decays into three or more particles, as these involve high-dimensional operators [77]. Figure 1 shows a diagram of this process. We can organize the two-daughter processes into (I) invisible and (II) visible decays. Note that in (I), if one of the new particles decays into neutrinos, then this can be reduced to an effective three-body decay, which we have chosen to neglect. From these statements, it follows that in (I) $\nu_i \rightarrow \phi\psi$ and in (II) $\nu_i \rightarrow \nu_j\phi$, where ψ is a fermion and ϕ is a boson. Due to it being phenomenologically more interesting, we will restrict our examples to the visible decay scenario case, i.e., ψ is one of the SM neutrinos, and consider ϕ to be either a scalar or pseudoscalar.

A. Lagrangians of simplified models

In this work, we will use simplified models to introduce the aforementioned decay scenarios, as done, for example, in Refs. [78,79]. For simplicity, we write this section assuming that the neutrino is a Majorana field. This assumption can be relaxed by introducing right-handed neutrinos [77], which would be related to Dirac mass terms and would give rise to a different phenomenology due to the lack of $\nu \rightarrow \bar{\nu}$ transitions and visible decay. With this assumption, the scalar-neutrino interaction is [80]

$$\mathcal{L}_{\text{int}} = \frac{g_{ij}^s}{2} \bar{\nu}_i^c \nu_j \phi + i \frac{g_{ij}^p}{2} \bar{\nu}_i^c \gamma_5 \nu_j \phi, \quad (1)$$

where $g_{ij}^s, (g_{ij}^p)$ are the (pseudo)scalar couplings that control the transition strength from parent (i) to daughter (j): $\nu_i \rightarrow \nu_j \phi$. In other words, g carries two indices: one for the parent neutrino mass eigenstate and another for the daughter neutrino mass eigenstate. Note that we assume $\hbar = c = 1$ throughout, except where we explicitly restore constants to estimate decay lengths.

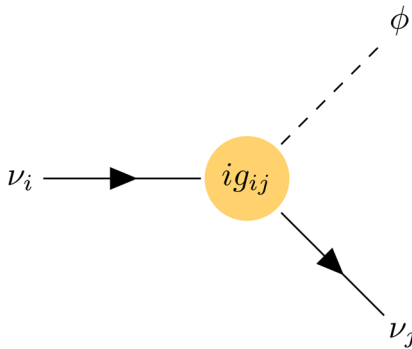


FIG. 1. Decay of a massive neutrino state to a lighter neutrino mass state and a scalar ϕ .

B. Decay rates

In the case where the boson is massless, our scenario is analogous to neutrino-Majoron decays. As in that case, there are two scenarios induced by Eq. (1). The first one is a chirality-preserving process, whose partial decay rate is [78,81]

$$\Gamma(\nu_i^{(\pm)} \rightarrow \nu_j^{(\pm)} \phi) = \frac{m_i^2}{16\pi x_{ij} E_p} [(g_{ij}^s)^2 f(x_{ij}) + (g_{ij}^p)^2 g(x_{ij})], \quad (2)$$

where we have introduced the parent-to-daughter mass ratio, $x_{ij} = m_i/m_j > 1$, and have labeled the energy of the parent neutrino, ν_i , by E_p . The second one is a chirality-violating process

$$\Gamma(\nu_i^{(\pm)} \rightarrow \nu_j^{(\mp)} \phi) = \frac{m_i^2}{16\pi x_{ij} E_p} [(g_{ij}^s)^2 + (g_{ij}^p)^2] k(x_{ij}). \quad (3)$$

In both cases, the auxiliary functions are given by [81]

$$f(x) = \frac{x}{2} + 2 + \frac{2}{x} \log x - \frac{2}{x^2} - \frac{1}{2x^3}, \quad (4a)$$

$$g(x) = \frac{x}{2} - 2 + \frac{2}{x} \log x + \frac{2}{x^2} - \frac{1}{2x^3}, \quad (4b)$$

$$k(x) = \frac{x}{2} - \frac{2}{x} \log x - \frac{1}{2x^3}, \quad (4c)$$

where we have dropped the indices for clarity. If the lightest neutrino is massless, then for approximately eV sterile neutrinos, the smallest $x_{ij} \sim 10^2 \gg 1$, while if the lightest neutrino saturates the current kinematic limits, then the smallest $x_{ij} \sim 10$. In the limit of $m_i \gg m_j$, the partial decay rates given in Eqs. (2) and (3) are just [81]

$$\Gamma_{ij} = [(g_{ij}^s)^2 + (g_{ij}^p)^2] \frac{m_i^2}{32\pi E_p}. \quad (5)$$

In any case, the neutrinos that we are considering are relativistic, and thus the products of the decay will travel along the direction of the beam [78] and the relevant quantity is the energy distribution of the daughter in the lab frame. In the relativistic limit, the expression for this quantity simplifies if we assume either pure scalar ($g^p \equiv 0$) or pure pseudoscalar ($g^s \equiv 0$) cases. We will make this assumption throughout the rest of the paper, and in particular, we will assume purely scalar couplings in our analysis. For the chirality-preserving process, the energy distribution takes the form [79]

$$\frac{1}{\Gamma_{ij}} \frac{d}{dE_d} \Gamma(\nu_i^{(\pm)} \rightarrow \nu_j^{(\pm)} \phi) = \frac{x_{ij}^2}{x_{ij}^2 - 1} \frac{1}{E_p^2 E_d} \frac{(E_p \pm x_{ij} E_d)^2}{(x_{ij} \pm 1)^2}, \quad (6)$$

where $+$ corresponds to the pure scalar case and $-$ to the pure pseudoscalar one, and E_d labels the energy of the

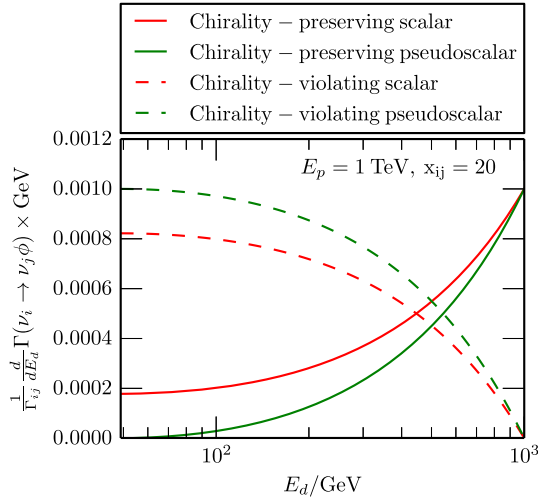


FIG. 2. Decay daughter energy distributions for chirality-preserving (solid) and chirality-violating (dashed) processes, for the scalar (red) and pseudoscalar (green) cases. In all these cases, we have set the parent energy to 1 TeV and $x_{ij} = 20$. These energy distributions are given in Eqs. (6) and (7).

daughter neutrino, ν_j . For the chirality-violating process, the distribution takes the form

$$\frac{1}{\Gamma_{ij}} \frac{d}{dE_d} \Gamma(\nu_i^{(\pm)} \rightarrow \nu_j^{(\mp)} \phi) = \frac{x_{ij}^2}{x_{ij}^2 - 1} \frac{E_p - E_d}{E_p^2 E_d} \frac{x_{ij}^2 E_d - E_p}{(x_{ij} \pm 1)^2}. \quad (7)$$

In both cases, due to kinematic constraints, the daughter energy is bounded to $E_p/x_{ij}^2 \leq E_d \leq E_p$ [79]. In the limit with $x_{ij} \gg 1$, which is the case for approximately eV sterile neutrinos, there is no distinction between the scalar and pseudoscalar scenarios. As can be seen from the energy dependence of these relationships, the chirality-preserving processes produce harder daughters, while the chirality-violating ones produce softer daughters (see Fig. 2). It is important to note that the chirality-preserving processes dominate the visible decay due to the fact that the atmospheric neutrino flux is a steeply falling power law, $\phi(E) \sim E^{-3.7}$ [82,83]; the soft daughters in the chirality-violating case are hidden below a large flux which reduces the visible case to the less interesting invisible decay scenario. The chirality-violating process in the Majorana context induces transitions between neutrinos and antineutrinos, but not if the term arises from Dirac neutrinos. In this latter case, the right-handed neutrinos are sterile and do not interact. Note that x_{ij} diverges as $m_j \rightarrow 0$, but all decay rates and differential decay rates remain finite in this limit, so decays to massless daughters are well defined in this framework. Finally, to easily compare with existing constraints on the neutrino lifetime, we introduce the partial lifetime $\tau_{ij} = 1/\Gamma_{ij}$.

C. Existing constraints

Constraints exist on the lifetime of neutrino mass eigenstates ν_i for $i < 4$, i.e., for the active neutrinos.

The constraints depend on the neutrino mass ordering as well as the absolute neutrino mass. In the normal ordering (NO), ν_3 and ν_2 are unstable and can decay to ν_1 , which is stable. On the other hand, in the inverted ordering (IO), ν_3 is stable and the others unstable. Cosmology constrains both the sum of neutrino masses, such that $\sum_i m_i \lesssim 0.12$ at 95% C.L. [84], and the radiative neutrino decay lifetime, to $\gtrsim 10^{19}$ s [85,86]. However, constraints from cosmology on the presence of a fourth neutrino are model dependent; assumptions required include the thermal history of the Universe and the influence of dark energy on the expansion history [87]. Moreover, sterile neutrino thermalization can be suppressed by a number of new physics scenarios [88–96]; if sterile neutrinos do not thermalize, the bounds do not apply.

On the other hand, given results from neutrino oscillation experiments [97], all neutrino masses cannot be zero. The largest decay rate will be achieved when the stable neutrino is assumed to be massless, i.e., $m_1 = 0$ or $m_3 = 0$, for NO or IO, respectively. With this optimistic assumption, in IO the unstable neutrino masses cannot be less than ~ 0.05 eV and in NO m_2 cannot be smaller than ~ 0.008 eV and m_3 satisfies the same bound as for IO. The lifetime of a neutrino of mass m_i is given by $\tau_i^{-1} = \sum_j \tau_{ij}^{-1}$, with $\tau_{ij}^{-1} = \Gamma_{ij}$, and the total decay rate in the lab frame is a function of τ_i/m_i . Constraints on this quantity will depend on the mass ordering: for NO, ν_2 decay is constrained by solar experiments, with $\tau_2/m_2 \gtrsim 7 \times 10^{-4}$ s eV $^{-1}$ [98], and ν_3 is limited by atmospheric and long-baseline experiments, with $\tau_3/m_3 \gtrsim 9 \times 10^{-11}$ s eV $^{-1}$ [60]; for IO, $\tau_1/m_1 \gtrsim 4 \times 10^{-3}$ s eV $^{-1}$ and $\tau_2/m_2 \gtrsim 7 \times 10^{-4}$ s eV $^{-1}$ are constrained by solar experiments [98]. In contrast, direct constraints on ν_4 have not been set.

Constraints on neutrino decay can be obtained indirectly from measurements of meson decays [99–101]. These set strict limits on the neutrino decay process but are flavor dependent; thus they must be used with care. For example, from kaon decay, the following combination is constrained [99]:

$$\sum_{\alpha} |g_{e\alpha}|^2 < 3 \times 10^{-5}, \quad (8)$$

where α runs over all neutrino flavors. Constraints from supernova 1987A are of similar order [100]. These flavor couplings are related to the ones in Eq. (1) by

$$g_{\alpha\beta} = \sum_{ij} g_{ij} U_{\alpha i} U_{\beta j}^*. \quad (9)$$

For simplicity, let us first consider the case where only one g_{4j} is nonzero. In this case $g_{\alpha\beta} = g_{4j} U_{\alpha 4} U_{\beta j}^*$, where for short-baseline motivated sterile neutrinos $U_{\alpha 4} \sim O(0.1)$ [102] and from standard neutrino measurements $U_{\beta j} \sim O(0.1)$ for $j < 4$ [3], which implies that $g_{4j} \leq O(0.1)$. For this size of coupling, an eV-scale sterile neutrino lifetime

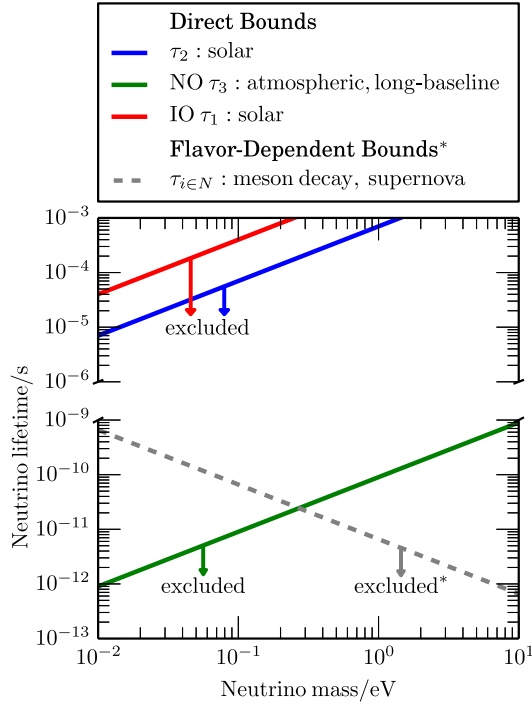


FIG. 3. Direct bounds and flavor-dependent bounds on neutrino lifetimes as a function of the neutrino mass. Constraints are shown for both normal and inverted standard neutrino orderings; in both cases we assume a $3 + 1$ sterile model. The flavor-dependent bounds are shown as dashed lines and may be relaxed by cancellations as discussed in the text.

satisfies $\tau_4 > O(10)/\text{eV}$. With this lifetime constraint, as we will see in a later example, no interesting interplay exists between oscillations and decay. This is due to the fact that the scales of oscillation and decay, which are given by $E/\Delta m_{4j}^2$ and $E\tau_4/m_4$, respectively, are very different. This implies that to have an interesting interplay, more than one of the g_{4j} needs to be nonzero so that a cancellation can occur in Eq. (9), leading to a decreased bound in τ_4 . The scenarios showcased later in this work include only one decay channel. These can be extended to include an additional decay channel so as to avoid the meson bounds with cancellations of order of 1 in 100, without significantly changing the physics conclusions of our examples.

We summarize the constraints discussed in this section in Fig. 3 for both active mass states and the mostly sterile state, ν_4 .

III. NEUTRINO OSCILLATIONS AND DECAY

We will now develop a formalism that incorporates both oscillations and decay in a consistent way. We will follow the calculation in Refs. [60,103] for invisible decay, and for visible decay we follow Refs. [64,78,79] but in the density matrix representation. We will work with a $(3 + 1)$ model, which adds one sterile state to the three active neutrinos,

although the model generalizes readily to $(3 + N)$ for generic N .

A. Neutrino oscillations

We will begin with the most familiar model, which includes vacuum oscillations exclusively, ignoring decay and matter effects. We have

$$H_{\text{vacuum}} = \frac{\Delta M^2}{2E}, \quad (10)$$

where ΔM^2 is a diagonal matrix with entries $(\Delta M^2)_{ii} = \Delta m_{i1}^2$: the neutrino mass-squared splittings. Conjugation into the flavor basis with the Pontecorvo-Maki-Nakagawa-Sakata matrix U_ν (appropriately extended to include the sterile state) mixes the mass states into flavor states as follows:

$$\nu_\alpha = \sum U_{\nu;\alpha,i} \nu_i. \quad (11)$$

This mixing gives rise to vacuum oscillations when at least one of the mass splittings is nonzero.

We are interested in analyzing TeV-scale neutrinos in IceCube. At these energies, matter effects become important, so we introduce a term modeling neutrino scattering off of electrons and nucleons as an effective matter potential [104–106]. The flavor states are eigenstates of the corresponding Hamiltonian term V_{matter} . In the flavor basis, this term takes the form $V_{\text{matter}} = \text{diag}(V_e, V_\mu, V_\tau, 0)$, where the fourth eigenvalue is zero because it corresponds to a sterile neutrino state. Thus the total Hamiltonian in the mass basis is given by

$$H_0(E, l) = H_{\text{vacuum}}(E) + U_\nu V_{\text{matter}}(E, l) U_\nu^\dagger, \quad (12)$$

where the neutrino potentials depend on the electron $[N_e(l)]$ and neutron $[N_n(l)]$ number density profiles, and l is the position of the neutrino ensemble along the baseline.

B. Invisible neutrino decay

Modeling decay in an evolving neutrino system is not a trivial matter, because it involves the addition of daughter particles to the state space. In the visible decay case, we will treat these new states explicitly. In the case of invisible decay, the daughter states are irrelevant, and one can get around this added complexity by introducing an effective non-Hermitian Hamiltonian, H , which gives rise to a nonunitary evolution when restricted to the state space of the parent neutrinos. Intuitively, the nonunitarity of the associated time evolution operator corresponds to the loss of probability current from the parent state space into the daughter space. Following Ref. [103] we can construct H by the explicit addition of an anti-Hermitian term

$$H = H_0 - i\frac{1}{2}\Gamma, \quad (13)$$

where Γ is a Hermitian operator that is diagonal in the mass basis, where it is just $\Gamma = \text{diag}(\Gamma_i(E), \dots)$, where $\Gamma_i(E)$, the decay rate of the i th neutrino, is given by Eq. (5). The factor of $\frac{1}{2}$ is necessary for the survival probability of a neutrino created in the ν_i mass eigenstate to follow the exponential decay formula

$$P_{i \rightarrow i} = |\langle \nu_0(l) | \nu_0 = \nu_i \rangle|^2 = e^{-\Gamma_i l}. \quad (14)$$

In a two-flavor system, the active neutrino vacuum survival probability can be written, under the assumption that the lighter of the two neutrinos is stable, as [60]

$$P_{\alpha \rightarrow \alpha} = \cos^4 \theta + \frac{1}{2} e^{-\frac{\Gamma_2 l}{2}} \cos\left(\frac{\Delta m^2 l}{2E}\right) \sin^2 2\theta + e^{-\Gamma_2 l} \sin^4 \theta, \quad (15)$$

where θ is the two-flavor mixing angle and Γ_2 is the decay rate of the heavier mass state with mass m_2 . Equations (14) and (15) are valid only in the case of invisible decay in vacuum and are included here for completeness.

C. Visible neutrino decay

In this paper, we will concentrate on visible neutrino decay. In this case, Eq. (13) cannot describe the full system evolution because it ignores the evolution of the daughter states. To treat the daughter states explicitly, we first need to extend our formalism from a single, monoenergetic neutrino state to a set of neutrino states indexed by the set of energies relevant to our analysis. We then promote each of these states to an ensemble of states, described by an $n \times n$ density matrix $\rho(E)$, where n is the number of neutrino species under consideration. In the density matrix formalism, evolution due to the Hamiltonian given in Eq. (13) can be written as

$$\frac{\partial \rho(E, l)}{\partial l} = -i[H_0, \rho] - \frac{1}{2}\{\Gamma, \rho\}, \quad (16)$$

where l is the position of the neutrino ensemble along the baseline, square brackets indicate the commutator, and curly brackets indicate the anticommutator. The factor of $\frac{1}{2}$ appears for a similar reason as in Eq. (13). This formalism has already been implemented in an efficient way in the context of neutrino oscillations in a package called **NUSSQUIDS** [107,108]. The decay rate operator is given by

$$\Gamma(E) = \sum_i \Gamma_i(E) \Pi_i, \quad (17)$$

where Π_i is the projector to the i th mass eigenstate and Γ_i is given by the sum of partial rates Γ_{ij} over all daughter states

ν_j lighter than the parent state ν_i . The Γ_{ij} are given by the sum of the chirality-preserving Γ_{ij} from Eq. (2) and the chirality-violating Γ_{ij} from Eq. (3) in the case of Majorana neutrinos, or by partial rates Γ_{ij} corresponding to purely chirality-violating processes in the case of Dirac neutrinos.

Thus far, we have modeled only the loss of neutrinos using the Γ term in Eq. (16). The advantage of this extended formalism is that it can accommodate terms that generate transitions between neutrinos at different energies. We then complement the Γ term describing the loss of neutrinos from an ensemble at one energy with a “regeneration” term, \mathcal{R} , describing the appearance of these neutrinos in ensembles at lower energies. In this way, we keep track of the daughter states and account for their subsequent evolution.

Let us assume that neutrinos are Majorana. For clarity, we will separate the contributions to regeneration into the chirality-preserving processes (CPP) and the chirality-violating processes (CVP). In the first case, we add the following term to the right-hand side Eq. (16):

$$\mathcal{R}(E_d) = \sum_{i,j} \int_{E_d}^{x_{ij}^2 E_d} dE_p \left(\text{Tr}[\rho(E_p) \Pi_i(E_p)] \times \left(\frac{d\Gamma(E_p, E_d)}{dE_d} \right)_{ij}^{\text{CPP}} \Pi_j(E_d) \right), \quad (18)$$

where E_p is the parent energy, E_d is the daughter energy, Tr is the trace operation, and the differential decay rate is given in Eq. (6). When this term is added to Eq. (16), we set $E_d = E$. We have an additional contribution from $\nu \rightarrow \bar{\nu}$ in the chirality-violating process, in which case we should add

$$\mathcal{R}(E_d) += \sum_{i,j} \int_{E_d}^{x_{ij}^2 E_d} dE_p \left(\text{Tr}[\bar{\rho}(E_p) \bar{\Pi}_i(E_p)] \times \left(\frac{d\Gamma(E_p, E_d)}{dE_d} \right)_{ij}^{\text{CVP}} \Pi_j(E_d) \right), \quad (19)$$

where $\bar{\rho}$ corresponds to antineutrinos and the differential rate is given by Eq. (7). Because we consider either purely scalar or purely pseudoscalar cases, the differential rates for CVP and CPP must be chosen accordingly when constructing \mathcal{R} . This boils down to getting the signs right in Eqs. (6) and (7). Similar equations hold for antineutrinos by replacing ρ by $\bar{\rho}$ and changing the projectors Π to $\bar{\Pi}$, and vice versa. Note that there is no regeneration in the Dirac case, because the decay is through a chirality-violating process which produces sterile daughters. We have implemented this formalism in **NUSSQUIDS** [107,108]; see the Appendix for details.

IV. EXAMPLE OF APPLICATION TO ICECUBE

The IceCube experiment is an ideal testing ground for the model presented here. The collaboration has released a

400 GeV to 20 TeV single-year data set associated with a sterile neutrino search [9], and an additional six years of data are available to the collaboration. In this section, we use the released data set to explore some of the nuances of including decays as additional phenomena in the IceCube search. We will only consider the decay channel $\nu_4 \rightarrow \nu_3 \phi$, with the following ν_4 lifetimes: (A) $\tau_4 = 10 \text{ eV}^{-1}$, (B) $\tau_4 = 1 \text{ eV}^{-1}$, (C) $\tau_4 = 0.1 \text{ eV}^{-1}$, and $\tau_4 = \infty \text{ eV}^{-1}$, corresponding to no decay. For $\tau = 1 \text{ eV}^{-1}$, $\hbar c \tau \approx 0.2 \text{ } \mu\text{m}$.

A. The IceCube experiment and released data set

The IceCube detector, located in the Antarctic ice below the South Pole station, observes Cherenkov radiation from interactions of neutrinos that have traversed the Earth. In the 400 GeV to 20 TeV energy range, muon neutrinos are primarily due to decays of kaons produced by cosmic rays impinging on the atmosphere [83]. This analysis makes use of through-going muons that are produced in charged-current ν_μ interactions in the ice or bedrock below the detector. The muons produced by neutrinos in this energy range are above critical energy. Hence, the muon energy can be determined from the stochastic light emission profile. The direction of the muon can be determined through reconstruction of the Cherenkov-light time and spatial distribution and is expressed as an angle, θ_Z , with respect to the zenith.

The Cherenkov light is observed via digital optical modules (DOMs), with photomultiplier tubes as the light sensors [109,110]. The detector consists of 5160 DOMs on 86 vertical strings. The intrastring DOM separation is 17 m and the interstring separation is approximately 125 m. The energy resolution of the detector is $\sigma_{\log_{10}(E_\mu/\text{GeV})} \sim 0.5$ and the angular resolution, $\sigma_{\cos(\theta_Z)}$, varies from 0.005 to 0.015.

The released data set contains 20 145 well-reconstructed events, described in Refs. [9,111,112]. This release is associated with a sterile neutrino search with null results at 90% C.L. [9]. The power of the sterile neutrino analysis arose from the matter effects that were expected for neutrinos that crossed the core and mantle [113]. This was predicted to

lead to an observable deficit of ν_μ events in IceCube for parameters that were consistent with short-baseline anomalies [16,17]. The deficit was expected to be localized to specific regions of E_μ and $\cos(\theta_Z)$, depending on the sterile neutrino parameter space. As a result of the striking signature, IceCube was able to perform a powerful search. The null result significantly changed the parameter landscape for $3 + 1$ searches [102].

The released data provides energy and angle information for each data event. It also provides Monte Carlo information on an event-by-event basis. Information on handling of multiple error sources is provided. Using this data set, one can reconstruct the IceCube search results well, as was demonstrated in Ref. [102]. The appendix of that paper provides step-by-step instructions for use of the data release, which we follow here.

B. IceCube oscillograms

We refer to an “oscillogram” as a plot of the expected change in neutrino flux from creation in the atmosphere to arrival at IceCube, as a function of true neutrino zenith angle and true neutrino energy. Effects that may change the neutrino flux include oscillation, matter effects, absorption, and decay. The minimal $3 + 1$ sterile neutrino model is parametrized by a mass-squared splitting, Δm_{41}^2 , and a mixing angle, θ_{24} . Figure 4 shows the shape effects in the $\bar{\nu}_\mu$ spectrum for the $3 + 1$ sterile neutrino model with parameters $\Delta m_{41}^2 = 1 \text{ eV}^2$ and $\sin^2 2\theta_{24} = 0.1$, for the four lifetimes listed previously. In Fig. 4, for the no-decay scenario as well as for example points A and B, the depletion of $\bar{\nu}_\mu$ ’s in the region $E_{\bar{\nu}_\mu}^{\text{true}} \sim 300 \text{ GeV}$ and $\cos \theta_Z^{\text{true}} \sim -1.0$ is due to matter effects [113]. Decreasing the lifetime of ν_4 decreases the magnitude of this feature and shifts its position. This is due to the fact that, as the ν_4 lifetime becomes smaller, its decay length is smaller than the oscillation scale. In other words, the decay operation breaks the coherence of the system, projecting into the mostly active mass states, preventing the development of oscillation. However, the flux at the detector is still different from the flux in the

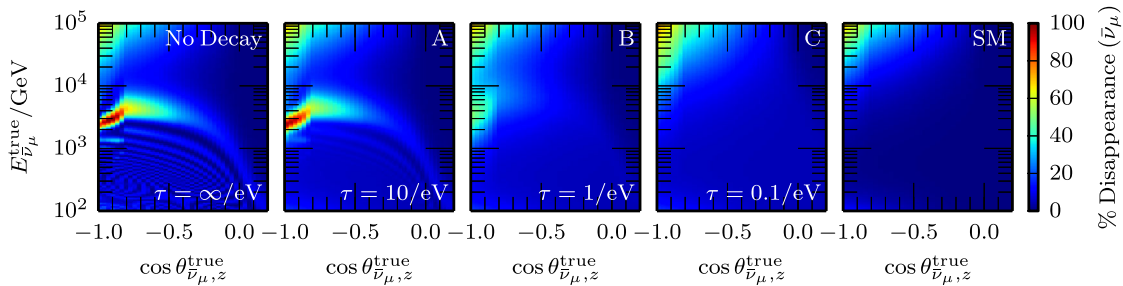


FIG. 4. Disappearance probability for muon antineutrinos for sterile neutrino parameters $\Delta m_{41}^2 = 1 \text{ eV}^2$, $\sin^2 2\theta_{24} = 0.1$, with various lifetimes, and for the SM. Plots from left to right show the effect of neutrino decay with lifetime $\tau = \infty, 10, 1$, and 0.1 eV^{-1} . The rightmost plot shows the SM case. In all three sterile neutrino plots, we assume the decay channel $\nu_4 \rightarrow \nu_3 \phi$. The visible Majorana scenario described in the text is assumed; oscillograms for invisible Majorana decay are within $\sim 3\%$ of the ones shown here. For $\tau = 1 \text{ eV}^{-1}$, $\hbar c \tau \approx 0.2 \text{ } \mu\text{m}$.

TABLE I. Systematic uncertainties treated as nuisance parameters in this analysis. Parameters are described in the text. The best-fit values of the parameters for the null hypothesis (no sterile neutrino), as well as the Gaussian priors' centers and widths, are given.

Parameter	Best-fit	Prior
Flux normalization	1.3	1 ± 0.4
$\Delta\gamma$	0.006	0 ± 0.05
K/ π ratio	1.1	1 ± 0.1
$\bar{\nu}/\nu$ ratio	1.0	1 ± 0.05
DOM efficiency	1.0	1 ± 1.0
Atmospheric density shift	-0.01	0 ± 0.0175

absence of oscillations. The depletion in the top-left corner of each plot in Fig. 4 is due to absorption of high-energy neutrinos crossing the Earth.

C. Data analysis and systematic uncertainties

The data is binned in reconstructed energy proxy and zenith angle. We use a binned Poisson log-likelihood function, $\log \mathcal{L}$, for the data, and incorporate systematic uncertainties by means of nuisance parameters, $\vec{\eta}$, with Gaussian priors. For each lifetime considered and for each point in a fine, logarithmic grid of $[\sin^2(2\theta_{24}), \Delta m_{41}^2]$, $\log \mathcal{L}(\sin^2(2\theta_{24}), \Delta m_{41}^2, \vec{\eta})$ is maximized with respect to a set of nuisance parameters.

Along with the “conventional flux” from pion and kaon decay, in principle a “prompt” contribution arises from the decays of heavier mesons, but it has yet to be observed [114]. For this reason, the prompt flux is neglected [115]. The atmospheric neutrino flux is the sum of the neutrino component and the antineutrino component, where the neutrino component is parametrized as

$$\phi_{\nu}^{\text{atm}} = N_0 \mathcal{F}(\delta) (\phi_{\nu}^{\pi} + R_{K/\pi} \phi_{\nu}^K) \left(\frac{E_{\nu}}{E_0} \right)^{-\Delta\gamma}, \quad (20)$$

where ϕ_{ν}^{π} and ϕ_{ν}^K are the fluxes of neutrinos originating from decays of pions and kaons, respectively. The overall flux normalization, N_0 , variations to the spectral index, $\Delta\gamma$, and the ratio of neutrinos originating from kaons and pions, $R_{K/\pi}$, are nuisance parameters. The pivot point for the spectral index change, E_0 , is at a midpoint energy such that changes to the spectral index do not dramatically change the overall flux normalization. The antineutrino flux is parametrized identically to the neutrino flux, up to a relative normalization factor, which is another nuisance parameter. The cosmic ray and hadronic models used are poly-gonato [116] and QGSJET-II-4 [117], respectively. Uncertainty in the atmospheric density profile is accounted for in a linear parametrization, $\mathcal{F}(\delta)$ [111,112].

The DOM efficiency is a final nuisance parameter. Monte Carlo data sets corresponding to several discrete values of DOM efficiency are publicly available [118].

A piecewise linear interpolation was fit to them, allowing us to treat the DOM efficiency as a continuous nuisance parameter. Table I gives the prior values of the nuisance parameters and the best-fit values for the no-sterile-neutrino hypothesis.

D. Results

We have chosen a few specific parameters to illustrate the effect of this model. To demonstrate that our analysis technique is robust and properly implemented, we first perform the analysis without decay. Figure 5 shows the best-fit nuisance parameters as functions of the sterile parameters.

The oscillograms shown in Fig. 4 indicate that introducing neutrino decay diminishes the strength of the sterile neutrino effect. In order to compare how much the model power changes when we introduce decay, we compare the profile likelihood with and without decay for the scenarios discussed in the previous section. The difference in profile likelihood as a function of sterile neutrino parameters is shown in Fig. 6. In this figure, red colors indicate that the no-decay scenario is preferred whereas blue colors show preference for the decay solution. As the lifetime decreases, the decay scenario is preferred over the no-decay scenario for $\Delta m_{41}^2 \sim 0.1$ – 1 eV^2 . It is worth noting that the saturated blue color does not necessarily indicate a good fit to data.

Our main result is illustrated in Fig. 7, which compares the sterile neutrino hypothesis with decay to the standard three-neutrino scenario. In order to quantify the difference between models, we used the approximate Bayes factor, B_{01} , as a function of the sterile mixing angle and mass difference for the lifetimes discussed in this paper. The Bayes factor is approximate as we have used a profile instead of a marginal likelihood. In comparing hypotheses, we use the Jeffreys scale, where $0 < \log B_{01} < 1$, $1 < \log B_{01} < 2.5$, and $2.5 < \log B_{01} < 5$ correspond to weak, strong, and decisive evidence against a hypothesis, respectively [119]. We observe that for lifetimes on the order of 0.1 eV^{-1} , in the regions of parameter space that correspond to the allowed regions from sterile neutrino global fits to short-baseline data assuming no decay, the sterile neutrino hypothesis is not disfavored. For lifetimes greater than 1 eV^{-1} , the IceCube exclusion is robust under this new physics scenario.

The physics behind these results depends on the magnitudes of the relevant lengths, as briefly discussed in Sec. IV B. For the IceCube matter resonant enhancement to occur in the absence of decay, two conditions must be satisfied: 1) the involved densities must be such that matter potential is comparable to the vacuum Hamiltonian, and 2) the oscillation length needs to be smaller or comparable to the baseline; for a recent detailed discussion see Ref. [120]. As the ν_4 lifetime decreases, its decay length decreases. A short ν_4 decay length prevents the development of the

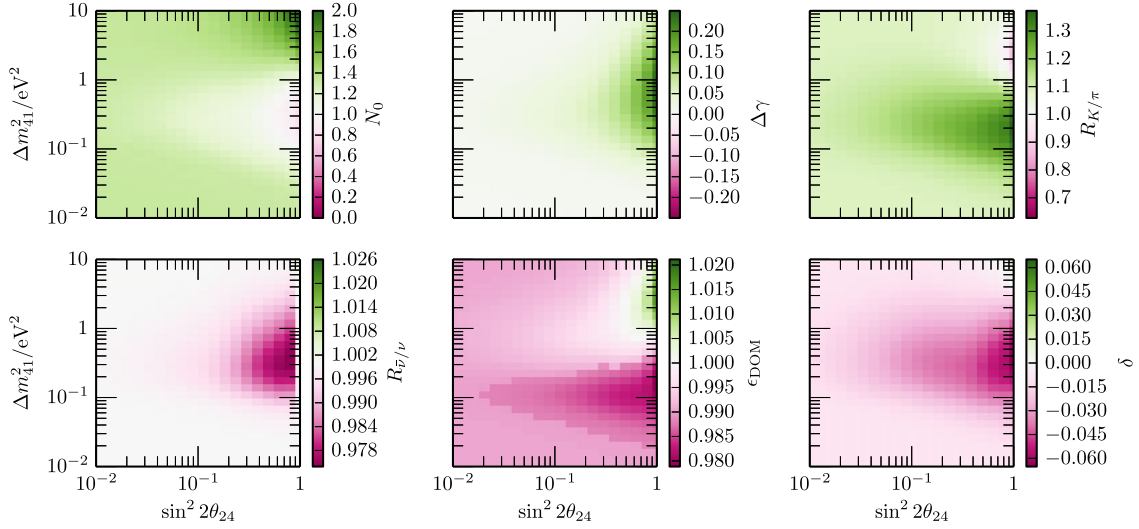


FIG. 5. Minimized nuisance parameters over a scan of sterile parameters for a 3 + 1 sterile neutrino model with a stable ν_4 . The set of nuisance parameters are (first row, from left to right) overall atmospheric flux normalization, change in cosmic ray spectral index, and ratio of atmospheric kaons to pions, (second row, from left to right) ratio of atmospheric muon antineutrinos to muon neutrinos, DOM efficiency, and atmospheric density uncertainty.

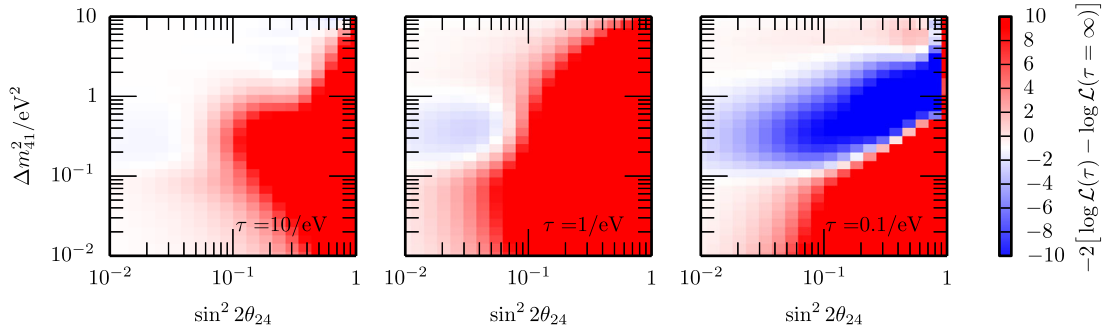


FIG. 6. Model comparison between a standard 3 + 1 model, and a 3 + 1 model with ν_4 decay, as a function of mixing angle and mass splitting, for three lifetimes. In each $[\Delta m^2_{24}, \sin^2 2\theta_{24}]$ bin, the likelihood for each model is evaluated using the given sterile mixing angle and mass. Plots from left to right show model comparisons for decay lifetimes $\tau = 10, 1$, and 0.1 eV^{-1} . In all these plots, we assume the decay channel $\nu_4 \rightarrow \nu_3 \phi$. For $\tau = 1 \text{ eV}^{-1}$, $\hbar c \tau \approx 0.2 \mu\text{m}$.

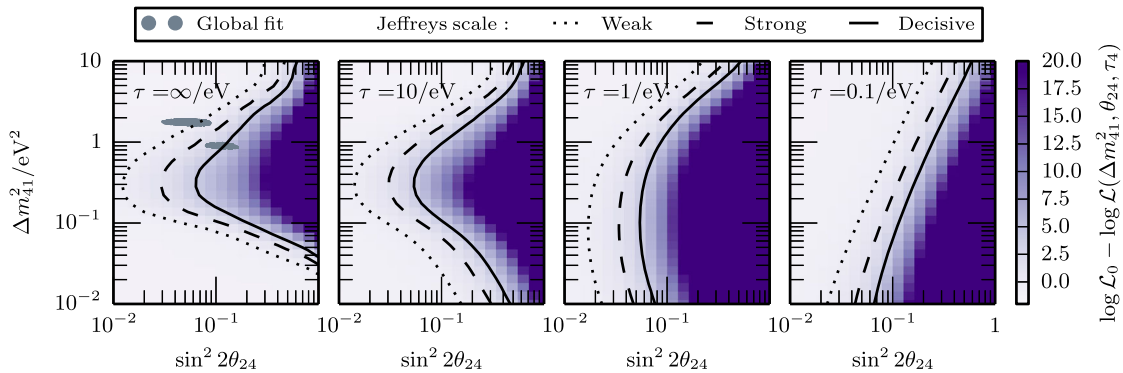


FIG. 7. Model comparison between a 3 + 1 model with decay and the no-sterile-neutrino scenario as a function of mixing angle and mass, for three lifetimes. Plots from left to right show model comparisons for decay lifetimes $\tau = \infty, 10, 1$, and 0.1 eV^{-1} . The dotted, dashed, and solid lines correspond to the Jeffreys scale criterion for weak, strong, and decisive evidence against the alternative hypothesis. In the left-most plot, the grey regions are the 90% confidence level credible intervals from global fits to short-baseline data [17]. In all these plots we assume the decay channel $\nu_4 \rightarrow \nu_3 \phi$. For $\tau = 1 \text{ eV}^{-1}$, $\hbar c \tau \approx 0.2 \mu\text{m}$.

matter resonance, as the $\bar{\nu}_4$ component of $\bar{\nu}_\mu$ decays before $\bar{\nu}_\mu$ can transition to $\bar{\nu}_s$. E.g. for case (C) $\tau = 0.1/\text{eV}$, where the matter feature is no longer observable, the lab frame decay length is approximately 10 and 100 km for 1 and 10 TeV, respectively.

V. CONCLUSIONS

We have reviewed the framework of neutrino decay with oscillations and presented it in a consistent manner using the density matrix formalism. We have further implemented this new physics scenario in the NUSQUIDS software package [121]. We have implemented the high-energy IceCube sterile analysis and then introduced the decay of ν_4 as an additional effect. We showed that for small values of the lifetime, $\tau \lesssim 0.1 \text{ eV}^{-1}$, the IceCube results' interpretation can be significantly changed. This is because, at these short ν_4 lifetimes, the decay length is shorter than the oscillation length, preventing the development of active-to-sterile oscillation. Thus, neutrino decay can dramatically alter the landscape of eV-sterile neutrinos and will need to be studied in the context of global fits.

ACKNOWLEDGMENTS

The authors are supported by U.S. National Science Foundation Grant No. 1505858. M.H.M. is funded NSF Graduate Research Fellowships Program Grant No. 1122374. We would also like to thank Sergio Palomares-Ruiz, Alberto Gago, Christopher Weaver, and Tianlu Yuan for carefully reading this draft and providing us with very useful comments. Finally, we would like to thank Jean DeMerit for carefully proofreading our work.

APPENDIX: NUSQUIDS DECAY IMPLEMENTATION

NUSQUIDS [108] is a C++ package that calculates the evolution of an ensemble of neutrinos considering oscillations as well as neutrino scattering. Thus it is an easily extendable toolbox for neutrino oscillation experiments and neutrino telescopes. It is written on top of the SQUIDS library [107], which implements the density matrix formalism in a numerically optimal way.

In this work we have implemented a NUSQUIDS-derived class that incorporates neutrino decay as discussed in the main text, and can be obtained from Ref. [121]. We make two additions to the NUSQUIDS virtual functions that govern neutrino noncoherent losses and ensemble interactions: `nuSQUIDS::GammaRho` and `nuSQUIDS::InteractionsRho`. To the first function we have added a term as given by Eq. (17) and to the second function we have added \mathcal{R} as given in Eqs. (19) and (20).

1. Constructors

The class specialization is called NUSQUIDSDecay. The main constructor, or “coupling constructor” has the following signature:

```
nuSQUIDSDecay(marray<double, 1> e_nodes,
               unsigned int numneu,
               NeutrinoType NT,
               bool iinteraction,
               bool decay_regen,
               bool pscalar,
               std::vector<double> m_nu,
               gsl_matrix* couplings),
```

where `e_nodes` is a one-dimensional array that gives the energy nodes, `numneu` specifies the number of neutrino states, `iinteraction` toggles neutrino scattering with matter due to deep inelastic scattering interactions, `pscalar` toggles scalar or pseudoscalar couplings (as in the paper, the code assumes either purely scalar or purely pseudoscalar couplings), `decay_regen` toggles visible and invisible decay inclusion, `m_nu` is a vector that contains the absolute neutrino masses, and `couplings` is a square real matrix containing g_{ij}^s or g_{ij}^p as specified by the `pscalar` bool. The code calculates the decay rate matrices according to equations given in Sec. II B from the provided couplings. As a consequence, this constructor has the assumption that the neutrinos are Majorana “baked in.”

If the user wishes to describe Dirac neutrinos with a different Lagrangian, they can compute their own decay rates and supply them to the following, alternative “partial rate” constructor. Its signature is as follows:

```
nuSQUIDSDecay(marray<double, 1> e_nodes,
               unsigned int numneu,
               NeutrinoType NT,
               bool iinteraction,
               bool decay_regen,
               bool pscalar,
               bool majorana,
               std::vector<double> m_nu,
               gsl_matrix* rate_matrices[2]).
```

The variables with names matching those in the other constructor have the same meanings, but in this version the user can specify the partial widths, Γ_{ij} in the rest frame of the decay, instead of the couplings. These should be provided in `rate_matrices` as an array of two square matrices where the index corresponds to the CPP or CVP process, respectively. The `pscalar` Boolean, as before, determines whether these rates are interpreted as scalar or pseudoscalar decay rates. For example, if `pscalar=true` then `rate_matrices[0]= $\Gamma_{ij}^{\text{CPP},p}$` . The code assumes that the user has calculated these matrices properly. For this reason, if the user is assuming a Majorana neutrino with the Lagrangian given in Eq. (1) the use of the coupling constructor is encouraged to minimize the probability of errors.

2. Public members

The class inherits all public members of the `NUSQUIDS` class. The most important among them are `EvolveState`, which performs the calculation and `EvalFlavor`, which returns the flavor content. We will not discuss these functions since they are better described in the `NUSQUIDS` manual. The new public member is

`Set_DecayRegeneration(bool opt)`: if set to false sets $\mathcal{R} \equiv 0$. This removes the effects of visible decay, reducing the simulation to the invisible decay scenario.

3. Provided examples

Two examples are provided with the code. The first one, `couplings_example.cpp`, uses the coupling constructor and the second one, `partial_rate_example.cpp`, uses the rate constructor. Both the examples calculate the oscillograms corresponding to atmospheric neutrino oscillations. In order to run the examples, we provide the atmospheric neutrino flux assuming the poly-gonato cosmic ray model and QGSJER-II-04 interaction model calculated with Ref. [122]. The `NUSQUIDSDECAY` class documentation is included in the code release.

-
- [1] Y. Fukuda *et al.* (Super-Kamiokande Collaboration), *Phys. Rev. Lett.* **81**, 1562 (1998).
 - [2] Q. R. Ahmad *et al.* (SNO Collaboration), *Phys. Rev. Lett.* **89**, 011301 (2002).
 - [3] M. Gonzalez-Garcia, M. Maltoni, and T. Schwetz, *J. High Energy Phys.* **11** (2014) 052.
 - [4] C. Athanassopoulos *et al.* (LSND Collaboration), *Phys. Rev. Lett.* **77**, 3082 (1996).
 - [5] A. Aguilar-Arevalo *et al.* (LSND Collaboration), *Phys. Rev. D* **64**, 112007 (2001).
 - [6] A. A. Aguilar-Arevalo *et al.* (MiniBooNE Collaboration), *arXiv:1207.4809*.
 - [7] G. Mention, M. Fechner, T. Lasserre, T. A. Mueller, D. Lhuillier, M. Cribier, and A. Letourneau, *Phys. Rev. D* **83**, 073006 (2011).
 - [8] J. N. Bahcall, P. I. Krastev, and E. Lisi, *Phys. Lett. B* **348**, 121 (1995).
 - [9] M. G. Aartsen *et al.* (IceCube Collaboration), *Phys. Rev. Lett.* **117**, 071801 (2016).
 - [10] M. G. Aartsen *et al.* (IceCube Collaboration), *Phys. Rev. D* **95**, 112002 (2017).
 - [11] P. Adamson *et al.* (MINOS Collaboration), *Phys. Rev. Lett.* **107**, 011802 (2011).
 - [12] K. Abe *et al.* (Super-Kamiokande Collaboration), *Phys. Rev. D* **91**, 052019 (2015).
 - [13] B. Armbruster *et al.* (KARMEN Collaboration), *Phys. Rev. D* **65**, 112001 (2002).
 - [14] G. Cheng *et al.* (SciBooNE and MiniBooNE Collaborations), *Phys. Rev. D* **86**, 052009 (2012).
 - [15] F. Dydak *et al.*, *Phys. Lett. B* **134**, 281 (1984).
 - [16] J. Kopp, P. A. N. Machado, M. Maltoni, and T. Schwetz, *J. High Energy Phys.* **05** (2013) 050.
 - [17] G. H. Collin, C. A. Argüelles, J. M. Conrad, and M. H. Shaevitz, *Nucl. Phys. B* **908**, 354 (2016).
 - [18] C. Giunti and M. Laveder, *Phys. Rev. D* **84**, 073008 (2011).
 - [19] S. Gariazzo, C. Giunti, M. Laveder, and Y. F. Li, *J. High Energy Phys.* **06** (2017) 135.
 - [20] E. Ma, G. Rajasekaran, and I. Stancu, *Phys. Rev. D* **61**, 071302 (2000).
 - [21] E. Ma and G. Rajasekaran, *Phys. Rev. D* **64**, 117303 (2001).
 - [22] C. Dib, J. C. Helo, S. Kovalenko, and I. Schmidt, *Phys. Rev. D* **84**, 071301 (2011).
 - [23] S. N. Gninenko, *Phys. Rev. D* **83**, 015015 (2011).
 - [24] S. N. Gninenko, *Phys. Rev. Lett.* **103**, 241802 (2009).
 - [25] A. Strumia, *Phys. Lett. B* **539**, 91 (2002).
 - [26] H. Murayama and T. Yanagida, *Phys. Lett. B* **520**, 263 (2001).
 - [27] G. Barenboim, L. Borissov, and J. D. Lykken, *arXiv:hep-ph/0212116*.
 - [28] M. C. Gonzalez-Garcia, M. Maltoni, and T. Schwetz, *Phys. Rev. D* **68**, 053007 (2003).
 - [29] V. Barger, D. Marfatia, and K. Whisnant, *Phys. Lett. B* **576**, 303 (2003).
 - [30] J. S. Diaz and V. A. Kostelecky, *Phys. Lett. B* **700**, 25 (2011).
 - [31] G. Barenboim and N. E. Mavromatos, *J. High Energy Phys.* **01** (2005) 034.
 - [32] M. Sorel, J. M. Conrad, and M. Shaevitz, *Phys. Rev. D* **70**, 073004 (2004).
 - [33] Y. Farzan, T. Schwetz, and A. Y. Smirnov, *J. High Energy Phys.* **07** (2008) 067.
 - [34] A. de Gouvêa and Y. Grossman, *Phys. Rev. D* **74**, 093008 (2006).
 - [35] H. Pas, S. Pakvasa, and T. J. Weiler, *Phys. Rev. D* **72**, 095017 (2005).
 - [36] M. Carena, Y.-Y. Li, C. S. Machado, P. A. N. Machado, and C. E. M. Wagner, *arXiv:1708.09548*.
 - [37] S. Hollenberg, O. Micu, H. Pas, and T. J. Weiler, *Phys. Rev. D* **80**, 093005 (2009).
 - [38] K. M. Zurek, *J. High Energy Phys.* **10** (2004) 058.
 - [39] D. B. Kaplan, A. E. Nelson, and N. Weiner, *Phys. Rev. Lett.* **93**, 091801 (2004).
 - [40] T. Schwetz, *J. High Energy Phys.* **02** (2008) 011.
 - [41] K. S. Babu and S. Pakvasa, *arXiv:hep-ph/0204236*.
 - [42] B. Armbruster *et al.*, *Phys. Rev. Lett.* **90**, 181804 (2003).
 - [43] A. Gaponenko *et al.* (TWIST Collaboration), *Phys. Rev. D* **71**, 071101 (2005).

- [44] Y. Bai, R. Lu, S. Lu, J. Salvado, and B. A. Stefanek, *Phys. Rev. D* **93**, 073004 (2016).
- [45] S. Hollenberg, O. Micu, and H. Pas, *Phys. Rev. D* **80**, 053010 (2009).
- [46] X.-Q. Li, Y. Liu, and Z.-T. Wei, *Eur. Phys. J. C* **56**, 97 (2008).
- [47] A. E. Nelson, *Phys. Rev. D* **84**, 053001 (2011).
- [48] J. Liao and D. Marfatia, *Phys. Rev. Lett.* **117**, 071802 (2016).
- [49] E. Akhmedov and T. Schwetz, *J. High Energy Phys.* **10** (2010) 115.
- [50] D. K. Papoulias and T. S. Kosmas, *Adv. High Energy Phys.* **2016**, 1490860 (2016).
- [51] Z. G. Berezhiani, G. Fiorentini, M. Moretti, and A. Rossi, *Z. Phys. C* **54**, 581 (1992).
- [52] A. S. Joshipura, E. Masso, and S. Mohanty, *Phys. Rev. D* **66**, 113008 (2002).
- [53] J. F. Beacom and N. F. Bell, *Phys. Rev. D* **65**, 113009 (2002).
- [54] A. Bandyopadhyay, S. Choubey, and S. Goswami, *Phys. Lett. B* **555**, 33 (2003).
- [55] S. Choubey, S. Goswami, and D. Majumdar, *Phys. Lett. B* **484**, 73 (2000).
- [56] A. Bandyopadhyay, S. Choubey, and S. Goswami, *Phys. Rev. D* **63**, 113019 (2001).
- [57] V. D. Barger, J. G. Learned, S. Pakvasa, and T. J. Weiler, *Phys. Rev. Lett.* **82**, 2640 (1999).
- [58] G. L. Fogli, E. Lisi, A. Marrone, and G. Scioscia, *Phys. Rev. D* **59**, 117303 (1999).
- [59] V. D. Barger, J. G. Learned, P. Lipari, M. Lusignoli, S. Pakvasa, and T. J. Weiler, *Phys. Lett. B* **462**, 109 (1999).
- [60] M. C. Gonzalez-Garcia and M. Maltoni, *Phys. Lett. B* **663**, 405 (2008).
- [61] S. Choubey, S. Goswami, and D. Pramanik, *J. High Energy Phys.* **02** (2018) 055.
- [62] S. Choubey, S. Goswami, C. Gupta, S. M. Lakshmi, and T. Thakore, *Phys. Rev. D* **97**, 033005 (2018).
- [63] S. Palomares-Ruiz, S. Pascoli, and T. Schwetz, *J. High Energy Phys.* **09** (2005) 048.
- [64] S. Palomares-Ruiz, *J. Phys. Conf. Ser.* **39**, 307 (2006).
- [65] P. Coloma and O. L. G. Peres, [arXiv:1705.03599](https://arxiv.org/abs/1705.03599).
- [66] M. Lindner, T. Ohlsson, and W. Winter, *Nucl. Phys. B* **622**, 429 (2002).
- [67] M. Kachelriess, R. Tomas, and J. W. F. Valle, *Phys. Rev. D* **62**, 023004 (2000).
- [68] S. Ando, *Phys. Lett. B* **570**, 11 (2003).
- [69] G. L. Fogli, E. Lisi, A. Mirizzi, and D. Montanino, *Phys. Rev. D* **70**, 013001 (2004).
- [70] P. D. Serpico, *Phys. Rev. Lett.* **98**, 171301 (2007).
- [71] S. Hannestad and G. Raffelt, *Phys. Rev. D* **72**, 103514 (2005).
- [72] M. Maltoni and W. Winter, *J. High Energy Phys.* **07** (2008) 064.
- [73] I. M. Shoemaker and K. Murase, *Phys. Rev. D* **93**, 085004 (2016).
- [74] M. Bustamante, J. F. Beacom, and K. Murase, *Phys. Rev. D* **95**, 063013 (2017).
- [75] R. A. Gomes, A. L. G. Gomes, and O. L. G. Peres, *Phys. Lett. B* **740**, 345 (2015).
- [76] T. Abrahão, H. Minakata, H. Nunokawa, and A. A. Quiroga, *J. High Energy Phys.* **11** (2015) 001.
- [77] J. Schechter and J. W. F. Valle, *Phys. Rev. D* **25**, 774 (1982).
- [78] M. Lindner, T. Ohlsson, and W. Winter, *Nucl. Phys. B* **607**, 326 (2001).
- [79] A. M. Gago, R. A. Gomes, A. L. G. Gomes, J. Jones-Perez, and O. L. G. Peres, *J. High Energy Phys.* **11** (2017) 022.
- [80] M. E. Peskin and D. V. Schroeder, *An Introduction to Quantum Field Theory* (Westview, Boulder, CO, 1995).
- [81] C. Kim and W. Lam, *Mod. Phys. Lett. A* **05**, 297 (1990).
- [82] M. Honda, M. S. Athar, T. Kajita, K. Kasahara, and S. Midorikawa, *Phys. Rev. D* **92**, 023004 (2015).
- [83] T. K. Gaisser, R. Engel, and E. Resconi, *Cosmic Rays and Particle Physics* (Cambridge University Press, Cambridge, England, 2016).
- [84] N. Palanque-DeLabrouille *et al.*, *J. Cosmol. Astropart. Phys.* **11** (2015) 011.
- [85] A. Mirizzi, D. Montanino, and P. D. Serpico, *Phys. Rev. D* **76**, 053007 (2007).
- [86] S.-H. Kim, K.-i. Takemasa, Y. Takeuchi, and S. Matsuura, *J. Phys. Soc. Jpn.* **81**, 024101 (2012).
- [87] K. N. Abazajian and M. Kaplinghat, *Annu. Rev. Nucl. Part. Phys.* **66**, 401 (2016).
- [88] K. N. Abazajian, *Astropart. Phys.* **19**, 303 (2003).
- [89] B. Dasgupta and J. Kopp, *Phys. Rev. Lett.* **112**, 031803 (2014).
- [90] S. Hannestad, R. S. Hansen, and T. Tram, *Phys. Rev. Lett.* **112**, 031802 (2014).
- [91] L. Bento and Z. Berezhiani, *Phys. Rev. D* **64**, 115015 (2001).
- [92] Y.-Z. Chu and M. Cirelli, *Phys. Rev. D* **74**, 085015 (2006).
- [93] R. Foot and R. R. Volkas, *Phys. Rev. Lett.* **75**, 4350 (1995).
- [94] G. Gelmini, S. Palomares-Ruiz, and S. Pascoli, *Phys. Rev. Lett.* **93**, 081302 (2004).
- [95] C. M. Ho and R. J. Scherrer, *Phys. Rev. D* **87**, 065016 (2013).
- [96] J. Hamann, S. Hannestad, G. G. Raffelt, and Y. Y. Y. Wong, *J. Cosmol. Astropart. Phys.* **09** (2011) 034.
- [97] M. C. Gonzalez-Garcia, M. Maltoni, and T. Schwetz, *J. High Energy Phys.* **11** (2014) 052.
- [98] J. M. Berryman, A. de Gouvêa, and D. Hernandez, *Phys. Rev. D* **92**, 073003 (2015).
- [99] V. D. Barger, W.-Y. Keung, and S. Pakvasa, *Phys. Rev. D* **25**, 907 (1982).
- [100] A. P. Lessa and O. L. G. Peres, *Phys. Rev. D* **75**, 094001 (2007).
- [101] P. S. Pasquini and O. L. G. Peres, *Phys. Rev. D* **93**, 053007 (2016); **93**, 079902(E) (2016).
- [102] G. H. Collin, C. A. Argüelles, J. M. Conrad, and M. H. Shaevitz, *Phys. Rev. Lett.* **117**, 221801 (2016).
- [103] J. M. Berryman, A. de Gouvêa, D. Hernández, and R. L. N. Oliveira, *Phys. Lett. B* **742**, 74 (2015).
- [104] L. Wolfenstein, *Phys. Rev. D* **17**, 2369 (1978).
- [105] S. P. Mikheev and A. Yu. Smirnov, *Yad. Fiz.* **42**, 1441 (1985) [*Sov. J. Nucl. Phys.* **42**, 913 (1985)].
- [106] E. K. Akhmedov, in *Proceedings of the 1999 Summer School in Particle Physics, Trieste, Italy, June 21–July 9, 1999*, edited by G. Senjanovic and A. Y. Smirnov (World Scientific, Singapore, 1999), p. 103.

- [107] C. A. Argüelles, J. Salvado, and C. N. Weaver, *Comput. Phys. Commun.* **196**, 569 (2015).
- [108] C. A. Argüelles, J. Salvado, and C. N. Weaver, *NUSQUIDS*, <https://github.com/arguelles/nuSQuIDS>.
- [109] A. Achterberg *et al.* (IceCube Collaboration), *Astropart. Phys.* **26**, 155 (2006).
- [110] M. G. Aartsen *et al.* (IceCube Collaboration), *J. Inst.* **12**, P03012 (2017).
- [111] B. J. P. Jones, Ph.D. thesis, MIT, 2015, <http://lss.fnal.gov/archive/thesis/2000/fermilab-thesis-2015-17.pdf>.
- [112] C. A. Argüelles, Ph. D. thesis, University of Wisconsin—Madison, 2015, <http://search.proquest.com/docview/1720322773>.
- [113] H. Nunokawa, O. L. G. Peres, and R. Zukanovich Funchal, *Phys. Lett. B* **562**, 279 (2003).
- [114] R. Enberg, M. H. Reno, and I. Sarcevic, *Phys. Rev. D* **78**, 043005 (2008).
- [115] A. Fedynitch, R. Engel, T. K. Gaisser, F. Riehn, and T. Stanev, *EPJ Web Conf.* **99**, 08001 (2015).
- [116] J. R. Hoerandel, *Astropart. Phys.* **19**, 193 (2003).
- [117] S. Ostapchenko, *Phys. Rev. D* **83**, 014018 (2011).
- [118] <http://icecube.wisc.edu/science/data/IC86-sterile-neutrino>.
- [119] R. Trotta, *arXiv:1701.01467*, <https://inspirehep.net/record/1507974/files/arXiv:1701.01467.pdf>.
- [120] S. T. Petcov, *Int. J. Mod. Phys. A* **32**, 1750018 (2017).
- [121] Z. Moss, M. Moulai, C. A. Argüelles, and J. Conrad, *NUSQUIDSDECAY*, <https://github.com/arguelles/nuSQuIDSDecay>.
- [122] A. Fedynitch, *MCEQ*, <https://github.com/afedynitch/MCEq>.

3.2 Incorporating IceCube data into global fits

Following [62], global fits were performed on short-baseline data using both a traditional $3 + 1$ model and the invisible decay version of the unstable sterile neutrino model, referred to as $3 + 1 + \text{decay}$ [25]. These fits used data from fourteen different neutrino experiments, excluding IceCube. Invisible decay refers to having no detectable daughter particles. It was found that the best-fit point of the unstable sterile neutrino model is preferred to that of the traditional $3 + 1$ model. The significance of the improvement is 2.6σ . Moreover, the observed tension between appearance and disappearance experiments is reduced, but not resolved. In the following publication, the one-year dataset from IceCube was incorporated into the global fit results [63].

Combining sterile neutrino fits to short-baseline data with IceCube data

M. H. Moulai^{1,*} C. A. Argüelles¹ G. H. Collin,^{1,2} J. M. Conrad¹ A. Diaz,¹ and M. H. Shaevitz³

¹*Department of Physics, Massachusetts Institute of Technology, Cambridge, Massachusetts 02139, USA*

²*Institute for Data, Systems, and Society, Massachusetts Institute of Technology, Cambridge, Massachusetts 02139, USA*

³*Department of Physics, Columbia University, New York, New York 10027, USA*



(Received 7 November 2019; accepted 19 February 2020; published 18 March 2020)

Recent global fits to short-baseline neutrino oscillation data have been performed finding preference for a sterile neutrino solution ($3 + 1$) over null. In the most recent iteration, it was pointed out that an unstable sterile neutrino ($3 + 1 + \text{decay}$) may be a better description of the data. This is due to the fact that this model significantly reduces the tension between appearance and disappearance datasets. In this work, we add a 1-year IceCube dataset to the global fit obtaining new results for the standard $3 + 1$ and $3 + 1 + \text{decay}$ sterile neutrino scenarios. We find that the $3 + 1 + \text{decay}$ model provides a better fit than the $3 + 1$, even in the presence of IceCube, with reduced appearance to disappearance tension. The $3 + 1 + \text{decay}$ model is a 5.4σ improvement over the null hypothesis and a 2.8σ improvement over the standard $3 + 1$ model.

DOI: [10.1103/PhysRevD.101.055020](https://doi.org/10.1103/PhysRevD.101.055020)

I. INTRODUCTION

Over the last decades, anomalies observed in short-baseline neutrino oscillation experiments [1,2] have motivated global fits that expand from a model containing three neutrinos to one that also includes a fourth mass state and a nonweakly interacting flavor state [3–6]. Hence, these so-called “ $3 + 1$ models” extend the neutral-lepton mixing matrix to be 4×4 , introducing three new independent mixing elements: U_{e4} , $U_{\mu 4}$, and $U_{\tau 4}$. The preferred regions of $|U_{e4}|$, $|U_{\mu 4}|$, and the new squared-mass difference, Δm_{41}^2 , have been reported in a recent global fit of the short-baseline data to a $3 + 1$ model [5].

A $3 + 1$ model can simultaneously explain anomalies observed in “appearance experiments” ($\bar{\nu}_{\mu} \rightarrow \bar{\nu}_e$) [1,2] and in “disappearance experiments” ($\bar{\nu}_e \rightarrow \bar{\nu}_e$) primarily due to reactor experiments [7–9]. However, in a $3 + 1$ model, the combined anomalies also predict a signal in $\bar{\nu}_{\mu}$ disappearance experiments. For oscillations in vacuum, observed through charged-current scattering, the elements $|U_{e4}|^2$ and $|U_{\mu 4}|^2$ define three mixing angles that characterize the amplitude of ν_e disappearance, ν_{μ} disappearance, and $\nu_{\mu} \rightarrow \nu_e$ appearance, respectively,

$$\begin{aligned}\sin^2 2\theta_{ee} &= 4(1 - |U_{e4}|^2)|U_{e4}|^2, \\ \sin^2 2\theta_{\mu\mu} &= 4(1 - |U_{\mu 4}|^2)|U_{\mu 4}|^2, \\ \sin^2 2\theta_{\mu e} &= 4|U_{e4}|^2|U_{\mu 4}|^2.\end{aligned}\quad (1)$$

Thus, the mixing angles measured in the three types of searches are not independent. In fact, for small mixing elements, they are approximately related in the following way:

$$\sin^2 2\theta_{ee} \sin^2 2\theta_{\mu\mu} \approx 4 \sin^2 2\theta_{\mu e}. \quad (2)$$

The squared-mass splitting must also be consistent for all three types of oscillations. The probability that all short-baseline data, observed anomalies, and constraints from null observations is a realization of the $3 + 1$ model is found to be extremely small [4]. This statement follows from a recent parameter goodness of fit test [10] (“PG test”) performed on the global data, which quantifies the tension as a disagreement at the 4.5σ [4] level.

If the anomalies are due to new physics, the underlying model may be more complicated than $3 + 1$. We have shown that adding another additional mass state, a model known as “ $3 + 2$,” does not reduce the tension [5]. Other modifications are also possible [11–22], and we have developed a $3 + 1$ model that incorporates decay of the largest mass state, m_4 [5,23]. In fact, this category of $3 + 1$ models was first considered as an explanation of the LSND observation in [24] and was later realized to weaken the muon-neutrino disappearance constraints in [23]. More recently, it has been suggested that if one considers visible decay with one or more decay daughters being detectable,

*marjon@mit.edu

Published by the American Physical Society under the terms of the [Creative Commons Attribution 4.0 International license](https://creativecommons.org/licenses/by/4.0/). Further distribution of this work must maintain attribution to the author(s) and the published article’s title, journal citation, and DOI. Funded by SCOAP³.

the low-energy excess of MiniBooNE can be well described by this category of models [25–27]. In the case of invisible decay, where the heavy neutrino has two decay daughters that are undetectable, this introduces only one additional parameter beyond the $3 + 1$ model, the lifetime of the heavy neutrino, τ . However, it also introduces two new, negligible-mass particles, the decay daughters, into the phenomenology. This model reduces the tension, measured by the parameter goodness of fit test, significantly to 3.2σ [5]. While this still suggests poor agreement, it points to the possibility of additional effects in the short-baseline sample.

The global fits described above were limited to experiments studying vacuum oscillations at $L/E \sim 1$ to 10 eV^2 . However, the IceCube experiment offers a relevant dataset that is very different from these short-baseline experiments. This experiment searches for a resonance signature from sterile-induced matter effects in upward-going antineutrinos, which have traveled through the Earth [28,29]. The oscillation amplitude is no longer given by the vacuum-oscillation mixing angle relations, Eq. (1), and instead takes on a complicated form, where $\sin^2 2\theta_{\mu\mu}$, the amplitude of the disappearance, depends on $|U_{\mu 4}|$ and also $|U_{\tau 4}|$; see Refs. [30–33] for a detailed discussion. Thus, IceCube brings additional information to the global fits, since the vacuum-oscillation results are insensitive to $|U_{\tau 4}|$ [3].

A $3 + 1$ model has been explored for a combined short-baseline and IceCube global fit for the first time in [3] and later in [4]. In this paper, we will follow the same procedure of [3] to include IceCube in the latest global fits given in [5], and we will expand the result to include $3 + 1 + \text{decay}$.

II. ICECUBE

The IceCube Neutrino Observatory is located in the Antarctic continent close to the geographic South Pole [34]. IceCube is a gigaton-scale ice-Cherenkov detector made out of arrays of photomultiplier tubes encapsulated in pressure-resisting vessels buried in the clear Antarctic glacier ice [35]. IceCube has measured the atmospheric neutrino spectrum from 10 GeV [36], using a denser inner part of the detector called DeepCore [37], to 100 TeV [38]. The atmospheric neutrino flux is dominated by the so-called conventional component, which is due to the decay of kaons, pions, and muons [39]. At the lower energies, below 100 GeV, neutrinos from pion and muon decay dominate the neutrino flux and IceCube has used them to measure the atmospheric oscillation parameters [36]. In this energy range, IceCube is also sensitive to eV-scale sterile neutrinos by looking for modifications on top of the predicted standard three-neutrino oscillation pattern [40], as similarly done by SuperKamiokande [41]. At TeV energies, neutrino oscillations driven by the known squared-mass differences turn off, as their oscillation length becomes much larger than the Earth's diameter. It was pointed out in [28], that at TeV energies matter effects will

induce a large disappearance of muon-antineutrinos for squared-mass differences compatible with the LSND anomaly, due to effects previously studied in broader contexts in [42–46]. IceCube has performed a search for sterile neutrinos using 1 year of data [29]. This analysis used a high-purity muon-neutrino event selection designed to search for an astrophysical component in the northern sky [47]. The analysis was performed with neutrinos between 400 GeV and 20 TeV in energy; this range was chosen to avoid contamination from high-energy astrophysical neutrinos and to minimize uncertainties in local ice properties at lower energies.

The IceCube Collaboration provided a data release associated with this analysis [29]. This data release includes over 20,000 atmospheric ν_μ and $\bar{\nu}_\mu$ events, as well as the Monte Carlo that was used. In this work, we use the analysis tools we developed in [3,23], which use the nusQuIDS package to calculate neutrino oscillation probabilities [48,49]. In our analysis of the IceCube data, we consider two sources of uncertainties. One source of uncertainty is the atmospheric neutrino flux, which we parametrize by means of nuisance parameters. We consider the overall normalization of the atmospheric flux, the cosmic-ray slope, the uncertainty in the atmospheric density, the ratio of kaon-to-pion production yields, and the ratio of neutrino-to-antineutrino production. The second source of uncertainty is the detector. As discussed in [50,51], in this analysis we restrict ourselves to the leading detector systematic, namely the overall efficiency of the IceCube modules. Following [29], the IceCube log-likelihood can be written as

$$\ln \mathcal{L} = \min_{\eta} \left(\sum_{i=1}^{N_{\text{bins}}} [x_i \ln \mu_i(\vec{\theta}, \vec{\eta}) - \mu_i(\vec{\theta}, \vec{\eta}) - \ln x_i!] \right. \\ \left. + \frac{1}{2} \sum_{\eta} \frac{(\eta - \bar{\eta})^2}{\sigma_{\eta}^2} \right), \quad (3)$$

where x_i is the number of data events in the i th bin; μ_i is the Monte Carlo expectation for the number of events in the i th bin, assuming sterile neutrino parameters $\vec{\theta}$ and nuisance parameters $\vec{\eta}$; and each nuisance parameter, η , has a Gaussian constraints of mean, $\bar{\eta}$, and standard deviation, σ_{η} . We use the systematic treatment and analysis framework from [23] to calculate the IceCube likelihood.

For both the $3 + 1$ and $3 + 1 + \text{decay}$ global fits, the IceCube likelihood was calculated for a randomly selected subset of parameter-set points from the corresponding Markov Chain Monte Carlo from [5]. This global analysis used experiments where vacuum-oscillation probabilities are valid and, in the stable $3 + 1$ model, those were parametrized in terms of $|U_{e4}|$, $|U_{\mu 4}|$, and Δm_{41}^2 . The datasets used include all relevant muon-(anti)neutrino disappearance, electron-(anti)neutrino disappearance, and muon-to-electron (anti)neutrino appearance measurements; a list of the experiments used can be found in the Supplemental Material [52]. There are four notable

exceptions: (i) the Daya Bay result [53], as it does not significantly impact the preferred best-fit region ($\Delta m_{41}^2 > 1 \text{ eV}^2$) [3]; (ii) the reactor antineutrino anomaly, due to the large uncertainties in the reactor flux modeling made manifest by the so-called 5 MeV reactor bump [54,55]; (iii) the low-energy atmospheric neutrino results from SuperKamiokande [41] and IceCube/DeepCore, [40] as these constraints only reach $|U_{\mu 4}| > 0.2$ which are covered by other experiments in the squared-mass splitting region of interest; and (iv) the recent MINOS+ two-detector fit [56,57], due to the lack of clear explanation of the origin of the sensitivity in the high-mass region and increased systematic model dependence, so instead we use the traditional far-to-near ratio measurement by MINOS [58].

Each point is a unique combination of $|U_{e4}|$, $|U_{\mu 4}|$, and Δm_{41}^2 ; the lifetime, τ , is an additional parameter for the $3 + 1 + \text{decay}$ scenario. In this work, we set $|U_{\tau 4}|$ to zero, as the short-baseline experiments are insensitive to it and this is a conservative choice in the case of IceCube [3]. Downsampling points from the global analysis [5] is necessary because the IceCube likelihood calculation is computationally time intensive. We include the best-fit parameter-set points corresponding to $3 + 1$ and $3 + 1 + \text{decay}$ found in [5]. For the $3 + 1$ analysis, 49,000 points were used, while for the $3 + 1 + \text{decay}$ analysis 82,000 points were used.

To convert the IceCube likelihood into a χ^2 , we calculate the log-likelihood ratio [3],

$$\ln \mathcal{LR}(\vec{\theta}) = \ln(\mathcal{L}(\vec{\theta})) - \ln(\mathcal{SP}\{(x_i)\}), \quad (4)$$

where $\mathcal{SP}\{(x_i)\}$ is the saturated Poisson likelihood, and then assume Wilks' theorem, namely $\chi^2 = -2 \ln \mathcal{LR}$ [59,60]. To incorporate IceCube into the global fits, we add the IceCube χ^2 to the χ^2 from the short-baseline-only fits [5].

To determine the effect that IceCube data has on the tension for both the $3 + 1$ and $3 + 1 + \text{decay}$ models, we calculate the IceCube likelihood for a random downsampling of parameter points from the recent fits to only disappearance short-baseline experiments. We convert the IceCube likelihood to a χ^2 and add it to the short-baseline disappearance χ^2 . The fit to the appearance experiments remains unchanged.

III. RESULTS

In this section, we summarize the result of incorporating IceCube into our recent short-baseline-only global fit. Results for fitting a standard $3 + 1$ model are discussed in Sec. III A, while results for fitting a $3 + 1 + \text{decay}$ model are shown in Sec. III B. A summary of the χ^2 values for various fits and additional figures for all analyses performed in this work are given in the Supplemental Material [52].

A. $3 + 1$

In this section, we report the impact of adding IceCube to the short-baseline-only $3 + 1$ fit. Figure 1 shows the frequentist allowed regions without IceCube data (top) and with IceCube data incorporated (bottom), for a random downsampling of parameter points used in the recent global fit [5]. The allowed regions are shown in terms of Δm_{41}^2 and $\sin^2 2\theta_{\mu e}$, given by Eq. (1), at 90%, 95%, and 99% confidence levels. The best-fit points are indicated in each panel with a star. Before including IceCube data, the

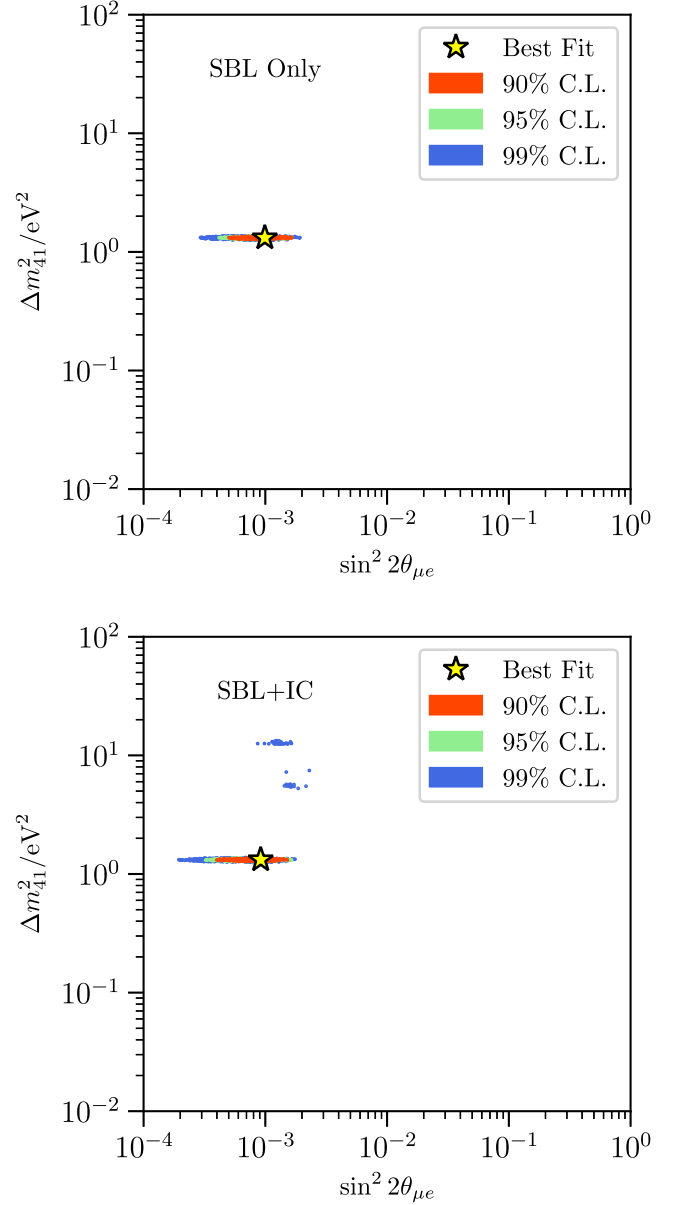


FIG. 1. The $3 + 1$ allowed regions for fits to short-baseline (SBL) experiments with and without IceCube (IC). The top panel shows the allowed regions when only considering the short-baseline experiments, while the bottom panel shows them with IceCube incorporated. Frequentist confidence regions are shown at the 90% (red), 95% (green), and 99% (blue) confidence levels.

TABLE I. $3 + 1$ model best-fit parameters. Each row corresponds to a different dataset used. The columns give the best-fit value of the parameter for the listed dataset.

$3 + 1$	Δm_{41}^2 (eV ²)	$ U_{e4} $	$ U_{\mu 4} $
SBL	1.32	0.116	0.135
IC	6.97	...	0.155
SBL + IC	1.32	0.116	0.131

downsampled points produce allowed regions that are consistent with our previous result and are shown here for completeness. Incorporating IceCube data pushes the island at $\Delta m_{41}^2 \approx 1.3$ eV² to slightly smaller $\sin^2 2\theta_{\mu e}$ and creates new islands at higher masses at the 99% confidence level. A table of the best-fit parameters is given in Table I and the best-fit $\Delta\chi^2$ is given in Table III. The obtained best-fit values on the $3 + 1$ model are in tension with the MINOS+ results not included in this work for the reasons mentioned in Sec. II. The significance of the best-fit point of the $3 + 1$ model compared to the null hypothesis, i.e., three neutrinos, is 4.9σ , slightly lower than it is without IceCube, 5.1σ . We have performed the parameter goodness of fit test to quantify the tension in the dataset. The significance of this tension with IceCube included is 4.8σ , which is slightly higher than the value without including IceCube, which is 4.5σ .

B. $3 + 1 + \text{decay}$

Global fit results for the $3 + 1 + \text{decay}$ model are shown in Fig. 2. The top row of this figure shows the allowed

regions without including IceCube, which are consistent with previous results, while the bottom row shows the allowed regions with IceCube incorporated. The allowed regions without considering IceCube span 3 orders of magnitude in τ , and are shown in three panels, each corresponding to the indicated range in τ . The allowed regions without IceCube occur in two distinct regions in Δm_{41}^2 . IceCube data eliminate the lower squared-mass difference island and collapses the allowed values to a narrow range around $\Delta m_{41}^2 \approx 1.4$ eV².

A table of the best-fit parameters is given in Table II and the best-fit $\Delta\chi^2$ is given in Table III. The significance of the best-fit point of the $3 + 1 + \text{decay}$ model compared to the three-neutrino hypothesis is 5.4σ , slightly lower than it is without IceCube, which is 5.6σ . Notably, the $3 + 1 + \text{decay}$ model is preferred to the standard $3 + 1$ model by 2.8σ . Our global-fit combines three different oscillation channels and the $3 + 1 + \text{decay}$ model introduces features in all three; see Supplemental Material [52] for details. In the reactor electron-antineutrino disappearance measurements, the best-fit decay reduces the oscillation features at low energies where the statistics are larger. Similarly, in muon-neutrino disappearance measurements, it reduces the oscillation amplitude for baselines greater than the decay length. In the appearance channel, for scales relevant for MiniBooNE, the appearance probability maintains the spectral shape but has increased normalization. Tension in the fits remains, at 3.5σ with IceCube, yet it is reduced by about 1.3σ compared to the standard $3 + 1$ model. Finally, note that the inclusion of absolute reactor flux normalization could yield important information to distinguish between models. The preferred

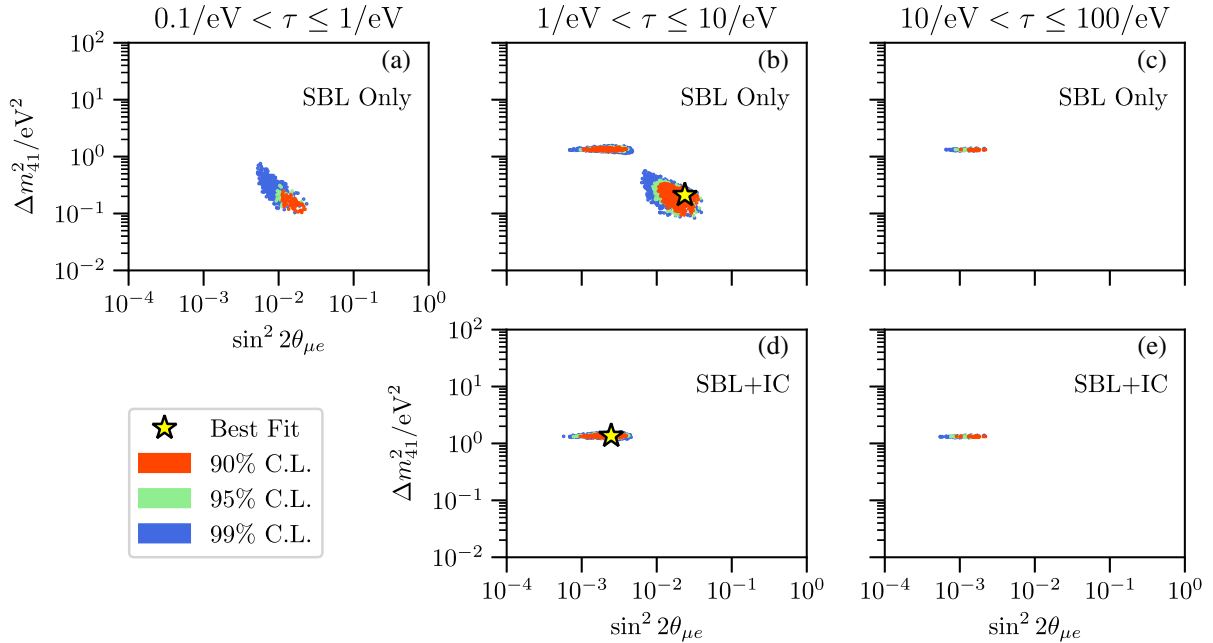


FIG. 2. The $3 + 1 + \text{decay}$ frequentist allowed regions. The top row is the result of the fit using only the short-baseline (SBL) experiments, while the bottom row includes IceCube (IC). Each vertical column corresponds to a given range of ν_4 lifetime, τ . The smallest range of lifetimes when including IceCube is not shown as it contains no points. The colors of the points indicate 90% (red), 95% (green), and 99% (blue) confidence levels.

TABLE II. $3 + 1 + \text{decay}$ model best-fit parameters. Each row corresponds to a different dataset used. The columns give the best-fit value of the parameter for the listed dataset. For $\tau = 1 \text{ eV}^{-1}$, $c\tau = 0.2 \text{ } \mu\text{m}$.

$3 + 1 + \text{decay}$	$\Delta m_{41}^2 \text{ (eV}^2\text{)}$	$\tau \text{ (eV}^{-1}\text{)}$	$ U_{e4} $	$ U_{\mu 4} $
Short-baseline	0.21	1.96	0.428	0.180
IceCube	6.22	8.11	...	0.124
Short-baseline + IceCube	1.35	4.50	0.238	0.105

TABLE III. Comparison of best-fit χ^2 values. The first row gives the difference in χ^2 and degrees of freedom between the null hypothesis (no sterile neutrino) and the best-fit values from global fits to a $3 + 1$ model and $3 + 1 + \text{decay}$ model. The second row gives the difference in best-fit χ^2 and degrees of freedom between a $3 + 1$ model and a $3 + 1 + \text{decay}$ model. The results in this table include IceCube data.

	$3 + 1$	$3 + 1 + \text{decay}$
$(\Delta\chi^2/\Delta\text{d.o.f.})_{\text{Null}}$	31.7/3	40.7/4
$(\Delta\chi^2/\Delta\text{d.o.f.})_{3+1}$...	9.1/1

parameters of the $3 + 1 + \text{decay}$ increase the electron-antineutrino disappearance from approximately 3% in the $3 + 1$ best-fit point to 10% for reactor neutrino scales of interest. However, the estimated neutrino flux uncertainties range from 2% to 6% in 1–6 MeV [61]; note also that the baseline flux model predictions did not foresee the appearance of a deviation at the 10% level known as the 5 MeV bump. Given these uncertainties, we have performed a normalization independent analysis. Including a reliable reactor flux uncertainty estimation would impact our obtained best-fit point.

IV. CONCLUSION

We have studied the impact of adding 1 year of IceCube high-energy atmospheric data to our short-baseline light sterile neutrino global fits. We considered two models in this work: one where the heavy neutrino mass state is stable and one where it decays to invisible particles. We summarize our findings here:

- (i) For the case of stable neutrino states, we find that the best-fit solution to the short-baseline data is only slightly changed; the largest change is in $|U_{\mu 4}|$ which goes from 0.135 to 0.131. Adding IceCube data makes two new solutions appear at the

99% C.L. at larger squared-mass differences; these are at approximately 10 eV^2 and 5 eV^2 , with $\sin^2 2\theta_{\mu e} \sim 10^{-3}$. Even though the IceCube analysis is a null-like result, the best-fit $3 + 1$ point is still significantly preferred over the null hypothesis by a $\Delta\chi^2 = 32$ with 3 degrees of freedom. This corresponds to a 4.9σ rejection of the null model. As expected, adding the IceCube dataset increases the tension between appearance and disappearance datasets which, measured using the parameter goodness of fit test, worsens from a p-value of 3.4×10^{-6} without IceCube to 8.1×10^{-7} with it.

- (ii) For the model where the heaviest mass state is allowed to decay into invisible particles, the preferred values of the parameters have changed significantly. The new best-fit point results in a squared-mass difference of 1.35 eV^2 , a lifetime of 4.5 eV^{-1} , and mixing elements $|U_{e4}| = 0.238$ and $|U_{\mu 4}| = 0.105$. As in the case of a stable neutrino mass states, this scenario is preferred over the null three-neutrino hypothesis at high significance, 5.6σ without IceCube and 5.4σ with it. This model was already preferred with respect to the $3 + 1$ scenario at the 2.7σ level [5], but with the addition of the IceCube data this preference increases to the 2.8σ level. Finally, the tension is slightly worse when adding the IceCube data in this model; the p-value for the parameter goodness of fit test decreases from 8.0×10^{-4} to 2.7×10^{-4} . Nevertheless, this model is still a factor of ~ 300 improvement in p-value with respect to the stable sterile neutrino scenario.

In conclusion, the $3 + 1 + \text{decay}$ scenario best-fit parameters have been significantly changed with the addition of 1 year of IceCube data. The new best-fit solution is still an improvement over the $3 + 1$ scenario since it improves the overall fit and reduces the tension between appearance and disappearance experiments. We expect that the upcoming 8-year IceCube high-energy sterile analysis may significantly impact the light sterile neutrino interpretation of the short-baseline anomalies.

ACKNOWLEDGMENTS

M. H. M., C. A. A., J. M. C., and A. D. are supported by NSF Grant No. PHY-1801996. M. H. M. is also supported by NSF GRFP-1122374. M. H. S. is supported by NSF Grant No. PHY-1707971. We thank Austin Schneider for useful comments.

[1] A. A. Aguilar-Arevalo *et al.* (LSND Collaboration), *Phys. Rev. D* **64**, 112007 (2001).

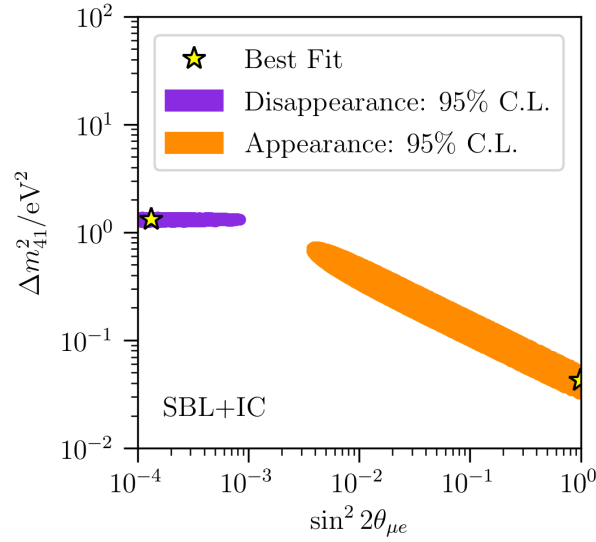
[2] A. A. Aguilar-Arevalo *et al.* (MiniBooNE Collaboration), *Phys. Rev. Lett.* **121**, 221801 (2018).

- [3] G. H. Collin, C. A. Argüelles, J. M. Conrad, and M. H. Shaevitz, *Phys. Rev. Lett.* **117**, 221801 (2016).
- [4] M. Dentler, A. Hernández-Cabezudo, J. Kopp, P. A. N. Machado, M. Maltoni, I. Martinez-Soler, and T. Schwetz, *J. High Energy Phys.* **08** (2018) 010.
- [5] A. Diaz, C. A. Argüelles, G. H. Collin, J. M. Conrad, and M. H. Shaevitz, [arXiv:1906.00045](https://arxiv.org/abs/1906.00045).
- [6] S. Böser, C. Buck, C. Giunti, J. Lesgourgues, L. Ludhova, S. Mertens, A. Schukraft, and M. Wurm, *Prog. Part. Nucl. Phys.* **111**, 103736 (2020).
- [7] G. Mention, M. Fechner, T. Lasserre, T. A. Mueller, D. Lhuillier, M. Cribier, and A. Letourneau, *Phys. Rev. D* **83**, 073006 (2011).
- [8] I. Alekseev *et al.* (DANSS Collaboration), *Phys. Lett. B* **787**, 56 (2018).
- [9] Y. J. Ko *et al.* (NEOS Collaboration), *Phys. Rev. Lett.* **118**, 121802 (2017).
- [10] M. Maltoni and T. Schwetz, *Phys. Rev. D* **68**, 033020 (2003).
- [11] S. N. Gninenko, *Phys. Rev. Lett.* **103**, 241802 (2009).
- [12] S. N. Gninenko, *Phys. Rev. D* **83**, 015015 (2011).
- [13] M. Masip, P. Masjuan, and D. Meloni, *J. High Energy Phys.* **01** (2013) 106.
- [14] A. Radionov, *Phys. Rev. D* **88**, 015016 (2013).
- [15] M. Blennow, P. Coloma, E. Fernandez-Martinez, J. Hernandez-Garcia, and J. Lopez-Pavon, *J. High Energy Phys.* **04** (2017) 153.
- [16] P. Ballett, S. Pascoli, and M. Ross-Lonergan, *Phys. Rev. D* **99**, 071701 (2019).
- [17] E. Bertuzzo, S. Jana, P. A. N. Machado, and R. Z. Funchal, *Phys. Rev. Lett.* **121**, 241801 (2018).
- [18] C. A. Argüelles, M. Hostert, and Y.-D. Tsai, *Phys. Rev. Lett.* **123**, 261801 (2019).
- [19] J. Liao, D. Marfatia, and K. Whisnant, *Phys. Rev. D* **99**, 015016 (2019).
- [20] P. B. Denton, Y. Farzan, and I. M. Shoemaker, *Phys. Rev. D* **99**, 035003 (2019).
- [21] P. Ballett, M. Hostert, and S. Pascoli, [arXiv:1903.07589](https://arxiv.org/abs/1903.07589).
- [22] O. Fischer, A. Hernández-Cabezudo, and T. Schwetz, [arXiv:1909.09561](https://arxiv.org/abs/1909.09561).
- [23] Z. Moss, M. H. Moulai, C. A. Argüelles, and J. M. Conrad, *Phys. Rev. D* **97**, 055017 (2018).
- [24] S. Palomares-Ruiz, S. Pascoli, and T. Schwetz, *J. High Energy Phys.* **09** (2005) 048.
- [25] I. Esteban, Light sterile neutrino decay and the short-baseline anomalies, <https://doi.org/10.5281/zenodo.3509890> (2019).
- [26] M. Dentler, I. Esteban, J. Kopp, and P. Machado, [arXiv:1911.01427](https://arxiv.org/abs/1911.01427).
- [27] A. de Gouvêa, O. L. G. Peres, S. Prakash, and G. V. Stenico, [arXiv:1911.01447](https://arxiv.org/abs/1911.01447).
- [28] H. Nunokawa, O. L. G. Peres, and R. Z. Funchal, *Phys. Lett. B* **562**, 279 (2003).
- [29] M. G. Aartsen *et al.* (IceCube Collaboration), *Phys. Rev. Lett.* **117**, 071801 (2016).
- [30] A. Esmaili and A. Y. Smirnov, *J. High Energy Phys.* **06** (2013) 026.
- [31] M. Lindner, W. Rodejohann, and X.-J. Xu, *J. High Energy Phys.* **01** (2016) 124.
- [32] E. Akhmedov, *J. High Energy Phys.* **08** (2016) 153.
- [33] M. Blennow, E. Fernandez-Martinez, J. Gehrlein, J. Hernandez-Garcia, and J. Salvado, *Eur. Phys. J. C* **78**, 807 (2018).
- [34] M. G. Aartsen *et al.* (IceCube Collaboration), *J. Instrum.* **12**, P03012 (2017).
- [35] M. G. Aartsen *et al.* (IceCube Collaboration), *Nucl. Instrum. Methods Phys. Res., Sect. A* **711**, 73 (2013).
- [36] M. G. Aartsen *et al.* (IceCube Collaboration), *Phys. Rev. Lett.* **120**, 071801 (2018).
- [37] R. Abbasi *et al.* (IceCube Collaboration), *Astropart. Phys.* **35**, 615 (2012).
- [38] M. G. Aartsen *et al.* (IceCube Collaboration), *Eur. Phys. J. C* **77**, 692 (2017).
- [39] T. K. Gaisser and M. Honda, *Annu. Rev. Nucl. Part. Sci.* **52**, 153 (2002).
- [40] M. G. Aartsen *et al.* (IceCube Collaboration), *Phys. Rev. D* **95**, 112002 (2017).
- [41] K. Abe *et al.* (Super-Kamiokande Collaboration), *Phys. Rev. D* **91**, 052019 (2015).
- [42] E. K. Akhmedov, *Yad. Fiz.* **47**, 475 (1988) [*Sov. J. Nucl. Phys.* **47**, 301 (1988)].
- [43] P. I. Krastev and A. Y. Smirnov, *Phys. Lett. B* **226**, 341 (1989).
- [44] M. Chizhov, M. Maris, and S. T. Petcov, [arXiv:hep-ph/9810501](https://arxiv.org/abs/hep-ph/9810501).
- [45] M. V. Chizhov and S. T. Petcov, *Phys. Rev. Lett.* **83**, 1096 (1999).
- [46] E. K. Akhmedov and A. Y. Smirnov, *Phys. Rev. Lett.* **85**, 3978 (2000).
- [47] M. G. Aartsen *et al.* (IceCube Collaboration), *Phys. Rev. Lett.* **115**, 081102 (2015).
- [48] C. A. Argüelles Delgado, J. Salvado, and C. N. Weaver, *Comput. Phys. Commun.* **196**, 569 (2015).
- [49] C. A. Argüelles, J. Salvado, and C. N. Weaver, nuSQuIDS, <https://github.com/Arguelles/nuSQuIDS> (2015).
- [50] C. A. A. Delgado, Ph. D. thesis, University of Wisconsin-Madison, 2015.
- [51] B. J. P. Jones, MIT (2015), Ph.D. thesis, <http://lss.fnal.gov/archive/thesis/2000/fermilab-thesis-2015-17.pdf>.
- [52] See Supplemental Material at <http://link.aps.org/supplemental/10.1103/PhysRevD.101.055020> for frequentist allowed regions for separate fits to appearance datasets and disappearance datasets, more detail on the preferred region of the $3 + 1 +$ decay model, the list of experiments included in the fits, and a table of χ^2 values that summarize the results.
- [53] F. P. An *et al.* (Daya Bay Collaboration), *Phys. Rev. Lett.* **117**, 151802 (2016).
- [54] P. Huber, *Nucl. Phys. B* **908**, 268 (2016).
- [55] M. Dentler, Á. Hernández-Cabezudo, J. Kopp, M. Maltoni, and T. Schwetz, *J. High Energy Phys.* **11** (2017) 099.
- [56] P. Adamson *et al.* (MINOS + Collaboration), *Phys. Rev. Lett.* **122**, 091803 (2019).
- [57] P. Adamson *et al.* (MINOS + and Daya Bay Collaborations), [arXiv:2002.00301](https://arxiv.org/abs/2002.00301).
- [58] P. Adamson *et al.* (MINOS Collaboration), *Phys. Rev. Lett.* **117**, 151803 (2016).
- [59] S. S. Wilks, *Ann. Math. Stat.* **9**, 60 (1938).
- [60] C. Patrignani *et al.* (Particle Data Group), *Chin. Phys. C* **40**, 100001 (2016).
- [61] L. Hayen, J. Kostensalo, N. Severijns, and J. Suhonen, *Phys. Rev. C* **100**, 054323 (2019).

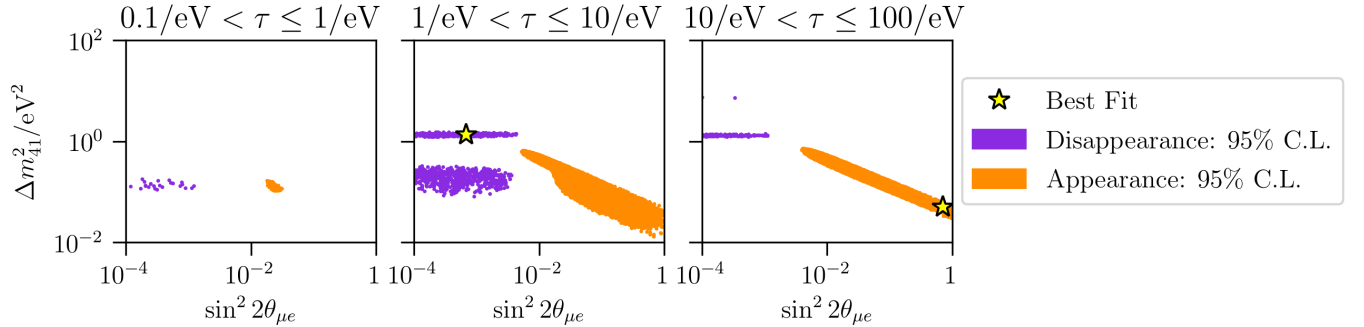
Supplementary Material

Illustrating tension between appearance and disappearance

Suppl. Fig. 1 and Suppl. Fig. 2 show frequentist allowed regions to separate fits to the appearance datasets and disappearance datasets at 95% confidence level, on plots of Δm_{41}^2 versus $\sin^2 2\theta_{\mu e}$. Suppl. Fig. 1 shows results for a 3+1 model, while Suppl. Fig. 2 shows results for a 3+1+decay model, separated into three lifetime decades. The disappearance datasets include IceCube. The best-fit points for each fit are indicated. In neither model is there overlap in the appearance and disappearance confidence intervals at 95%, indicating tension in the fits.



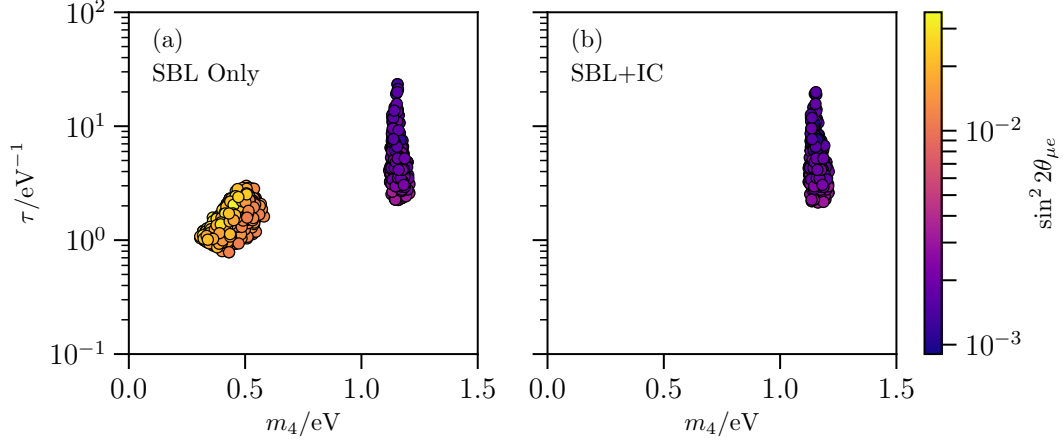
SUPPL. FIG. 1: *Preferred regions for separate appearance and disappearance 3+1 fits.* Frequentist 95% C.L. regions for fits to a 3+1 model, performed separately to appearance-only data and disappearance-only data, are shown. There is no overlap, indicating tension in the fits.



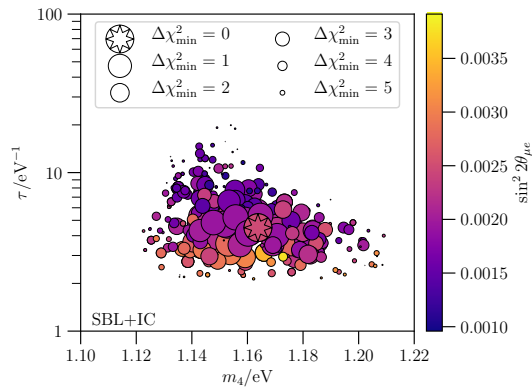
SUPPL. FIG. 2: *Preferred regions for separate appearance and disappearance 3+1+decay fits.* Frequentist 95% C.L. allowed regions for fits to a 3+1+decay model, performed separately to appearance-only data and disappearance-only data, are shown. There is no overlap, indicating tension in the fits.

Preferred regions of 3+1+decay

Suppl. Fig. 3 and Suppl. Fig. 4 show the global-fit result for a 3+1+decay model at 95% C.L. as a function of the three relevant parameters: lifetime (τ), heavy neutrino mass (m_4), and appearance amplitude ($\sin^2 2\theta_{\mu e}$). Suppl. Fig. 3 shows the result for Short-Baseline only (left) and IceCube incorporated (right). Suppl. Fig. 4 shows the result including IceCube, where the preference for each parameter point is indicated by the marker size.



SUPPL. FIG. 3: *3+1+Decay model allowed regions at 90% C.L.* The left panel shows the allowed regions when considering only the SBL dataset, while the right panel shows them with IceCube included. In both panels, the horizontal axis shows the new mass state mass, m_4 , the vertical axis its lifetime, τ , and the color scale the appearance amplitude. When considering only the SBL data two populations exist: one with large mixings and small masses ($\sin^2 2\theta_{\mu e} \sim 10^{-2}$ and $m_4 \sim 0.5$ eV) and another with smaller mixing and larger masses ($\sin^2 2\theta_{\mu e} \sim 10^{-3}$ and $m_4 \sim 1.25$ eV). When including IceCube the large mass population is removed. For $\tau = 1$ eV $^{-1}$, $c\tau = 0.2$ μm .



SUPPL. FIG. 4: *3+1+Decay model allowed regions using the SBL and IceCube data at 95% C.L. shown with parameter point preference.* In this figure the markers show the preference for a particular point, the horizontal axis shows the new mass state mass, m_4 , the vertical axis its lifetime, τ , and the color scale the mixing amplitude. The best-fit point is shown as the largest marker with the star symbol imprinted. Points with decreasing preference, with respect to the best-fit point, are drawn with smaller markers. For $\tau = 1$ eV $^{-1}$, $c\tau = 0.2$ μm .

List of experiments included

The data sets used in this work include neutrino and antineutrino sets; they are are:

- **Muon-to-electron neutrino appearance** ($\nu_\mu \rightarrow \nu_e$): MiniBooNE (BNB) [1], MiniBooNE (NuMI) [2], NOMAD [3], LSND [4], and KARMEN [5].
- **Muon-neutrino disappearance** ($\nu_\mu \rightarrow \nu_\mu$): SciBooNE/MiniBooNE [6], CCFR [7], CDHS [8], MINOS [9], and IceCube [10].
- **Electron-neutrino disappearance** ($\nu_e \rightarrow \nu_e$): KARMEN/LSND cross section [11], Bugey [12], NEOS [13], DANSS [14], SAGE [15], GALLEX [16], and PROSPECT [17].

Table of χ^2

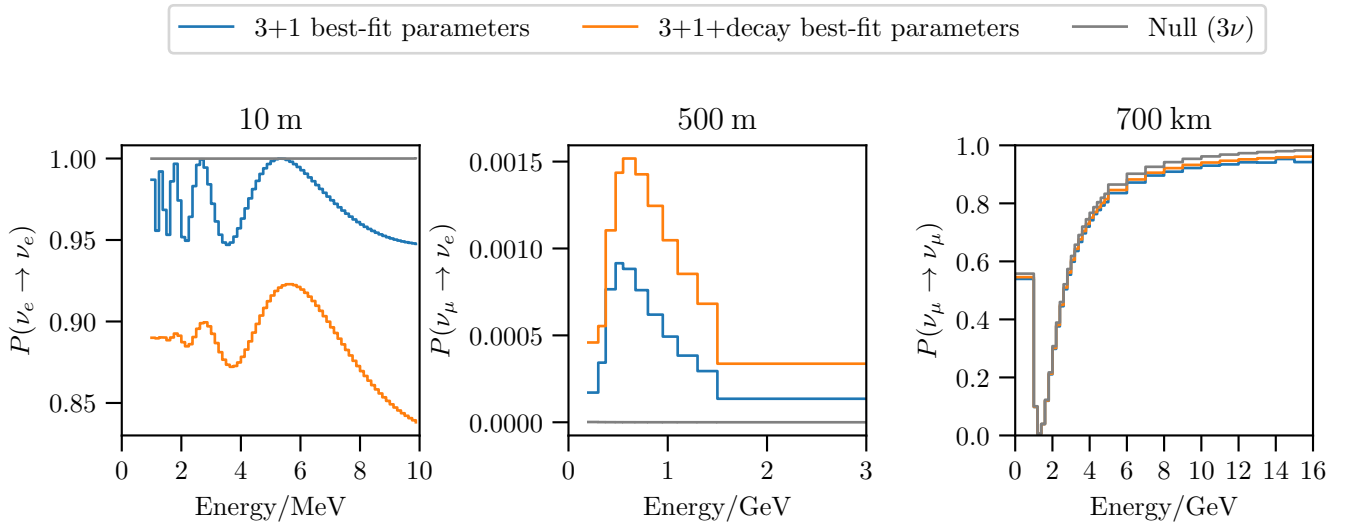
Suppl. Tbl. I reports the χ^2 obtained for the two different models considered in this work. For each model, we report the best-fit χ^2 for the short-baseline dataset only and this set with IceCube included as different columns. We also report the χ^2 obtained when separating the data into appearance and disappearance experiments in order to evaluate the parameter goodness of fit.

Fit type Dataset	3ν (Null) SBL	3ν (Null) SBL+IC	3+1 SBL	3+1 SBL+IC	3+1+Decay SBL	3+1+Decay SBL+IC
Best fit χ^2/dof p-value	492.7 / 509 0.69	672.5 / 718 0.89	458.4 / 506 0.94	640.8 / 715 0.98	449.9 / 505 0.96	631.84 / 714 0.99
Null vs. Sterile $\Delta\chi^2/\Delta\text{dof}$ p-value: $N\sigma$			34.3 / 3 1.7E-07 5.1	31.7 / 3 6.0E-07 4.9	42.8 / 4 1.2E-8 5.6	40.7 / 4 3.1E-8 5.4
3+1 vs. 3+1+decay $\Delta\chi^2/\Delta\text{dof}$ p-value: $N\sigma$					8.5 / 1 0.0036 2.7	9.0 / 1 0.0027 2.8
PG Test $(\chi^2/\text{dof})_{\text{app}}$ $(\chi^2/\text{dof})_{\text{dis}}$ $(\chi^2/\text{dof})_{\text{glob}}$ $(\chi^2/\text{dof})_{\text{PG}}$ p-value $N\sigma$			77.3 / 2 355.8 / 3 458.4 / 3 25.2 / 2 3.4E-6 4.5	77.3 / 2 535.5 / 3 640.8 / 3 28.0 / 2 8.1E-7 4.8	77.4 / 3 355.8 / 4 449.9 / 4 16.7 / 3 8.0E-4 3.2	77.4 / 3 535.4 / 4 631.8 / 4 19.0 / 3 2.7E-4 3.5

SUPPL. TABLE I: **Summary of χ^2 obtained in this global fit for different models, datasets and splits.** Each column corresponds to a particular combination of model (3ν , 3+1, or 3+1+decay) and dataset (SBL or SBL plus IceCube, SBL+IC). The first section gives the best-fit χ^2 , degrees of freedom (dof), and p-value. The second section compares a given sterile model (3+1 or 3+1+decay) and the three-neutrino model via the χ^2 difference for best-fit parameters for a fixed dataset. The third section contains the comparison between the 3+1 and 3+1+decay models, both with and without IceCube data. Finally, the fourth section reports the p-value for the parameter goodness of fit test for the 3+1 and 3+1+decay models, both with and without IceCube data.

Oscillation probabilities at best-fit parameter points

Suppl. Fig. 5 shows the oscillation probabilities at the best-fit parameter points for the 3+1 and 3+1+decay models. This figure is meant to illustrate and provide intuition on the difference between these two models and help understand why one is preferred over the other in our fits. Thus, we compare the oscillation probabilities relevant to three categories of experiments included in our fits: (left) short-baseline reactor measurements, (center) MiniBooNE, and (right) long-baseline accelerator measurements, like MINOS. In each plot, we show the oscillation probability averaged over each energy bin, with a binning chosen to reflect that used in the relevant experiment or experiment category. At the longest baselines, the 3+1 oscillations vary so rapidly with energy that the energy resolution of the detector prohibits resolving individual oscillation peaks. This makes the long-baseline muon-neutrino disappearance analysis a normalization only search, which are known to be less sensitive than shape analyses. The best-fit 3+1+decay parameters predicts a normalization slightly closer to the null hypothesis than the best-fit 3+1 parameters do. At the smallest baselines and lowest energies of reactor experiments, the oscillations are damped and only noticeable at larger energies where the reactor neutrino statistics are smaller. Finally, for MiniBooNE’s energies and baseline, the shape predicted by the two models remains similar, but the normalization is increased in the decay scenario.



SUPPL. FIG. 5: **Illustration of transition probabilities.** In these figures, blue indicates the 3+1 model at best-fit parameters, orange indicates the corresponding point in the 3+1+decay model, and grey indicates the null hypothesis (three neutrinos). In each panel, probabilities plotted are the average over each bin in energy, where the binning is chosen to reflect the experimental binning. The left panel shows the electron-neutrino survival probability in the energy range relevant for reactor experiments at a ten meter baseline. The center panel shows the muon-neutrino to electron-neutrino appearance probability for the energy and baseline scales relevant for the MiniBooNE measurement. Finally, the right panel shows the muon-neutrino survival probability for the energy range of long-baseline neutrino experiments that probe the atmospheric oscillation scale, like MINOS. In this panel, the 3+1 oscillations occur too rapidly to be resolved.

-
- [1] A. A. Aguilar-Arevalo et al. (MiniBooNE), Phys. Rev. Lett. **121**, 221801 (2018), 1805.12028.
 - [2] P. Adamson et al. (MiniBooNE, MINOS), Phys. Rev. Lett. **102**, 211801 (2009), 0809.2447.
 - [3] P. Astier et al. (NOMAD), Phys. Lett. **B570**, 19 (2003), hep-ex/0306037.
 - [4] C. Athanassopoulos et al. (LSND), Phys. Rev. Lett. **81**, 1774 (1998), nucl-ex/9709006.
 - [5] B. Armbruster et al. (KARMEN), Phys. Rev. **D65**, 112001 (2002), hep-ex/0203021.
 - [6] K. B. M. Mahn et al. (SciBooNE, MiniBooNE), Phys. Rev. **D85**, 032007 (2012), 1106.5685.
 - [7] I. E. Stockdale et al., Phys. Rev. Lett. **52**, 1384 (1984).
 - [8] F. Dydak et al., Phys. Lett. **134B**, 281 (1984).
 - [9] P. Adamson et al. (MINOS), Phys. Rev. Lett. **117**, 151803 (2016), 1607.01176.
 - [10] M. G. Aartsen et al. (IceCube), Phys. Rev. Lett. **117**, 071801 (2016), 1605.01990.
 - [11] J. M. Conrad and M. H. Shaevitz, Phys. Rev. **D85**, 013017 (2012), 1106.5552.

- [12] Y. Declais et al., Nucl. Phys. **B434**, 503 (1995).
- [13] Y. J. Ko et al. (NEOS), Phys. Rev. Lett. **118**, 121802 (2017), 1610.05134.
- [14] I. Alekseev et al. (DANSS), Phys. Lett. **B787**, 56 (2018), 1804.04046.
- [15] J. N. Abdurashitov et al. (SAGE), Phys. Rev. **C80**, 015807 (2009), 0901.2200.
- [16] F. Kaether, W. Hampel, G. Heusser, J. Kiko, and T. Kirsten, Phys. Lett. **B685**, 47 (2010), 1001.2731.
- [17] J. Ashenfelter et al. (PROSPECT), Phys. Rev. Lett. **121**, 251802 (2018), 1806.02784.

3.3 More on the phenomenology of unstable sterile neutrinos in IceCube

The results of combining the one-year IceCube data set with the global fit results from short-baseline measurements motivated further study of the unstable sterile neutrino model in IceCube. Decay of the fourth mass state causes two effects. One effect is a dampening of oscillation. The second effect is an overall disappearance of these particles. Transition probabilities as a function of baseline for muon antineutrinos traversing the diameter of the Earth are shown in Fig. 3-1. Transition probabilities as a function of energy for muon antineutrinos of energies 1 TeV and 2.3 TeV are shown in Fig. 3-2 for muon antineutrinos and Fig. 3-3 for muon neutrinos. These probabilities are calculated with `nuSQUIDSDecay` [62]. In all of these figures, the additional mass-squared splitting and mixing amplitude are $\Delta m_{41}^2 = 1.0 \text{ eV}^2$ and $\sin^2 2\theta_{24} = 0.1$. Furthermore, all these figures show transition probabilities for four values of the square of the coupling that mediates the decay, g^2 . The relationship between this coupling, g , the mass of the fourth neutrino mass state, m_4 , and its lifetime, τ is [62]

$$\tau = \frac{16\pi}{g^2 m_4}, \quad (3.2)$$

where it has been approximated that the lightest mass state is ν_1 and it is massless. The traditional $3 + 1$ model corresponds to $g^2 = 0$.

Decay of the fourth mass state causes a dampening of the oscillation between the muon and sterile flavors, shown in Fig. 3-1. In the top panel, the scenario with $g^2 = 0$ causes oscillations that appear in the true neutrino cosine zenith distribution, shown in the oscillograms in the publication in Section 3.1 and later in Section 6.3. This effect disappears very quickly with non-zero decay-mediating coupling, g^2 . While IceCube has good angular resolution, the angular binning and the energy resolution wash out these fine features in the reconstructed event distribution, as will be shown in Section 6.3.

Decay of the fourth mass state shifts the disappearance maximum to a longer

baseline, shown in Fig. 3-1. As g^2 goes from zero to 4π , there is a crossover in disappearance probabilities at fixed baseline. The shift in the position of the disappearance maximum moves the resonance in cosine zenith. This will be observable in the expected event distributions.

Decay of the fourth mass state widens the resonance seen in Fig. 3-2 (top). Below 200 GeV, oscillation between the muon and tau flavors becomes significant. This appears as disappearance of the muon flavor in Figs 3-2 and 3-3, without associated increase of the sterile flavor. At the highest energies, the Earth becomes opaque to neutrinos: a muon neutrino is likely to interact before crossing the diameter of the Earth. This causes the dramatic disappearance of muon flavor without associated increase in the sterile flavor.

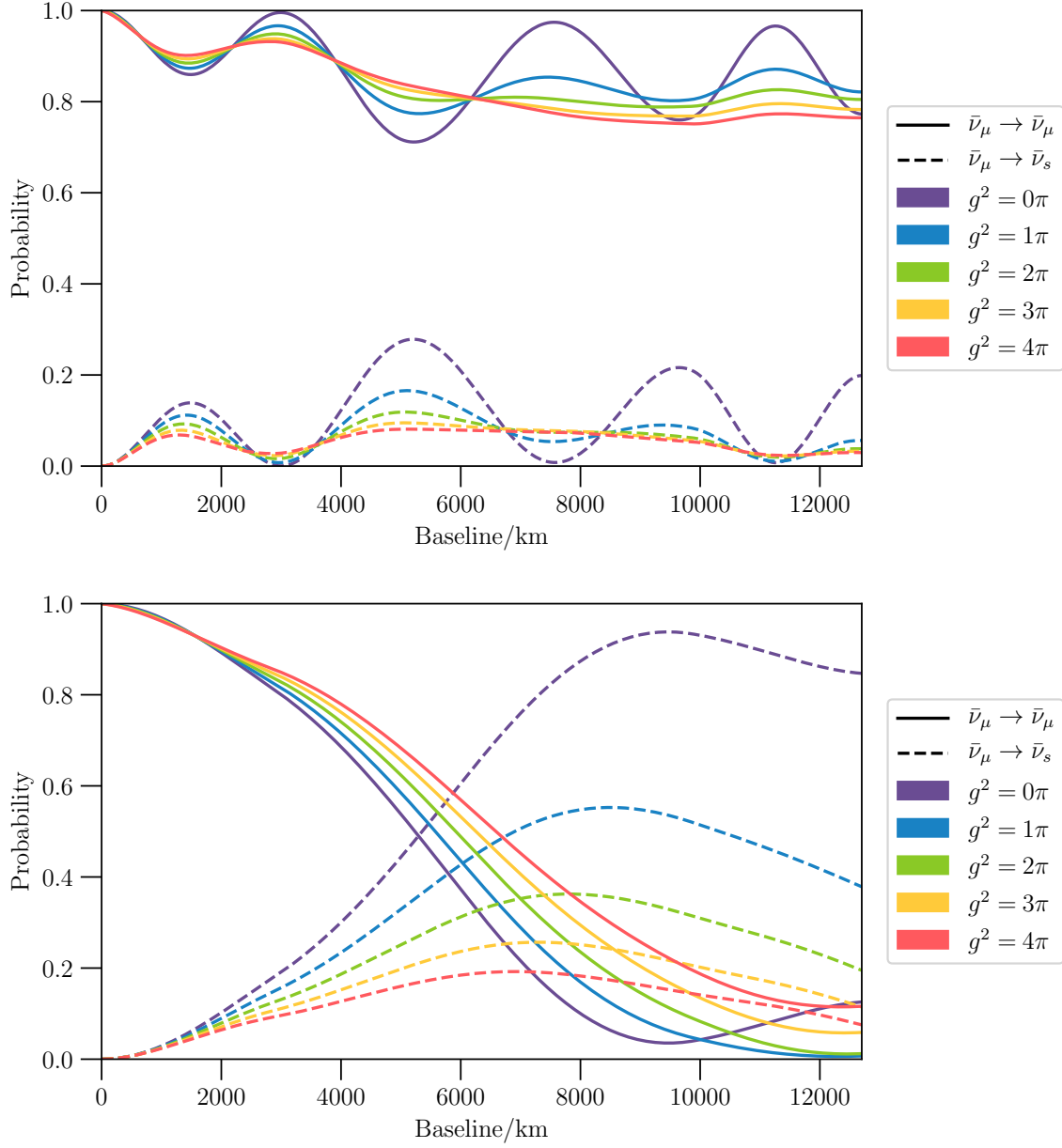


Figure 3-1: Transition probabilities of a 1 TeV (top) and 2.3 TeV (bottom) muon antineutrino traversing the diameter of the Earth for an unstable sterile neutrino model with invisible decay and parameters $\Delta m_{41}^2 = 1.0 \text{ eV}^2$ and $\sin^2 2\theta_{24} = 0.1$. The four different colors correspond to four values of the decay-mediating coupling, g^2 , where $g^2 = 0$ corresponds to a traditional 3+1 model, i.e. no neutrino decay. The solid curves correspond to muon antineutrino survival probabilities. The dashed curves correspond to the probability of antineutrino oscillating into the sterile flavor.

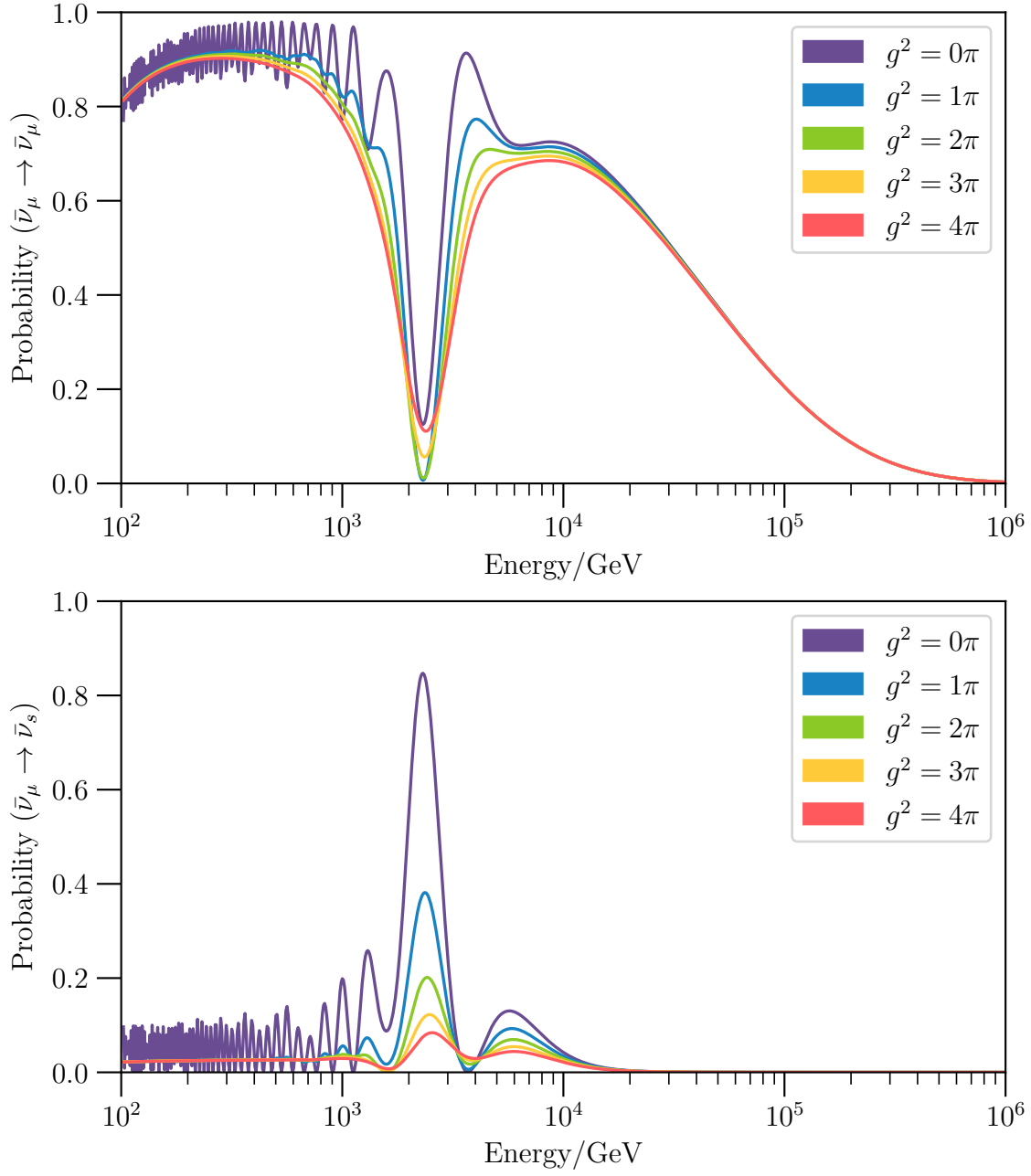


Figure 3-2: Probabilities, shown as a function of energy, of muon antineutrinos traversing the diameter of the Earth to (top) survive in the muon flavor and (bottom) transition to the sterile flavor, assuming an unstable sterile neutrino model with invisible decay and parameters $\Delta m_{41}^2 = 1.0 \text{ eV}^2$ and $\sin^2 2\theta_{24} = 0.1$. The four different colors correspond to four values of the decay-mediating coupling, g^2 , where $g^2 = 0$ corresponds to a traditional 3+1 model, i.e. no neutrino decay. At the highest energies, the survival probability of muon antineutrinos goes to zero because of the likelihood of interactions within the Earth.

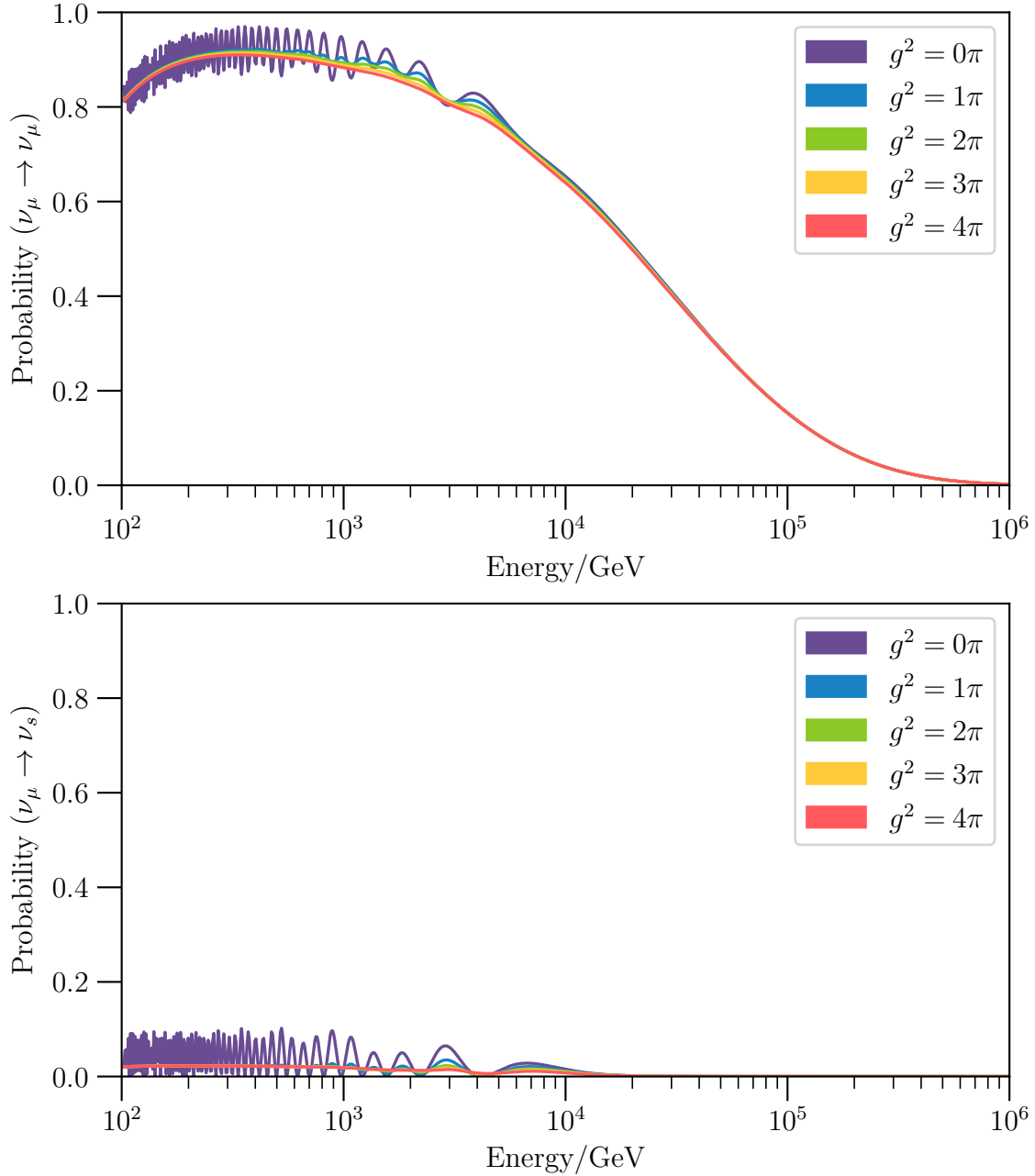


Figure 3-3: Probabilities, shown as a function of energy, of muon neutrinos traversing the diameter of the Earth to (top) survive in the muon flavor and (bottom) transition to the sterile flavor, assuming an unstable sterile neutrino model with invisible decay and parameters $\Delta m_{41}^2 = 1.0 \text{ eV}^2$ and $\sin^2 2\theta_{24} = 0.1$. The four different colors correspond to four values of the decay-mediating coupling, g^2 , where $g^2 = 0$ corresponds to a traditional 3+1 model, i.e. no neutrino decay. At the highest energies, the survival probability of muon neutrinos goes to zero because of the likelihood of interactions within the Earth.

Chapter 4

The IceCube neutrino detector

4.1 The IceCube Neutrino Observatory

The IceCube Neutrino Observatory (ICNO) is located at the Amundsen-Scott South Pole Station in Antarctica [64]. The ICNO is depicted in Fig. 4-1, with the Eiffel Tower shown for scale. The ICNO has two detector components. One component is the in-ice array, IceCube, which uses a cubic kilometer of clear, Antarctic ice to detect high-energy neutrinos via the emission of Cherenkov radiation. IceCube is located deep in the ice and is described in section 4.2. The second component, IceTop, is a surface array that detects cosmic ray air showers and is only mentioned for completeness. As depicted in Fig. 4-1, the in-ice array has a more-densely instrumented sub-array, named DeepCore, which detects neutrinos at lower energies than the main array [65]. The IceCube Laboratory, housing a farm of computer servers, is at the surface [64]. Data collected in the array are sent to the IceCube Laboratory, where they are processed and filtered. Interesting data are sent to the north over satellite.

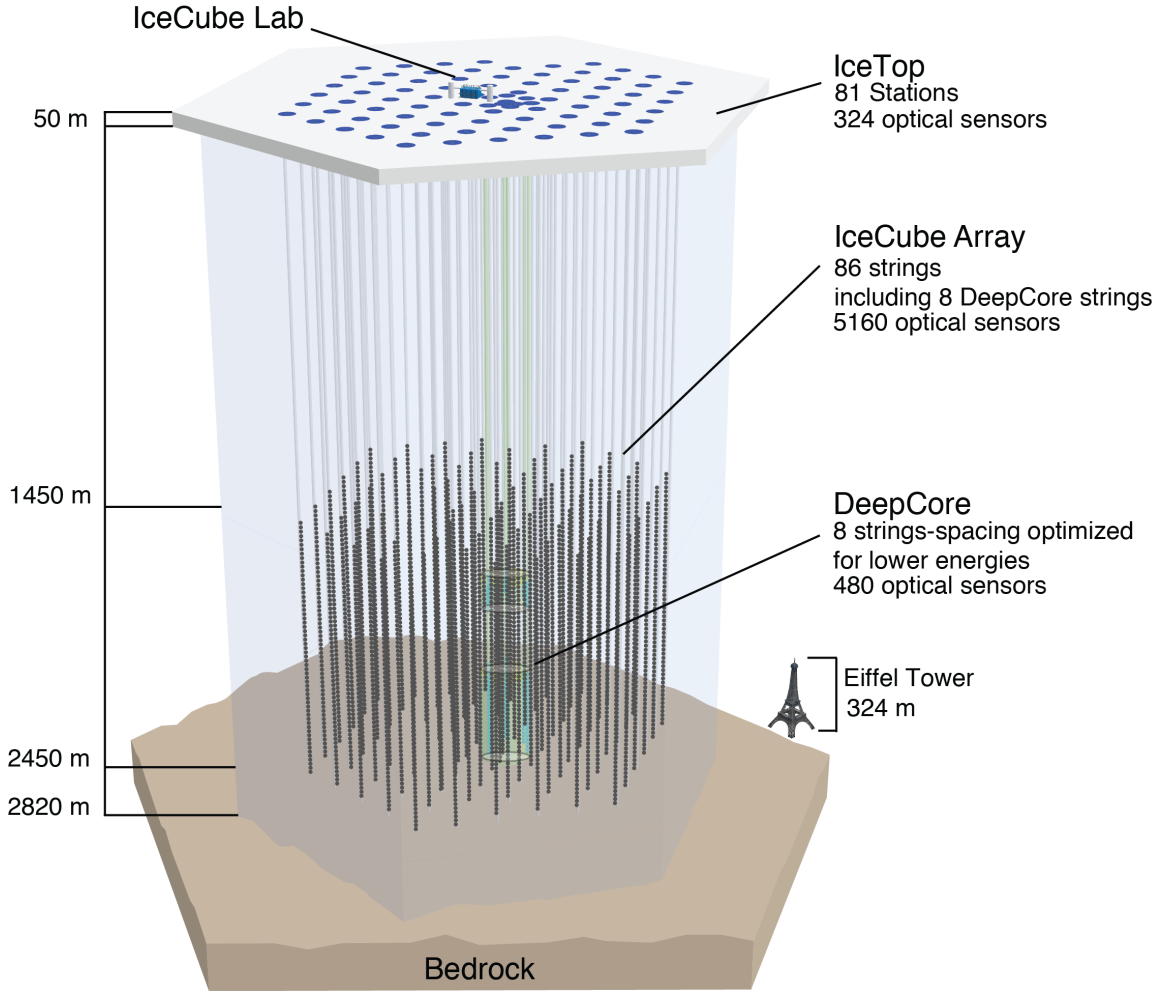


Figure 4-1: Schematic illustration of the IceCube Neutrino Observatory. Credit: IceCube Collaboration.

4.2 IceCube in-ice array

IceCube instruments a cubic kilometer of ice with optical sensors [64]. This large volume is desirable because the atmospheric and astrophysical neutrino fluxes fall steeply with energy. The South Pole ice cap is about 3 km deep, and IceCube instruments depths between 1450 m and 2850 m below the surface. The optical sensors, called Digital Optical Modules (DOMs), are described in Section 4.3. Altogether, 5160 DOMs hang on 86 bundled cables called strings. Of the 86 strings, 78 are spaced 125 m apart horizontally in a hexagonal array. On these strings, the 60 DOMs per string are separated by 17 m vertically. There are 8 additional strings that are part

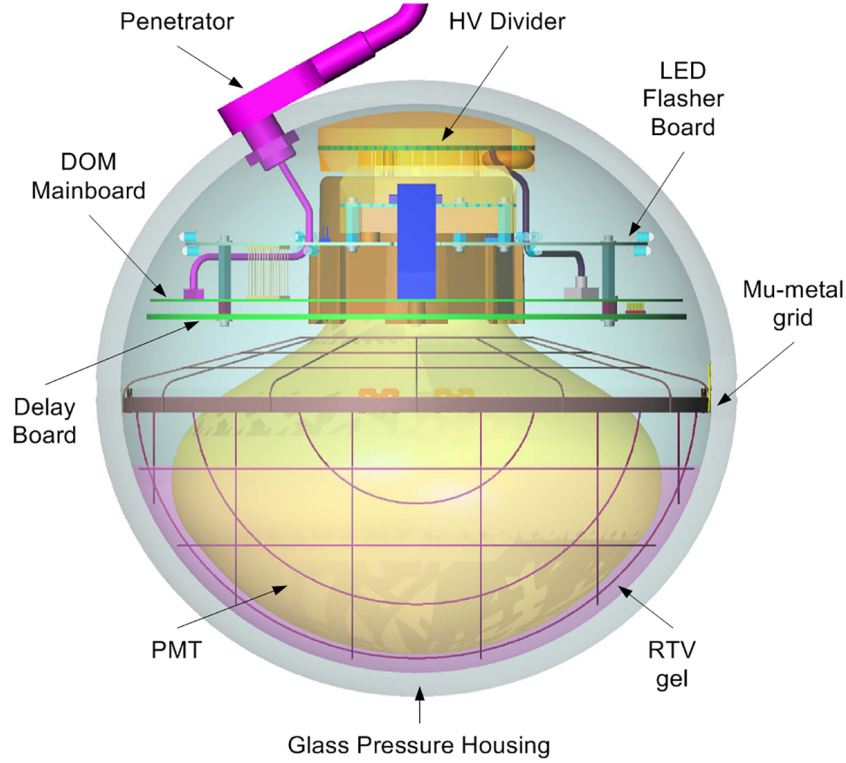


Figure 4-2: Schematic illustration of an IceCube digital optical module (DOM). Credit: IceCube Collaboration.

of DeepCore. These DeepCore-specific strings are positioned closer together horizontally, and below 1750 m below the surface, the DOMs are positioned closer together vertically [65].

4.3 Digital Optical Module

The DOM is the basic unit of both detection and data acquisition (DAQ) in IceCube. DOMs are capable of bidirectional communication with adjacent DOMs and the central DAQ at the IceCube Laboratory and executing calibration tasks. A schematic of a digital optical module (DOM) is shown in Fig. 4-2. Each DOM houses a 10" Hamamatsu photo-multiplier tube (PMT). The regular DOMs use Hamamatsu R7081-02 PMTs while some DOMs in DeepCore use a higher quantum efficiency version, Hamamatsu 47081-02MOD [66]. The PMT is positioned downwards-facing in a glass pressure sphere. Approximately 1 cm of clear silicone gel between the PMT

window and the glass housing both mechanically supports the PMT and optically couples it to the glass. The glass housing is made of low-radioactivity borosilicate glass and can withstand 250 bar [64]. A mu-metal grid surrounds the bulb of the PMT to shield it from the ambient South Pole magnetic field, which is 550 mG at an angle of 17° from vertical.

DOMs have several circuit boards. The Main Board digitizes PMT signals, communicates with adjacent DOMS and the central DAQ, and powers and directs all DOM subsystems as needed. The LED Flasher Board produces light within the array for the purposes of calibration [64, 67]. The standard Flasher Board has 12 light-emitting diodes, with six pointing out horizontally and six tilted up at 51.6° . The Flasher Board is used to calibrate the position of DOMs in the ice and to measure the optical properties of the ice. The remaining circuit boards produce the high voltage for the PMT, set and monitor the PMT high voltage, and delay PMT signals.

4.4 The ice

The deep glacial ice at the South Pole is a good medium for detection of Cherenkov radiation because it is exceptionally clear: the effective scattering length and absorption length are order 10 m and 100 m, respectively, for light at 400 nm. At depths below 1450 m, there are no bubbles naturally present [68]. There are, however, impurities such as dust. The concentration of dust varies throughout the ice in a tilted, depth-dependent manner [69]. Most notable is the presence of an approximately 100 m thick dust layer at a depth of about 2000 m; in this dust layer, scattering and absorption of light is much worse [67]. The temperature and pressure also vary in the ice, modifying photon propagation. As well as inhomogeneous, the optical properties of the ice have been found to be anisotropic [70]. Light birefringence in ice polycrystals has been proposed as an explanation of the anisotropy [71]. The optical properties thus requires calibration and modeling [64, 68, 70].

The dust concentration and tilt of the ice have been measured with laser dust loggers. After six IceCube boreholes were water drilled for the installation of strings,

laser dust loggers were deployed to measure the amount of dust. Optical profiles of the boreholes were produced, with a resolution of approximately 2 mm [72]. A tilt map of the ice was produced from comparison of measurements as a function of depth for the different boreholes.

The optical properties of the glacial ice can be described with a six-parameter ice model and a table of depth-dependent coefficients [67,69]. The scattering component of the model makes use of Mie scattering theory, which describes the scattering of photons off targets of general sizes and predicts the scattering angle distribution for any wavelength [68,73]. The depth-dependent coefficients correspond to scattering and absorption lengths. The absorption coefficient is the inverse of the average distance a photon travels before absorption. The scattering coefficient is the inverse of the average distance between consecutive scatters; an effective scattering coefficient is more useful for modeling the ice, as most scatters are in the forward direction. The coefficients are estimated for the wavelength 400 nm. The wavelength-dependency of these coefficients is modelled. The coefficients can be considered average values for 10 m thick layers. Calibration data, using light from the LEDs in the DOMS, is fit to this model to determine these coefficients [67]. There is excellent agreement between the effective scattering coefficient extracted from flasher data and the average dust log [67]. The values of the effective scattering coefficient and the dust absorption coefficient at 400 nm for the ice model used in this work are shown in Fig. 4-3.

The “hole ice” is the refrozen ice in the boreholes that had been hot-water drilled for installation of the detector [64,67]. The hole ice is about 60 cm in diameter and froze naturally. It has worse optical properties than the undisturbed glacial ice. The hole ice has two components. The outer component, at radii about 8-30 cm, is clear, but has an effective scattering length of about 50 cm, greatly diminished compared to that of the glacial ice. The inner component, about 16 cm in diameter, is called the bubble column. It is hypothesized that air introduced during drilling is pushed to the center of the borehole during refreezing. The bubble column has an even shorter scattering length. Two video cameras deployed on one of the strings recorded the freezing process and confirm the presence of the bubble column, which appears

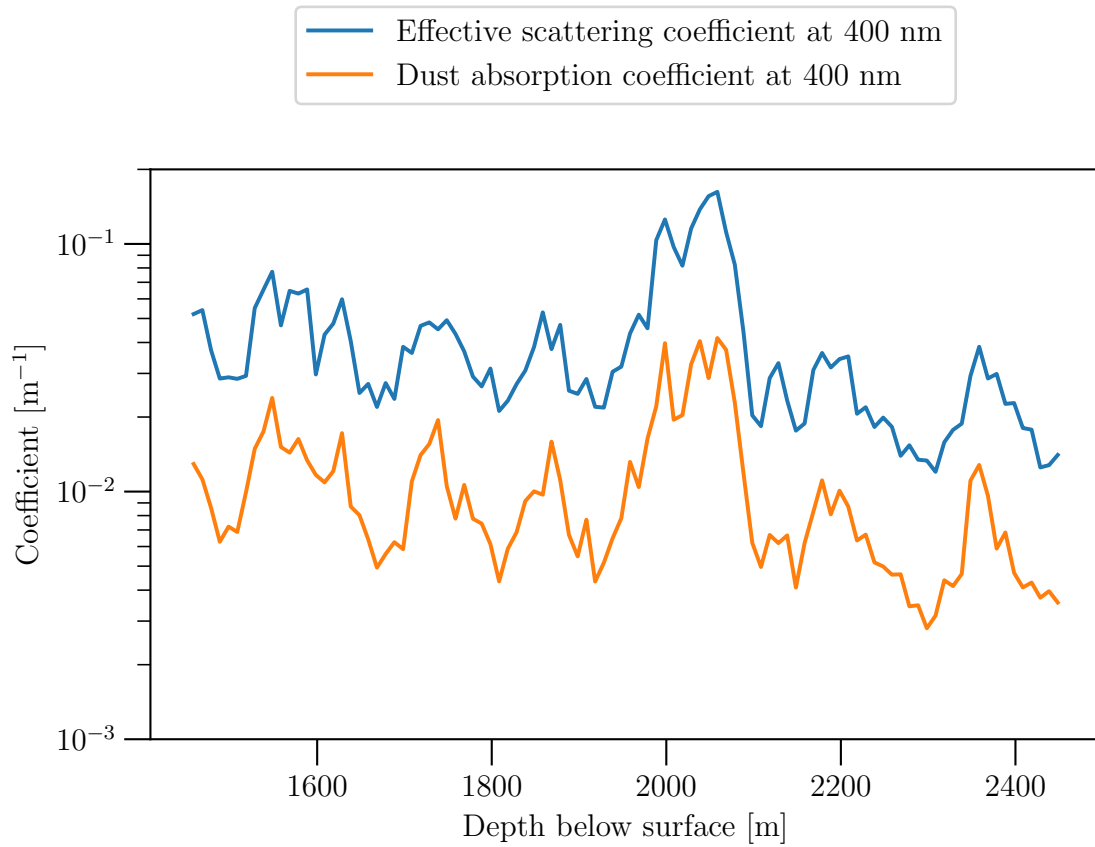


Figure 4-3: Effective scattering and dust absorption coefficients at 400 nm from the Spice3.2 ice model.

opaque, as well as fits to calibration flasher data.

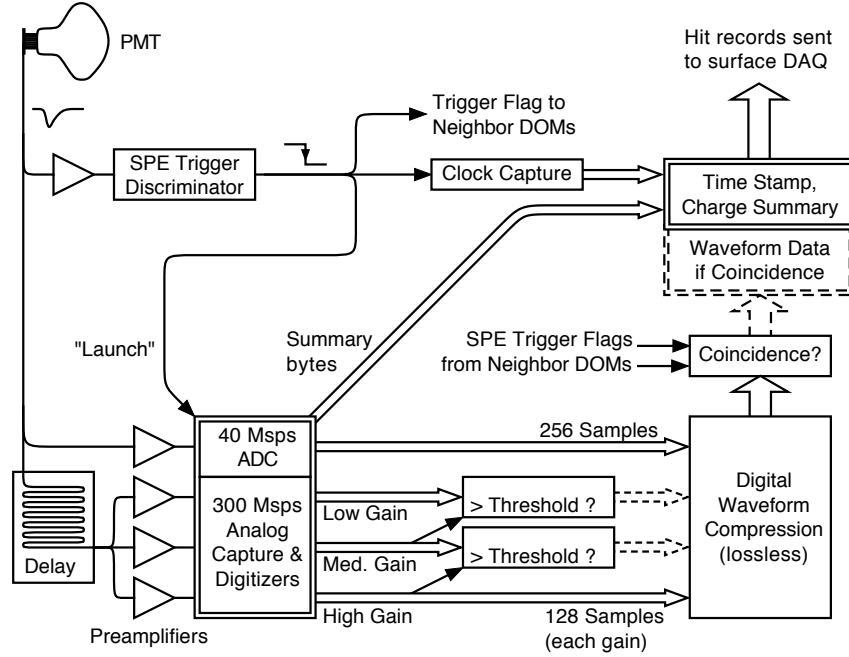


Figure 4-4: Data flow from PMT to central DAQ at the surface. Figure from [64].

4.5 Data acquisition

Data flow from the PMT to the central DAQ at the IceCube Laboratory is depicted schematically in Fig. 4-4. The PMT gain is about 10^7 [66] for a single photon. The output signal of the PMT is AC-coupled with a toroidal transformal [64]. This output is then routed to a discriminator, which is set to fire when the voltage corresponds to 0.25 single photoelectrons (SPE). This is called a “hit” and begins a “launch”. The time is captured. Four digitizers, one continuously sampling fast Analog-to-Digital Converter (fADC) and three custom Analog Transient Waveform Digitizers (ATWD), are used to capture the PMT signal. The signal has been routed through a delay board before reaching the three ATWDs. The three ATWDs have low, medium, and high gain, to capture a wide range of PMT signals. Using dedicated wiring, the DOM communicates with the nearest and next-to-nearest DOMS up and down on the string, to determine whether there is a local coincidence of hits. This will determine how much information is transmitted to the surface. In the case of a local coincidence, the hit is called called a Hard Local Coincidence (HLC) hit, and a timestamp, charge summary and waveform data are sent. In the case of no local coincidence, the hit is

called Soft Local Coincidence (SLC) hit, and only a timestamp and charge summary are sent.

At the IceCube Laboratory, a filter searches for events likely to correspond to muons [64]. Due to the morphology, these events are called tracks. All up-going tracks are selected. Data are sent to the north over satellite.

4.6 Description of neutrino interaction

At energies above 100 GeV, neutrinos interact via Deep Inelastic Scattering (DIS), where a neutrino scatters off one quark in a nucleon [74]. The products of this interaction are a hadronic shower and an outgoing lepton. In muon neutrino charged-current interactions, the outgoing lepton is a muon. The leading-order Feynman diagram for charged-current muon neutrino DIS is shown in Fig. 4-5. The cross sections for charged-current interactions above 100 GeV are given in Fig. 4-6, for both neutrinos, in light green, and antineutrinos, in dark green.

The fraction of neutrino energy, E_ν , that goes into the hadronic shower is the in-elasticity, y . The muon energy, E_μ , is then $(1 - y)E_\nu$. For energies in the range 100 GeV – 20 TeV, the mean inelasticity, $\langle y \rangle$, is approximately 0.4 – 0.5 [75, 76]. The mean inelasticity as a function of neutrino energy is shown in Fig. 4-7. The curves are mean inelasticity predictions for neutrinos (blue), antineutrinos (green), and the flux-averaged combination of neutrinos and antineutrinos (red). The black crosses show measurements from IceCube.

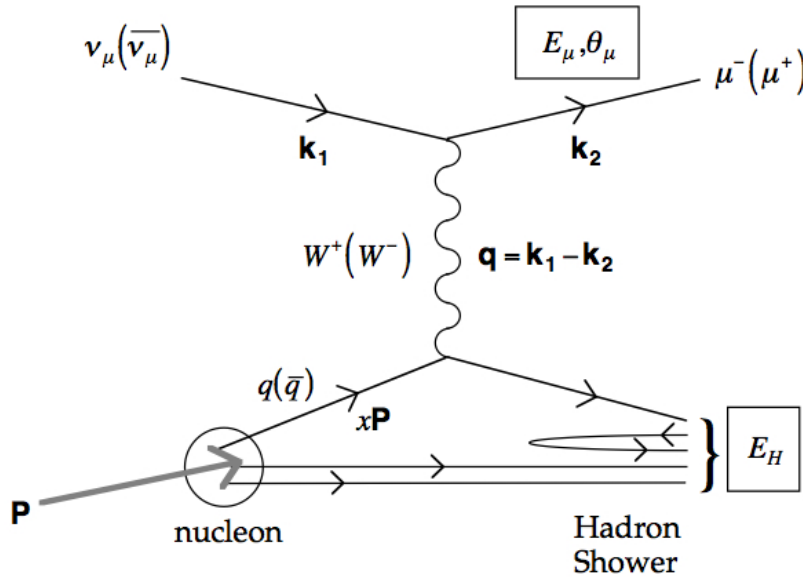


Figure 4-5: Feynman diagram for the first-order contribution to muon-neutrino, charged-current DIS. Figure from [77].

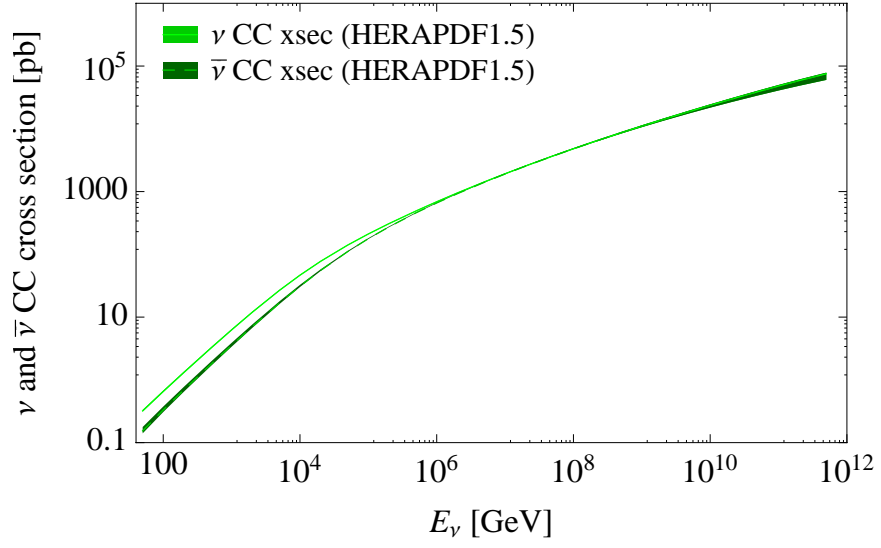


Figure 4-6: Neutrino and antineutrino charged-current cross sections. Figure from [78].

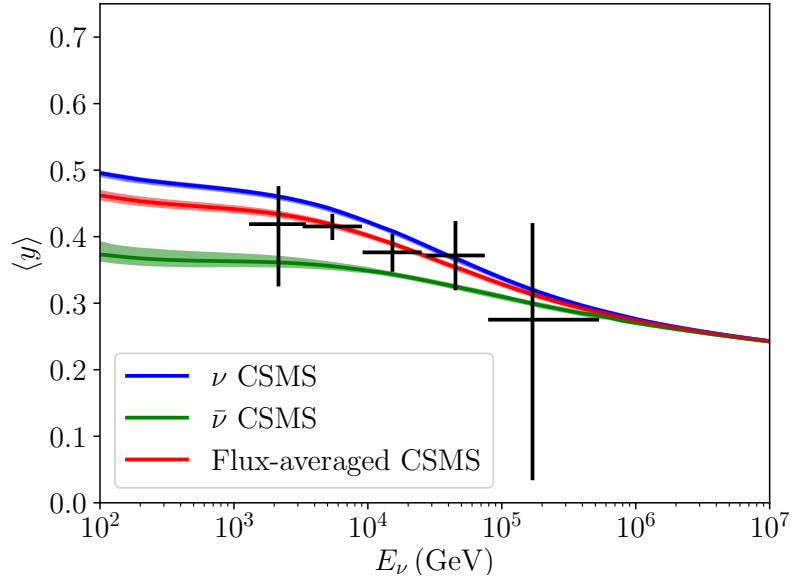


Figure 4-7: Mean inelasticity as a function of neutrino energy. Figure from [76].

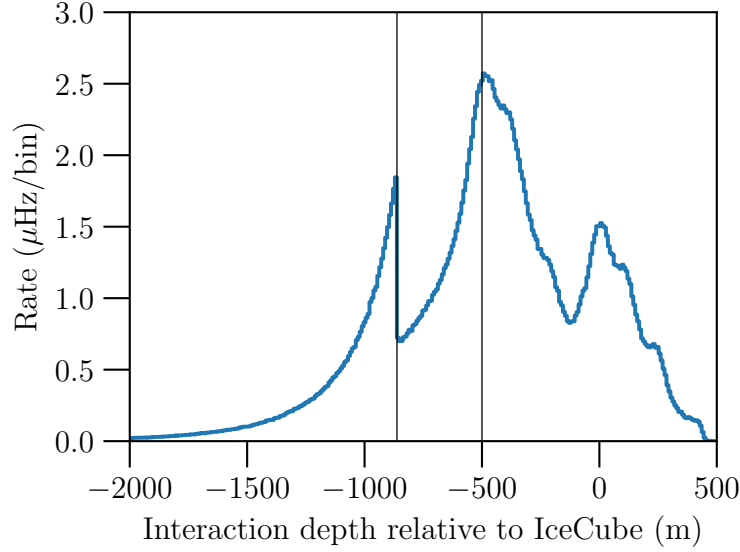


Figure 4-8: Distribution of neutrino interaction depth relative to IceCube, from simulation. The vertical line at -862 m denotes the transition between bedrock and ice. The vertical line at -500 m denotes the bottom of the detector.

In the events relevant for this thesis, neutrino interaction occurs either in the bedrock or ice below IceCube. About 20% of the interactions occur in the bedrock, shown in Fig. 6-5. The hadronic shower is contained outside the detector. The muon enters the detector and is observed. The muon, traveling faster than the speed of light in ice, will radiate Cherenkov light, which may be detected by DOMs. The muon will lose energy as it traverses the ice. Ionization, pair production, bremsstrahlung and photonuclear interactions all contribute to muon energy losses [79]. The average stopping power of each process as a function of muon energy is shown in Fig. 4-10 (top). Below approximately 2 TeV, ionization dominates. Above this energy, the other, radiative processes dominate. Secondary particles produced in these interactions include delta electrons, bremsstrahlung photons, excited nuclei and pairs of electrons [80]. The energy spectra for these secondary particles, for the case of a 10 TeV muon traveling through rock, is given in Fig. 4-10 (bottom). Charged secondaries of sufficiently high energy will themselves produce Cherenkov radiation, which may be detected by DOMs. These processes are stochastic, resulting in bursts of energy loss along the muon's trajectory. The muon is likely to exit the detector, as muons in the energy

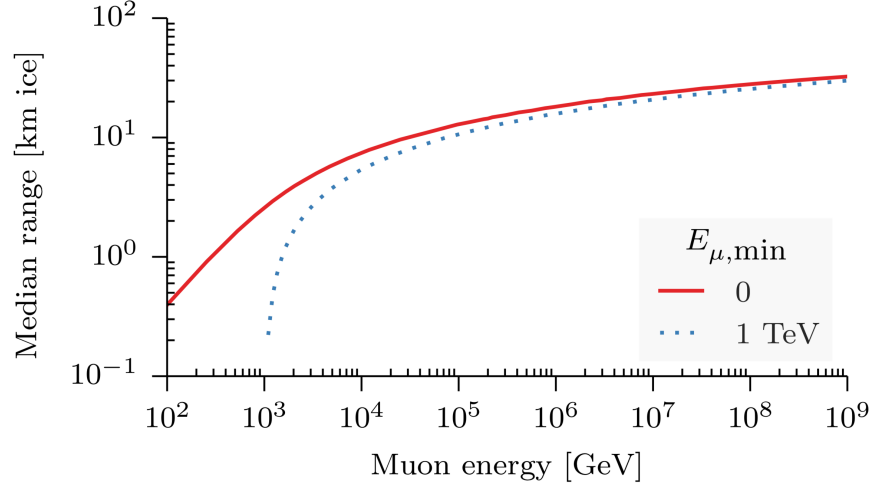


Figure 4-9: Muon range in ice as a function of initial muon energy, calculated with PROPOSAL [80]. The solid, red curve shows the median muon range. The dotted blue curve shows the range at which 50% of muons will have kinetic energy larger than 1 TeV. Figure from [81].

range 500 GeV – 10 TeV can travel kilometers of ice. The median range of muons is shown in Fig. 4-9. Event displays for two muons are shown in Figs. 4-11 and 4-12 .

Muons and antimuons have opposite electric charges. Other experiments may distinguish them by imposing a magnetic field and observing the direction in which their trajectories curve. IceCube has no such magnetic field, and therefore no ability to distinguish between muons and antimuons. This means that IceCube cannot distinguish between muon neutrinos, which would be tagged by the presence of a muon, and muon antineutrinos, which would be tagged by the presence of an antimuon.

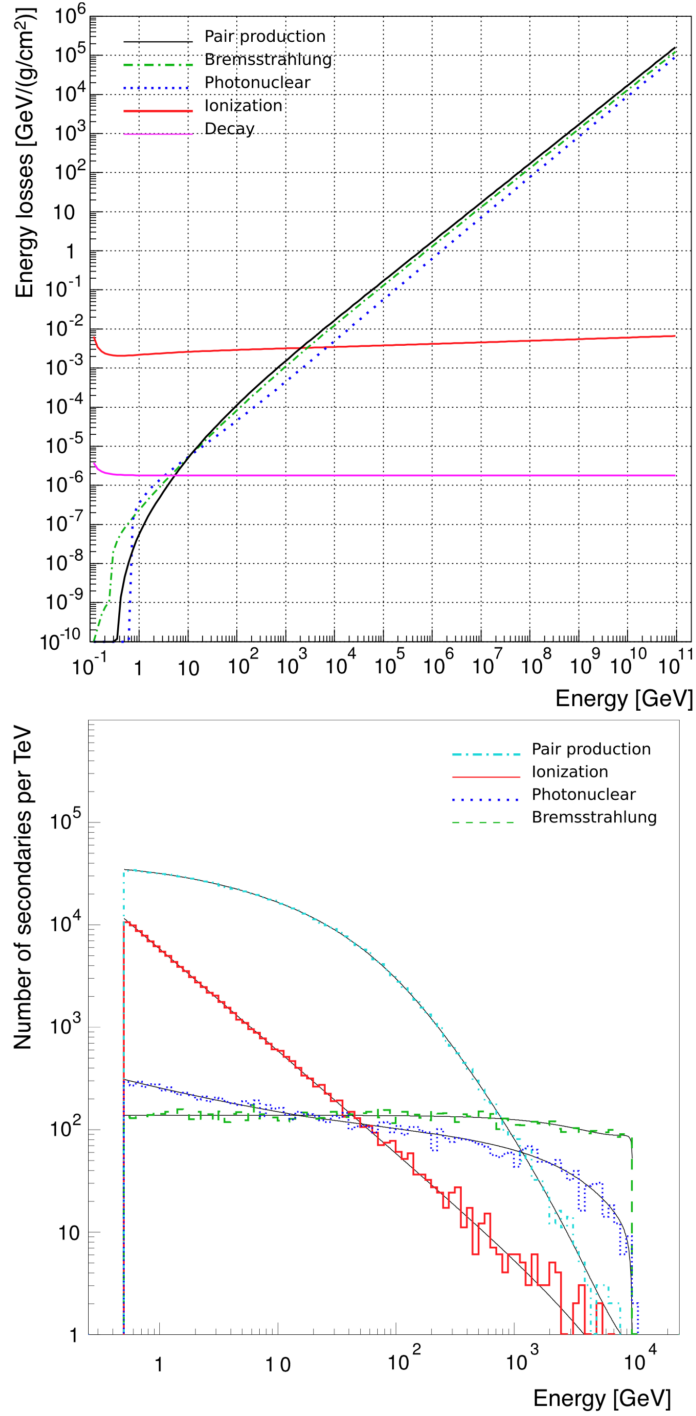


Figure 4-10: (Top) Energy losses for muons in ice. (Bottom) Energy spectra of secondary particles for a 10 TeV muon traveling through rock. All calculations performed with PROPOSAL [80]. Figures from [80].

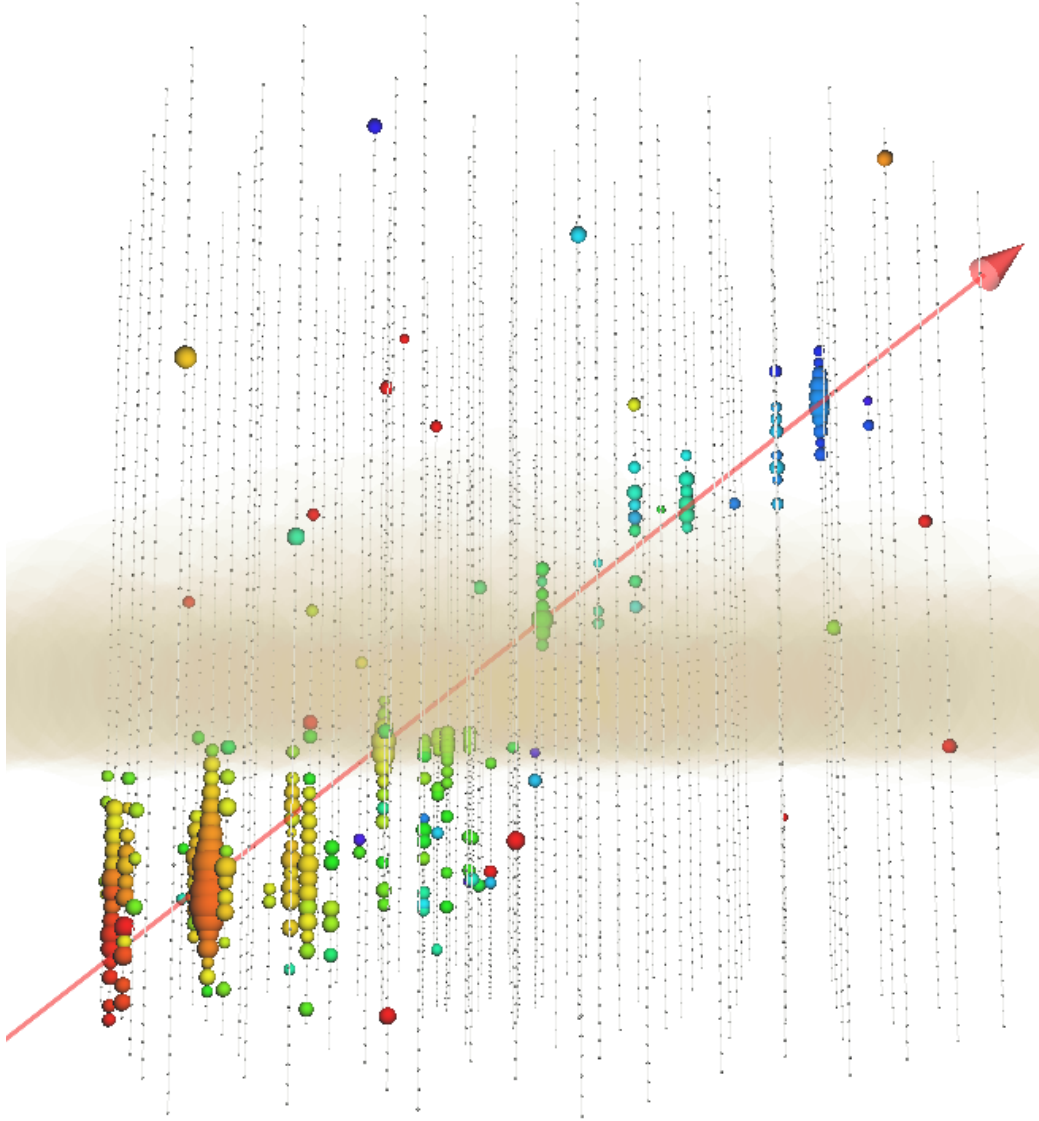


Figure 4-11: Event display for an up-going muon. The thin, grey, vertical lines correspond to the 86 IceCube strings. The small grey dots on the strings are the DOMs that did not see light. The DOMs that observed light are shown as colored spheres. The color of the sphere indicates timing, where red DOMs saw light at the earliest times and blue DOMs at the latest times. The larger the size of the sphere, the more light was observed. The reconstructed muon trajectory is shown a red line. The reconstructed muon energy is 5.2 TeV. Figure courtesy of Sarah Mancina.

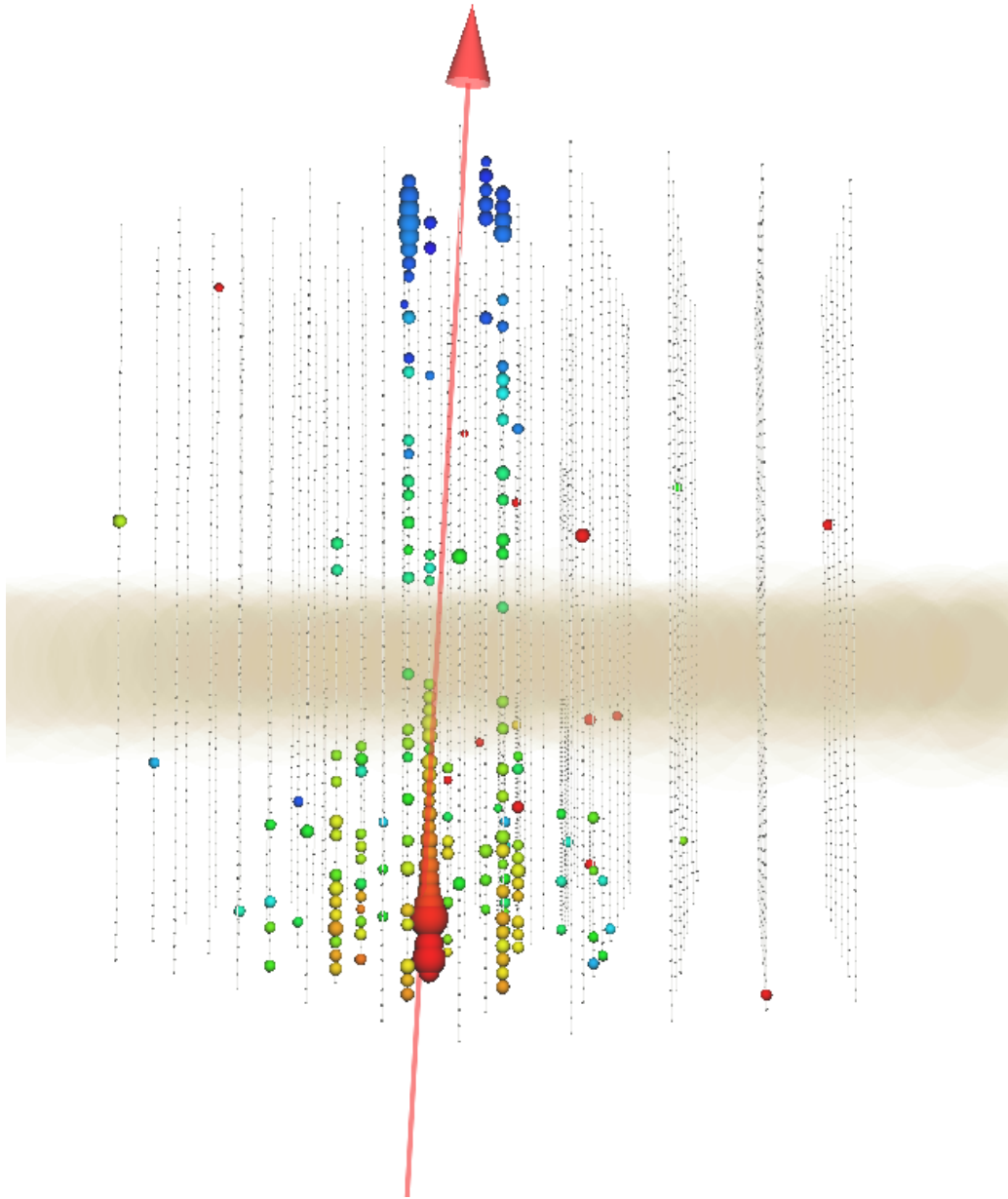


Figure 4-12: Event display for an up-going muon. The thin, grey, vertical lines correspond to the 86 IceCube strings. The small grey dots on the strings are the DOMs that did not see light. The DOMs that observed light are shown as colored spheres. The color of the sphere indicates timing, where red DOMs saw light at the earliest times and blue DOMs at the latest times. The larger the size of the sphere, the more light was observed. The reconstructed muon trajectory is shown a red line. The reconstructed muon energy is 7.0 TeV. Figure courtesy of Sarah Mancina.

4.7 Muon reconstruction

The analysis is performed using reconstructed muon properties: the reconstructed muon energy – also referred to as the muon energy proxy – and the reconstructed cosine of the muon’s zenith angle, $\cos\theta_z$, where the zenith angle is the angle with respect to the North Pole-South Pole axis. Events from the horizon have $\cos\theta_z = 0$, while events coming from the North Pole have $\cos\theta_z = -1$. The direction of the muon is reconstructed based off the arrival time of the first photon to reach each DOM, as well as the charge of all pulses from each DOM [54,82]. The reconstruction algorithm considers the shape of Cherenkov cone, as well as scattering and absorption of photons within the ice. The resolution of the angular reconstruction is $0.005 - 0.015$ in $\cos\theta_z$. The angular reconstruction is described further in [54].

The energy resolution is much worse than the angular resolution. It is so large it is described in terms of the \log_{10} of the energy: $\sigma_{\log_{10}(E_\mu)} \sim 0.4$. This is due to the stochastic nature of the muon’s energy loss and the fact that the muon is not contained within the detector. Both of these are evident in Figs 4-11 and 4-12. The muon energy is related to its energy loss per unit length, which is proportional to the light produced and thus the light observed by the detector. The muon energy reconstruction algorithm used here, **MuEx**, uses an analytical expression for the observed light, taking into consideration the depth-dependent optical properties of the ice [82,83]. The relationship between neutrino energy and reconstructed muon energy is shown in Figs. 4-13 and 4-14.

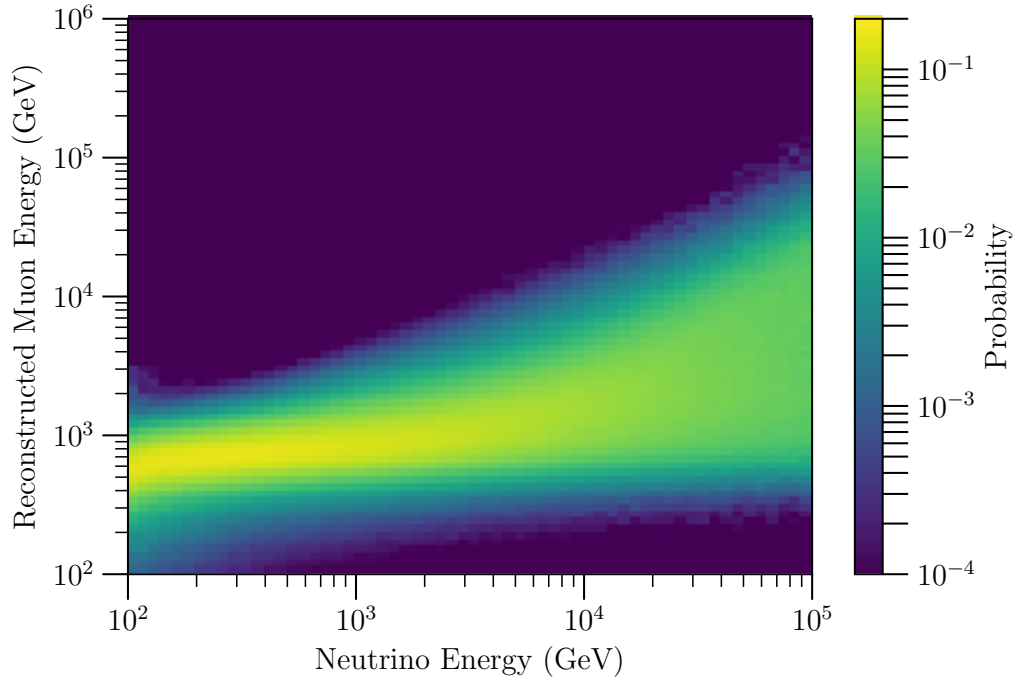


Figure 4-13: The probability of obtaining a given reconstructed muon energy as a function of true neutrino energy.

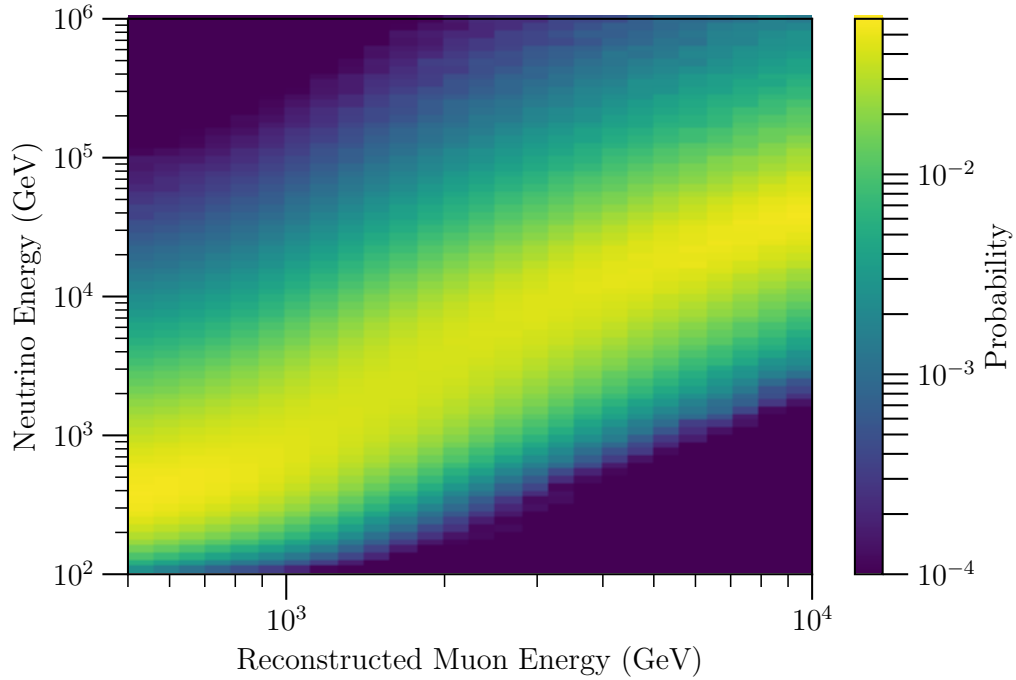


Figure 4-14: The probability distribution of neutrino energy as a function of reconstructed muon energy. This probability distribution assumes a neutrino flux proportional to E^{-2} , where E is the neutrino energy.

Chapter 5

Atmospheric neutrino fluxes

5.1 The coupled cascade equations

Atmospheric neutrinos comprise the vast majority of neutrinos observed by the IceCube detector. They arise from the interactions of primary cosmic rays with nuclei in the Earth's atmosphere [84]. These collisions produce hadronic showers. Secondary particles decay to atmospheric neutrinos. A cosmic ray air shower is depicted schematically in Fig. 5-1. The evolution of particle populations during the hadronic cascade is described by the coupled cascade equations [84]. These are coupled, differential transport equations that describe the propagation, interaction, and decay of particles. The coupled cascade equation for the flux, $\Phi_{E_i}^h$, of particle h in discrete energy bin E_i and at atmospheric slant depth, X , is given by Eq. 5.1,

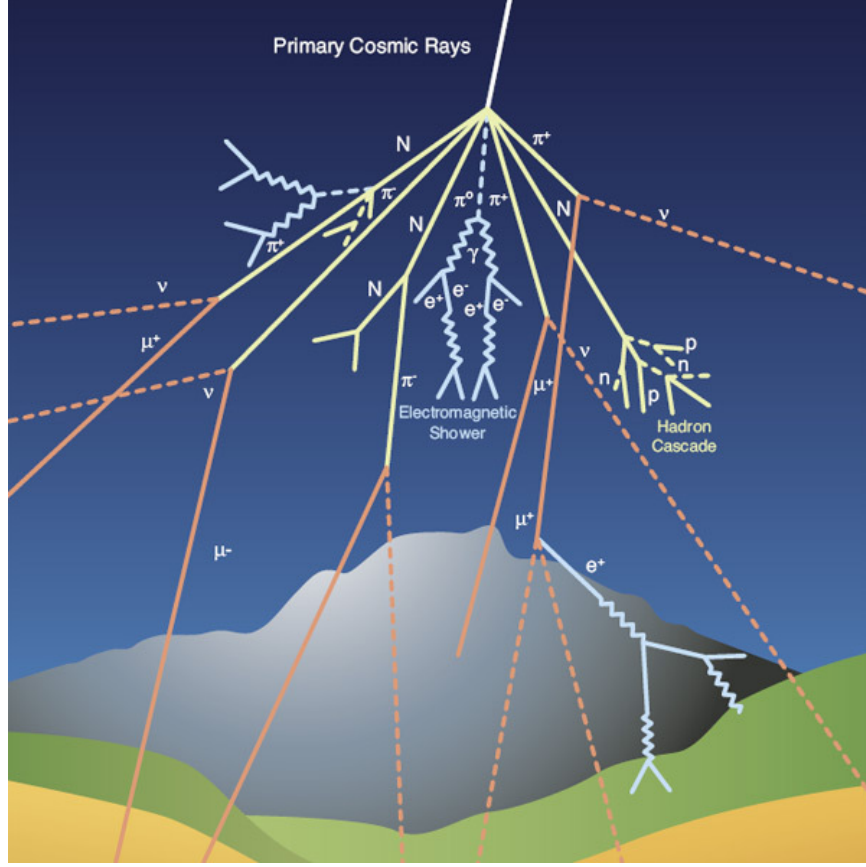


Figure 5-1: Schematic illustration of a cosmic ray air shower. Figure from CERN [85].

$$\begin{aligned}
\frac{d\Phi_{E_i}^h}{dX} = & -\frac{\Phi_{E_i}^h}{\lambda_{\text{int}, E_i}^h} \\
& -\frac{\Phi_{E_i}^h}{\lambda_{\text{dec}, E_i}^h(X)} \\
& + \sum_{E_k \geq E_i} \sum_l \frac{C_{l(E_k) \rightarrow h(E_i)}}{\lambda_{\text{int}, E_k}^l} \Phi_{E_k}^l \\
& + \sum_{E_k \geq E_i} \sum_l \frac{d_{l(E_k) \rightarrow h(E_i)}}{\lambda_{\text{dec}, E_k}^l(X)} \Phi_{E_k}^l.
\end{aligned} \tag{5.1}$$

The first term accounts for the loss of particle h due to interactions, with interaction length

$$\lambda_{\text{int}, E_i}^h = \frac{m_{\text{air}}}{\sigma_{p\text{-air}}^{\text{inel}}}, \tag{5.2}$$

where m_{air} is the mean mass of nuclei in the air, and $\sigma_{p-\text{air}}^{\text{inel}}$ is the inelastic cross section between a proton and an air nucleus. The second term accounts for loss of particle h due to decay, with decay length

$$\lambda_{\text{dec}, E_i}^h(X) = \frac{c\tau_h E_i \rho_{\text{air}}(X)}{m_h}, \quad (5.3)$$

where τ_h and m_h are the lifetime and mass of particle h , and $\rho_{\text{air}}(X)$ is the density of the air at slant depth X . The third term accounts for gain of particle h due to interactions of other particle species; the coefficients representing this, $c_{l(E_k) \rightarrow h(E_i)}$, are determined from hadronic interaction models. The fourth term accounts for gain of particle h due to the decay of other particle species. The atmospheric slant depth, X is given by

$$X(h_0) = \int_0^{h_0} dl \rho_{\text{air}}(h_{\text{atm}}(l)), \quad (5.4)$$

where ρ_{air} is the mass density of the air as a function of the atmospheric height, h_{atm} , and the density is integrated along the path, l , of the cascade.

In this work, the atmospheric neutrino flux is calculated with the program **Matrix Cascade Equations (MCEq)**. MCEq casts the coupled cascade equations as a matrix equation, which it solves numerically [86,87]. Over fifty baryons, mesons, and leptons are considered in the calculations. The calculation requires three inputs; these inputs are informed by a wide range of collider and fixed target experiments, as we will discuss below. One input is the primary cosmic ray model, which describes the composition and spectra of the incoming particles. Another is the hadronic interaction model, which describes the cross sections of interactions in the cascade. The last is the description of the temperature or density profile of the atmosphere.

The combined muon neutrino and antineutrino spectrum, and partial contributions from the various parent particles, are shown in Fig. 5-2. These spectra were calculated with MCEq and assume Thunman-Ingelman-Gondolo [88] as the primary cosmic ray flux model and SIBYLL-2.3 RC1 [89] as the hadronic interaction model. The atmospheric muon neutrino flux is comprised of the *conventional* component and the *prompt* component, shown in Fig. 5-2. The conventional flux originates in the

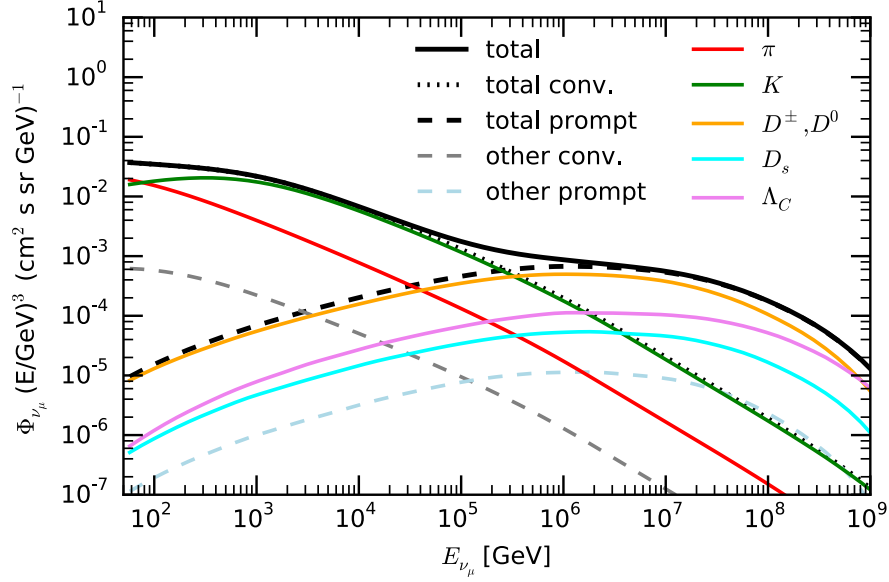


Figure 5-2: Energy spectrum of atmospheric muon neutrinos and antineutrinos, as well as the partial contributions to the total flux, as calculated with MCEq. The spectrum is scaled by the energy cubed. Figure from [86].

decays of charged pions, charged kaons, and muons. Muon neutrinos come from the decays:

$$\begin{aligned}
 \pi^+ &\rightarrow \mu^+ + \nu_\mu \\
 K^+ &\rightarrow \mu^+ + \nu_\mu \\
 \mu^- &\rightarrow e^- + \bar{\nu}_e + \nu_\mu
 \end{aligned}
 \tag{5.5}$$

while muon antineutrinos come from the decays of the oppositely charged particles. Above around 100 GeV, neutrinos from kaon decays are predominant to those from either pion or muon decays. The prompt flux comes from the decays of heavier particles, such as charmed mesons, although it has yet to be observed. It is expected to be predominant at energies above about 10^5 GeV.

5.2 Cosmic ray and hadronic interaction models

There is a range of available models that describe the flux and composition of primary cosmic rays. The various models make different assumptions about the

sources of cosmic rays and also are informed by different datasets. The models considered in this work are PolyGonato [90], Hillas-Gaisser 2012 H3a [91], and Zatsepin-Sokolskaya/PAMELA [92,93]. These models account for cosmic ray hydrogen, helium, and heavier nuclei. The Hillas-Gaisser 2012 H3a model, which is the one used in this work, includes five groups of nuclei: hydrogen, helium, carbon-nitrogen-oxygen, magnesium-aluminium-silicon, and iron. The all-particle cosmic ray energy spectrums predicted by these models are shown by the curves on Fig. 5-3. Data, from various ground-based arrays, are shown as points [94–109]. The abrupt change in the all-particle spectrum at about $10^{6.5}$ GeV is called the “knee” of the cosmic ray spectrum. One can see that the data sets have a large spread in the knee region, and this will need to be addressed as a systematic uncertainty.

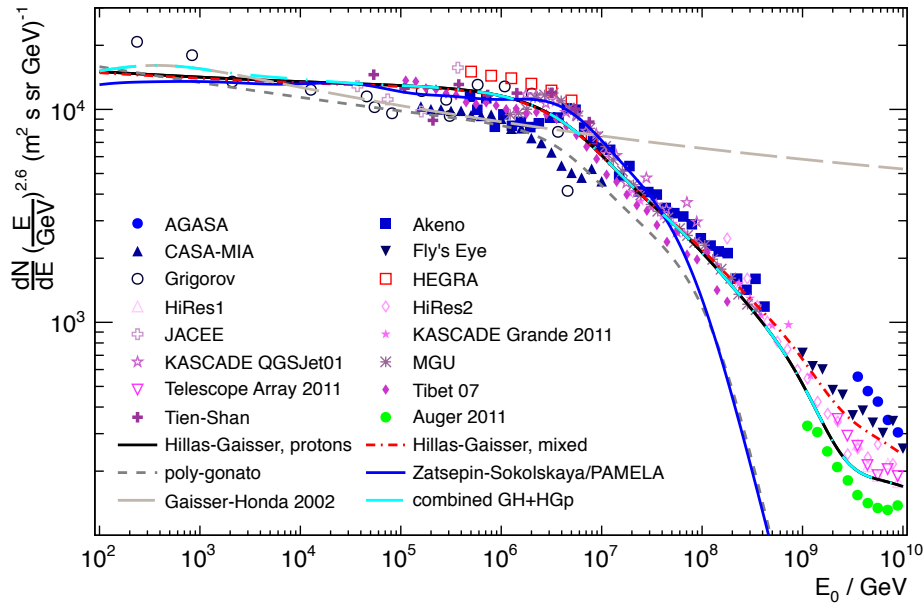


Figure 5-3: All-particle cosmic ray spectrum. Model predictions are shown as solid or dashed curves. Data from ground-based arrays are shown as points [94–109]. Figure from [87].

A selection of models are available to describe the hadronic interactions in cosmic ray air showers. The models considered in this work are SIBYLL-2.3c [110], SIBYLL-2.3 [111], EPOS-LHC [112], and QGSJET-II-04 [113]. These models are tuned to data from accelerator experiments. Data from Large Hardon Collider, which has run at around 10 TeV, can constrain the interactions of cosmic ray particles at the

knee [114]. This is because of the Lorentz transformation between these two reference frames: detectors at the Large Hardon Collider operate in the center-of-mass frame, while the atmosphere, which is impinged by cosmic rays, is effectively a fixed target. The center-of-mass energy of cosmic ray interactions is

$$\sqrt{s} \simeq \sqrt{2Em}, \quad (5.6)$$

where E is the energy of the cosmic ray, m is the mass of the target particle, and the mass of the cosmic ray particle is negligible compared to its energy.

The hadronic interaction models do not come with uncertainties and there is significant discrepancy between the models [115]. Three of the properties that vary between the models are the inelastic cross sections, the shower multiplicity, and interaction elasticity. This causes different predictions of the atmospheric neutrino and antineutrino fluxes. In particular, the ratio of the muon neutrinos to muon antineutrinos varies largely. This is an important systematic uncertainty for the work in this thesis, as the matter resonance due to the presence of a sterile neutrino is expected to appear in the muon antineutrino flux alone.

5.3 Barr scheme for hadronic interaction uncertainties

The Barr scheme is a method for assigning hadronic interaction uncertainties for the purpose of calculating conventional atmospheric neutrino fluxes [116, 117]. Uncertainties are assigned based on measurements of the production of charged pions and kaons from projectiles impinging on targets,

$$\begin{aligned} pN &\rightarrow \pi^\pm X \\ pN &\rightarrow K^\pm X. \end{aligned} \quad (5.7)$$

Label	Incident energy, E_i	Meson	x_{lab}	Uncertainty
G	>30 GeV	π^\pm	0 – 0.1	30%
H	>30 GeV	π^\pm	0.1 – 1	15%
I	>500 GeV	π^\pm	0.1 – 1	$12.2\% \times \log_{10}(E_i/500 \text{ GeV})$
W	>30 GeV	K^\pm	0 – 0.1	40%
Y	>30 GeV	K^\pm	0.1 – 1	30%
Z	>500 GeV	K^\pm	0.1 – 1	$12.2\% \times \log_{10}(E_i/500 \text{ GeV})$

Table 5.1: Estimated uncertainties in the production of charged kaons and pions. Values from [117].

The projectile, p , is most often a proton. The target N , is a light element, for example, beryllium, carbon or aluminium. The other products, X , are unconstrained. Uncertainties are given as a function of E_i , the incident particle’s energy, and x_{lab} , the fraction of the incident particle’s energy that is carried by the secondary meson.

Uncertainties are assigned based off the consistency between datasets, as well as the amount of extrapolation that is necessary between different nuclear targets, energies, and values of the transverse momentum. The assigned uncertainties for incident particle energies above 30 GeV are given in Table 5.1.

Since the conventional flux is predominantly composed of kaons, in the energy range relevant for this thesis, the kaon production uncertainties are more important than the pion production uncertainties. The G, H, and I uncertainties from Table 5.1 are therefore not explicitly incorporated into the analysis. The uncertainties on the production of oppositely charged kaons are considered separately. Six *Barr parameters* – WP, WM, YP, YM, ZP, ZM – refer to the uncertainties in Table 5.1, where the suffix P indicates it references the production of positively charged kaons, and the suffix M indicates it references that of negatively charged kaons.

The propagation of these uncertainties to the muon neutrino and antineutrino fluxes is calculated with MCEq as in [118, 119]. For each of the six Barr parameters, \mathcal{B}_i , muon neutrino and antineutrino flux derivatives are calculated:

$$\frac{\partial \Phi}{\partial \mathcal{B}_i} = \frac{\Phi(\mathcal{B}_i = \delta) - \Phi(\mathcal{B}_i = -\delta)}{2\delta}. \quad (5.8)$$

For example, $\Phi(\text{YP} = \delta)$, is the flux where K^+ production in the region correlating to

Y has been increased by the relative amount δ compared to the nominal model. If one assumes the nominal flux prediction, Φ_0 , underestimates charged meson production by \mathcal{B}_i for each of the respective regions in this parameterization, a corrected flux prediction is

$$\Phi(\mathcal{B}_1, \mathcal{B}_2, \dots) = \Phi_0 + \sum_i \mathcal{B}_i \frac{\partial \Phi}{\partial \mathcal{B}_i}. \quad (5.9)$$

5.4 Atmospheric flux uncertainty treatment

The various combinations of cosmic ray and hadronic interaction models yield discrete predictions for the atmospheric muon neutrino and antineutrino fluxes, as well as their ratio. It is unknown which is the closest to the truth, and how close it is. A set of eight physically-motivated systematic uncertainties allows for a continuous range of flux predictions that cover the discrete ones. The normalization and composition of cosmic rays above the knee have a large uncertainty [87]. This leads to a large uncertainty in the normalization of the atmospheric neutrino flux. Here it is taken to be 40%. Additionally, there is an uncertainty in the spectral index of the cosmic ray flux, leading to one in the neutrino flux. In this work, the effect of the uncertainty in the spectral index, $\Delta\gamma$, on the neutrino flux is parameterized as

$$\Phi(E, \Delta\gamma) = \Phi(E) \left(\frac{E}{2.2 \text{ TeV}} \right)^{-\Delta\gamma}. \quad (5.10)$$

The uncertainty on $\Delta\gamma$ is taken to be 0.03. As discussed previously, the six Barr parameters, WP, WM, YP, YM, ZP, and ZM, represent the uncertainty in the production of charged kaons.

In this work, the central prediction of the neutrino flux is that from Hillas-Gaisser 2012 H3a as the cosmic ray model, and Sibyll2.3c as the hadronic interaction model. Figs. 5-4 to 5-9 show that the uncertainty on the flux prediction using this central model and considering this set of eight systematic uncertainties spans the predictions from the combinations of three cosmic ray models and four hadronic interaction models. In these plots, the curves represent the discrete flux predictions, the color

indicates the hadronic interaction model, and the linestyle indicates the cosmic ray model. The grey band shows the 1σ range of predictions based off the central model and the eight systematic uncertainties considered here. These uncertainties are considered uncorrelated, and their effects are added in quadrature. Figure 5-4 shows that these eight systematic uncertainties cover the discrete, predicted energy distributions of the muon neutrino and antineutrino fluxes. The distributions shown are averaged over the zenith angles. Figures 5-5 to 5-8 show these uncertainties cover the discrete, predicted cosine zenith distributions, at the energies 90 GeV, 900 GeV, 9 TeV and 90 TeV. Finally, Fig. 5-9 shows that the discrete predictions of the muon antineutrino to neutrino ratio, as a function of energy, are spanned by these systematic uncertainties.

A benefit of this uncertainty parameterization is that the discrepancy in the atmospheric fluxes from the various models can be included in an analysis in a continuous manner. It is not necessary to perform the sterile search analysis multiple times, assuming a different, discrete model each time, as was done in the one-year search [51, 120]. Instead one can incorporate these eight systematic uncertainties as continuous nuisance parameters that reflect the underlying physical uncertainties. Furthermore, the posterior distributions of these nuisance parameters are informative of the respective hadronic processes.

In addition to the eight atmospheric flux systematic uncertainties discussed here, the analysis in this thesis includes two more, mentioned here for completeness. One is the atmospheric density. The other is the cross section of kaons interacting with atmospheric nuclei. These will be discussed further in Chapter 6 and are not included in the envelopes shown here.

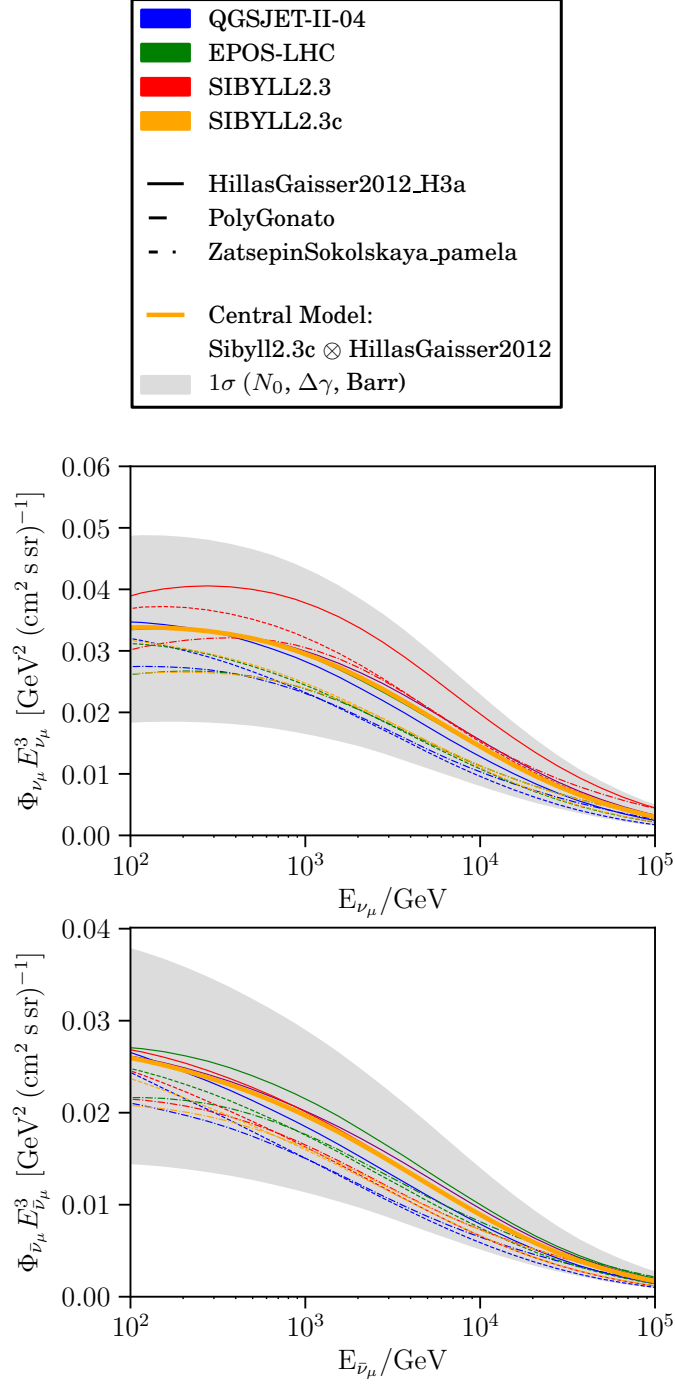


Figure 5-4: The spectrum of atmospheric muon (top) neutrinos and (bottom) antineutrinos. The fluxes are scaled by energy cubed. The different colors correspond to different hadronic interaction models. The different linestyles correspond to different primary cosmic ray models. The grey band represents the 1σ uncertainty around the central model when considering eight relevant nuisance parameters. The fluxes shown here are averaged over the cosine zenith angles.

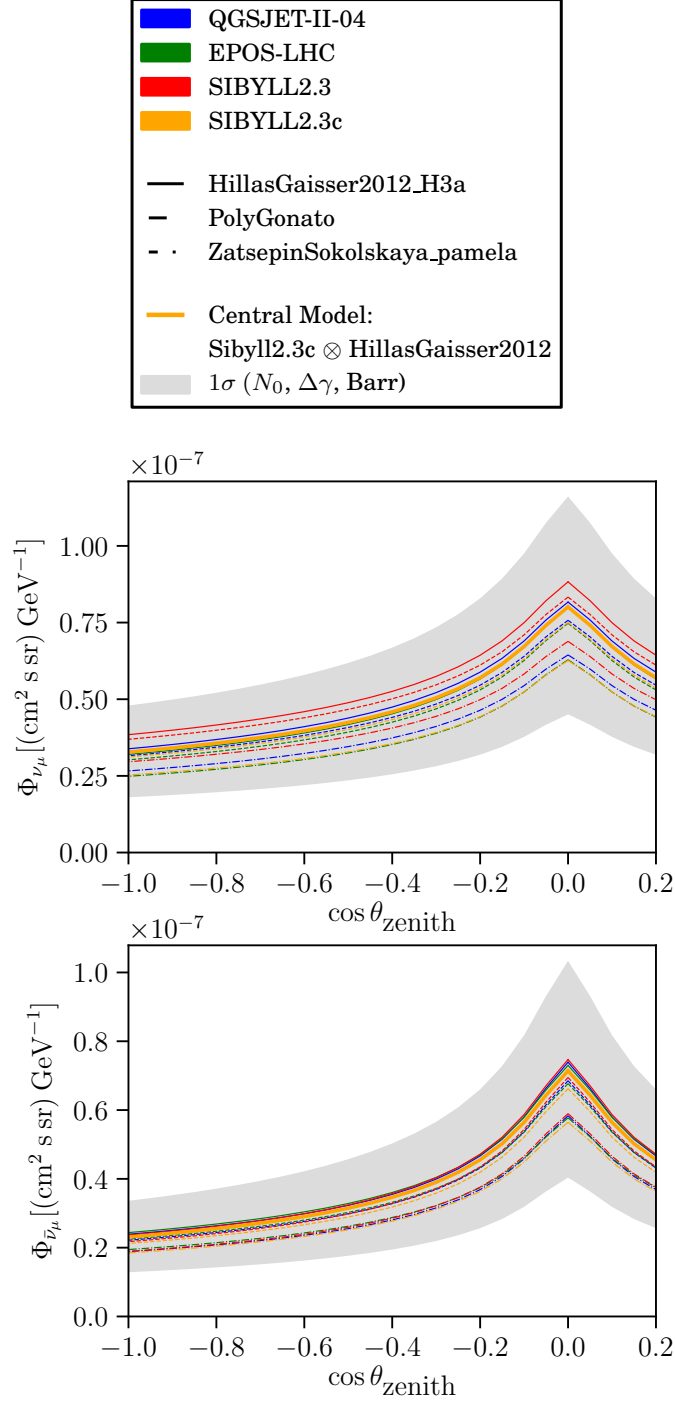


Figure 5-5: The angular distribution of atmospheric muon (top) neutrinos and (bottom) antineutrinos at 90 GeV. The different colors correspond to different hadronic interaction models. The different linestyles correspond to different primary cosmic ray models. The grey band represents the 1σ uncertainty around the central model when considering eight relevant nuisance parameters. The fluxes shown here are averaged over the cosine of the zenith angles.

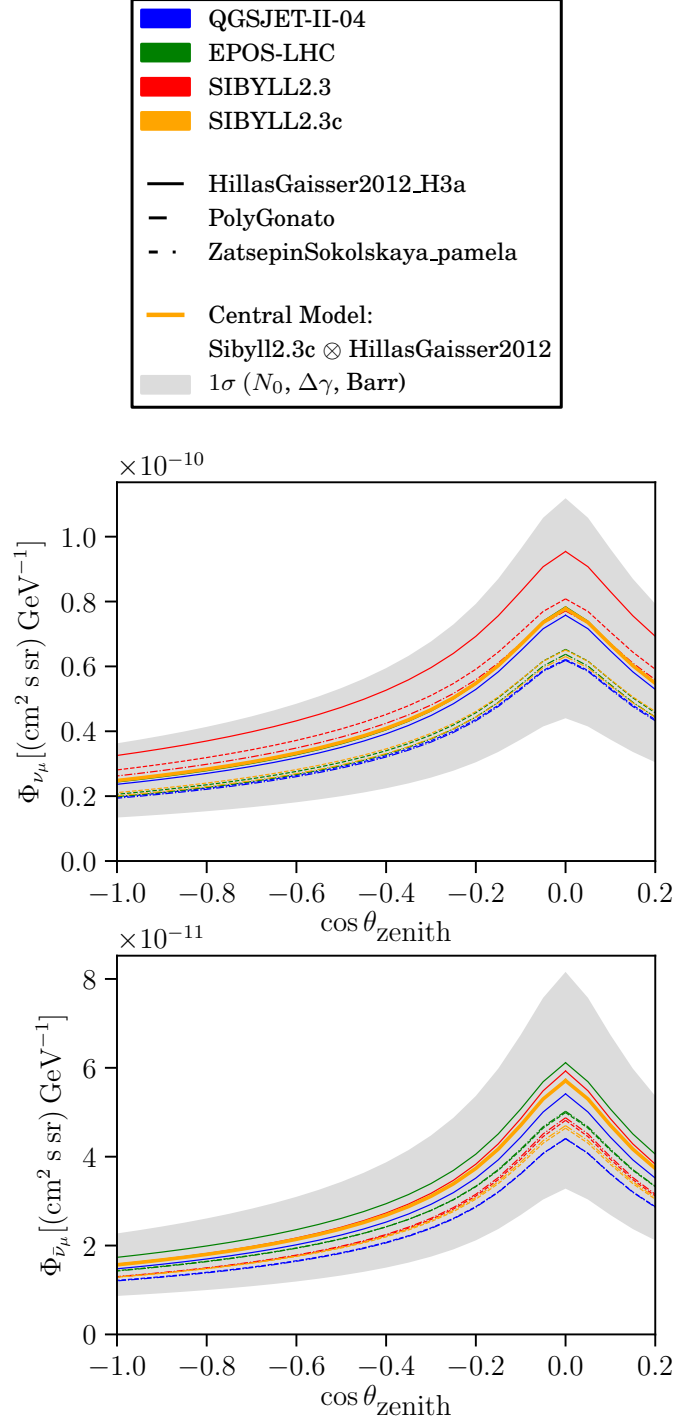


Figure 5-6: The angular distribution of atmospheric muon (top) neutrinos and (bottom) antineutrinos at 900 GeV. The different colors correspond to different hadronic interaction models. The different linestyles correspond to different primary cosmic ray models. The grey band represents the 1σ uncertainty around the central model when considering eight relevant nuisance parameters. The fluxes shown here are averaged over the cosine of the zenith angles.

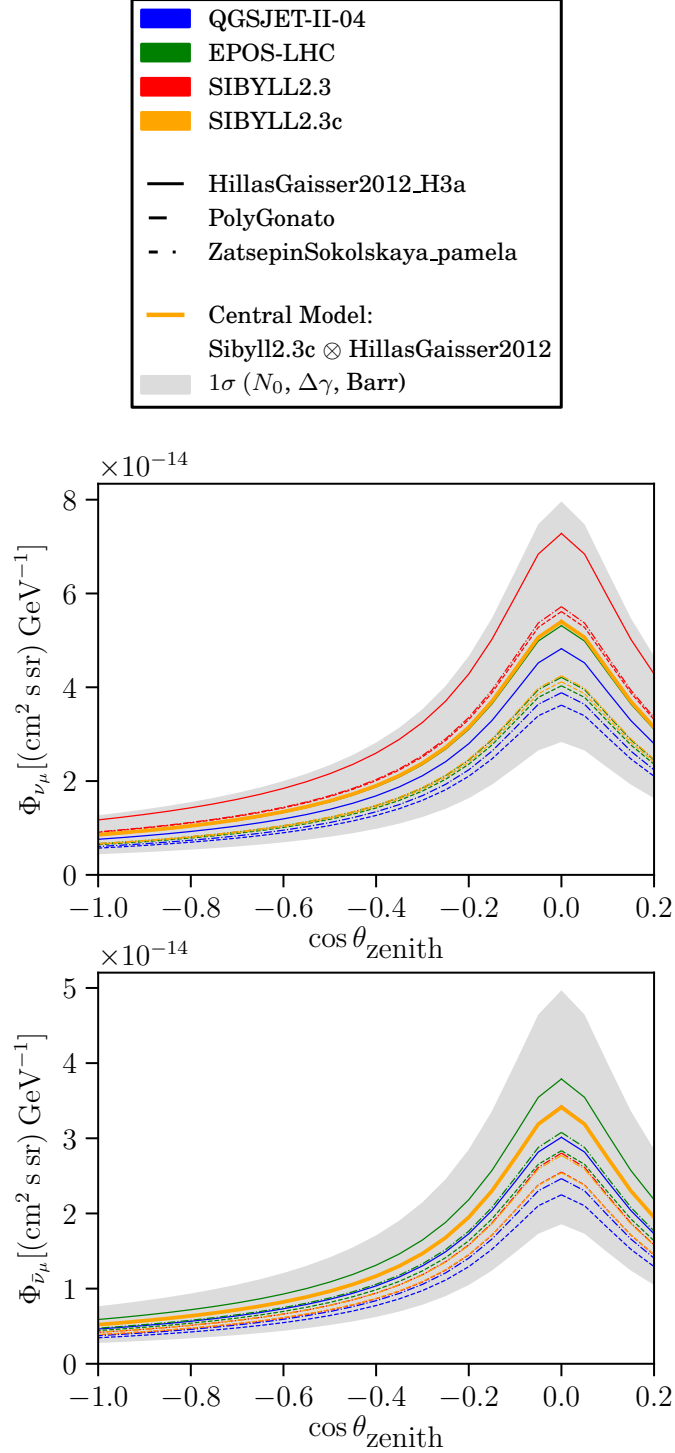


Figure 5-7: The angular distribution of atmospheric muon (top) neutrinos and (bottom) antineutrinos at 9 TeV. The different colors correspond to different hadronic interaction models. The different linestyles correspond to different primary cosmic ray models. The grey band represents the 1σ uncertainty around the central model when considering eight relevant nuisance parameters. The fluxes shown here are averaged over the cosine of the zenith angles.

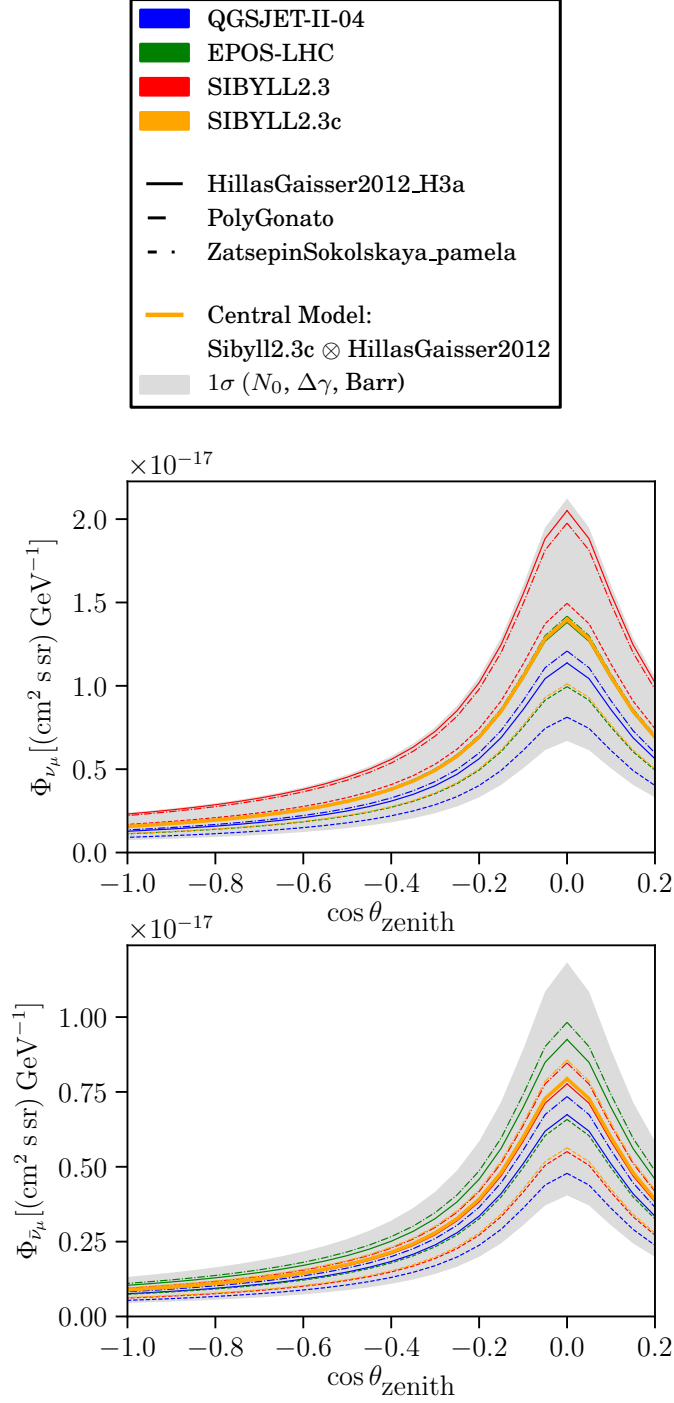


Figure 5-8: The angular distribution of atmospheric muon (top) neutrinos and (bottom) antineutrinos at 90 TeV. The different colors correspond to different hadronic interaction models. The different linestyles correspond to different primary cosmic ray models. The grey band represents the 1σ uncertainty around the central model when considering eight relevant nuisance parameters. The fluxes shown here are averaged over the cosine of the zenith angles.

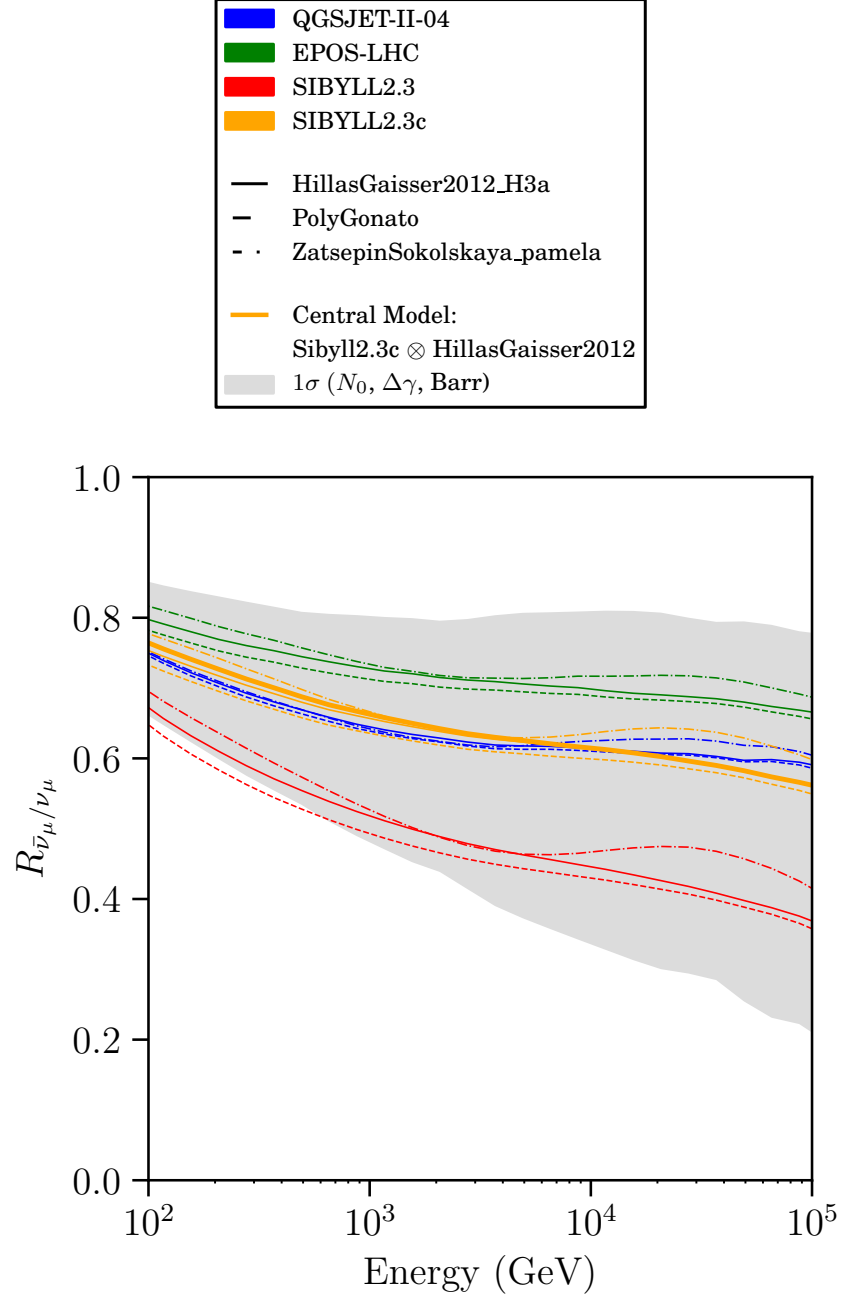


Figure 5-9: Ratio of atmospheric muon antineutrinos to neutrinos, as a function of energy. The different colors correspond to different hadronic interaction models. The different linestyles correspond to different primary cosmic ray models. The grey band represents the 1σ uncertainty around the central model when considering eight relevant nuisance parameters. The fluxes shown here are averaged over the cosine of the zenith angles.

5.5 Neutrino flux at detector

For the work in this thesis, nine components to the total neutrino flux are calculated. Seven relate to the conventional atmospheric flux: the central model and the six Barr fluxes. The atmospheric density profile assumed in the calculation of these fluxes is based off data from AIRS satellite [121]. The prompt component of the conventional flux is included based on the prediction from the BERSS model [122]. The final component is the astrophysical flux.

Astrophysical neutrinos were discovered by IceCube [123]; their origin remains unknown. The model of the astrophysical flux used in this work is based on previous measurements from IceCube [124–127]. The astrophysical flux is assumed to be isotropic and to follow a single power law,

$$\frac{dN_{\nu_\mu, \bar{\nu}_\mu}}{dE} = N_{\text{astro}} \left(\frac{E}{100 \text{ TeV}} \right)^{-2.5}, \quad (5.11)$$

where the normalization is

$$N_{\text{astro}} = 0.787 \times 10^{-18} \text{ GeV}^{-1} \text{ sr}^{-1} \text{ s}^{-1} \text{ cm}^{-2}. \quad (5.12)$$

This assumes the astrophysical flux is equally composed of the electron, muon and tau flavors, and is equally composed of neutrinos and antineutrinos. The uncertainties on the normalization and spectral index are significant and correlated, and discussed further in Chapter 6.

The prediction of the neutrino flux incident on the Earth is converted into a prediction of the flux at the IceCube detector. This calculation is done with the neutrino evolution code `nuSQuIDS` [10]. This software accounts for processes that affects the propagation of neutrinos through the Earth. One process is neutrino oscillations between four flavors, including the effects due to matter. Another significant process is charged and neutral current interactions in the Earth, which lead to neutrino absorption at high energies and long baselines. A subdominant process is tau regeneration, which is the production of neutrinos from charged current interactions of tau

neutrinos and subsequent tau decay [128]. The Earth is assumed to be spherically symmetric. The density profile of the Earth is assumed to follow the Preliminary Reference Earth Model (PREM) [129].

Lastly, neutrino decay affects the propagation of neutrinos. This effect is handled by `nuSQUIDSDecay`, a class specialization of `nuSQuIDS` [62]. Neutrinos are assumed to be Dirac. The coupling that mediates the decay is assumed to be purely scalar. The fourth mass state may decay to a massless scalar and another neutrino. A right-handed neutrino would decay to a left-handed neutrino, while a right-handed antineutrino would decay to a left-handed antineutrino. These daughter neutrinos, as well as the daughter scalar particle, are not detectable. The value of the coupling is converted to a lifetime with Eq. 3.2. The `nuSQUIDSDecay` partial rate constructor is used, where the chirality-violating process rate is the inverse of the lifetime.

Chapter 6

Search for unstable sterile neutrinos

6.1 Data selection

This analysis uses a large set of well-reconstructed, upwards-going, high-energy, muon data events. This dataset is assembled using the event selection described briefly in this section. More details on the event selection can be found in [50, 54, 56, 82].

The event selection is a set of criteria designed to select signal events with high efficiency and to reject background events, yielding a high purity. The signal events are upwards-going muons. These are known to come from the charged-current interactions of atmospheric and astrophysical muon neutrinos and antineutrinos. The dominant background is atmospheric muons from cosmic ray air showers. IceCube detects these at a rate of about 3 kHz, while the rate of signal events is about 1 mHz [130]. Simulation is used to tune the background rejection of the event selection. The software **CORSIKA** (COsmic Ray SIMulations for KAscade) is used to simulate muon production in cosmic ray air showers in the atmosphere [131, 132]. **PROPPOSAL** is then used to propagate the muons through the firn and ice to the detector [80]. The simulated cosmic ray muons are then weighted according to the Hillas-Gaisser H3a cosmic ray model [133]. Other backgrounds include neutral current neutrino events and charged-current electron and tau neutrino events. These events are associated with cascades, which have a very different morphology than the signal track-like events, allowing them to be readily rejected. Furthermore, the flux of atmospheric electron

and tau neutrinos is subdominant to that of muon neutrinos. The electron and tau neutrino backgrounds are also simulated.

The event selection criteria is the union of two sets of criteria, or filters, described further in [50, 54, 56, 82]. All events are required to:

- Pass the IceCube muon filter, which identifies track-like events.
- Have at least 15 DOMs triggered, with at least 6 triggered on direct light. Direct light is photons which have not significantly scattered, as determined by timing.
- Have a reconstructed track length, based off of direct light, of at least 200 m.
- Have a relatively smooth distribution of direct light along the track.
- Have a reconstructed energy between 500 GeV and 9976 TeV.
- Originate from or below the horizon: $\cos(\theta_{\text{zenith}}) \leq 0$.

The event selection has a 99.9% purity as determined from simulation. The expected composition of the event selection is given in Table 6.1. The energy and cosine zenith distributions of these events is shown in 6-1.

Event Type	Expected Count
Conventional atmospheric ν_μ	$315,214 \pm 561$
Astrophysical ν_μ	$2,350 \pm 48$
Prompt atmospheric ν_μ	481 ± 22
All ν_τ	23 ± 5
All ν_e	1 ± 1
Atmospheric μ	18 ± 4

Table 6.1: Expected partial contributions to the event selection. Table recreated from [54, 56].

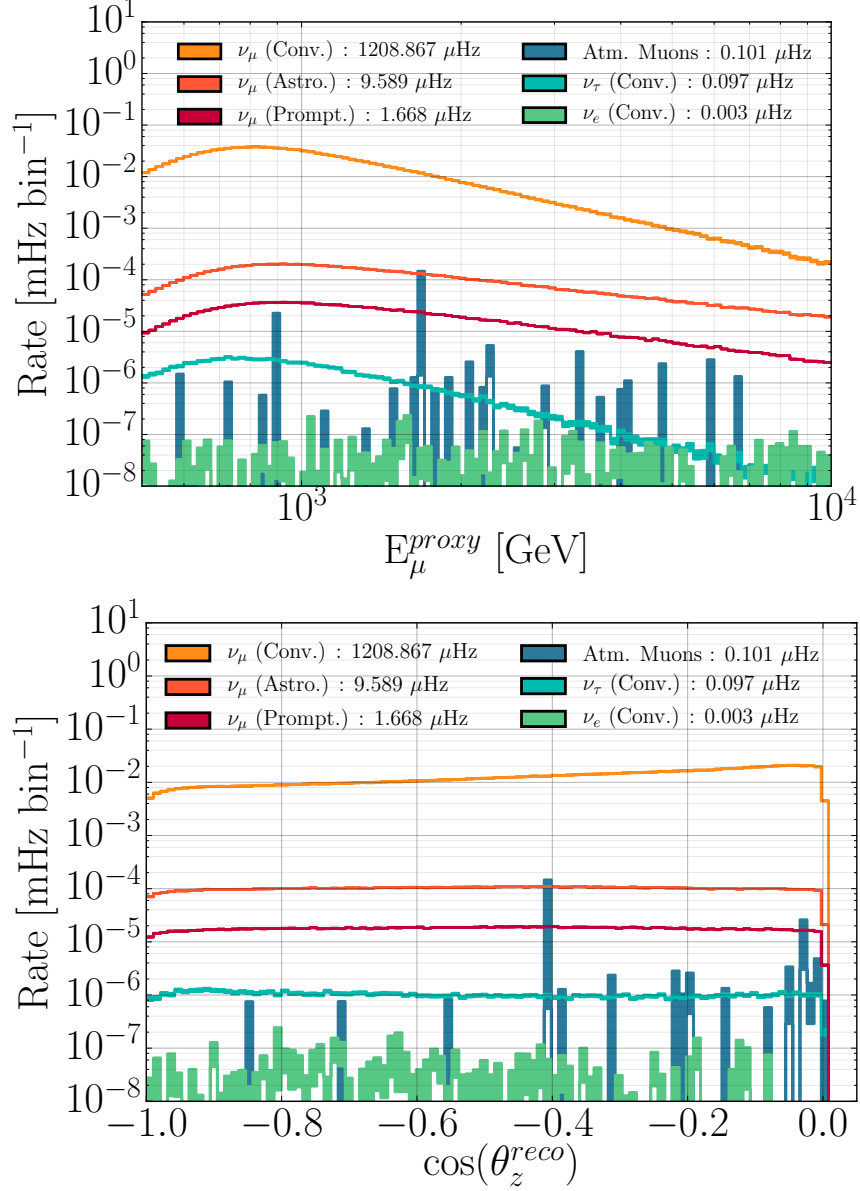


Figure 6-1: (Top) Reconstructed energy distribution and (bottom) reconstructed cosine zenith distribution of the constituents of the event selection, as determined from simulation. Figures from [54, 56]

6.2 Systematic uncertainties

6.2.1 Nuisance parameters

The treatment of systematic uncertainties in this analysis is almost identical to that of the eight-year traditional 3+1 search and more detailed descriptions can be found in [50, 54, 56]. Eighteen systematic uncertainties are incorporated into the analysis with nuisance parameters. These uncertainties are grouped into two broad categories: those relating to the total neutrino flux and those relating to detection. A table of these nuisance parameters, their prior central values, their prior widths, and the boundaries on them is given in Table 6.2.

As described in Chapter 5, ten nuisance parameters are used to describe the uncertainties on atmospheric neutrino flux. One is the conventional atmospheric flux normalization: $\Phi_{\text{Conv.}}$. Another is the uncertainty on the spectral index of the atmospheric flux: $\Delta\gamma_{\text{atm}}$. This shifts both the conventional and prompt atmospheric fluxes. There are six uncertainties in the production of charged kaons in cosmic ray air showers. These are the six Barr parameters WM, WP, YM, YP, ZM, and ZP, previously discussed in Chapter 5. Another is the uncertainty in the atmospheric density, which has been shown to affect the neutrino flux [134]. This effect is calculated using the reported systematic uncertainty of measurements from the AIRS satellite [121]. Lastly, there is an uncertainty on the cross section of kaons interacting with atmospheric nuclei, largely nitrogen and oxygen nuclei: σ_{KA} . This causes an uncertainty in the energy of the kaons when they decay. In the parameterization here, 1σ represents 7.5% of the nominal cross section.

Two nuisance parameters are used to describe the uncertainties on the astrophysical neutrino flux. They are the astrophysical flux normalization and the uncertainty on the astrophysical spectral index. These are correlated and are derived from previous IceCube measurements [123, 124, 126, 127].

The two final uncertainties that affect the flux of neutrinos at the detector are the neutrino-nucleon and antineutrino-nucleon cross sections. These cross sections enter the analysis twice: during propagation of the neutrino flux across the Earth

and during interactions near the detector. The latter had previously been studied and deemed negligible [51, 52]. The effects of the cross section uncertainties on the flux incident at the detector are included here.

Four nuisance parameters describe the uncertainties in the detection of neutrinos and antineutrinos. One is the effective efficiency of detecting photons, which is referred to as the DOM efficiency. The DOM efficiency reflects properties of the DOM itself, such as the photocathode, collection, and wavelength efficiencies, as well as global effects that prevents detection of photons. These include shadowing from cables, and some properties of the bulk and hole ice. The effect is determined from simulation sets where photons are down-sampled.

Another detector uncertainty is due to the effect of the hole ice, represented by the “forward hole ice” parameter. The refrozen ice in the drilled boreholes has different optical properties from the bulk of the ice in the detector. In particular, there is additional scattering near the DOMs. As a result, the angular acceptance of the DOMs is different from laboratory measurements. The “forward hole ice” parameter reflects uncertainty in the zenith-dependence of the angular acceptance of DOMs.

Finally, this analysis includes two nuisance parameter related to the bulk ice, that is, the undisturbed, natural ice between and beyond the drilled boreholes. This analysis uses the “SnowStorm” method to calculate the effect of the uncertainties, which are highly correlated, of the many parameters in the ice model, shown in Fig. 4-3 [135]. The Fourier transform of the depth-dependent coefficients is analyzed. The analysis-level effect of the most significant modes is encoded into two, correlated, effective gradients. These are referred to as “Ice Gradient 0” and “Ice Gradient 1”.

The shapes of the eighteen nuisance parameter systematics are shown in Figs. 6-2 and 6-3. These figures show the fractional change that a positive 1σ variation of each of the nuisance parameters causes,

$$\frac{(\text{Nominal} + 1\sigma \text{ variation}) - \text{Nominal}}{\text{Nominal}}, \quad (6.1)$$

assuming the null hypothesis, that is, only three neutrinos. The shapes of these

Parameter	Central	Prior (Constraint)	Boundary
Detector parameters			
DOM efficiency	0.97	0.97 ± 0.10	[0.94, 1.03]
Bulk Ice Gradient 0	0.0	$0 \pm 1.0^*$	NA
Bulk Ice Gradient 1	0.0	$0 \pm 1.0^*$	NA
Forward Hole Ice	-1.0	-1.0 ± 10.0	[-5, 3]
Conventional flux parameters			
Normalization ($\Phi_{\text{conv.}}$)	1.0	1.0 ± 0.4	NA
Spectral shift ($\Delta\gamma_{\text{conv.}}$)	0.00	0.00 ± 0.03	NA
Atm. Density	0.0	0.0 ± 1.0	NA
Barr WM	0.0	0.0 ± 0.40	[-0.5, 0.5]
Barr WP	0.0	0.0 ± 0.40	[-0.5, 0.5]
Barr YM	0.0	0.0 ± 0.30	[-0.5, 0.5]
Barr YP	0.0	0.0 ± 0.30	[-0.5, 0.5]
Barr ZM	0.0	0.0 ± 0.12	[-0.25, 0.5]
Barr ZP	0.0	0.0 ± 0.12	[-0.2, 0.5]
Astrophysical flux parameters			
Normalization ($\Phi_{\text{astro.}}$)	0.787	$0.787 \pm 0.36^*$	NA
Spectral shift ($\Delta\gamma_{\text{astro.}}$)	0	$0.0 \pm 0.36^*$	NA
Cross sections			
Cross section σ_{ν_μ}	1.00	1.00 ± 0.03	[0.5, 1.5]
Cross section $\sigma_{\bar{\nu}_\mu}$	1.000	1.000 ± 0.075	[0.5, 1.5]
Kaon energy loss σ_{KA}	0.0	0.0 ± 1.0	NA

Table 6.2: Table of nuisance parameters, their central values, their priors and boundaries. Correlation between two nuisance parameters is indicated with *. Table reproduced from [56].

systematic effects have been shown previously in [54, 56]. One notable difference is that in [54, 56] the overall normalization effects had been removed from all shapes except for the atmospheric and astrophysical flux normalizations. Two other differences relate to the Barr gradient and astrophysical fluxes, and are noted in Section 6.2.2.

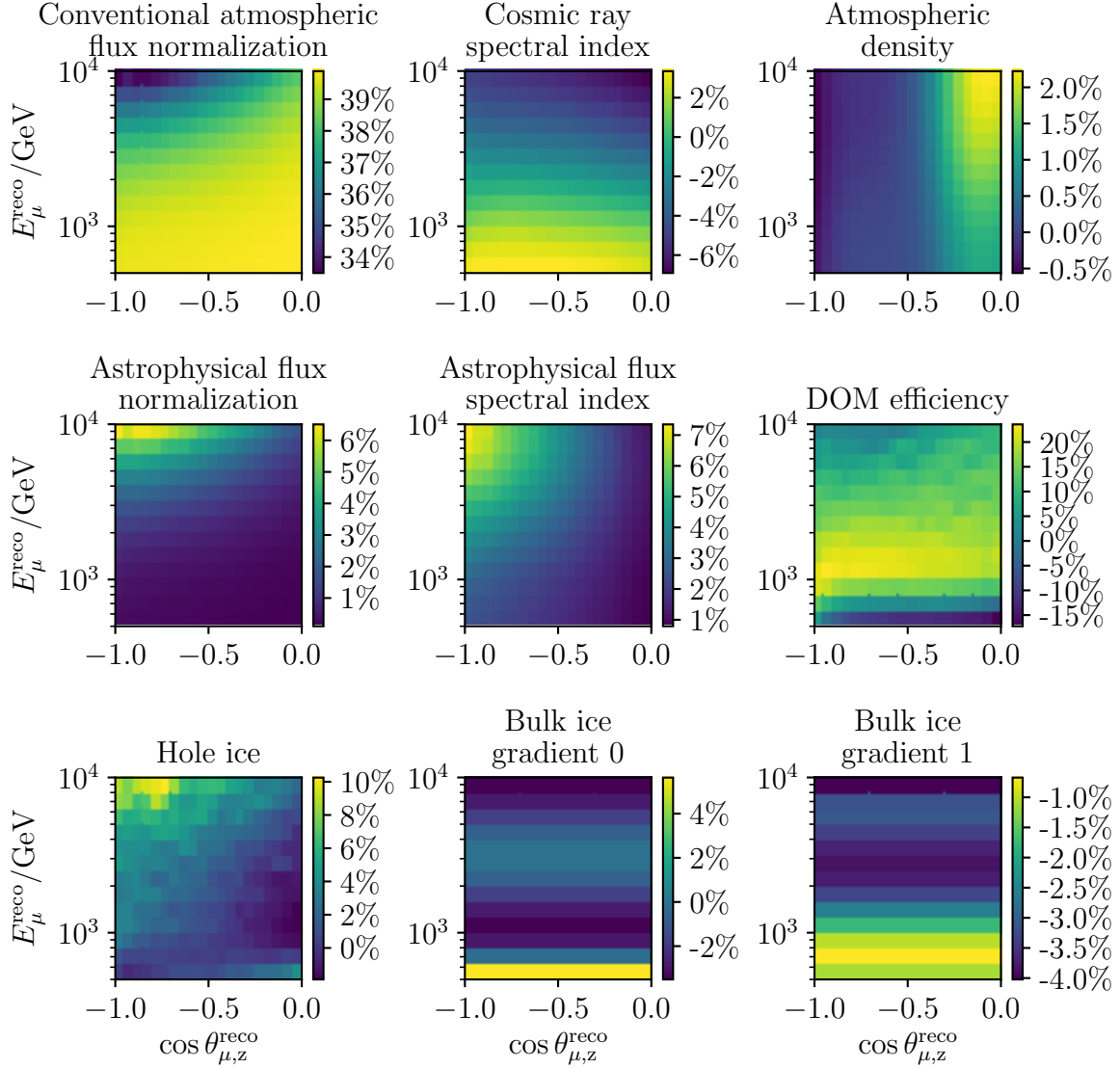


Figure 6-2: Percent difference between the expected event distribution with one nuisance parameter value increased by 1σ and the nominal expectation, shown for half the nuisance parameters. The expectations assume no sterile neutrino.

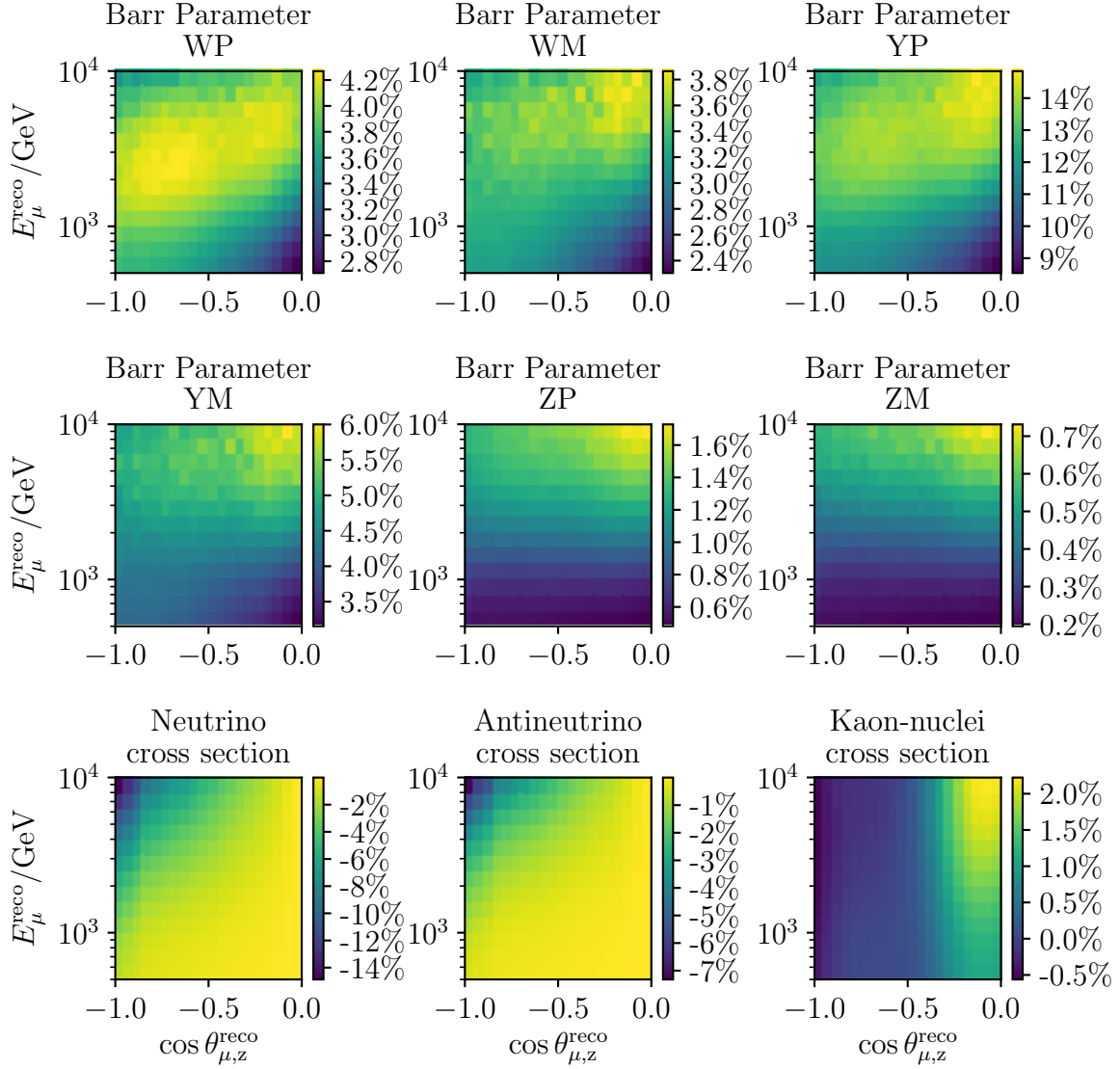


Figure 6-3: Percent difference between the expected event distribution with one nuisance parameter value increased by 1σ and the nominal expectation, shown for half the nuisance parameters. The expectations assume no sterile neutrino.

6.2.2 Minor systematic improvements from traditional 3+1 search

Three minor improvements were made after the eight-year traditional 3+1 search:

- This analysis assumes a livetime of 7.634 years instead of 7.6. No additional data was added. The assumed value of the livetime was changed to be more precise.
- The Barr gradients are calculated using atmospheric data from the AIRS satellite, instead of using a model of the atmosphere (US Standard) [121,136]. This makes the Barr gradient calculations consistent with that of the conventional atmospheric flux.
- The astrophysical and prompt fluxes are calculated with a more accurate model of the Earth's density profile. This model has 3 km of ice below the surface of the Earth, instead of 30 km of ice. This change makes the calculation of these fluxes consistent with that of the conventional atmospheric flux.

These changes were made for consistency and accuracy, and are not expected to significantly affect the result.

6.2.3 The Antarctic bedrock

The Antarctic bedrock is located approximately 362 m below the bottom of the detector. Approximately 20% of all the muons in the event selection originate in the bedrock. However, this fraction has a zenith dependence, peaking at the smallest zenith angles, as well as an energy dependence, which peaks at lower energies, shown in Fig. 6-4. Two uncertainties associated with the bedrock are its position and its density.

Several measurements of the position of the bedrock have been made. The PolarGap campaign has made LIDAR and RADAR measurements over the South Pole [137,138]. Deviations of about 45 m in the bedrock depth across the detector

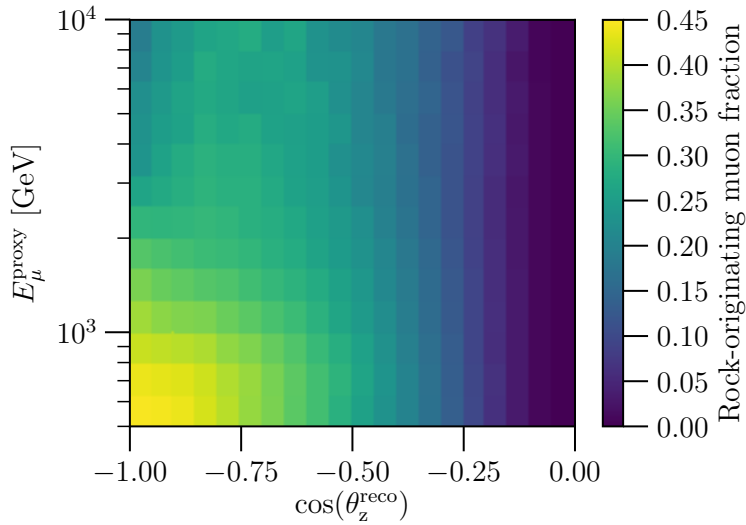


Figure 6-4: Fraction of events per bin that originate in the bedrock, rather than in the ice, as determined from simulation.

are indicated from the data [139]. Simulation studies were performed to study the effect of an uncertainty on the bedrock position. A simulation set was made where the position of the bedrock was raised 50 m with respect to the nominal position. The muon rate was found to be consistent with that of the nominal geometry, up to the level of the statistical uncertainty, shown in Fig. 6-5. The uncertainty in the position of the bedrock is thus deemed negligible for this work.

The uncertainty of the density of the bedrock beneath the Antarctic ice sheet is about 7% [140–142]. An increase in density could cause two counteracting effects. A higher bedrock density would provide more targets for neutrino interactions, increasing the number of muons that are produced. However, a higher bedrock density would also provide more targets for muon interactions, causing more muons to range out before reaching the detector, or causing them to reach the detector with a lower energy. The detector’s efficiency drops rapidly with energy below about 1 TeV. A precise understanding of the overall bedrock effect requires dedicated simulation studies with low statistical uncertainty. Preliminary results suggest the effect of the bedrock density uncertainty is small: less than 2%. This is small or comparable to the expected statistical uncertainty, shown in Fig. 6-6. The simulation studies are ongoing and

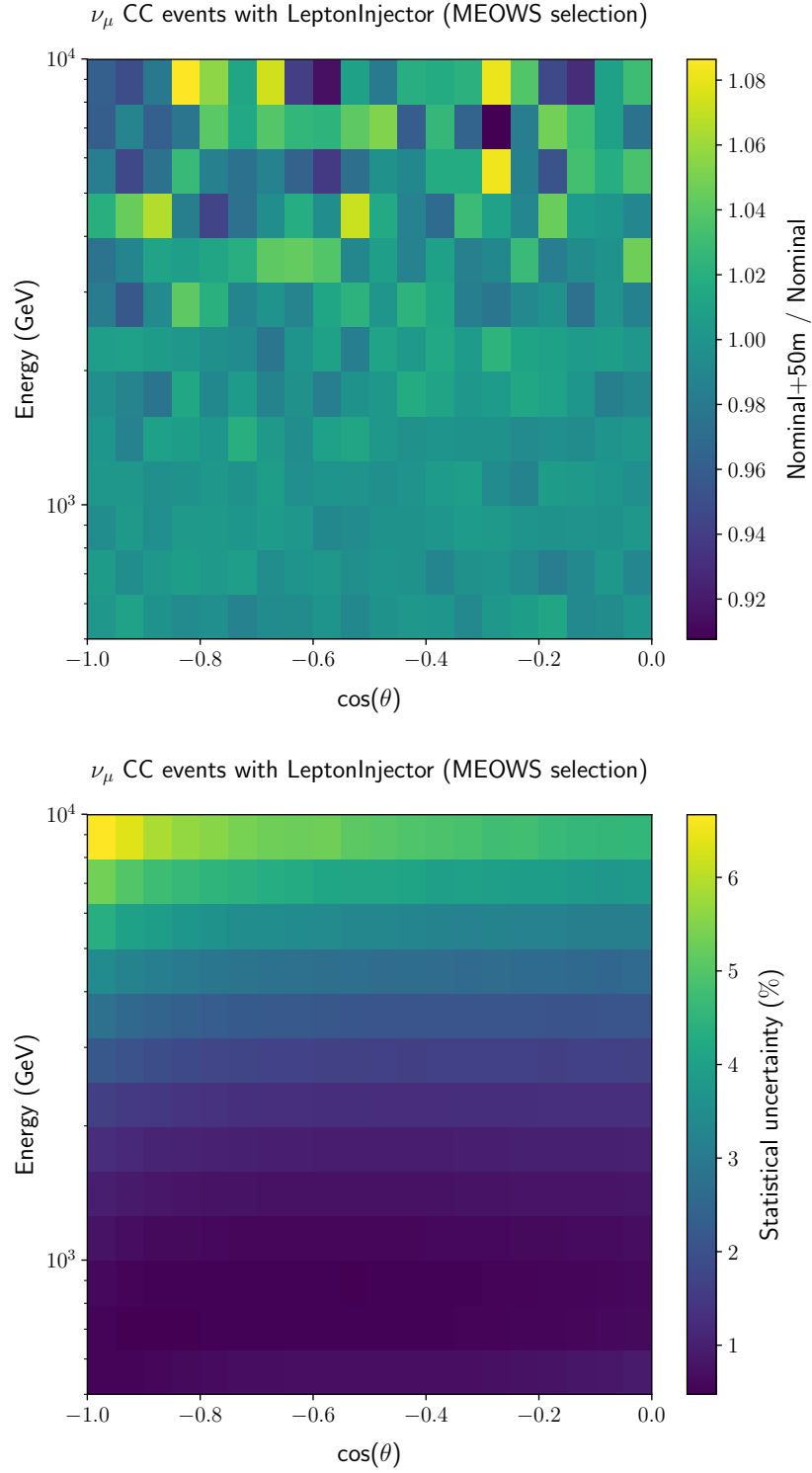


Figure 6-5: (Top) The ratio of muon events per bin for a geometry with the bedrock raised 50 m to that for the nominal geometry. (Bottom) The statistical uncertainty in the simulation sets plotted above. Figures courtesy of David Vannerom.

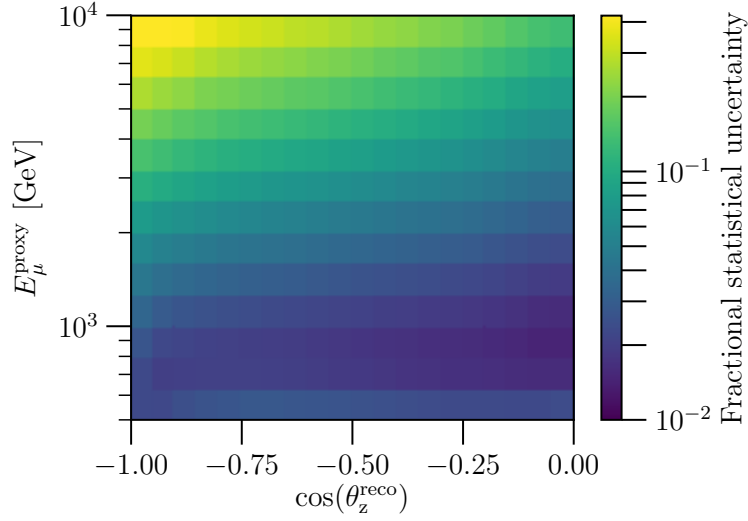


Figure 6-6: Expected fractional statistical uncertainty per bin, assuming only three neutrinos. The asymmetrical Poisson errors are calculated using the Garwood method and averaged [143–145].

were not able to be fully completed and understood in time for this thesis. Therefore, the result presented in this thesis does not include this potential systematic effect. Future work will incorporate the effect of the bedrock density, if necessary, once it is understood. However, at present we believe the bedrock systematic uncertainty will be negligible.

6.3 Oscillograms and expected event distributions

This section presents the expected event distributions assuming a sterile neutrino with parameters $\Delta m_{41}^2 = 1.0 \text{ eV}^2$, $\sin^2 2\theta_{24} = 0.1$, and three values for the decay-mediating coupling, $g^2 = 0, 2\pi$, and 4π . The oscillograms in Figs. 6-7 and 6-8 show the disappearance probabilities at the detector in true quantities. Figure 6-7 shows the disappearance probability of muon antineutrinos, and Fig. 6-8 shows the disappearance probability of muon neutrinos. In both these figures, the left-most panel, corresponds to a standard 3+1 model, or no ν_4 neutrino decay, while the middle two panels correspond to non-zero values of the coupling, which causes ν_4 decay. The rightmost panel corresponds to the three-neutrino model. The features

of the oscillograms are explained in Section 3.1.IV.B.

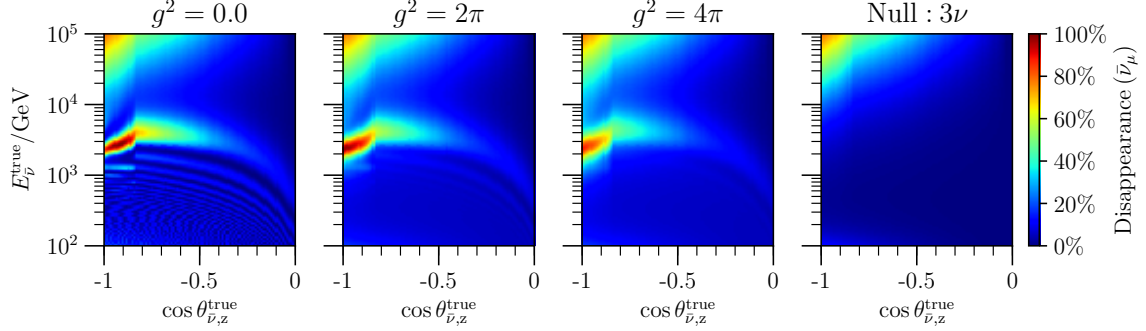


Figure 6-7: Muon antineutrino disappearance as a function of true energy and angle. The left three panels show the prediction for a 3+1 sterile neutrino model with $\Delta m_{41}^2 = 1.0 \text{ eV}^2$ and $\sin^2 2\theta_{24} = 0.1$ and three values of the decay-mediating coupling. The leftmost panel corresponds to a traditional 3+1 model. The rightmost panel corresponds to the scenario where there are only three neutrinos.

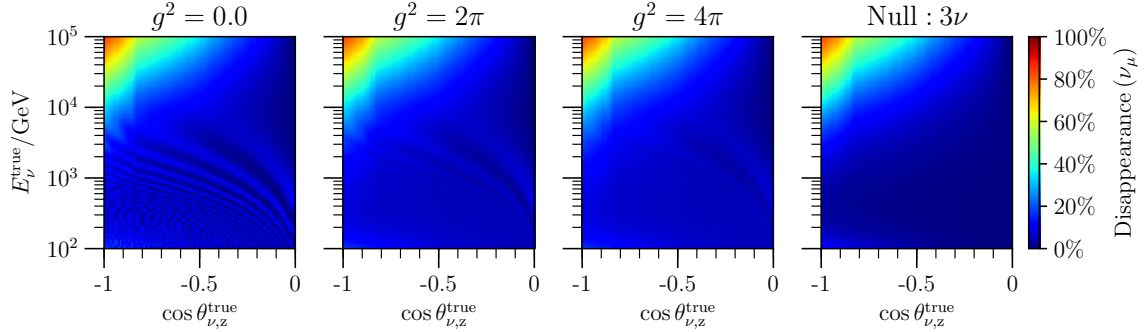


Figure 6-8: Muon neutrino disappearance as a function of true energy and angle. The left three panels show the prediction for a 3+1 sterile neutrino model with $\Delta m_{41}^2 = 1.0 \text{ eV}^2$ and $\sin^2 2\theta_{24} = 0.1$ and three values of the decay-mediating coupling. The leftmost panel corresponds to a traditional 3+1 model. The rightmost panel corresponds to the scenario where there are only three neutrinos.

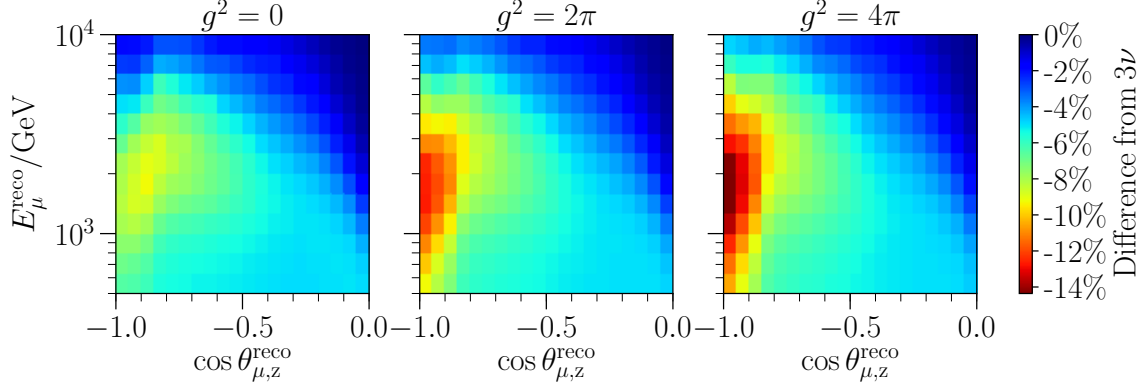


Figure 6-9: Expected event distributions, shown as a percent difference from the three-neutrino model, for sterile neutrino parameters $\Delta m_{41}^2 = 1.0 \text{ eV}^2$, $\sin^2 2\theta_{24} = 0.1$, and three values of the decay-mediating coupling, $g^2 = 0$, 2π , and 4π .

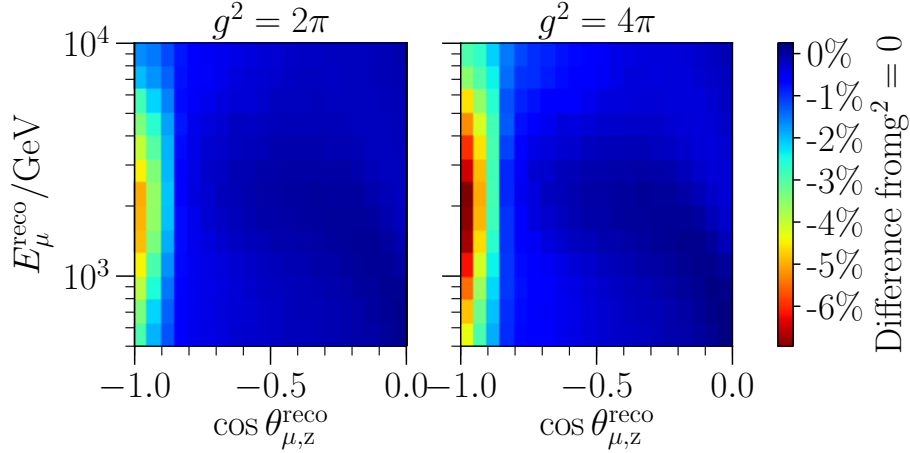


Figure 6-10: Expected event distributions, shown as a percent difference from the traditional 3+1 model, for sterile neutrino parameters $\Delta m_{41}^2 = 1.0 \text{ eV}^2$, $\sin^2 2\theta_{24} = 0.1$, and two values of the decay-mediating coupling, 2π , and 4π .

The expected event distributions for these same parameters are shown in Fig. 6-9 as a percent difference from the three-neutrino scenario. For these fixed values of Δm_{41}^2 and $\sin^2 2\theta_{24}$, the traditional 3+1 model predicts a maximum 9% per-bin deficit, which increases with non-zero g^2 up to 14% and shifts in position to the minimum cosine zenith value. A comparison between the expected event distributions between zero and non-zero values of g^2 for fixed Δm_{41}^2 and $\sin^2 2\theta_{24}$ is shown in Fig. 6-10. Nonzero g^2 causes a deficit of events at the smallest cosine zenith angles, up to about 7% per bin.

6.4 Likelihood function

The Poisson likelihood function for a single bin is

$$\mathcal{L}(\vec{\theta}|k) = \frac{\lambda(\vec{\theta})^k e^{-\lambda(\vec{\theta})}}{k!} \quad (6.2)$$

where $\lambda(\vec{\theta})$ is the predicted bin count assuming hypothesis $\vec{\theta}$ and k is the experimental bin count. However, finite Monte Carlo statistics do not allow for exact determination of the expected bin count, $\lambda(\vec{\theta})$. Therefore, following [146], we use an effective likelihood that accounts for finite Monte Carlo statistics,

$$\mathcal{L}_{\text{Eff}}(\vec{\theta}|k) = \left(\frac{\mu}{\sigma^2}\right)^{\frac{\mu^2}{\sigma^2}+1} \Gamma\left(k + \frac{\mu^2}{\sigma^2} + 1\right) \left[k! \left(\frac{\mu}{\sigma^2} + 1\right)^{k + \frac{\mu^2}{\sigma^2} + 1} \Gamma\left(\frac{\mu^2}{\sigma^2} + 1\right) \right]^{-1} \quad (6.3)$$

where μ and σ^2 depend on $\vec{\theta}$ and Monte Carlo weights. The parameters μ and σ^2 are given by,

$$\begin{aligned} \mu &\equiv \sum_{i=1}^m w_i \\ \sigma^2 &\equiv \sum_{i=1}^m w_i^2, \end{aligned} \quad (6.4)$$

where m is the number of Monte Carlo events in the bin, and w_i is the weight of the i^{th} event, assuming $\vec{\theta}$.

To account for systematic uncertainties, nuisance parameters with Gaussian priors on their values are used. The statistical likelihood from Eq. 6.3 is multiplied by:

$$\mathcal{L}(\theta_{\vec{\eta}}) = \prod_{\eta} \frac{1}{\sqrt{2\pi\sigma_{\eta}^2}} e^{-\frac{(\theta_{\eta} - \Theta_{\eta})^2}{2\sigma_{\eta}^2}} \quad (6.5)$$

where θ_{η} , Θ_{η} , and σ_{η} are the value, prior central value, and prior width of nuisance parameter η . The prior central values and widths are given in Table 6.2.

6.5 Parameter scan

The analysis is performed over a three-dimensional scan of the physics parameters: Δm_{41}^2 , $\sin^2 2\theta_{24}$, and g^2 . The parameters Δm_{41}^2 and $\sin^2 2\theta_{24}$ are sampled log-uniformly in the ranges $0.01 - 47 \text{ eV}^2$ and $0.01 - 1$, respectively, with ten samples per decade for each parameter. These choices are driven by the region where the anomalies discussed earlier appear. The parameter g^2 is sampled in steps of $\pi/2$ in the range $0 - 4\pi$, where $g^2 = 0$ corresponds to infinite ν_4 lifetime. The upper limit on scanned values of g^2 is chosen to preserve unitarity and perturbability, which are assumed by the calculations [147].

6.6 Frequentist analysis and Asimov sensitivity

The frequentist analysis assumes Wilks' theorem [148]. This allows confidence level intervals to be drawn based on the logarithm of the profile likelihood ratio. That is

$$\Delta\text{LLH}(\vec{\theta}) = \ln(\mathcal{L}(\hat{\vec{\theta}})) - \ln(\mathcal{L}(\vec{\theta})), \quad (6.6)$$

where $\hat{\vec{\theta}}$ is the set of physics and nuisance parameters that maximizes $\mathcal{L}(\vec{\theta})$, i.e. the best fit. The test statistic, TS, is

$$\text{TS}(\vec{\theta}) = -2\Delta\text{LLH}(\vec{\theta}). \quad (6.7)$$

Wilks' theorem states that, assuming certain criteria are met, in a likelihood space with n degrees of freedom, this test statistic has a χ^2 -distribution, with n degrees of freedom, χ_n^2 . The confidence level C runs through all points $\vec{\theta}$ where

$$\int_0^{\text{TS}(\vec{\theta})} dx \chi_n^2(x) = C. \quad (6.8)$$

The values of the test statistic that satisfy Eq. 6.8 for several confidence levels, and for one and three degrees of freedom (DOF), are given in Table 6.3. If the assumptions underlying Wilks' theorem are strongly violated, the contours drawn using this tech-

nice may have improper coverage. Coverage of the contours will be checked using the Feldman Cousins method, which is always accurate but is computationally intensive, at a later date [149].

Confidence Level	1 DOF	3 DOF
68.27%	1.00	3.53
90%	2.71	6.25
95%	3.84	7.82
99%	6.63	11.34

Table 6.3: Critical values of the χ^2 test statistic for one and three degrees of freedom. Values from [4].

The sensitivity is approximated by the Asimov sensitivity [150]. The Asimov sensitivity is calculated over a scan of the three parameters, assuming three degrees of freedom and Wilks' theorem, and is shown in Fig. 6-11. Increased sensitivity is observed for larger values of g^2 for fixed values of $\Delta m_{41}^2 = 1.0 \text{ eV}^2$, $\sin^2 2\theta_{24} = 0.1$ around $\Delta m_{41}^2 = 1 \text{ eV}^2$. An exact sensitivity would be calculated from an ensemble simulated pseudoexperiments, using the Feldman-Cousins method [149]. This is computationally expensive and will be completed later.

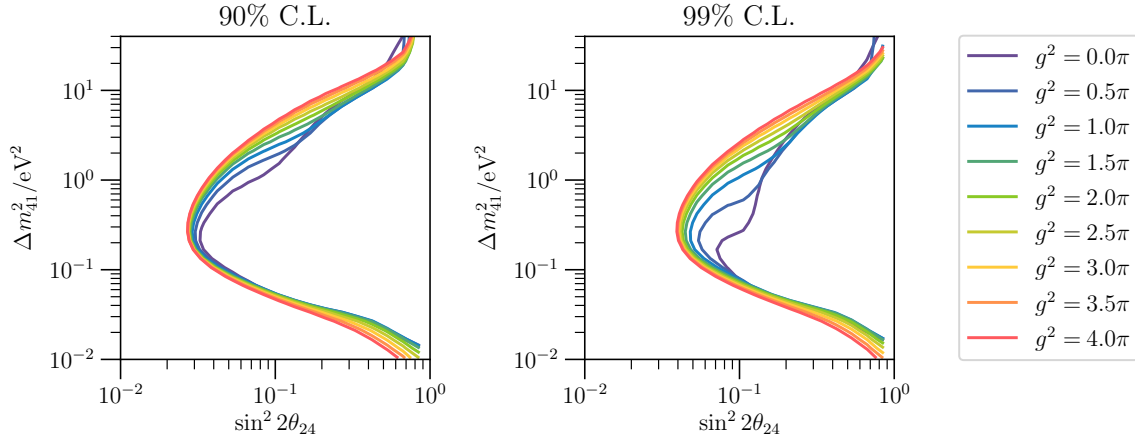


Figure 6-11: Asimov sensitivity.

6.7 Bayesian analysis

A Bayesian analysis is performed in addition to the frequentist analysis. The Bayesian evidence is computed for every sterile neutrino parameter point in the scan, as well as for the three-neutrino model. The evidence is defined as:

$$\mathcal{E}(\vec{\Theta}) = \int d\vec{\eta} \mathcal{L}(\vec{\Theta}, \vec{\eta}) \Pi(\vec{\eta}) \quad (6.9)$$

where $\Pi(\vec{\eta})$ are the Gaussian priors on the nuisance parameters. The integral is calculated with the MultiNest algorithm [151]. The evidence for each sterile neutrino model is compared to that of the three-neutrino model. The ratio of these evidences is the Bayes factor:

$$B_{ij} = \frac{\mathcal{E}_i}{\mathcal{E}_j} \quad (6.10)$$

The Bayes factor is interpreted with Jeffreys scale, which quantifies the strength of evidence preferring one model, i , over the other, j . For negative values of the Bayes factor, model j is preferred over i .

$\log_{10} B_{ij}$	Strength of evidence
$0 - 0.5$	Weak
$0.5 - 1$	Substantial
$1 - 1.5$	Strong
$1.5 - 2$	Very strong
> 2	Decisive

Table 6.4: Strength of evidence determined from the Bayes factor. Adapted from [57]

Chapter 7

Results

Good agreement between data and the Monte Carlo description of the best-fit point is found. The projected distributions of reconstructed muon energy and reconstructed cosine zenith angle for both the data and the best-fit expectation are shown in Fig. 7-1. The best-fit distribution accounts for the best-fit sterile parameters and the best-fit systematic values. Pearson χ^2 tests assuming three degrees of freedom yield p-values of 46% and 43% for the energy proxy and cosine zenith distributions, respectively.

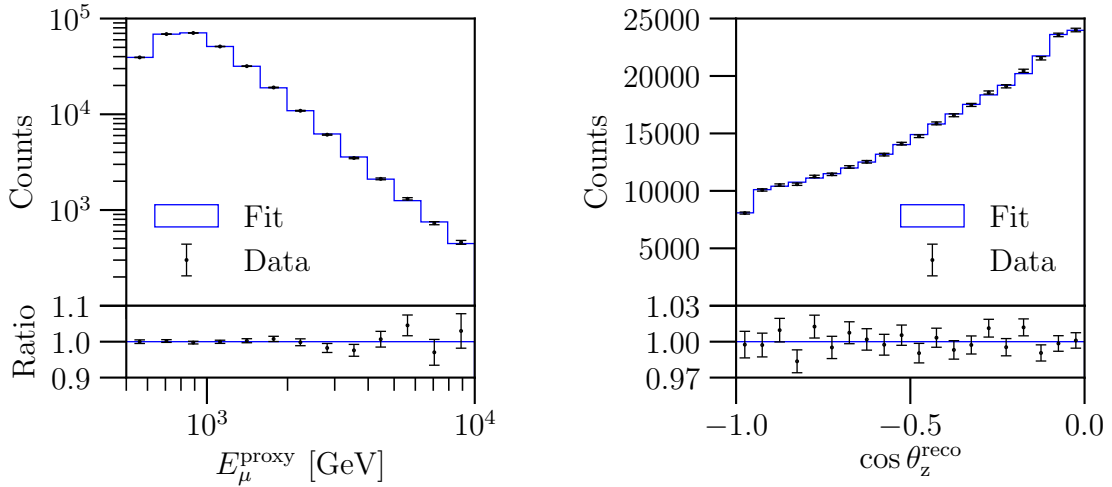


Figure 7-1: Projected reconstructed energy and cosine zenith distributions of the data compared to the best-fit expectation, including the best-fit systematics.

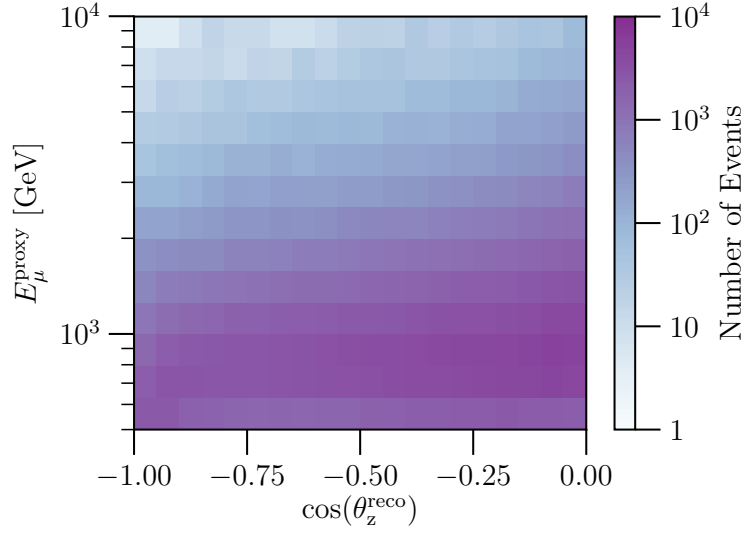


Figure 7-2: The binned, two-dimensional distribution of the eight-year dataset. The same dataset is used in [54, 56] and this plot is a reproduction of a plot from those references.

The eight-year dataset contains 305,735 reconstructed events. The two-dimensional distribution of the data is shown in Fig. 7-2.

The best-fit point occurs at $\Delta m_{41}^2 = 6.6 \text{ eV}^2$, $\sin^2 2\theta_{24} = 0.33$, and $g^2 = 2.5\pi$. The three-neutrino hypothesis is rejected with a p -value of 2.8%, assuming three degrees of freedom. The best-fit physics and nuisance parameters and their uncertainties are given in Table 7.1. The reported 1σ ranges come from marginalizing over all other parameters. The result of the frequentist analysis is shown in Figs. 7-3 and 7-4. In Fig. 7-3, each of the nine panels corresponds to a fixed value of g^2 , and the solid, dashed, and dotted white curves represent the 90%, 95% and 99% C.L. regions, respectively. In Fig. 7-4, the three panels correspond to the three confidence levels, and the different colored curves correspond to different g^2 values. In both figures, the best fit point is marked with a star.

Parameter	Best fit $\pm 1\sigma$
Physics Parameters	
Δm_{41}^2	$6.7^{+3.9}_{-2.5} \text{ eV}^2$
$\sin^2 2\theta_{24}$	$0.33^{+0.20}_{-0.17}$
g^2	$2.5\pi \pm 1.5\pi$
Detector parameters	
DOM efficiency	0.9653 ± 0.0004
Bulk Ice Gradient 0	0.008 ± 0.015
Bulk Ice Gradient 1	0.35 ± 0.09
Forward Hole Ice	-3.5 ± 0.06
Conventional flux parameters	
Normalization ($\Phi_{\text{conv.}}$)	1.4 ± 0.1
Spectral shift ($\Delta\gamma_{\text{conv.}}$)	0.071 ± 0.001
Atm. Density	0.005 ± 0.035
Barr WM	-0.03 ± 0.04
Barr WP	-0.06 ± 0.02
Barr YM	0.08 ± 0.05
Barr YP	-0.21 ± 0.05
Barr ZM	-0.012 ± 0.004
Barr ZP	-0.031 ± 0.002
Astrophysical flux parameters	
Normalization ($\Phi_{\text{astro.}}$)	1.1 ± 0.05
Spectral shift ($\Delta\gamma_{\text{astro.}}$)	0.39 ± 0.03
Cross sections	
Cross section σ_{ν_μ}	0.998 ± 0.002
Cross section $\sigma_{\bar{\nu}_\mu}$	0.998 ± 0.003
Kaon energy loss σ_{KA}	-0.38 ± 0.04

Table 7.1: Best-fit physics and nuisance parameter values. The 1σ range are determined by marginalizing over all other parameters.

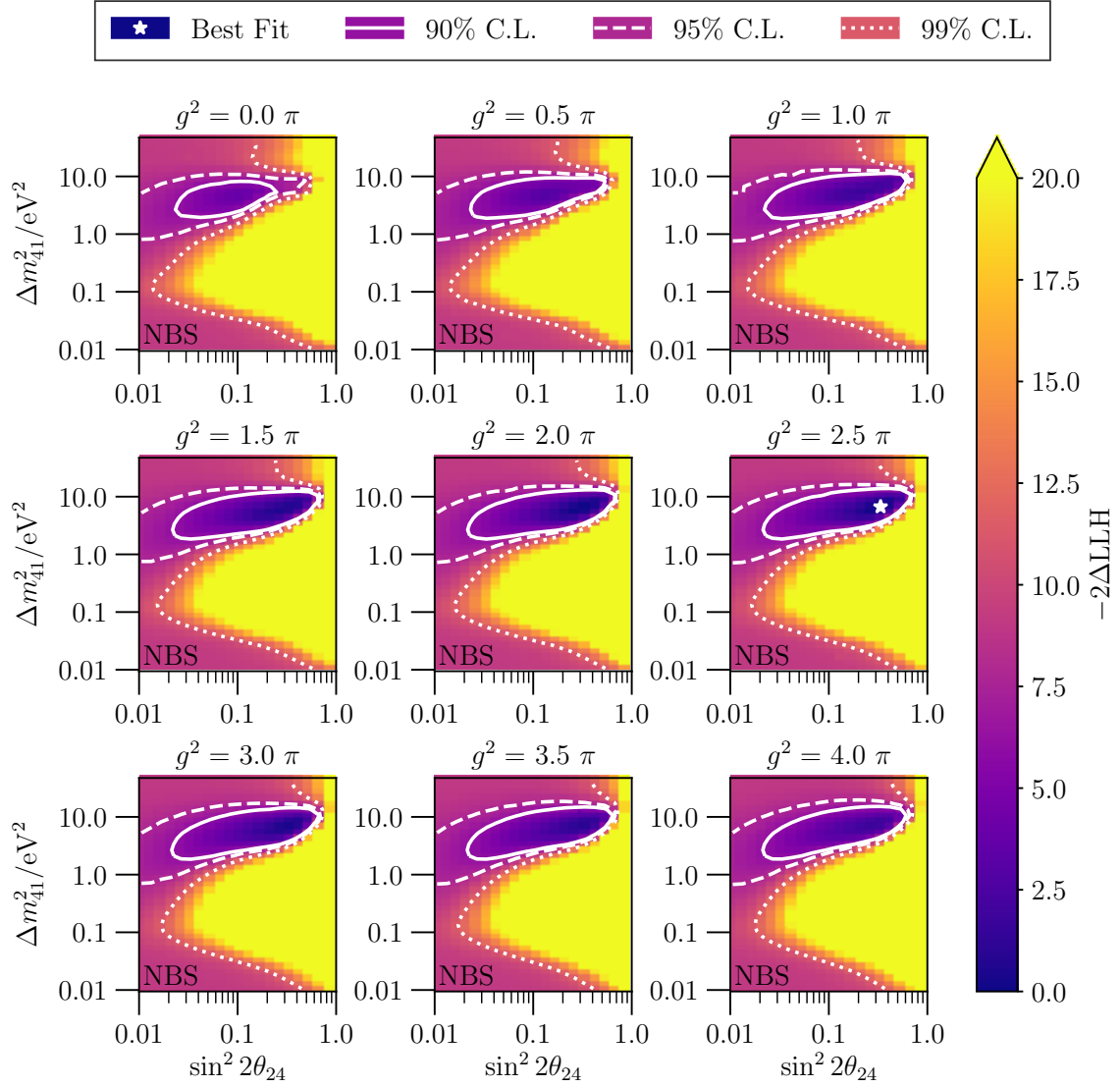


Figure 7-3: Result of the frequentist analysis. “NBS” means that this analysis did not include a bedrock systematic uncertainty. See Section 6.2.3.

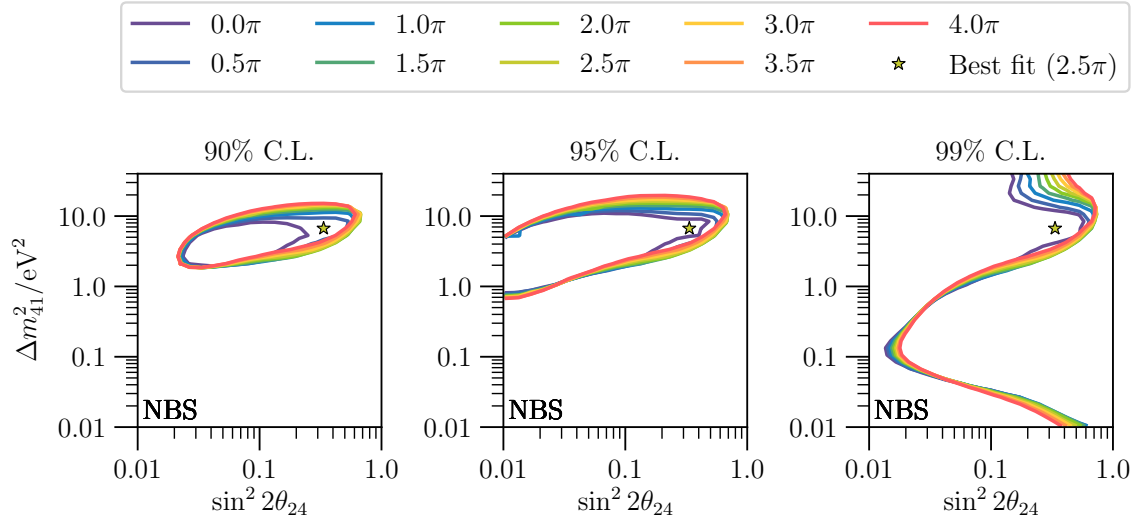


Figure 7-4: Result of the frequentist analysis. “NBS” means that this analysis did not include a bedrock systematic uncertainty. See Section 6.2.3.

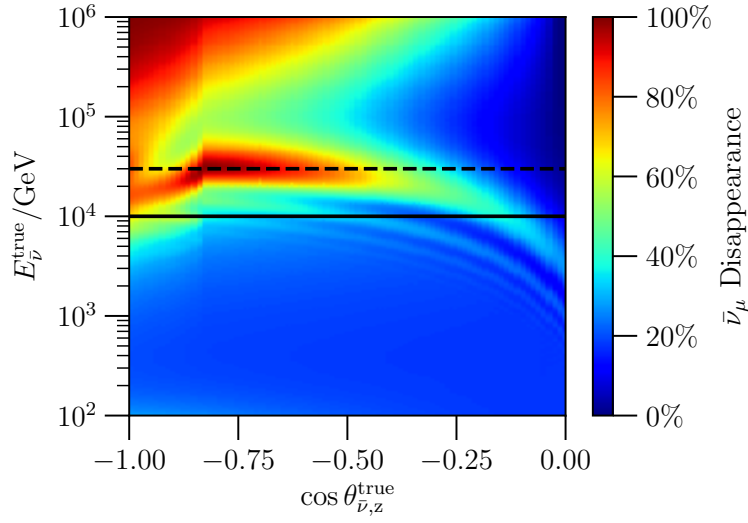


Figure 7-5: Oscillogram for the best-fit point. The lines at 10 TeV and 30 TeV indicate the true neutrino energy below which about 90% and 99% of the events are expected to be, respectively.

The oscillogram corresponding to the best-fit point is shown in Fig. 7-5. The horizontal line at 10 TeV indicates the true neutrino energy below which about 95% of the events are expected to be, based off of simulation and assuming the prior values of the nuisance parameters. The horizontal line at 30 TeV indicates the true energy below which about 99% of the events are expected to be.

The expected distribution of the best-fit point and data are each compared to a reference model in Fig. 7-6. The reference model is the expectation associated with the three neutrino hypothesis and the systematic values from the best-fit point. These comparisons are shape only; overall normalization effects have been removed. Both plots show a deficit of events in the upper left corner, a relative excess of events in the upper right corner, and a modest deficit of events in the bottom left corner. Low statistics at the highest energies yield large fluctuations in the data plot.

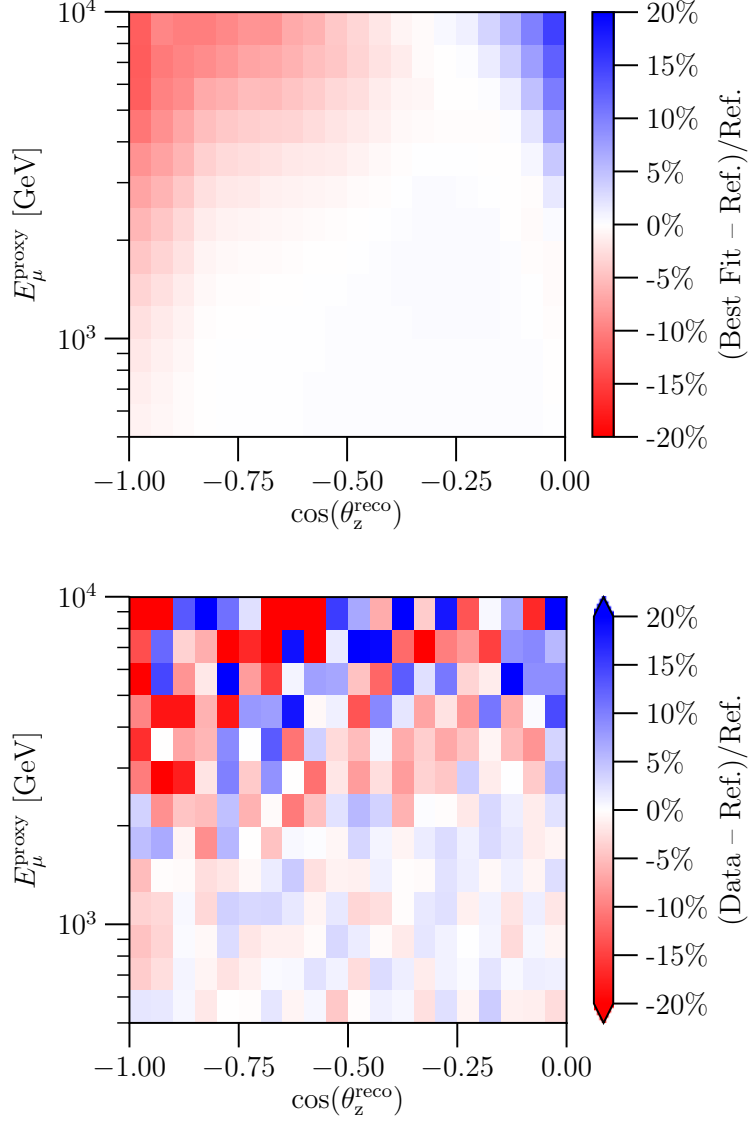


Figure 7-6: (Top) The shape-only percent difference between the best fit expectation and a reference model. (Bottom) The shape-only percent difference between the data and a reference model. The reference model is the expectation associated with the three-neutrino model and the best-fit systematics. Overall normalization effects have been removed.

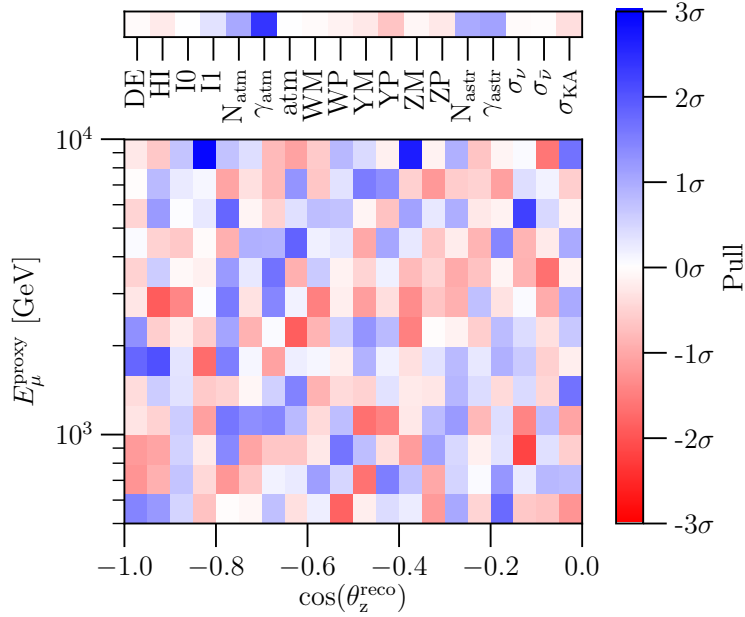


Figure 7-7: Systematic and data pulls at the best-fit point. The top panel shows the systematic pulls for each of the nuisance parameters. The main panel shows the data pulls.

Figure 7-7 shows the data and systematic pulls for the best-fit point. The data pull for the i^{th} bin is defined as

$$\text{Pull}_i \equiv \frac{\text{Data}_i - \text{Expectation}_i}{\sigma_{\text{Expectation}_i}}, \quad (7.1)$$

where $\sigma_{\text{Expectation}_i}$ is the asymmetrical Poisson error of the expectation. The Poisson error is calculated using the Garwood method [143–145]. The systematic pull for the i^{th} nuisance parameter is defined as

$$\text{Pull}_i \equiv \frac{\text{Fit}_i - \text{Prior Center}_i}{\text{Prior Width}_i}. \quad (7.2)$$

All systematics pull less than about 1σ , with the exception of the cosmic ray spectral shift, which pulls 2.4σ . The data pulls appear roughly uniformly distributed. The data and systematic pulls for the fit to the three-neutrino scenario and the best-fit of the subset of points corresponding to the traditional $3 + 1$ model are given in Appendix B.0.1. The fit values of the nuisance parameters for each point in the

scan are given in Appendix B.0.2.

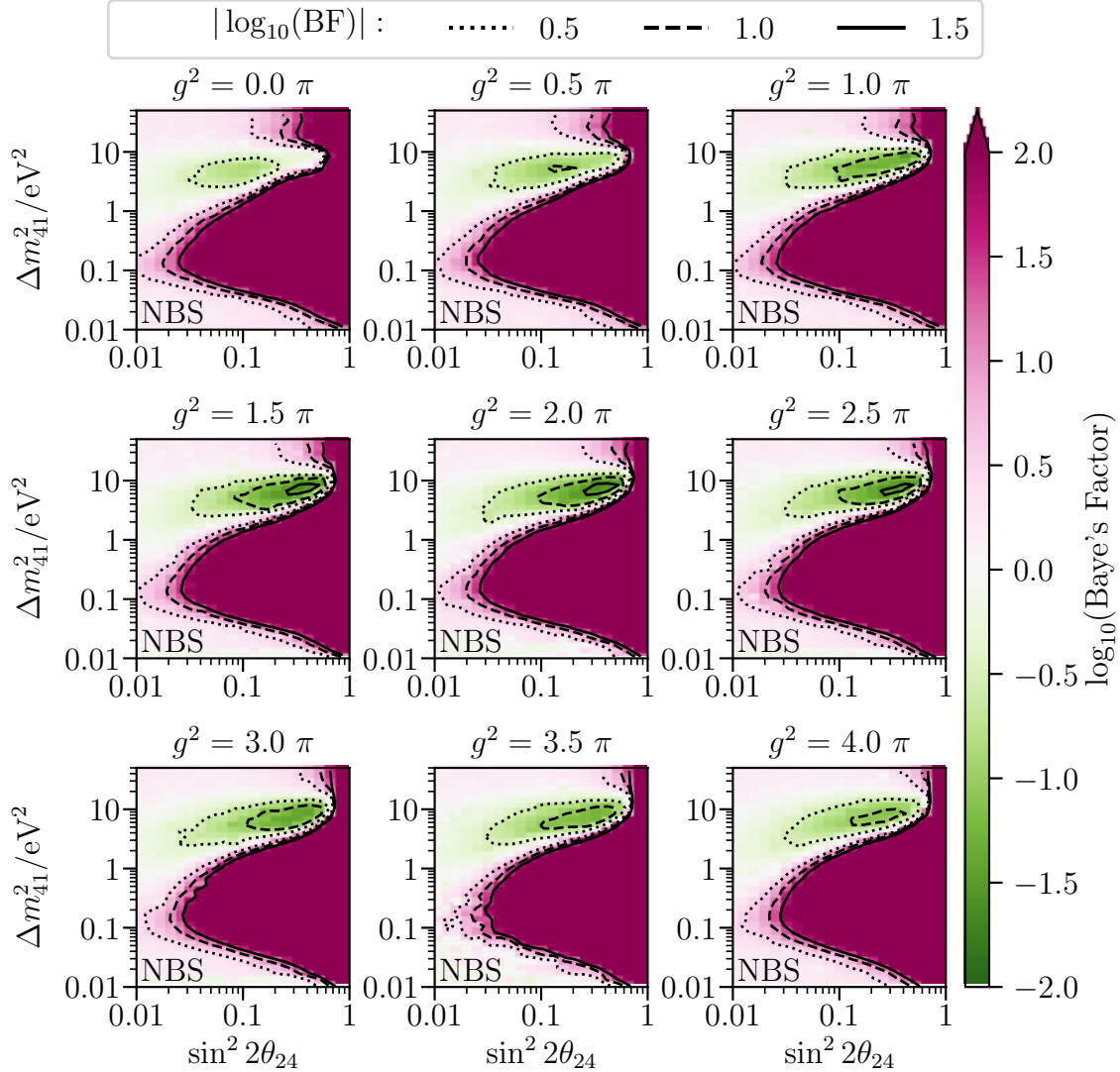


Figure 7-8: Result of the Bayesian analysis. “NBS” means the analysis did not include a bedrock systematic uncertainty. See Section 6.2.3.

The result of the Bayesian analysis is shown in Fig. 7-8. The best model has the parameters $\Delta m_{41}^2 = 6.6 \text{ eV}^2$, $\sin^2 2\theta_{24} = 0.33$, and $g^2 = 1.5\pi$. The Bayes’ factor is defined as the ratio of the evidence integral for a particular sterile neutrino model to the evidence integral for the three-neutrino model. The Bayes’ factor for the best model is 0.025, which corresponds to very strong evidence in favor of the best model. The model corresponding to the Frequentist best fit point is similarly favored over the three-neutrino model; the Bayes’ factor is 0.027. The posterior distributions of each

of the nuisance parameters for the best model are shown in Fig. 7-9. The correlation between all the nuisance parameters is shown in Fig. 7-10.

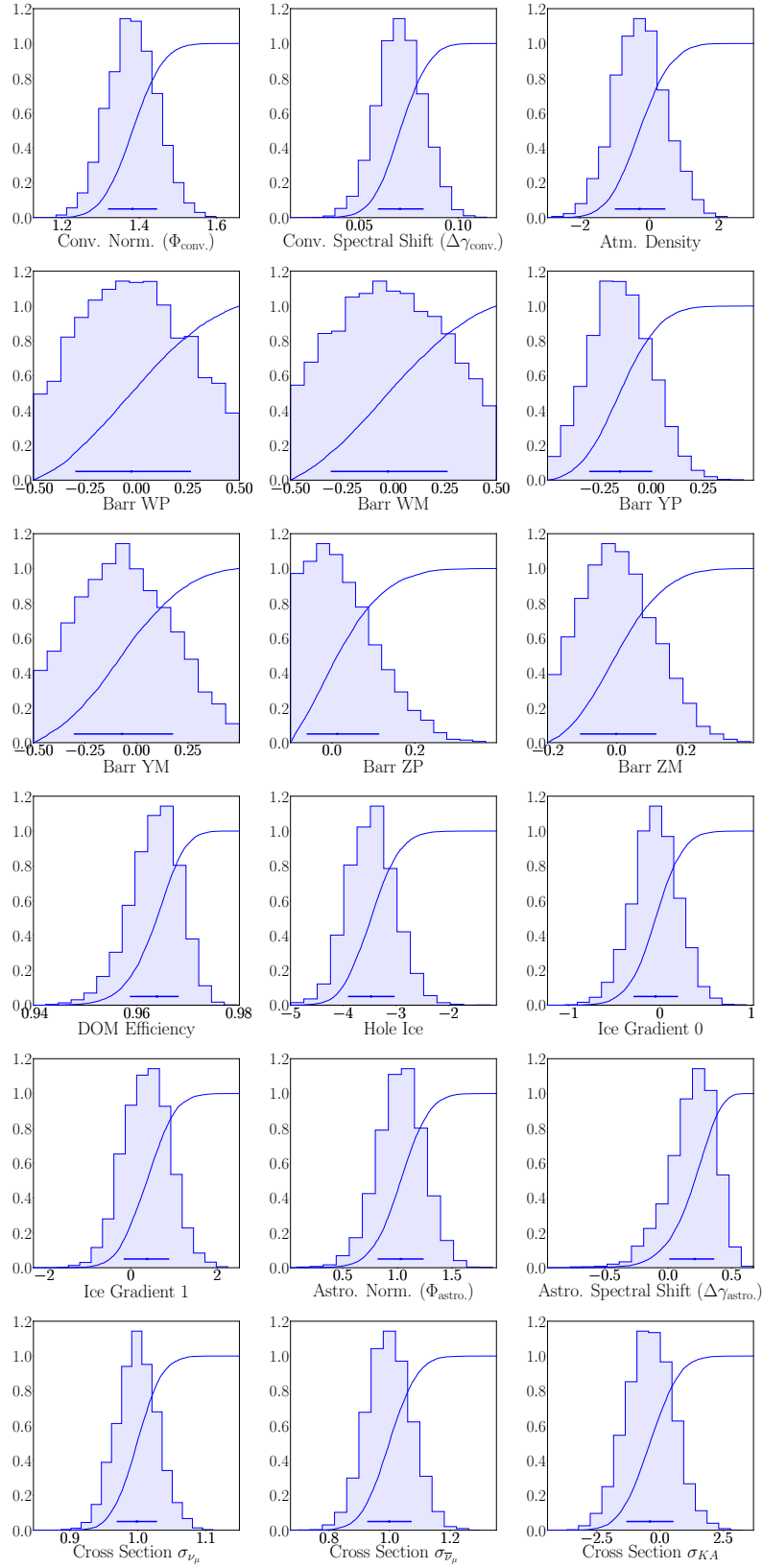


Figure 7-9: Posterior distributions of the nuisance parameters for the best model.

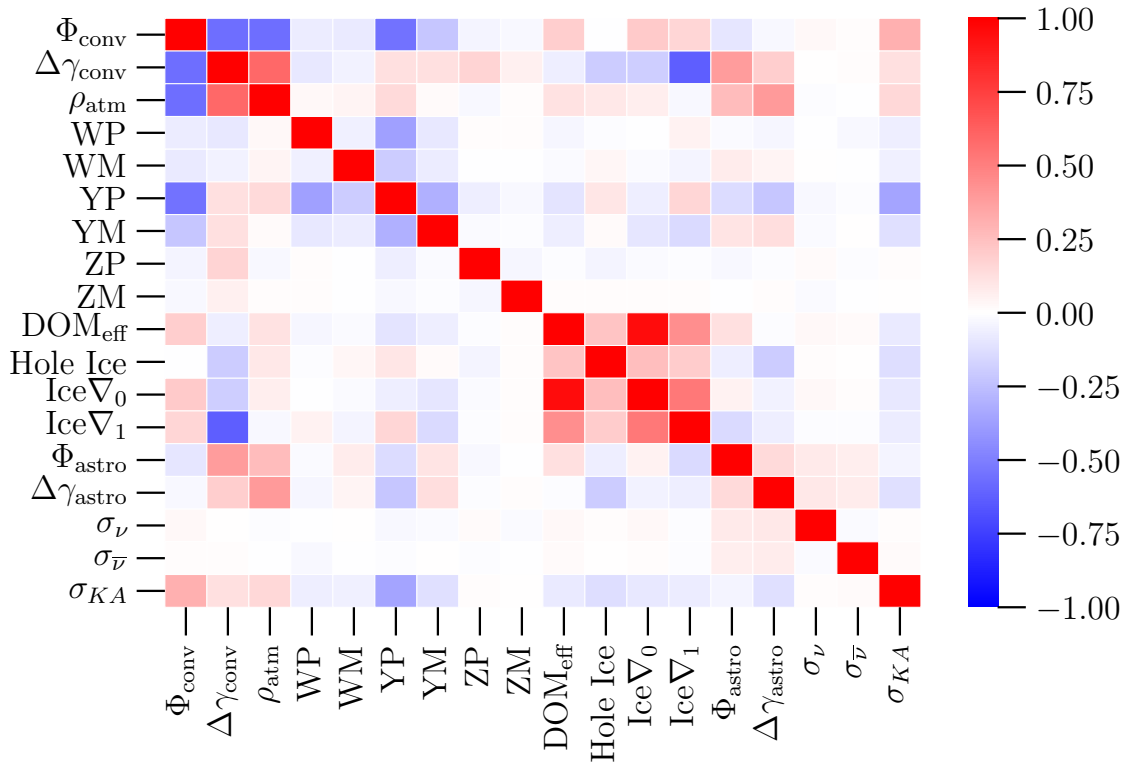


Figure 7-10: Correlation between the nuisance parameters.

The constraining power of the frequentist and Bayesian analyses on the value of g^2 are compared in Fig. 7-11. The black curve shows the $-2\Delta\text{LLH}$ value for each scanned value of g^2 , profiling over Δm_{41}^2 and $\sin^2 2\theta_{24}$. This is plotted on the left y-axis. The red curve shows the profiled value of the $\log_{10}(\text{Baye's factor})$ for each value of g^2 , and is plotted on the right y-axis. The two y-axes have a common scale. The value of $-2\Delta\text{LLH}$ for the three-neutrino model is 9.06, the top of the figure, while on the right hand side, $\log_{10}(\text{Baye's factor}) = 0$ corresponds to the three-neutrino model. The value of $g^2 = 0$ is rejected with a p -value of 4.9%.

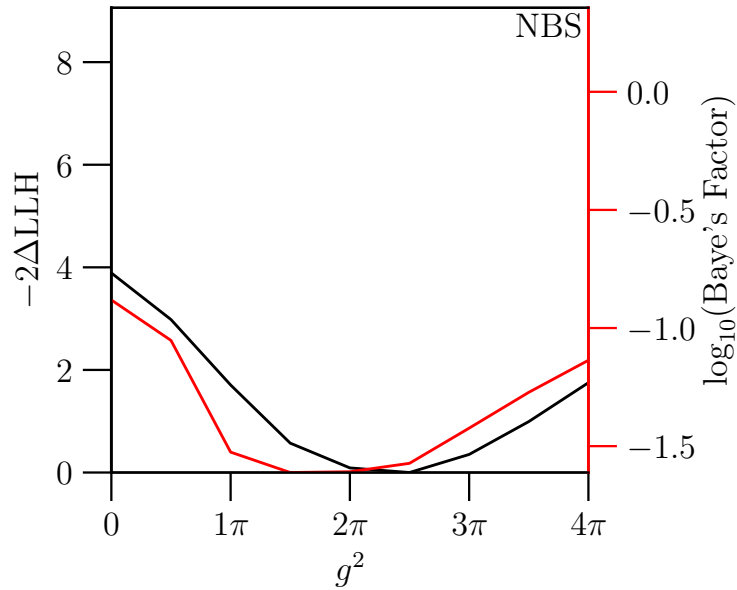


Figure 7-11: Profiled $-2\Delta\text{LLH}$, plotted on the left y-axis, and $\log_{10}(\text{Baye's factor})$, plotted on the right y-axis, versus g^2 . “NBS” means that this analysis did not include a bedrock systematic uncertainty.

7.1 Discussion

As in the traditional 3+1 eight-year search, the only nuisance parameter that pulls greater than 2σ is the cosmic ray spectral index shift, which pulls 2.4σ . For the three-neutrino fit, this parameter pulls 2.2σ . For the best fit of the subset of points with $g^2 = 0$, this parameter pulls 2.4σ . An upgraded systematic treatment for the cosmic ray flux is warranted. In particular, recent data show a break in the cosmic ray spectral index that is not accounted for in the cosmic ray model used here [152,153]. Nevertheless, the effect of the cosmic ray spectral index shift is purely in reconstructed energy, while the signal shape is two-dimensional.

In this analysis, the best fit of the subset of sampled points with $g^2 = 0$ is $\Delta m_{41}^2 = 4.2 \text{ eV}^2$ and $\sin^2 2\theta_{24} = 0.11$, which is consistent with the result from the traditional 3+1 eight-year search. Figure 7-12 show the difference in pulls between the best-fit point and the three-neutrino fit and best no-decay fit point, respectively. The red bins are where the best-fit expectation decreases the pulls. The blue bins are where the best-fit expectation increases the pulls. In comparison to both the three-neutrino fit and the traditional 3+1 best-fit, the overall best fit here reduces data pulls near the horizon at the higher energies, and for straight up-going events, especially at the lower energies. Statistical uncertainty for straight up-going events at the highest energies is large, so while the expected effect of the signal is large there, as shown in Fig. 7-6 (top), data pulls are expected to be small.

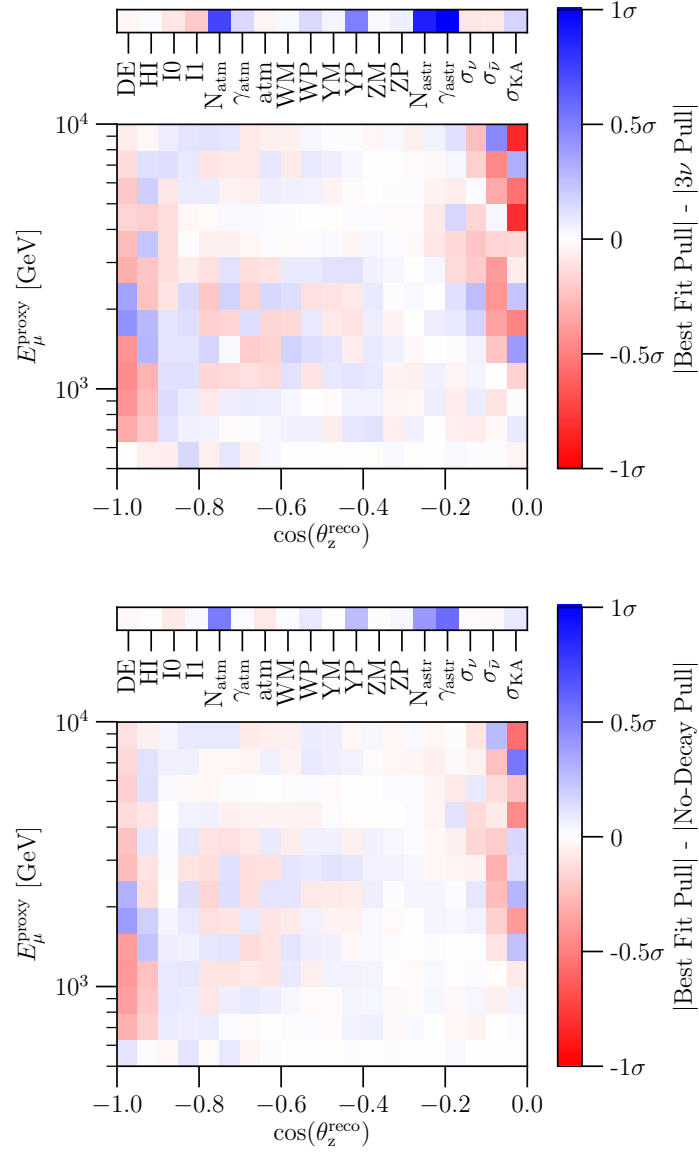


Figure 7-12: (Top) Difference in the absolute value of pulls between the best-fit point and the three neutrino model. (Bottom) Difference in the absolute value of pulls between the best-fit point and the best-fit of the subset of points corresponding to no decay.

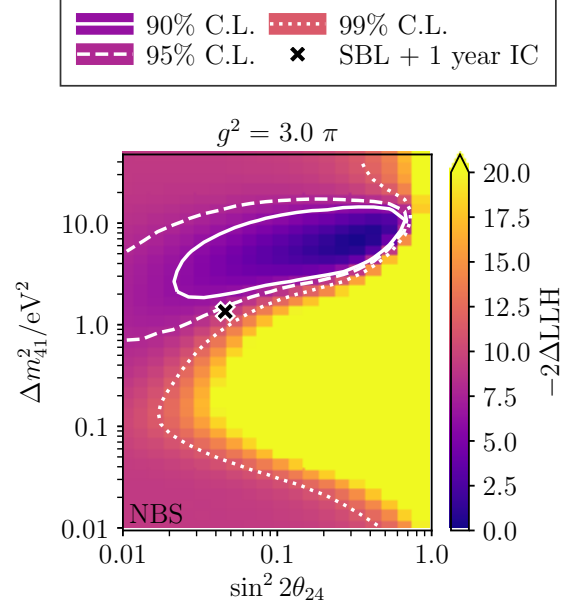


Figure 7-13: The $g^2 = 3\pi$ panel from the frequentist result. The best-fit point from combining global fits to short baseline data with one year of IceCube data is marked by an ‘x’. “NBS” means that this analysis did not include a bedrock systematic uncertainty. See Section 6.2.3.

The best-fit point from combining global fits to short baseline data with one year of IceCube data, discussed in Section 3.2, is $\Delta m^2_{41} = 1.35 \text{ eV}^2$, $\sin^2 2\theta_{24} = 0.05$ and $g^2 = 3.06\pi$. Rounding 3.06 to 3, the point is marked by an ‘x’ on the frequentist result panel for $g^2 = 3\pi$ in Fig. 7-13. This point sits just outside the 95% C.L. allowed region.

Chapter 8

Future prospects and conclusions

An eight-year search for light, unstable sterile neutrinos in the IceCube detector has found an anomalous result. The null hypothesis is rejected with a p -value of 2.8%, which is equivalent to 2.2σ . The frequentist analysis finds a best-fit point of $\Delta m_{41}^2 = 6.7 \text{ eV}^2$, $\sin^2 2\theta_{24} = 0.33$, and $g^2 = 2.5\pi$. This corresponds to a ν_4 lifetime of $\tau_4/m_4 = 6 \times 10^{-16} \text{ s/eV}$. The traditional 3+1 model is rejected with a p -value of 4.9%. The Bayesian analysis finds a best model with the same Δm_{41}^2 and $\sin^2 2\theta_{24}$ values as the frequentist best-fit, but the g^2 value is 1.5π . This model is preferred to the three-neutrino model by a factor of 41. The model associated with the frequentist best-fit is also a very good model, and is preferred to the three-neutrino model by a factor of 37.

This search scanned very coarsely in the g^2 , and somewhat coarsely in Δm_{41}^2 and $\sin^2 2\theta_{24}$. A finer scan is likely to find a better best fit. The frequentist analysis has assumed Wilks' theorem holds. The confidence interval limits should be verified using the Feldman Cousins test. If the effective number of degrees of freedom is less than three, the frequentist result will become more significant. A precise sensitivity based off of pseudoexperiments should also be calculated.

The effect of the systematic uncertainty of the bedrock density should be finalized. If it is an important systematic effect, the best fit point and best model may change. The systematic treatment of the conventional atmospheric neutrino flux can be improved. The cosmic ray flux models used in the development of this thesis do not

reflect a plethora of recent cosmic ray data [152–156]. An upgraded cosmic ray flux treatment that incorporates recent data, such as a global fit, would be an important improvement [157]. Similarly, the hadronic interaction uncertainties represented by the Barr parameters could be upgraded to reflect more recent measurements [158,159]. The hadronic interaction model used in this work, Sibyll 2.3c, has been upgraded to Sibyll 2.3d [160].

Future searches for light, sterile neutrinos in IceCube should extend to higher energies and consider nonzero values of θ_{14} and θ_{34} . They can look in an additional oscillation channel by using an independent dataset of cascade events, which correspond to electromagnetic and hadronic showers. One could simultaneously search for a disappearance of track events and an appearance of cascade events due to non-zero θ_{34} .

This sterile result is the first reported anomaly in neutrino disappearance experiments. It is expected to have a significant impact on the sterile neutrino landscape. Both this result and the recently published, standard $3 + 1$ model result should be incorporated into global fits. These results should reduce tension between appearance and disappearance experiments, but the extent of this remains unknown. Lastly, accelerator-based neutrino experiments, such as MicroBooNE, which have completely different systematic uncertainties than IceCube, can perform follow-up searches for muon neutrino disappearance due to unstable sterile neutrinos.

Appendix A

Specific contributions

All of the work in this thesis was done in collaboration with others. My specific contributions included:

- Studying and implementing systematic uncertainties and performing the analysis in [62].
- Calculating the IceCube likelihood to combine with short-baseline fit results and analyzing the results in [63].
- Studying the atmospheric neutrino flux uncertainties and implementing the Barr scheme in [55, 56].
- Performing the analysis for the IceCube search discussed in this thesis.
- Building portions of, developing calibration methods for, and testing new gasses in a time projection chamber discussed in Appendix C.

Appendix B

Supplementary figures

B.0.1 Data and systematic pulls

Figure B-1 shows the data and systematic pulls, as defined in Chapter 7, for the frequentist fit assuming three neutrinos. Figure B-2 shows the data and systematic pulls for the best fit of the subset of points corresponding to $g^2 = 0$, or the traditional 3+1 model.

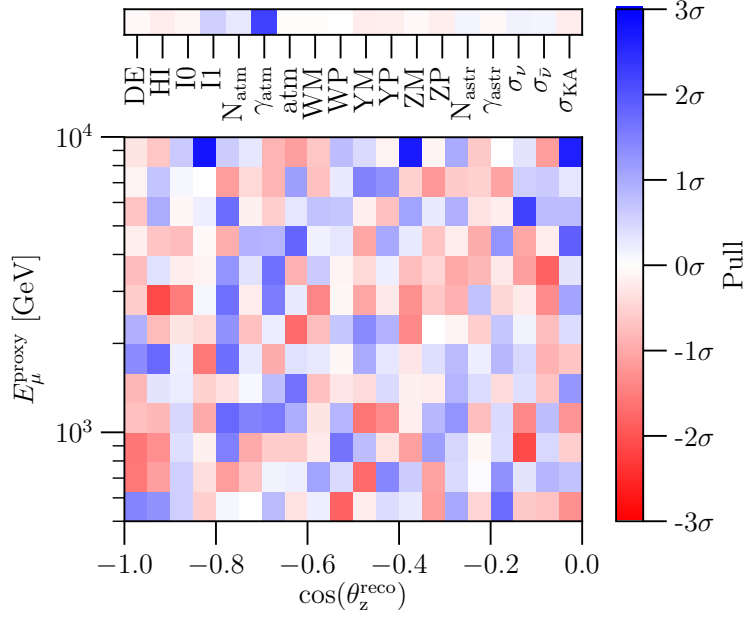


Figure B-1: Systematic and data pulls for the fit assuming three neutrinos. The top panel shows the systematic pulls for each of the nuisance parameters. The large, main panel shows the data pulls for each bin.

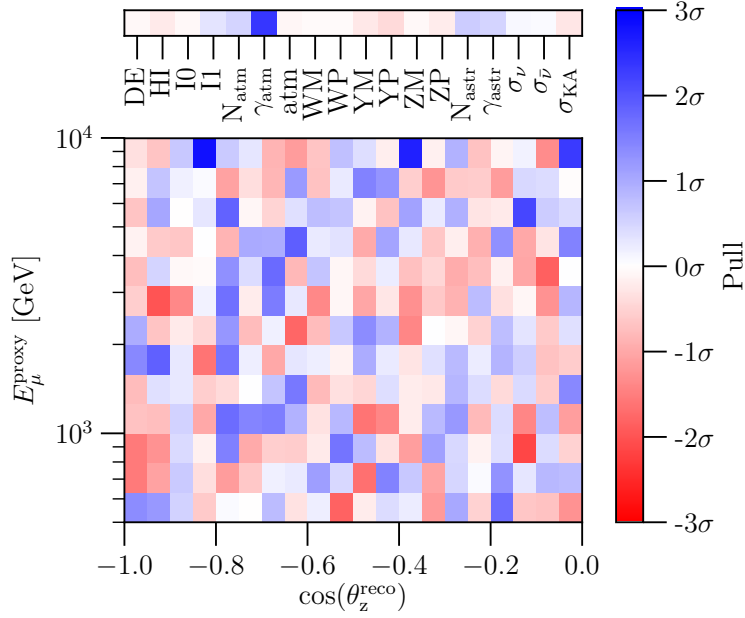


Figure B-2: Systematic and data pulls for the best fit of the subset of points associated with the traditional 3 + 1 model, i.e. $g^2 = 0$. The top panel shows the systematic pulls for each of the nuisance parameters. The large, main panel shows the data pulls for each bin.

B.0.2 Fit systematic values

Figures B-3 to B-20 show the fit values of each of the systematic parameters across the entire scanned physics space for the frequentist analysis.

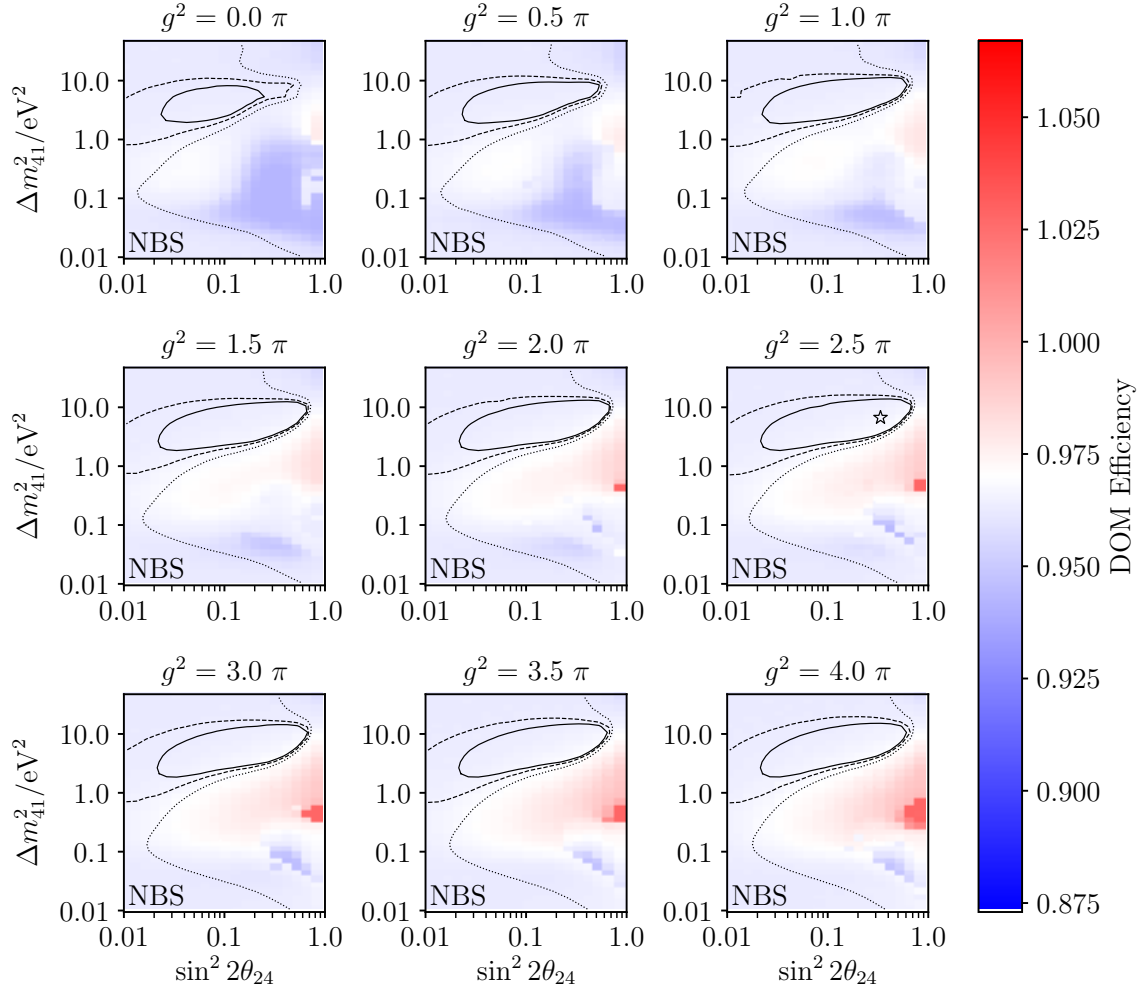


Figure B-3: The fit values of the DOM efficiency nuisance parameter from the frequentist analysis across the entire physics space. The color scale limits correspond to $\pm 1\sigma$. "NBS" means that no bedrock systematic uncertainty was included in this analysis.

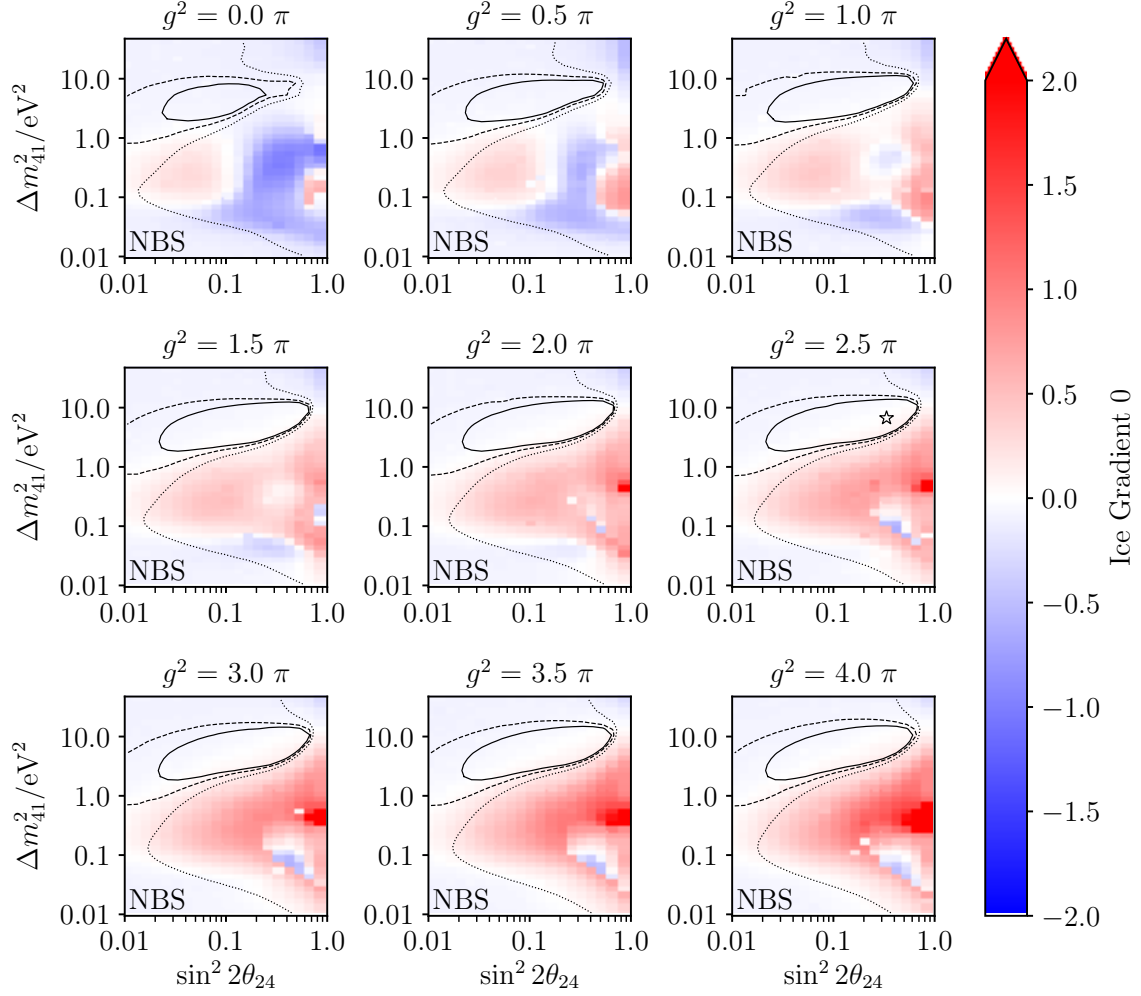


Figure B-4: The fit values of the Ice Gradient 0 nuisance parameter from the frequentist analysis across the entire physics space. The color scale limits correspond to $\pm 2\sigma$. “NBS” means that no bedrock systematic uncertainty was included in this analysis.

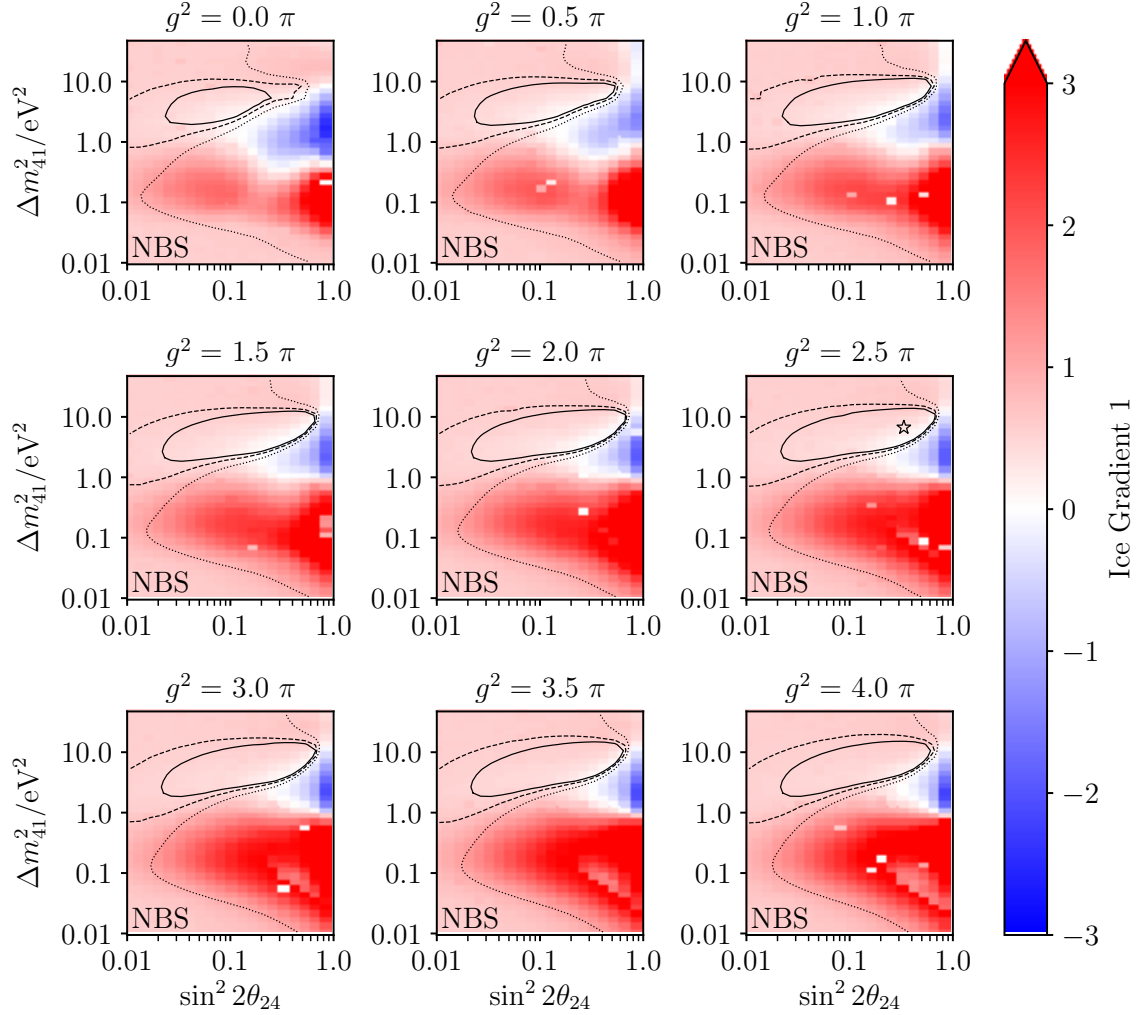


Figure B-5: The fit values of the Ice Gradient 1 nuisance parameter from the frequentist analysis across the entire physics space. The color scale limits correspond to $\pm 3\sigma$. “NBS” means that no bedrock systematic uncertainty was included in this analysis.

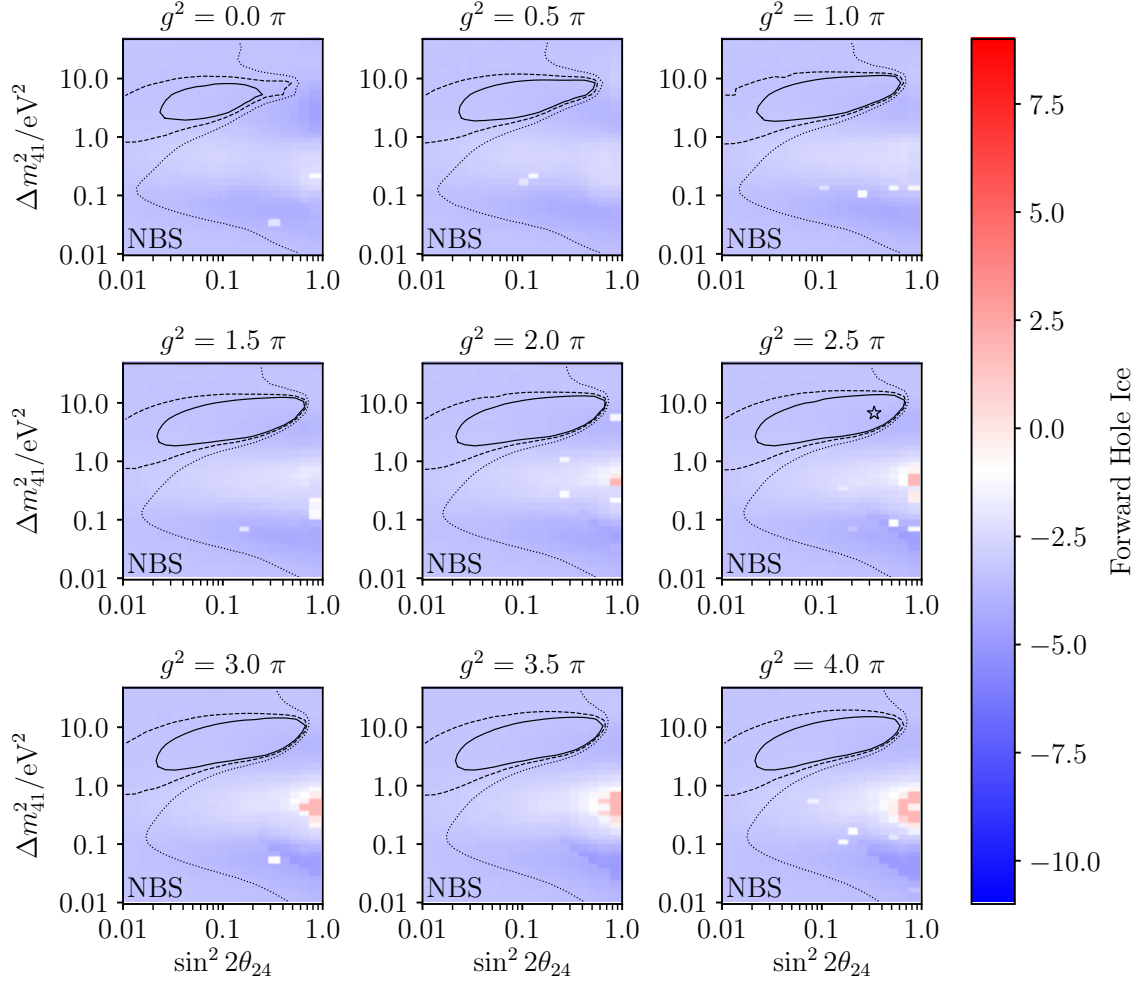


Figure B-6: The fit values of the forward hole ice nuisance parameter from the frequentist analysis across the entire physics space. The color scale limits correspond to $\pm 1\sigma$. "NBS" means that no bedrock systematic uncertainty was included in this analysis.

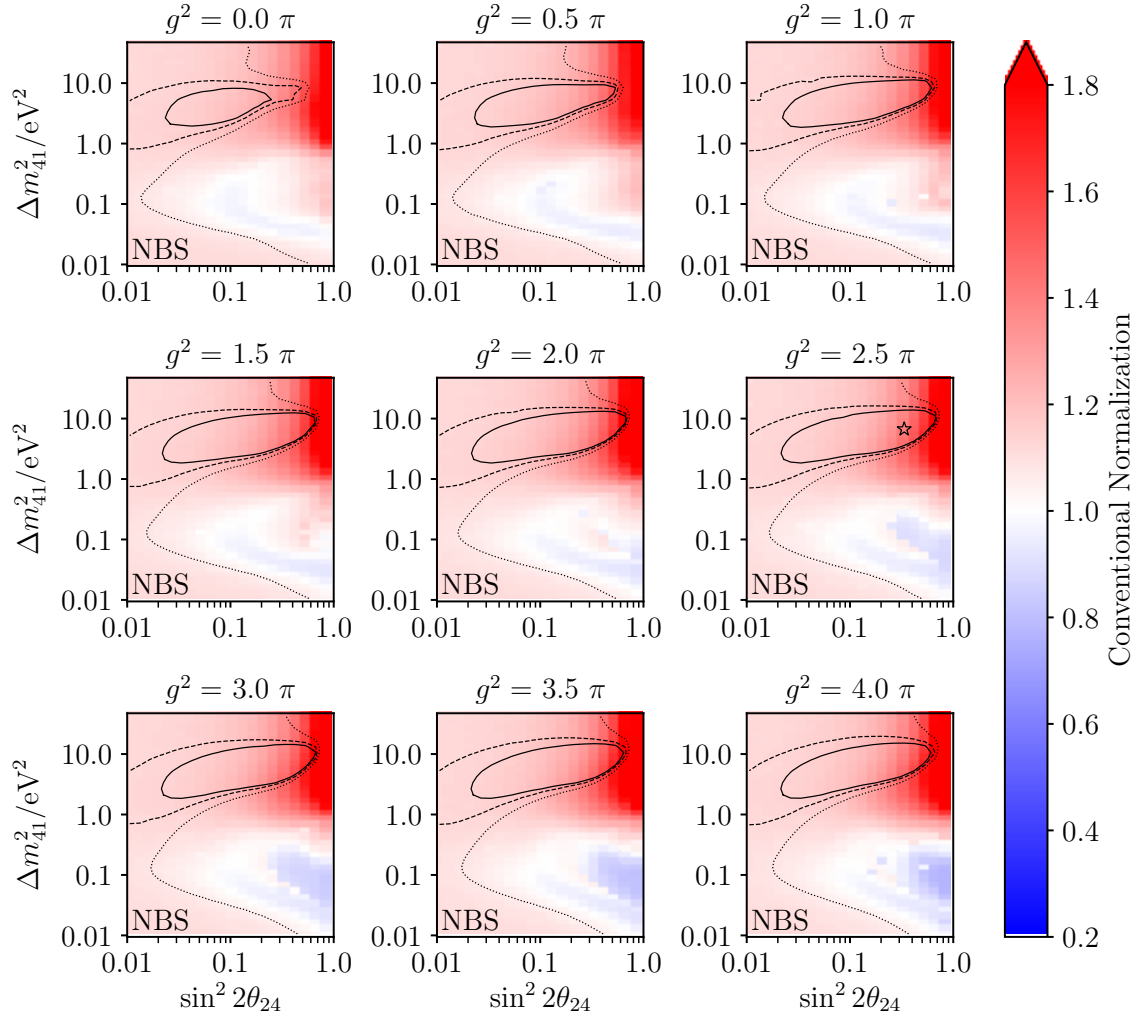


Figure B-7: The fit values of the conventional atmospheric normalization nuisance parameter from the frequentist analysis across the entire physics space. The color scale limits correspond to $\pm 2\sigma$. “NBS” means that no bedrock systematic uncertainty was included in this analysis. “NBS” means that no bedrock systematic uncertainty was included in this analysis.

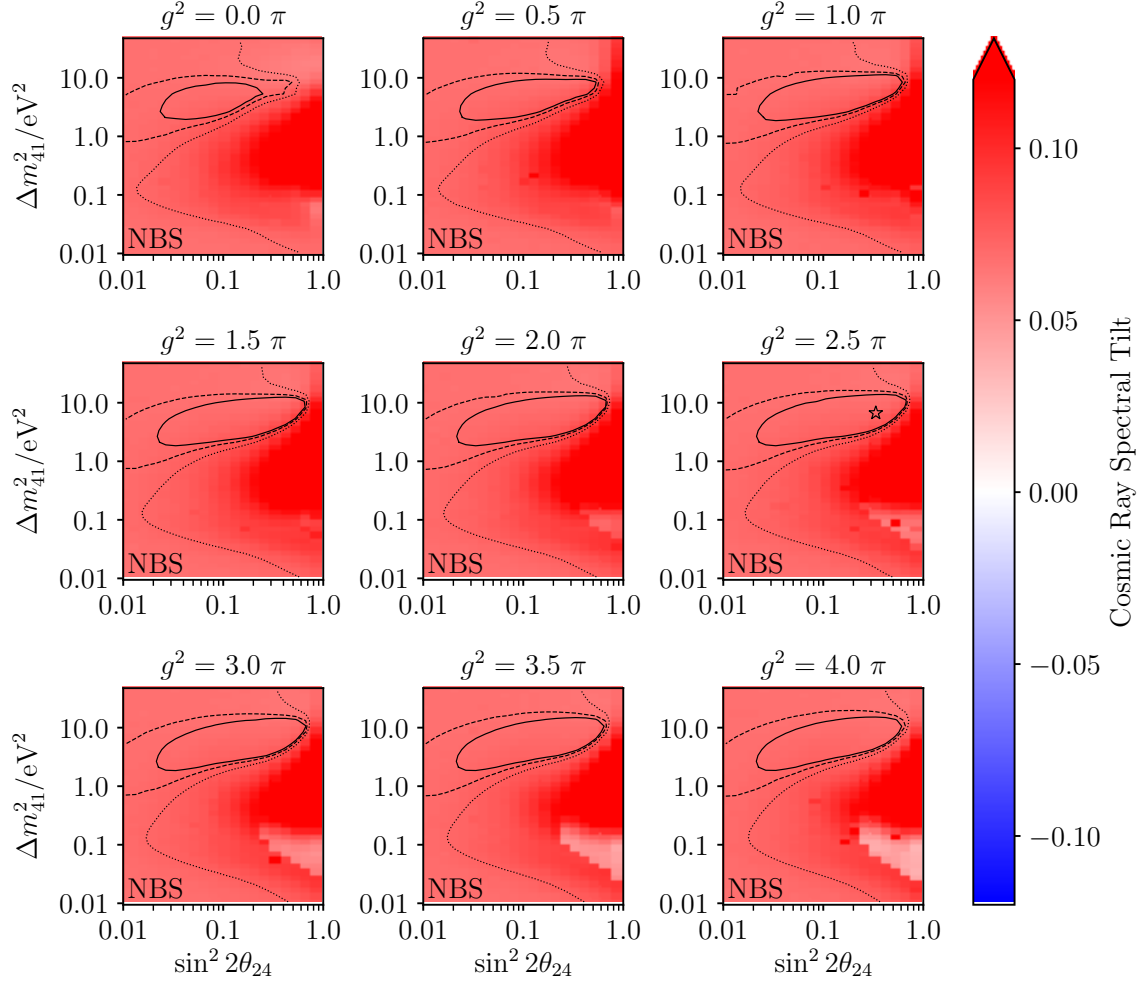


Figure B-8: The fit values of the cosmic ray spectral tilt nuisance parameter from the frequentist analysis across the entire physics space. The color scale limits correspond to $\pm 3\sigma$. "NBS" means that no bedrock systematic uncertainty was included in this analysis.

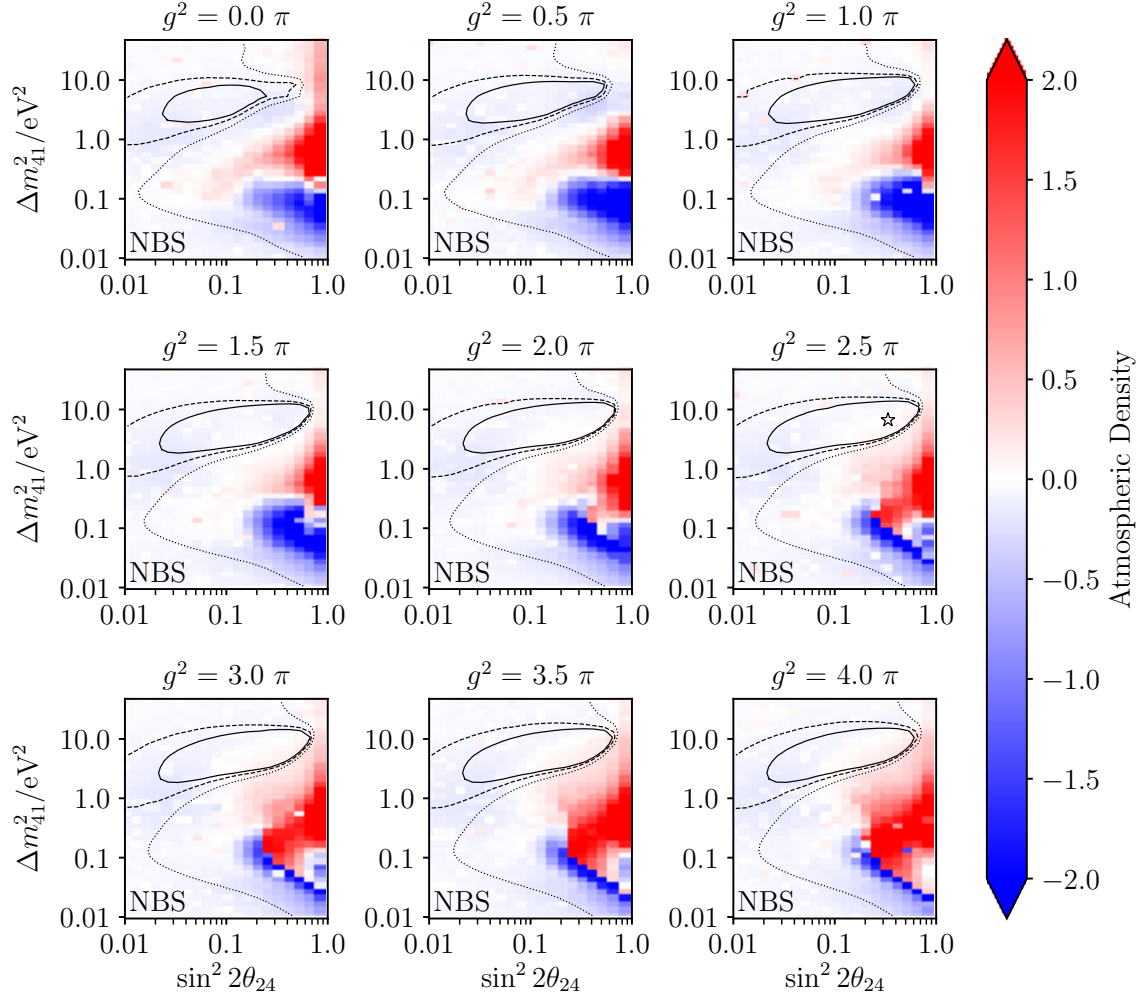


Figure B-9: The fit values of the atmospheric density nuisance parameter from the frequentist analysis across the entire physics space. The color scale limits correspond to $\pm 2\sigma$. “NBS” means that no bedrock systematic uncertainty was included in this analysis.

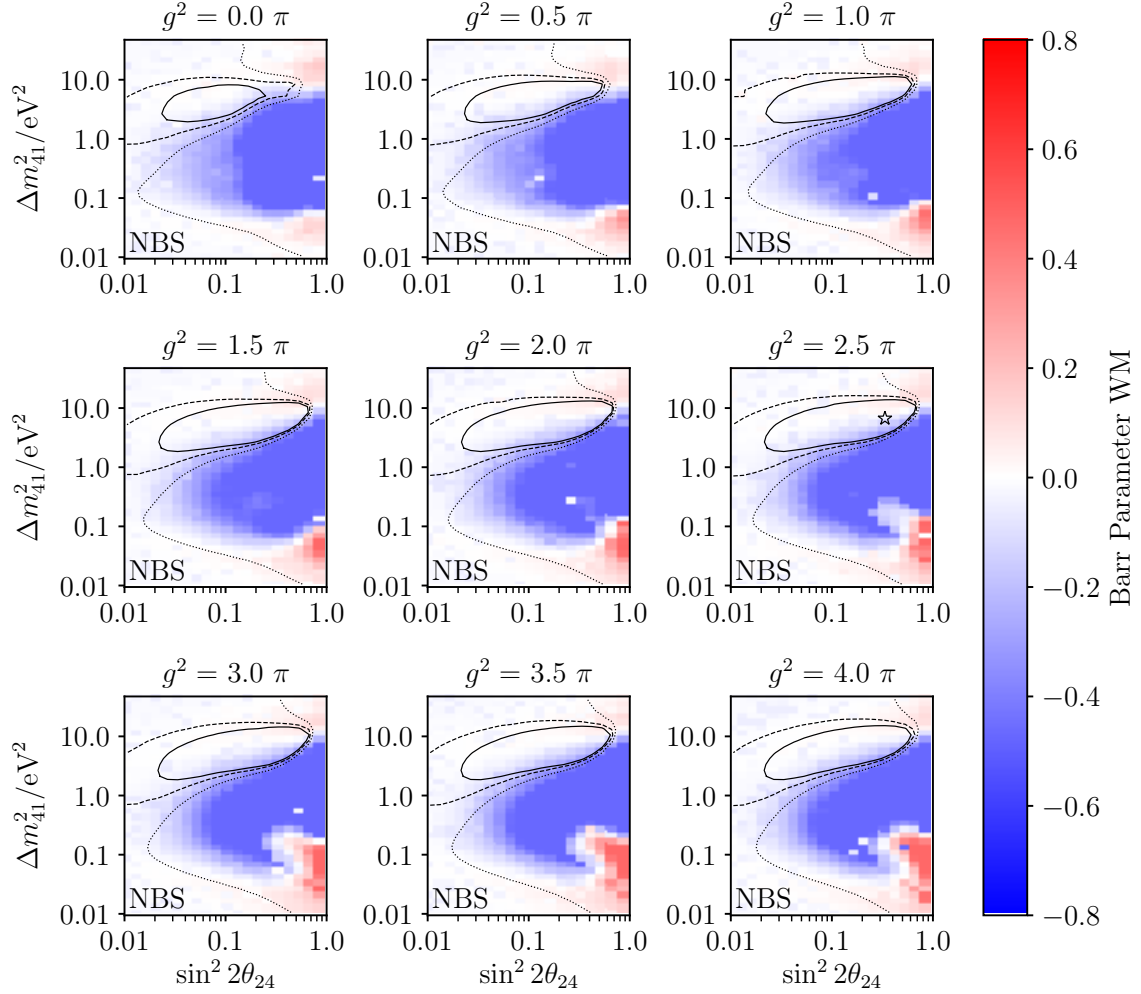


Figure B-10: The fit values of the Barr WM nuisance parameter from the frequentist analysis across the entire physics space. The color scale limits correspond to $\pm 2\sigma$. "NBS" means that no bedrock systematic uncertainty was included in this analysis.

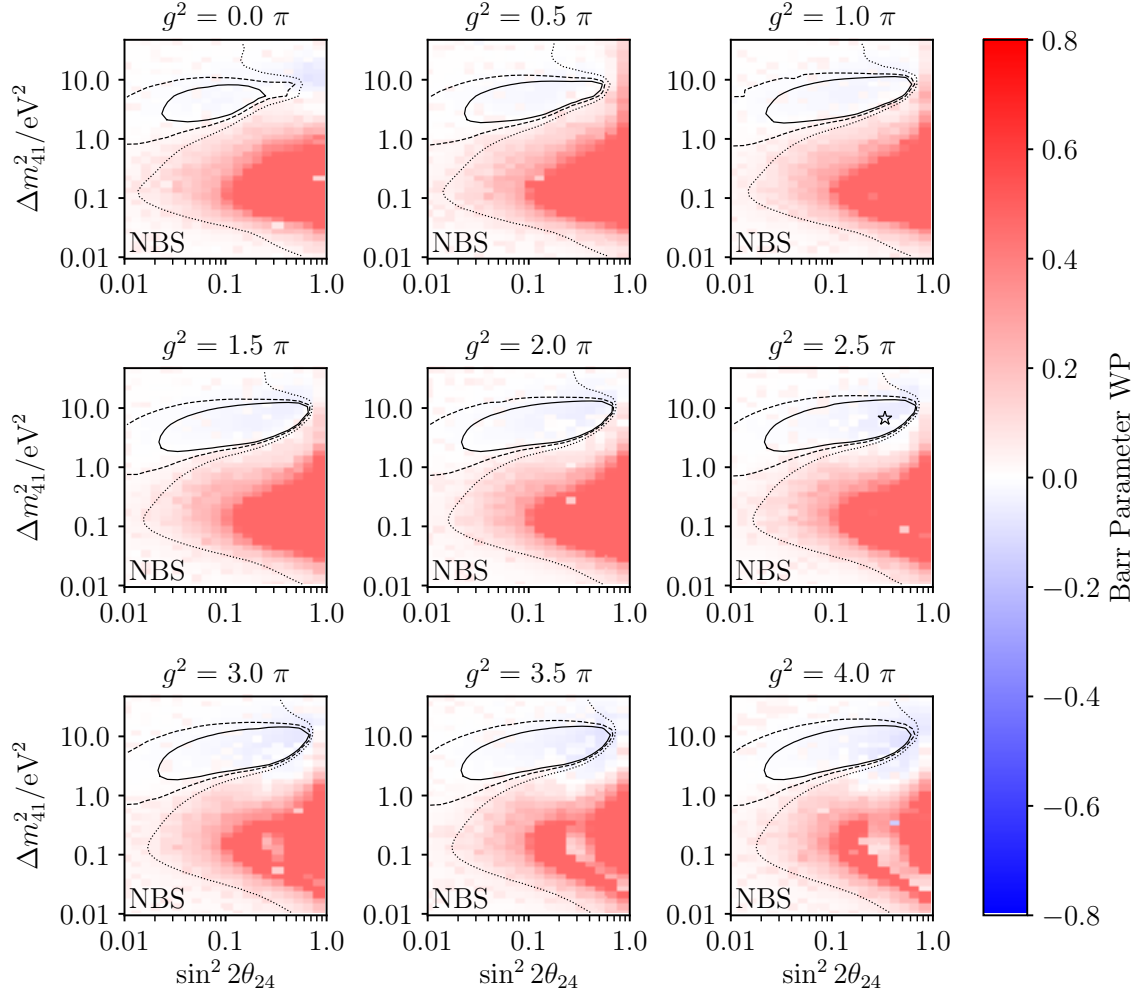


Figure B-11: The fit values of the Barr WP nuisance parameter from the frequentist analysis across the entire physics space. The color scale limits correspond to $\pm 2\sigma$. “NBS” means that no bedrock systematic uncertainty was included in this analysis.

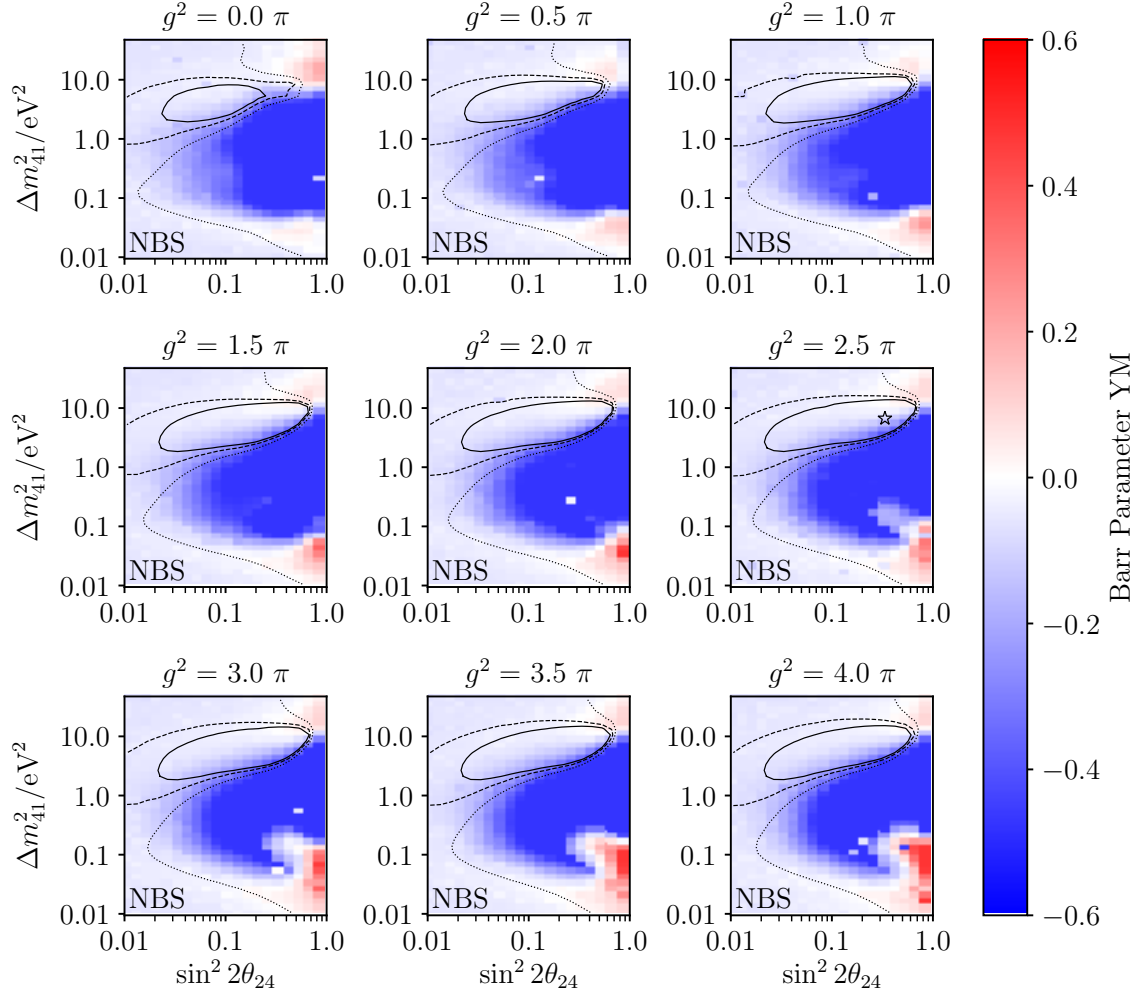


Figure B-12: The fit values of the Barr YM nuisance parameter from the frequentist analysis across the entire physics space. The color scale limits correspond to $\pm 2\sigma$. "NBS" means that no bedrock systematic uncertainty was included in this analysis.

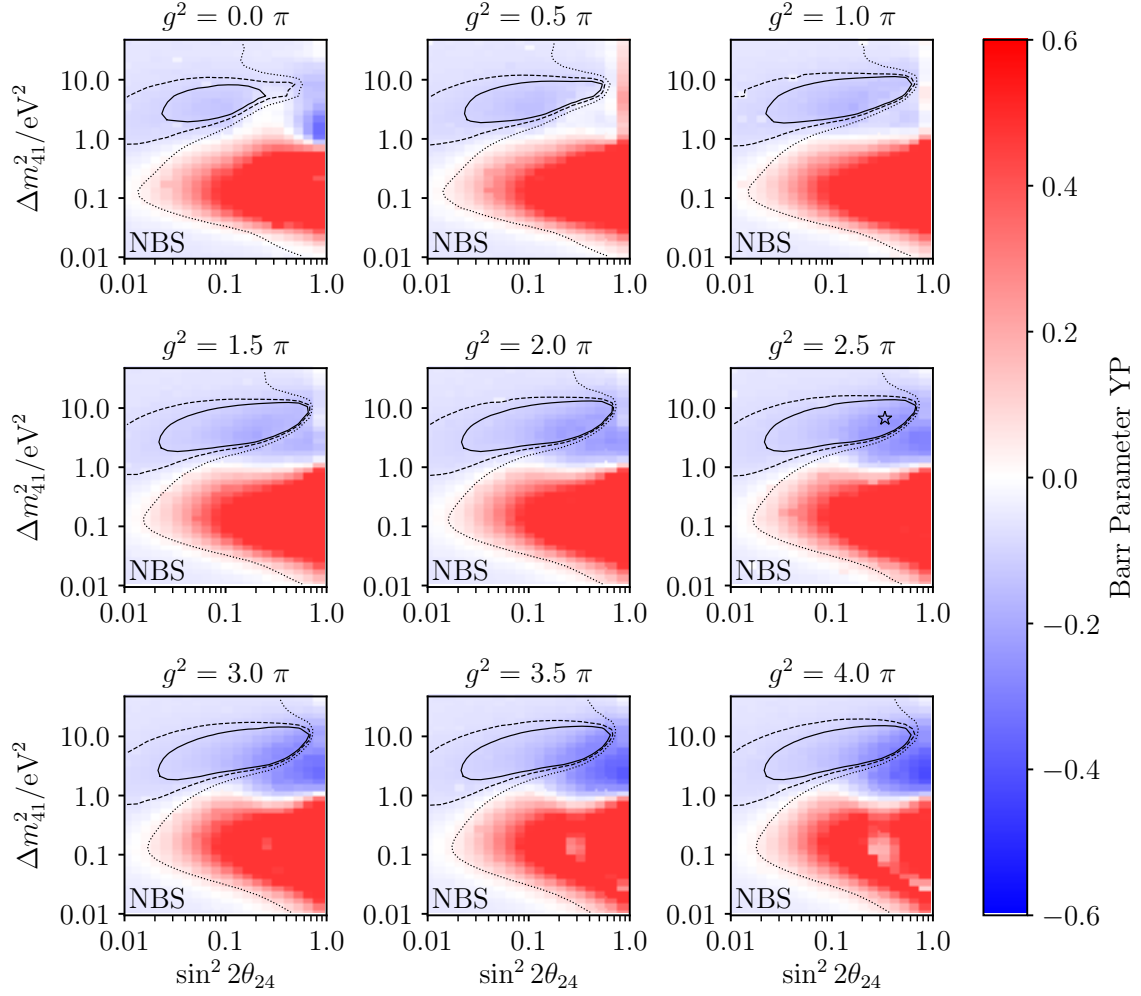


Figure B-13: The fit values of the Barr YP nuisance parameter from the frequentist analysis across the entire physics space. The color scale limits correspond to $\pm 2\sigma$. "NBS" means that no bedrock systematic uncertainty was included in this analysis.

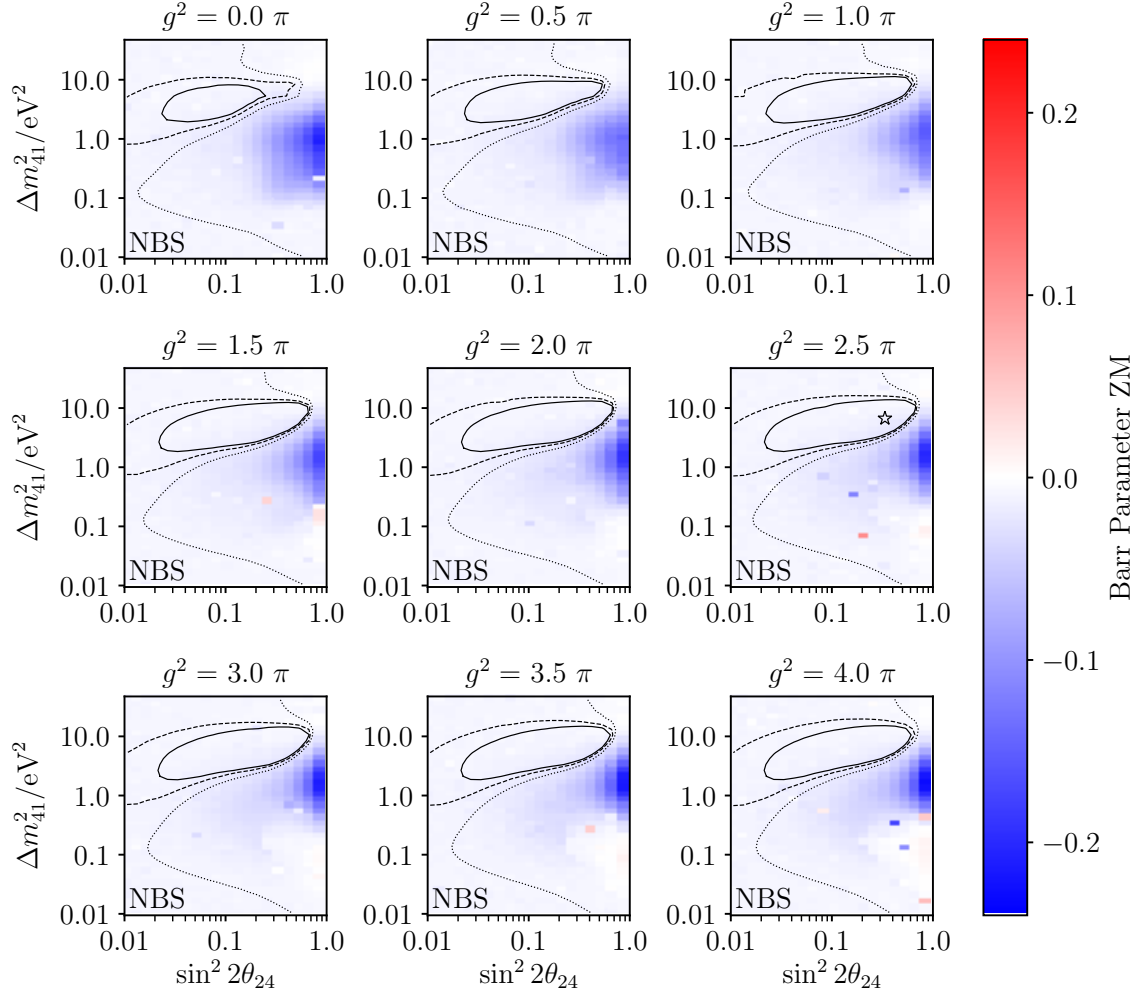


Figure B-14: The fit values of the Barr ZM nuisance parameter from the frequentist analysis across the entire physics space. The color scale limits correspond to $\pm 2\sigma$. "NBS" means that no bedrock systematic uncertainty was included in this analysis.

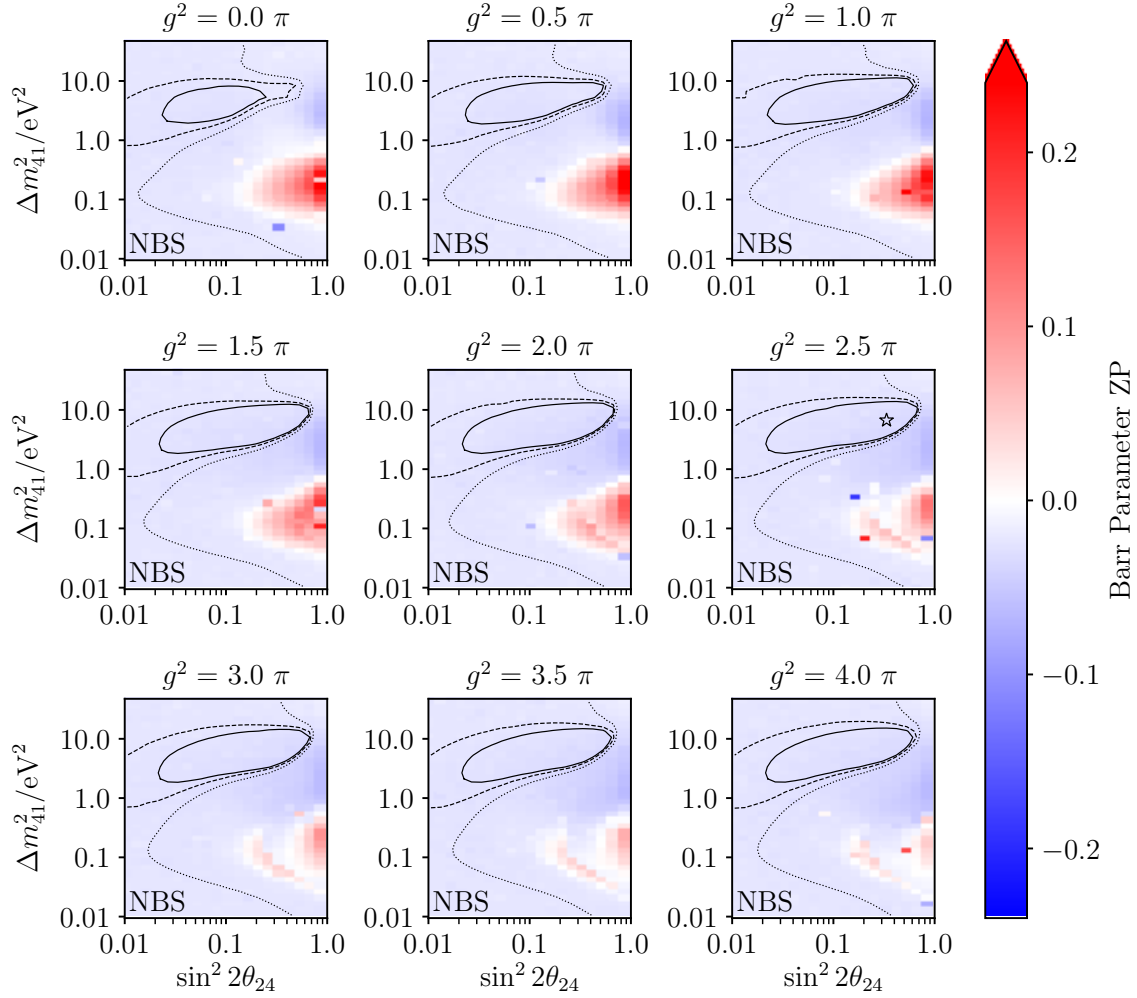


Figure B-15: The fit values of the Barr ZP nuisance parameter from the frequentist analysis across the entire physics space. The color scale limits correspond to $\pm 2\sigma$. "NBS" means that no bedrock systematic uncertainty was included in this analysis.

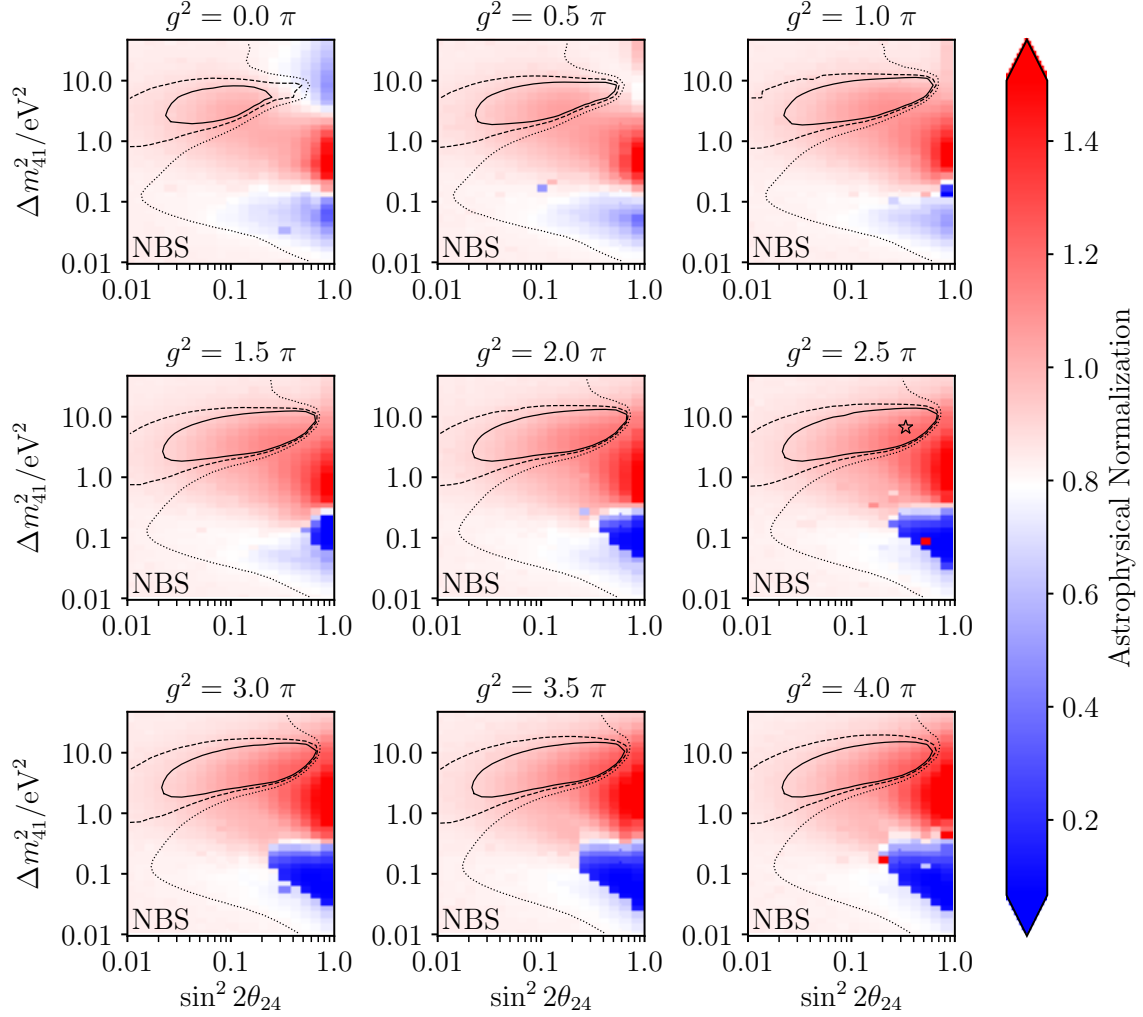


Figure B-16: The fit values of the astrophysical normalization nuisance parameter from the frequentist analysis across the entire physics space. The color scale limits correspond to $\pm 2\sigma$. “NBS” means that no bedrock systematic uncertainty was included in this analysis.

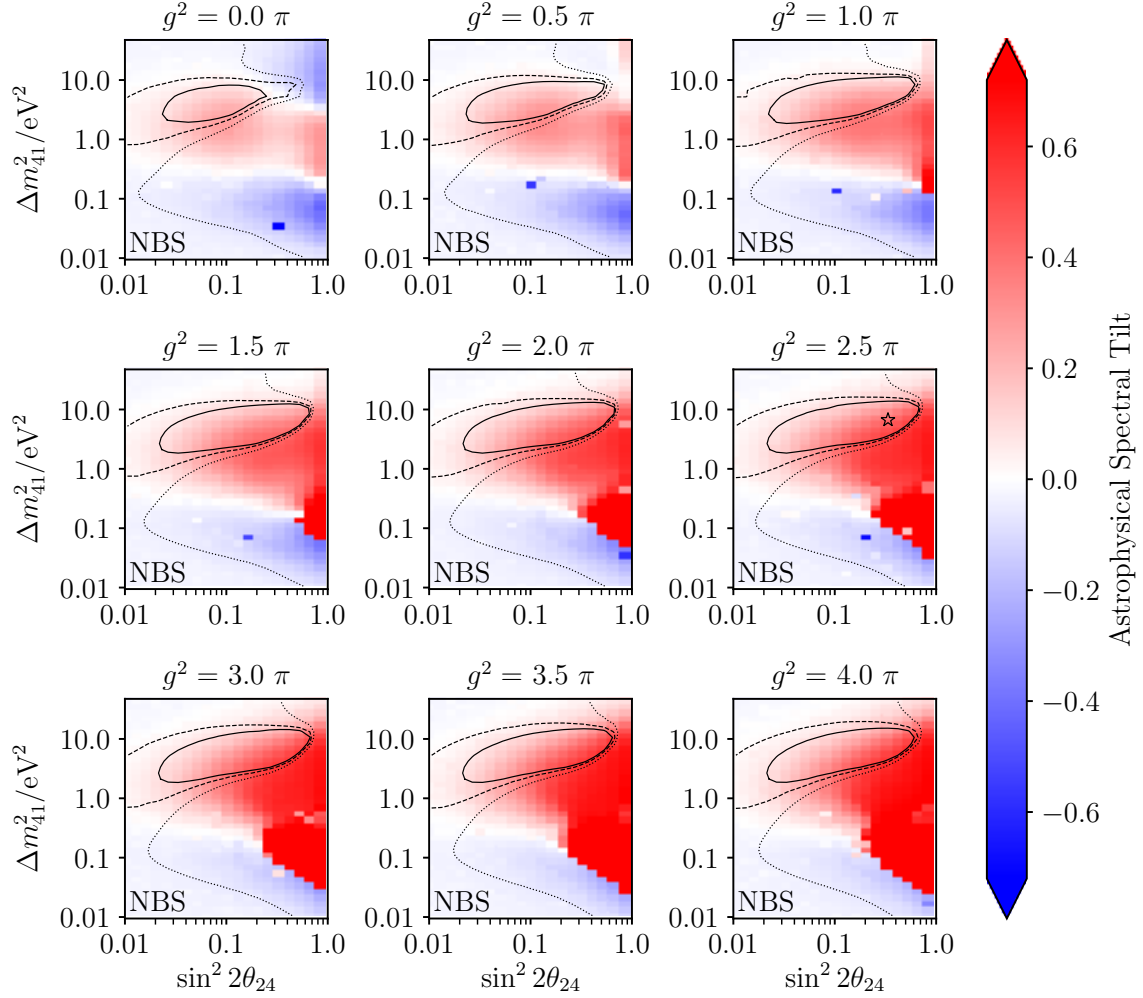


Figure B-17: The fit values of the astrophysical spectral tilt nuisance parameter from the frequentist analysis across the entire physics space. The color scale limits correspond to $\pm 2\sigma$. “NBS” means that no bedrock systematic uncertainty was included in this analysis.

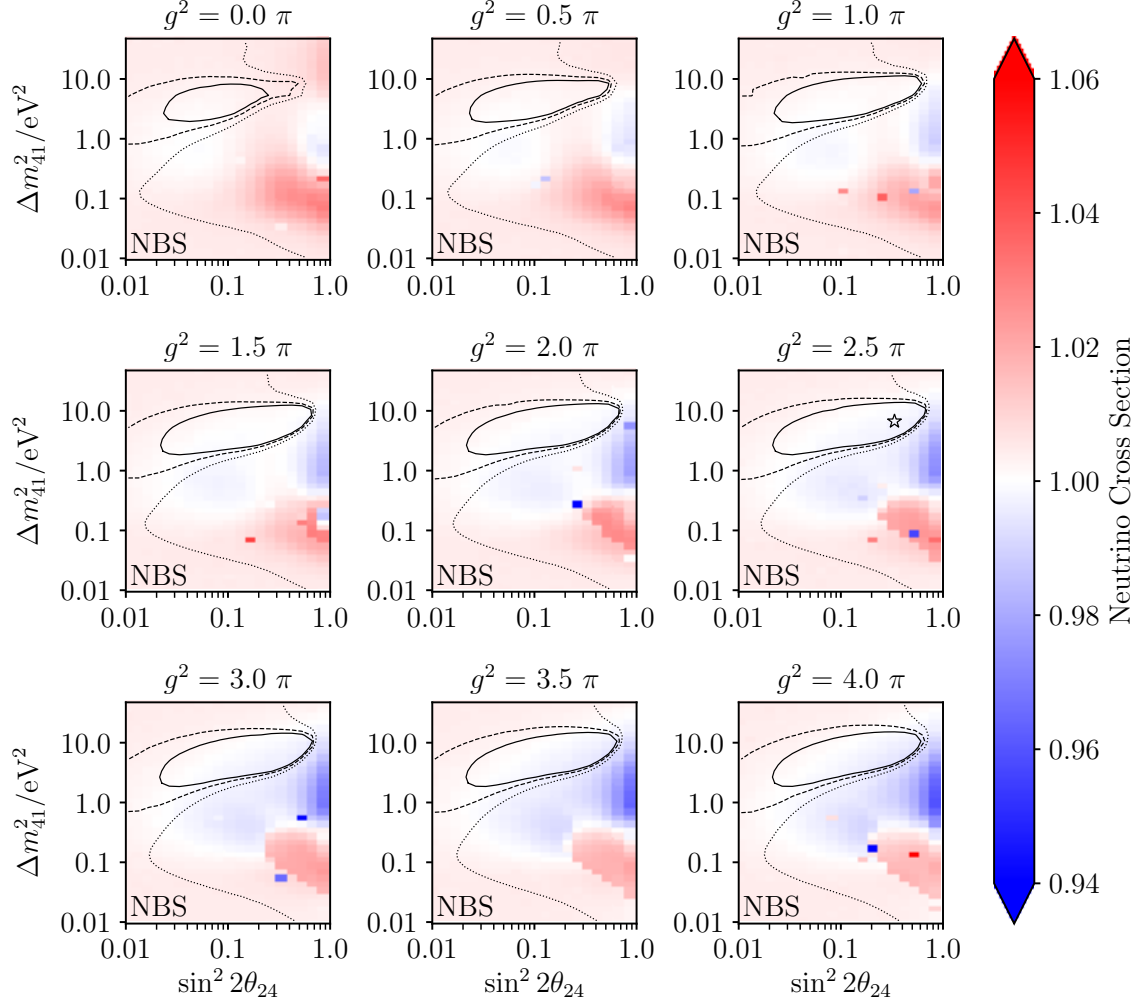


Figure B-18: The fit values of the neutrino cross section nuisance parameter from the frequentist analysis across the entire physics space. The color scale limits correspond to $\pm 1\sigma$. “NBS” means that no bedrock systematic uncertainty was included in this analysis.

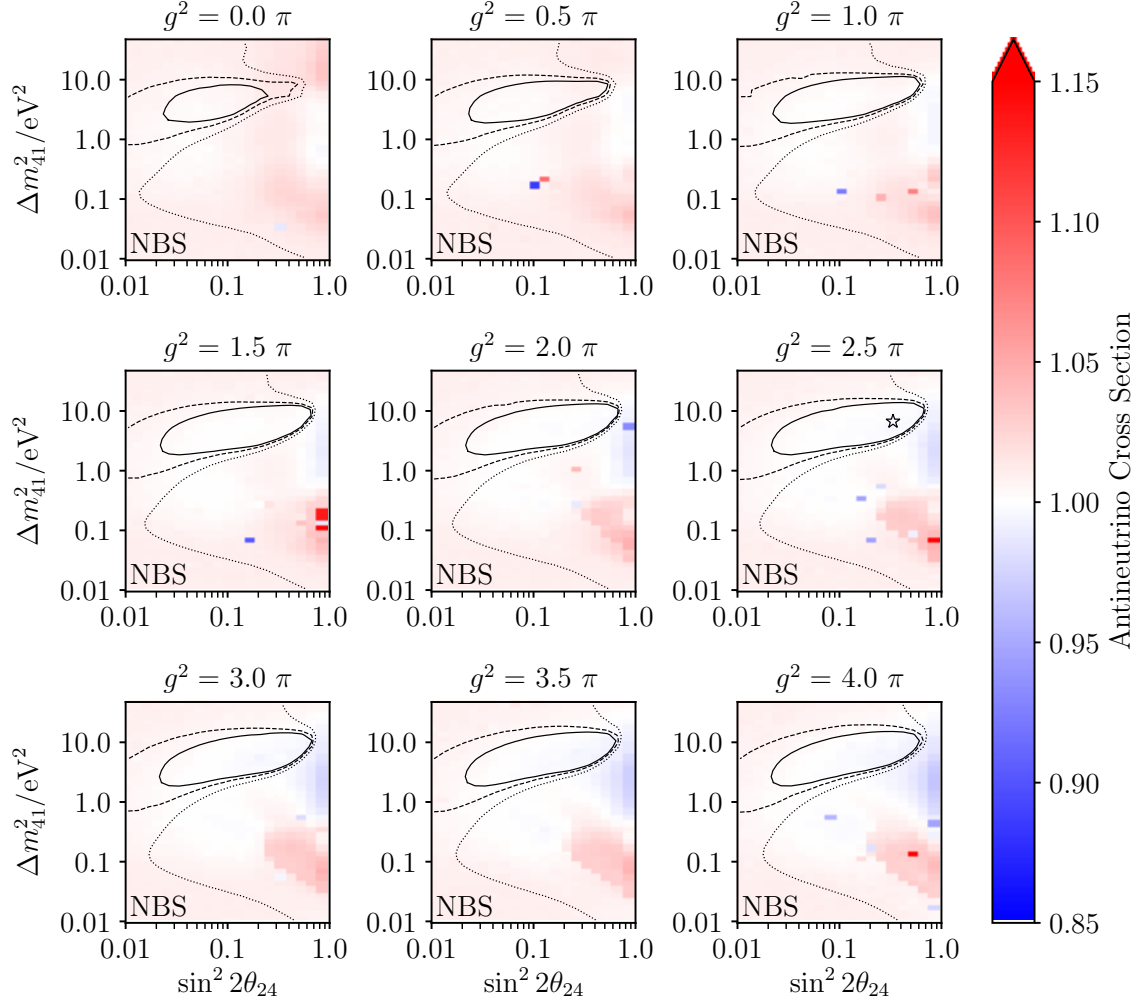


Figure B-19: The fit values of the antineutrino cross section nuisance parameter from the frequentist analysis across the entire physics space. The color scale limits correspond to $\pm 1\sigma$. "NBS" means that no bedrock systematic uncertainty was included in this analysis.

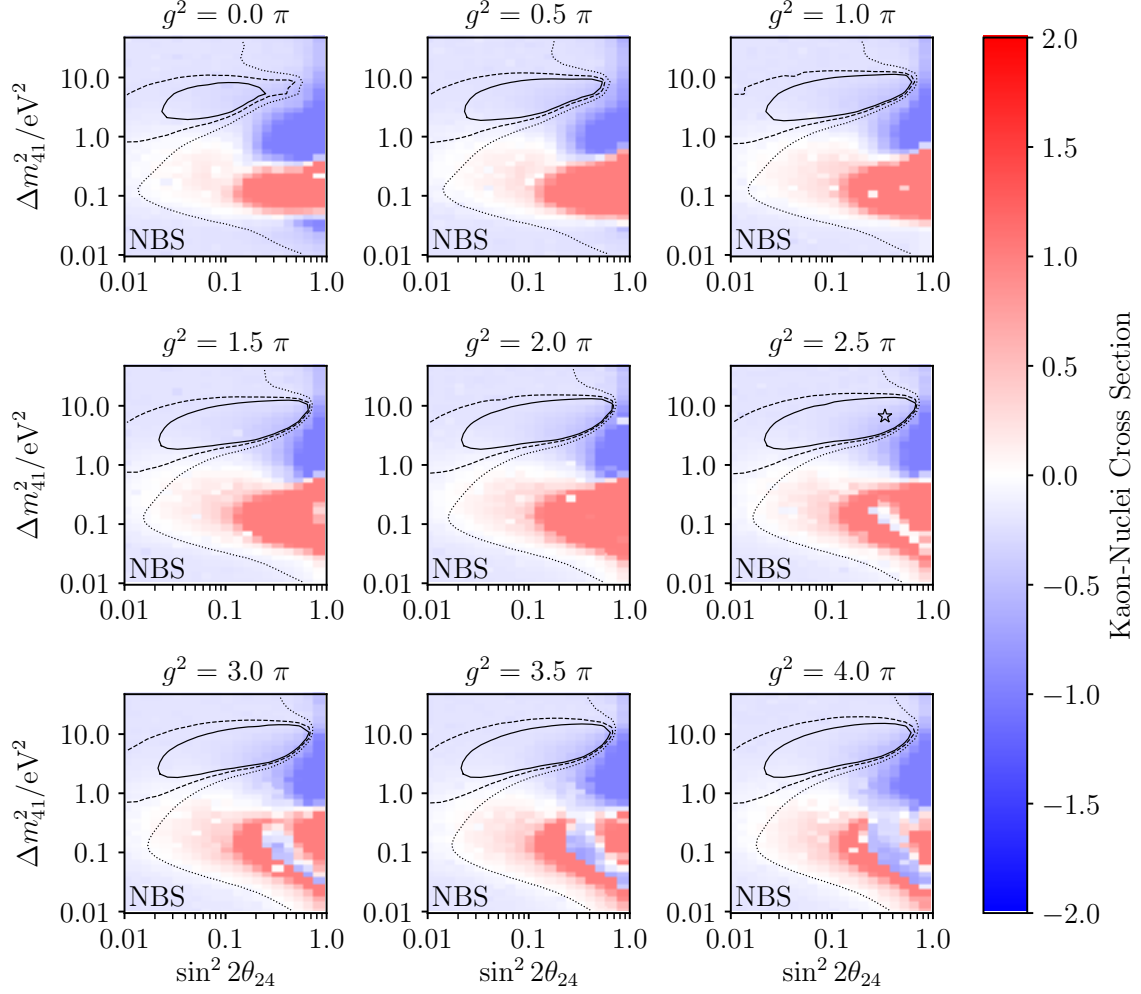


Figure B-20: The fit values of the kaon-nucleus cross section nuisance parameter from the frequentist analysis across the entire physics space. The color scale limits correspond to $\pm 1\sigma$. "NBS" means that no bedrock systematic uncertainty was included in this analysis.

Appendix C

MITPC

For completeness, this appendix describes work performed early in my doctoral studies on developing a novel neutron detector: the MIT/UMichigan Time Projection Chamber (MITPC). A helium and carbon tetrafluoride gaseous time projection chamber (TPC) with a CCD camera was developed and deployed at the Double Chooz experiment to measure the fast neutron background [161]. It was brought to Fermi National Accelerator Laboratory to measure the beam-induced neutron background on the Booster Neutrino Beamline; it ran in the SciBooNE enclosure. It was necessary to demonstrate that the detector could contain and reconstruct neutron-induced nuclear recoils at higher energies. This was done by replacing the neutron target, helium, with neon.

Demonstrating a directional detector based on neon for characterizing high energy neutrons

A. Hexley,^a M.H. Moulai,^a J. Spitz^{b,1} and J.M. Conrad^a

^a*Massachusetts Institute of Technology,
Cambridge, MA, 02139, U.S.A.*

^b*University of Michigan,
Ann Arbor, MI, 48109, U.S.A.*

E-mail: spitzj@umich.edu

ABSTRACT: MITPC is a gas-based time projection chamber used for detecting fast, MeV-scale neutrons. The standard version of the detector relies on a mixture of 600 torr gas composed of 87.5% ^4He and 12.5% CF_4 for precisely measuring the energy and direction of neutron-induced nuclear recoils. We describe studies performed with a prototype detector investigating the use of Ne, as a replacement for ^4He , in the gas mixture. Our discussion focuses on the advantages of Ne as the fast neutron target for high energy neutron events ($\lesssim 100\text{ MeV}$) and a demonstration that the mixture will be effective for this event class. We find that the achievable gain and transverse diffusion of drifting electrons in the Ne mixture are acceptable and that the detector uptime lost due to voltage breakdowns in the amplification plane is negligible, compared to $\sim 20\%$ with the ^4He mixture.

KEYWORDS: Neutron detectors (cold, thermal, fast neutrons); Particle tracking detectors (gaseous detectors)

Corresponding author.

Contents

1	Introduction	1
2	Configuration of the Detector	1
3	Neon Studies	4
3.1	Motivation	4
3.2	Reconstruction of High Energy Neutrons	5
3.3	Spark Rate	6
4	Conclusion	7

1 Introduction

The MIT and Michigan Time Projection Chamber (MITPC) is a directional fast neutron detector which relies on a CCD camera and the TPC technique for creating a three dimensional image of neutron-induced nuclear recoils within a gaseous volume. The detector ran for over a year at Double Chooz, a reactor-based neutrino experiment in France, under the name “Double Chooz Time Projection Chamber” (DCTPC), and is now installed in the Booster Neutrino Beamline (BNB) in the SciBooNE Enclosure at Fermi National Accelerator Laboratory (FNAL), where it will begin taking beam data in Fall 2015. Fast, MeV-scale neutrons represent a significant background for, among others, neutrinoless double beta decay, solar neutrino, reactor neutrino, coherent neutrino, and WIMP measurements. MITPC is designed to characterize neutron backgrounds, measuring rate as a function of energy, direction, depth underground, and rainfall [1]. MITPC can also be used to study fast neutron backgrounds in beam-based neutrino experiments. These neutrons, produced via neutrino interactions with materials in or around the detectors, are a background for a number of important neutrino processes, including low energy charged current and neutral current elastic scattering [2]. Further, understanding neutrino-induced neutrons as a function of neutrino energy, Q^2 , etc. is important for future oscillation and neutrino cross section measurements (see, e.g., ref. [3]). Neutrons usually represent missing energy in neutrino event reconstruction and it is and will be important to quantify this effect for the precise neutrino calorimetry that current and future cross section and oscillation measurements depend on. A number of experiments will study this topic specifically [4–6]. Informing these experiments, especially those using the BNB, about the energy and directionality of neutrino- and beam-related (“skyshine”) neutrons is MITPC’s main goal.

2 Configuration of the Detector

Two DCTPC detectors were constructed for use at Double Chooz: a prototype detector (2.8L) [1] and a full-size detector (originally 60L, now 40L). A paper describing the results of the DCTPC

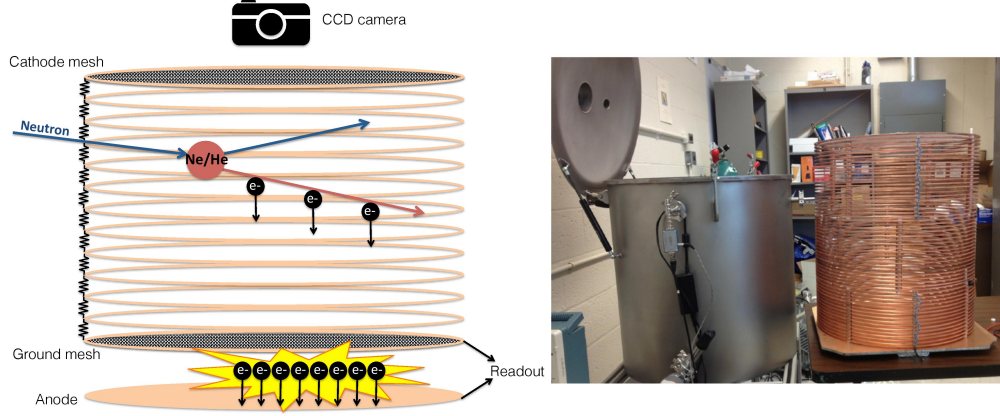


Figure 1. Left: a schematic of a neutron event occurring inside the detector. Right: the full size detector’s field cage next to the vacuum vessel.

run at Double Chooz is in preparation. MITPC is the reconfigured 40 L detector installed at FNAL. Here, we provide a brief description of MITPC to facilitate discussions of the Ne measurements performed with the prototype detector.

The TPC consists of a copper field cage, a cathode mesh, and an amplification plane placed in a vessel filled with gas. The field cage is located directly above the amplification plane, which consists of a copper anode plate and stainless-steel ground mesh separated by 0.4 mm. The gas composition is 87.5% of either ^4He (DCTPC at Double Chooz) or Ne (MITPC at FNAL), and 12.5% CF_4 . The CF_4 acts as the scintillator and quencher for the electron avalanche, while the ^4He or Ne acts as the primary neutron target. The gas is held at 600 torr.

The amplification plane is imaged by a CCD camera (U6 model made by Apogee Instruments Inc., featuring a Kodak KAF-1001E 1024×1024 pixel CCD chip) and charge is read out from both the anode and ground mesh. In the prototype detector used for the Ne studies, the field cage height (maximum drift distance) is 10 cm, the amplification plane is 24.7 cm in diameter, and the CCD camera images an area of $16.7 \text{ cm} \times 16.7 \text{ cm}$ in the center of the amplification plane. The reconstruction of events is described below and diagrammed in figure 1 (left).

When a fast neutron enters the detector and interacts with a target nucleus, the nucleus recoils and ionizes the surrounding gas, leaving a track in its wake. Electrons drift through the 150 V/cm electric field of the field cage between the cathode mesh and amplification plane, until they reach the latter. The electrons enter the amplification plane, a high field ($\sim 1750 \text{ V/mm}$) region between the ground mesh and the anode, and rapidly accelerate to create an ionization avalanche in the region of the track. The cascade produces a light signal that is imaged by the CCD and the charge in time is simultaneously collected by the anode and mesh planes via a set of preamplifiers.

A coincident signal on the three readouts (CCD, anode, and mesh) is considered an event. The 3D length of the event track is reconstructed by timing the difference between the start and end of the track arriving at the ground mesh, shown in figure 4 (bottom). The vertical length of the track is found after combining this information with the known drift velocity in the chamber. The length of the track on the CCD readout, the “CCD range”, is the 2D horizontal length of the track.

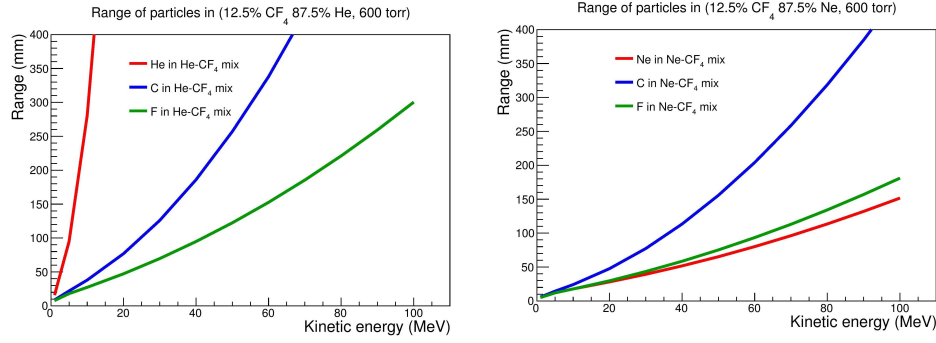


Figure 2. The relationship between range and kinetic energy for nuclei travelling through the He-based mixture (left) and Ne-based mixture (right), according to the SRIM software [7].

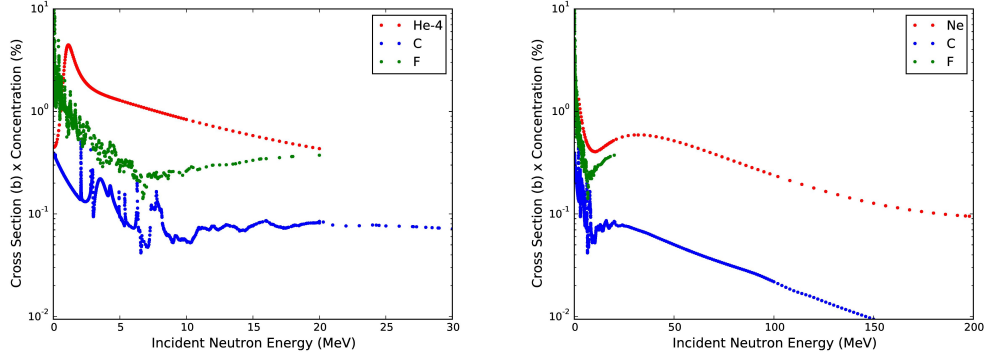


Figure 3. The neutron elastic interaction cross section (weighted by concentration in the gas mixture employed) versus neutron energy for the relevant target nuclei and energy ranges in the ⁴He gas mixture (left) and Ne gas mixture (right).

Using the SRIM software package, the results of which are shown in figure 2, we reconstruct the energy of the track based on its 3D length [7]. For reference, the energy resolution in the ⁴He mixture configuration is about 2% at a nuclear recoil energy of 5 MeV. As we are only able to fully reconstruct events that are fully contained inside the detector, any track that crosses the edge of the CCD imaging area is rejected from consideration.

The energy loss profile of a track can help in identifying the recoiling nucleus, but it is important to understand the expected neutron event rate on each target in the gas mixtures considered. The neutron elastic interaction cross sections (weighted by concentration in the gas mixture) as a function of incident neutron energy for ⁴He, Ne, C, and F nuclei are shown in figure 3 [8, 9]. The neutron-Ne elastic cross section surpasses ⁴He at about 15 MeV. In general, ⁴He/Ne dominates the interaction rate, as compared to CF₄, across the energy region of interest. The expected event rate on a ⁴He target is a factor of at least 2.5 greater than CF₄ in the neutron energy range 1–10 MeV. The ⁴He/CF₄ ratio begins to decrease after 10 MeV but is still at 1.4 at 15 MeV. Similarly, the Ne rate dominates over C; the ratio of Ne/C is ~ 10 across the neutron energy range 50–150 MeV. There is no F data available in this energy region. While the range vs. energy behavior is quite similar for Ne and F

nuclei, it may be possible to use a combination of calorimetry and track length in differentiating between the dE/dx curves in figure 2 (right). Even if this is not possible, however, one should remember that the ratio of Ne to F nuclei in the detector is 7 : 1.

3 Neon Studies

3.1 Motivation

The neutrons measured by DCTPC at Double Chooz originated from cosmic ray and radioactive sources. DCTPC was therefore tuned to accept neutron-induced nuclear recoils in the energy range 0.2–20 MeV. The neutrons of most interest at FNAL, however, are beam-induced neutrons which tend to be more energetic. The expected neutrino-induced neutron energy in the BNB ($\langle E_\nu \rangle = 0.8$ GeV) was studied using a Geant4- and GENIE-based simulation [10, 11] and found to be $\lesssim 400$ MeV. In this higher energy range, most relevant for the BNB, the large majority of neutron-induced ^4He nucleus recoils are not expected to be fully contained. The SRIM software package [7] results for the expected range as a function of nuclear recoil energy on the relevant nuclei are shown in figure 2. To fully contain a larger fraction of event tracks, we must use an element heavier than ^4He , which will tend to travel a shorter distance in the gas medium. We therefore have turned to heavier noble gases to act as the fast neutron target for MITPC running at FNAL.

Signal-to-noise, especially in consideration of the CCD signal, is an important aspect of this detection technology. Electron diffusion, drift velocity, amplification plane gain, impurity content, recombination, and electron attachment can all affect signal-to-noise. While each of these is relevant for the Ne study outlined here, our concern, and therefore our focus, has been on electron diffusion and the resulting potential signal-to-noise decrease. The relevant literature suggests that electrons diffuse significantly more in noble gases heavier than ^4He [12], since the momentum transfer cross section is lower for these heavy atoms. Importantly, however, mixing noble elements with CF_4 is known to improve diffusion significantly (see, e.g., ref. [13]). Increased transverse diffusion reduces a CCD track’s “brightness” (signal-to-noise ratio, nominally at $\sim 10 : 1$, with the CCD readout noise of $\sim 10\text{ e}^-$ RMS at 1 MHz dominating the sources of image noise) and can significantly jeopardize detector efficiency and energy resolution. Among the noble elements, Ne is expected to have the least diffusion after ^4He , so we chose it for our initial studies in searching for an adequate heavy target for the characterization of high energy neutrons.

A high gain is required in MITPC because the camera’s readout noise is significant (10 e^- RMS) and the focal length is 72 cm. Given the geometry and typical energy deposited, an $\sim 10^5$ amplified alpha track, for example, only produces about 100 e^- per CCD bin, resulting in a signal-to-noise of $\sim 10 : 1$. Track reconstruction, in consideration of direction and calorimetry, begins to suffer when the signal-to-noise drops below this level.

We ran tests comparing a Ne/ CF_4 mixture to a $^4\text{He}/\text{CF}_4$ mixture using the prototype detector at MIT. The objectives of our study were threefold: to study the diffusion in Ne, to determine whether we could obtain sufficient gain for high efficiency event reconstruction in MITPC, and to test the spark rate in the amplification plane. An ^{241}Am alpha source (4.4 MeV) was inserted into the center of the prototype detector 6.2 cm from the amplification plane. We ran tests with both Ne and ^4He

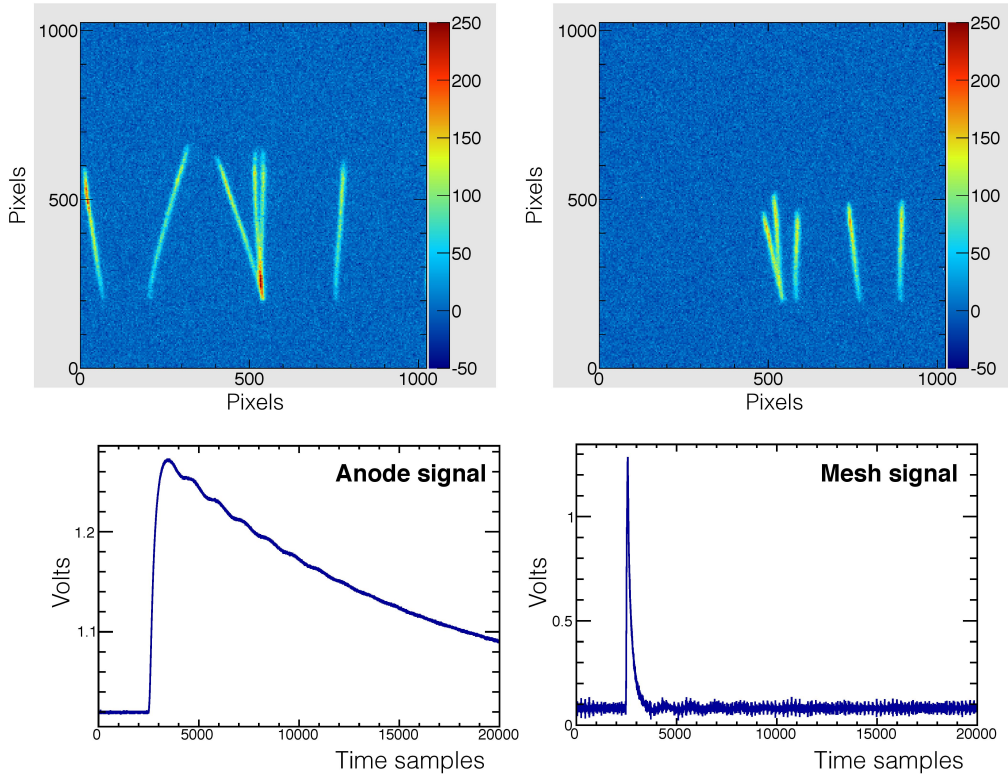


Figure 4. ^{241}Am alpha tracks in the ^4He (left) and Ne mixtures (right). The Z-axis is indicative of the “CCD weight” or brightness. The Bragg peaks, indicative of the alphas’ direction, are clearly visible. The resolution in the prototype detector is 0.16 mm/pixel. Bottom: example waveforms associated with a single alpha track, as seen by the mesh and anode conductors. The anode’s preamplifier has a significantly longer rise time than the mesh’s (1 ns). One time sample corresponds to 4 ns.

using a 600 torr gas mixture with a concentration fraction of 87.5% fast neutron target (^4He or Ne) and 12.5% CF_4 .

3.2 Reconstruction of High Energy Neutrons

Figure 4 shows CCD readout images of characteristic tracks in both the ^4He and Ne gas mixtures. It was immediately apparent that, in the Ne gas mixture, the track length was shorter and the slightly increased electron transverse diffusion would not compromise event reconstruction. The gain required to fully reconstruct events is also acceptable. Each image has multiple tracks because the alpha source was highly active and events often pile-up during readout. The waveforms associated with the signal can also be seen in figure 4. The timing information provides the extent of the track in the drift dimension.

The ^{241}Am source was very active, so while the camera exposure was 20 ms, its minimum value, multiple tracks occurred during each exposure. Due to a lack of shutter, the CCD remained exposed during readout. Events captured during readout can appear shifted horizontally, but actually originated at the source [1].

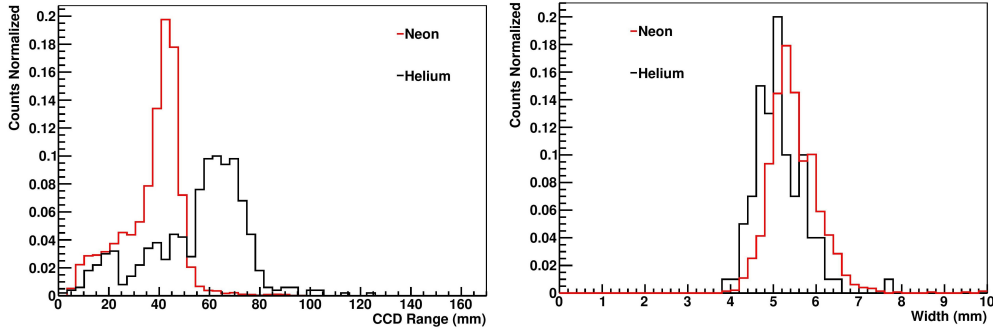


Figure 5. Left: the CCD range of tracks in the ^4He and Ne gas mixtures. Right: the characteristic track widths in the two mixtures.

As anticipated, figure 5 shows the significantly shorter CCD range of tracks in Ne compared to tracks in ^4He . The average track length in the ^4He mixture is 52% greater than in the Ne mixture. This, compounded with the fact that neutron-induced Ne recoils are significantly shorter than neutron-induced ^4He recoils, will allow MITPC to fully contain and reconstruct more energetic nuclear recoils ($\lesssim 100$ MeV). The track range as a function of kinetic energy for the relevant nuclei in the gas mixtures can be seen in figure 2. The characteristic energy loss as a function of distance can also be considered more desirable in the Ne mixture, as compared to the ^4He mixture, given that radiogenic alpha backgrounds can contribute significantly to event rate. Radiogenic alphas and neutron-induced ^4He recoils have identical energy loss profiles.

The transverse diffusion in pure Ne is expected to be about 4 times greater than that in ^4He , given MITPC’s typical drift field of ~ 150 V/cm and pressure of 600 torr [12], although the addition of CF_4 will reduce the size of the effect. As shown in figure 5, we found that the track width, related to transverse diffusion, in the Ne mixture (given a drift distance of 6.2 cm) was about 9% larger than with the ^4He mixture. In consideration of the full drift distance in MITPC (32 cm), the increased width neither compromises event reconstruction nor reduces the signal-to-noise ratio below an acceptable level.

3.3 Spark Rate

Voltage breakdowns (sparks) in the amplification plane occur frequently because the anode plate and ground mesh are 0.440 mm apart, with a potential difference of ~ 700 V between them. This high electric field is necessary in order to achieve the gain ($\sim 10^5$) required for viewing tracks with the CCD camera. The minimum signal-to-noise requirement for maximizing the CCD track reconstruction abilities is $\sim 10 : 1$. After a spark, data collection ceases for about 10 s to allow for the power supply and preamps to stabilize, for the anode to recharge and stabilize, and for hot pixels in the CCD camera, which can be created by very bright sparks, to dissipate. The downtime of 10 s is an empirically determined value. Lower spark rates are therefore desirable because they reduce downtime.

This plot was created with a cut on the CCD range of tracks, eliminating the low energy tails seen in the left plot in figure 5. This ensured that the tracks considered for the width measurement were parallel to the amplification plane, and therefore consistent with each other in terms of range and drift distance.

The spark rate with Ne mixture was found to be negligible. This can be compared to the $\sim 20\%$ downtime due to sparks experienced with the ^4He mixture. The reason for the lower spark rate is twofold. First, we were able to obtain sufficient gain with Ne while running at a lower voltage than we could with ^4He (680 V vs. 710 V). Second, Paschen’s law (see, e.g., ref. [14]) shows that the breakdown voltage for Ne is higher than that of ^4He at these operating conditions.

4 Conclusion

In conclusion, we find that filling the MITPC detector with a gas composition of 87.5% Ne and 12.5% CF_4 at 600 torr will allow the energy and directional reconstruction of neutron events up to 100 MeV and possibly higher. This is the nuclear recoil energy range expected for neutrino- and beam-induced neutrons at the BNB at FNAL. We find that the diffusion of electrons and the signal-to-noise observed in the Ne mixture is acceptable, and will not compromise event reconstruction. The spark rate in the Ne mixture was found to be negligible, and will improve the detector uptime by about 20%, as compared to ^4He running. The success of these tests serves as a demonstration that Ne is an optimal fast-neutron target for characterizing the energy and direction of 10 s-of-MeV neutrons using the TPC technology described. MITPC will begin running in the Ne configuration with beam data in October, 2015.

Acknowledgments

We have collaborated closely with J. Dawson and A. Houlier on the construction, running, and analysis of DCTPC. This work, to be published, has informed this result. We also thank Z. Moss and B.J.P. Jones for carefully reading this paper. The authors were supported by NSF-PHY-1505855.

References

- [1] J. Lopez, K. Terao, J.M. Conrad, D. Dujmic and L. Winslow, *A Prototype Detector for Directional Measurement of the Cosmogenic Neutron Flux*, *Nucl. Instrum. Meth. A* **673** (2012) 22 [[arXiv:1108.4894](#)].
- [2] MINIBOONE collaboration, A.A. Aguilar-Arevalo et al., *Measurement of the Neutrino Neutral-Current Elastic Differential Cross Section on Mineral Oil at $E_\nu \sim 1$ GeV*, *Phys. Rev. D* **82** (2010) 092005 [[arXiv:1007.4730](#)].
- [3] A.M. Ankowski, O. Benhar, P. Coloma, P. Huber, C.-M. Jen, C. Mariani et al., *Comparison of the calorimetric and kinematic methods of neutrino energy reconstruction in disappearance experiments*, *Phys. Rev. D* **92** (2015) 073014 [[arXiv:1507.08560](#)].
- [4] ANNIE collaboration, I. Anghel et al., *Letter of Intent: The Accelerator Neutrino Neutron Interaction Experiment (ANNIE)*, [arXiv:1504.01480](#).
- [5] C. Adams et al., *LArI-ND: Testing Neutrino Anomalies with Multiple LAr TPC Detectors at Fermilab*, FERMILAB-PROPOSAL-1053 (2013).
- [6] H. Chen et al., *Proposal for a New Experiment Using the Booster and NuMI Neutrino Beamlines: MicroBooNE*, FERMILAB-PROPOSAL-0974 (2007).

- [7] J.F. Ziegler, J.P. Biersack and U. Littmark, *The Stopping and Range of Ions in Matter*, Pergamon Press, 1985. SRIM and TRIM code available at <http://www.srim.org>.
- [8] National Nuclear Data Center, Brookhaven National Laboratory, *Sigma Evaluated Nuclear Data file (ENDF) Retrieval & Plotting*, December 2011. <http://www.nndc.bnl.gov/sigma/>.
- [9] *Evaluated Nuclear Data File, ENDF*, <https://www-nds.iaea.org/exfor/endl.htm>.
- [10] GEANT4 collaboration, S. Agostinelli et al., *GEANT4: A Simulation toolkit*, *Nucl. Instrum. Meth. A* **506** (2003) 250.
- [11] C. Andreopoulos et al., *The GENIE Neutrino Monte Carlo Generator*, *Nucl. Instrum. Meth. A* **614** (2010) 87 [[arXiv:0905.2517](https://arxiv.org/abs/0905.2517)].
- [12] E. Aprile, A.E. Bolotnikov, A.I. Bolozdynya and T. Doke, *Noble Gas Detectors*, Wiley-VCH (2006), table 3.1, p. 37.
- [13] H. Tomita, *Detector development for direction-sensitive dark matter research*, PhD thesis, Boston University (2011).
- [14] L.F. Berzak, S.E. Dorfman and S.P. Smith, *Paschen's Law in Air and Noble Gases* (2006) http://www-eng.lbl.gov/~shuman/XENON/REFERENCES&OTHER_MISC/paschen_report.pdf.



The work in this thesis was supported by the National Science Foundation.

Bibliography

- [1] D. Griffiths, *Introduction to elementary particles*. 2008.
- [2] M. Thomson, *Modern particle physics*. New York: Cambridge University Press, 2013.
- [3] C. Giunti and C. W. Kim, *Fundamentals of Neutrino Physics and Astrophysics*. 2007.
- [4] P. Zyla *et al.*, “Review of Particle Physics,” *PTEP*, vol. 2020, no. 8, p. 083C01, 2020.
- [5] J. Ellis, “TikZ-Feynman: Feynman diagrams with TikZ,” *Comput. Phys. Commun.*, vol. 210, pp. 103–123, 2017.
- [6] E. Akhmedov, “Quantum mechanics aspects and subtleties of neutrino oscillations,” in *International Conference on History of the Neutrino: 1930-2018*, 2019.
- [7] I. Esteban, M. Gonzalez-Garcia, M. Maltoni, T. Schwetz, and A. Zhou, “The fate of hints: updated global analysis of three-flavor neutrino oscillations,” *JHEP*, vol. 09, p. 178, 2020.
- [8] P. de Salas, D. Forero, S. Gariazzo, P. Martínez-Miravé, O. Mena, C. Ternes, M. Tórtola, and J. Valle, “2020 Global reassessment of the neutrino oscillation picture,” 6 2020.
- [9] F. Capozzi, E. Lisi, A. Marrone, and A. Palazzo, “Current unknowns in the three neutrino framework,” *Prog. Part. Nucl. Phys.*, vol. 102, pp. 48–72, 2018.
- [10] C. A. Argüelles Delgado, J. Salvado, and C. N. Weaver, “A simple quantum integro-differential solver (squids),” *Computer Physics Communications*, vol. 196, pp. 569 – 591, 2015.
- [11] C. A. Argüelles Delgado, J. Salvado, and C. N. Weaver, “nuSQuIDS,” 2015. <https://github.com/Arguelles/nuSQuIDS>.
- [12] J. M. Conrad, W. C. Louis, and M. H. Shaevitz, “The LSND and MiniBooNE Oscillation Searches at High Δm^2 ,” *Ann. Rev. Nucl. Part. Sci.*, vol. 63, pp. 45–67, 2013.

- [13] C. Athanassopoulos *et al.*, “The Liquid scintillator neutrino detector and LAMPF neutrino source,” *Nucl. Instrum. Meth. A*, vol. 388, pp. 149–172, 1997.
- [14] A. Aguilar-Arevalo *et al.*, “Evidence for neutrino oscillations from the observation of $\bar{\nu}_e$ appearance in a $\bar{\nu}_\mu$ beam,” *Phys. Rev. D*, vol. 64, p. 112007, 2001.
- [15] R. Burman, M. Potter, and E. Smith, “Monte carlo simulation of neutrino production by medium-energy protons in a beam stop,” *Nuclear Instruments and Methods in Physics Research Section A: Accelerators, Spectrometers, Detectors and Associated Equipment*, vol. 291, no. 3, pp. 621 – 633, 1990.
- [16] R. Burman, A. Dodd, and P. Plischke, “Neutrino flux calculations for the isis spallation neutron facility,” *Nuclear Instruments and Methods in Physics Research Section A: Accelerators, Spectrometers, Detectors and Associated Equipment*, vol. 368, no. 2, pp. 416 – 424, 1996.
- [17] A. Aguilar-Arevalo *et al.*, “Improved Search for $\bar{\nu}_\mu \rightarrow \bar{\nu}_e$ Oscillations in the MiniBooNE Experiment,” *Phys. Rev. Lett.*, vol. 110, p. 161801, 2013.
- [18] A. Aguilar-Arevalo *et al.*, “Updated MiniBooNE Neutrino Oscillation Results with Increased Data and New Background Studies,” June 2020. arXiv:2006.16883.
- [19] D. Adey *et al.*, “Improved Measurement of the Reactor Antineutrino Flux at Daya Bay,” *Phys. Rev. D*, vol. 100, no. 5, p. 052004, 2019.
- [20] G. Mention, M. Fechner, T. Lasserre, T. A. Mueller, D. Lhuillier, M. Cribier, and A. Letourneau, “Reactor antineutrino anomaly,” *Phys. Rev. D*, vol. 83, p. 073006, Apr 2011.
- [21] T. A. Mueller *et al.*, “Improved Predictions of Reactor Antineutrino Spectra,” *Phys. Rev. C*, vol. 83, p. 054615, 2011.
- [22] P. Huber, “On the determination of anti-neutrino spectra from nuclear reactors,” *Phys. Rev. C*, vol. 84, p. 024617, 2011. [Erratum: *Phys.Rev.C* 85, 029901 (2012)].
- [23] C. Giunti, Y. F. Li, B. R. Littlejohn, and P. T. Surukuchi, “Diagnosing the Reactor Antineutrino Anomaly with Global Antineutrino Flux Data,” *Phys. Rev. D*, vol. 99, no. 7, p. 073005, 2019.
- [24] Z. Atif *et al.*, “Search for sterile neutrino oscillation using RENO and NEOS data,” 11 2020.
- [25] A. Diaz, C. A. Argüelles, G. H. Collin, J. M. Conrad, and M. H. Shaevitz, “Where Are We With Light Sterile Neutrinos?,” *Phys. Rept.*, vol. 884, pp. 1–59, 2020.

- [26] P. Huber, “NEOS Data and the Origin of the 5 MeV Bump in the Reactor Antineutrino Spectrum,” *Phys. Rev. Lett.*, vol. 118, no. 4, p. 042502, 2017.
- [27] P. Anselmann *et al.*, “First results from the Cr-51 neutrino source experiment with the GALLEX detector,” *Phys. Lett. B*, vol. 342, pp. 440–450, 1995.
- [28] W. Hampel *et al.*, “Final results of the Cr-51 neutrino source experiments in GALLEX,” *Phys. Lett. B*, vol. 420, pp. 114–126, 1998.
- [29] F. Kaether, W. Hampel, G. Heusser, J. Kiko, and T. Kirsten, “Reanalysis of the GALLEX solar neutrino flux and source experiments,” *Phys. Lett. B*, vol. 685, pp. 47–54, 2010.
- [30] D. N. Abdurashitov *et al.*, “The Russian-American gallium experiment (SAGE) Cr neutrino source measurement,” *Phys. Rev. Lett.*, vol. 77, pp. 4708–4711, 1996.
- [31] J. N. Abdurashitov *et al.*, “Measurement of the response of the Russian-American gallium experiment to neutrinos from a Cr-51 source,” *Phys. Rev. C*, vol. 59, pp. 2246–2263, 1999.
- [32] J. N. Abdurashitov *et al.*, “Measurement of the response of a Ga solar neutrino experiment to neutrinos from an Ar-37 source,” *Phys. Rev. C*, vol. 73, p. 045805, 2006.
- [33] J. N. Abdurashitov *et al.*, “Measurement of the solar neutrino capture rate with gallium metal. III: Results for the 2002–2007 data-taking period,” *Phys. Rev. C*, vol. 80, p. 015807, 2009.
- [34] J. Kostensalo, J. Suhonen, C. Giunti, and P. C. Srivastava, “The gallium anomaly revisited,” *Phys. Lett. B*, vol. 795, pp. 542–547, 2019.
- [35] J. Kopp, P. A. N. Machado, M. Maltoni, and T. Schwetz, “Sterile Neutrino Oscillations: The Global Picture,” *JHEP*, vol. 05, p. 050, 2013.
- [36] K. N. Abazajian *et al.*, “Light Sterile Neutrinos: A White Paper,” 4 2012.
- [37] J. Barry, W. Rodejohann, and H. Zhang, “Light Sterile Neutrinos: Models and Phenomenology,” *JHEP*, vol. 07, p. 091, 2011.
- [38] M. Dentler, A. Hernández-Cabezudo, J. Kopp, P. A. N. Machado, M. Maltoni, I. Martinez-Soler, and T. Schwetz, “Updated Global Analysis of Neutrino Oscillations in the Presence of eV-Scale Sterile Neutrinos,” *JHEP*, vol. 08, p. 010, 2018.
- [39] S. Gariazzo, C. Giunti, M. Laveder, and Y. F. Li, “Updated Global 3+1 Analysis of Short-BaseLine Neutrino Oscillations,” *JHEP*, vol. 06, p. 135, 2017.

- [40] M. Maltoni, T. Schwetz, M. A. Tortola, and J. W. F. Valle, “Ruling out four neutrino oscillation interpretations of the LSND anomaly?,” *Nucl. Phys. B*, vol. 643, pp. 321–338, 2002.
- [41] M. Maltoni and T. Schwetz, “Testing the statistical compatibility of independent data sets,” *Phys. Rev. D*, vol. 68, p. 033020, 2003.
- [42] L. Wolfenstein, “Neutrino oscillations in matter,” *Physical Review D*, vol. 17, no. 9, p. 2369, 1978.
- [43] S. Mikheyev and A. Y. Smirnov, “Resonant amplification of ν oscillations in matter and solar-neutrino spectroscopy,” *Il Nuovo Cimento C*, vol. 9, no. 1, pp. 17–26, 1986.
- [44] Q. Liu, S. Mikheyev, and A. Y. Smirnov, “Parametric resonance in oscillations of atmospheric neutrinos?,” *Physics Letters B*, vol. 440, no. 3-4, pp. 319–326, 1998.
- [45] E. K. Akhmedov, “Parametric resonance in neutrino oscillations in matter,” *Pramana*, vol. 54, no. 1, pp. 47–63, 2000.
- [46] E. K. Akhmedov, “Neutrino physics,” in *ICTP Summer School in Particle Physics*, pp. 103–164, 6 1999.
- [47] H. Nunokawa, O. L. G. Peres, and R. Zukanovich Funchal, “Probing the LSND mass scale and four neutrino scenarios with a neutrino telescope,” *Phys. Lett. B*, vol. 562, pp. 279–290, 2003.
- [48] S. Choubey, “Signature of sterile species in atmospheric neutrino data at neutrino telescopes,” *JHEP*, vol. 12, p. 014, 2007.
- [49] S. Razzaque and A. Y. Smirnov, “Searching for sterile neutrinos in ice,” *JHEP*, vol. 07, p. 084, 2011.
- [50] M. Aartsen *et al.*, “Evidence for Astrophysical Muon Neutrinos from the Northern Sky with IceCube,” *Phys. Rev. Lett.*, vol. 115, no. 8, p. 081102, 2015.
- [51] B. J. Jones, *Sterile Neutrinos in Cold Climates*. PhD thesis, MIT, 2015.
- [52] C. A. Argüelles, *New physics with atmospheric neutrinos*. PhD thesis, The University of Wisconsin-Madison, 2015.
- [53] M. G. Aartsen *et al.*, “Searches for Sterile Neutrinos with the IceCube Detector,” *Phys. Rev. Lett.*, vol. 117, no. 7, p. 071801, 2016.
- [54] S. N. G. Axani, *Sterile Neutrino Searches at the IceCube Neutrino Observatory*. PhD thesis, MIT, 2019.

- [55] M. G. Aartsen *et al.*, “eV-Scale Sterile Neutrino Search Using Eight Years of Atmospheric Muon Neutrino Data from the IceCube Neutrino Observatory,” *Phys. Rev. Lett.*, vol. 125, no. 14, p. 141801, 2020.
- [56] M. G. Aartsen *et al.*, “Searching for eV-scale sterile neutrinos with eight years of atmospheric neutrinos at the IceCube Neutrino Telescope,” *Phys. Rev. D*, vol. 102, no. 5, p. 052009, 2020.
- [57] H. Jeffreys, *The Theory of Probability*. Oxford Classic Texts in the Physical Sciences, 1939.
- [58] P. B. Pal and L. Wolfenstein, “Radiative decays of massive neutrinos,” *Phys. Rev. D*, vol. 25, pp. 766–773, Feb 1982.
- [59] J. F. Nieves, “Two-photon decays of heavy neutrinos,” *Phys. Rev. D*, vol. 28, pp. 1664–1670, Oct 1983.
- [60] S. Palomares-Ruiz, S. Pascoli, and T. Schwetz, “Explaining LSND by a decaying sterile neutrino,” *JHEP*, vol. 09, p. 048, 2005.
- [61] S. Palomares-Ruiz, “Sterile neutrino decay and the LSND experiment,” *J. Phys. Conf. Ser.*, vol. 39, pp. 307–309, 2006.
- [62] Z. Moss, M. H. Moulai, C. A. Argüelles, and J. M. Conrad, “Exploring a nonminimal sterile neutrino model involving decay at IceCube,” *Phys. Rev. D*, vol. 97, no. 5, p. 055017, 2018.
- [63] M. H. Moulai, C. A. Argüelles, G. H. Collin, J. M. Conrad, A. Diaz, and M. H. Shaevitz, “Combining Sterile Neutrino Fits to Short Baseline Data with IceCube Data,” *Phys. Rev. D*, vol. 101, no. 5, p. 055020, 2020.
- [64] M. Aartsen *et al.*, “The IceCube Neutrino Observatory: Instrumentation and Online Systems,” *JINST*, vol. 12, no. 03, p. P03012, 2017.
- [65] R. Abbasi *et al.*, “The Design and Performance of IceCube DeepCore,” *Astropart. Phys.*, vol. 35, pp. 615–624, 2012.
- [66] R. Abbasi, Y. Abdou, T. Abu-Zayyad, J. Adams, J. Aguilar, M. Ahlers, K. Andeen, J. Auffenberg, X. Bai, M. Baker, and et al., “Calibration and characterization of the icecube photomultiplier tube,” *Nuclear Instruments and Methods in Physics Research Section A: Accelerators, Spectrometers, Detectors and Associated Equipment*, vol. 618, p. 139–152, Jun 2010.
- [67] M. Aartsen *et al.*, “Measurement of South Pole ice transparency with the IceCube LED calibration system,” *Nucl. Instrum. Meth. A*, vol. 711, pp. 73–89, 2013.

- [68] J. Lundberg, P. Miocinovic, T. Burgess, J. Adams, S. Hundertmark, P. Desiati, K. Woschnagg, and P. Niessen, “Light tracking for glaciers and oceans: Scattering and absorption in heterogeneous media with Photonics,” *Nucl. Instrum. Meth. A*, vol. 581, pp. 619–631, 2007.
- [69] M. Ackermann *et al.*, “Optical properties of deep glacial ice at the South Pole,” *J. Geophys. Res.*, vol. 111, no. D13, p. D13203, 2006.
- [70] M. Aartsen *et al.*, “The IceCube Neutrino Observatory Part VI: Ice Properties, Reconstruction and Future Developments,” in *33rd International Cosmic Ray Conference*, 9 2013.
- [71] D. Chirkin and M. Rongen, “Light diffusion in birefringent polycrystals and the IceCube ice anisotropy,” *PoS*, vol. ICRC2019, p. 854, 2020.
- [72] R. C. Bay, R. A. Rohde, P. B. Price, and N. E. Bramall, “South pole paleowind from automated synthesis of ice core records,” *Journal of Geophysical Research: Atmospheres*, vol. 115, no. D14, 2010.
- [73] G. Mie, “Beiträge zur optik trüber medien, speziell kolloidaler metallösungen,” *Annalen der Physik*, vol. 330, no. 3, pp. 377–445, 1908.
- [74] J. Formaggio and G. Zeller, “From eV to EeV: Neutrino Cross Sections Across Energy Scales,” *Rev. Mod. Phys.*, vol. 84, pp. 1307–1341, 2012.
- [75] R. Gandhi, C. Quigg, M. H. Reno, and I. Sarcevic, “Ultrahigh-energy neutrino interactions,” *Astropart. Phys.*, vol. 5, pp. 81–110, 1996.
- [76] M. Aartsen *et al.*, “Measurements using the inelasticity distribution of multi-TeV neutrino interactions in IceCube,” *Phys. Rev. D*, vol. 99, no. 3, p. 032004, 2019.
- [77] J. M. Conrad, M. H. Shaevitz, and T. Bolton, “Precision measurements with high-energy neutrino beams,” *Rev. Mod. Phys.*, vol. 70, pp. 1341–1392, 1998.
- [78] A. Cooper-Sarkar, P. Mertsch, and S. Sarkar, “The high energy neutrino cross-section in the Standard Model and its uncertainty,” *JHEP*, vol. 08, p. 042, 2011.
- [79] D. E. Groom, N. V. Mokhov, and S. I. Striganov, “Muon stopping power and range tables 10-MeV to 100-TeV,” *Atom. Data Nucl. Data Tabl.*, vol. 78, pp. 183–356, 2001.
- [80] J.-H. Koehne, K. Frantzen, M. Schmitz, T. Fuchs, W. Rhode, D. Chirkin, and J. Becker Tjus, “Proposal: A tool for propagation of charged leptons,” *Computer Physics Communications*, vol. 184, no. 9, pp. 2070 – 2090, 2013.

- [81] J. van Santen, *Neutrino Interactions in IceCube above 1 TeV: Constraints on Atmospheric Charmed-Meson Production and Investigation of the Astrophysical Neutrino Flux with 2 Years of IceCube Data taken 2010–2012*. PhD thesis, Wisconsin U., Madison, 11 2014.
- [82] C. Weaver, *Evidence for Astrophysical Muon Neutrinos from the Northern Sky*. PhD thesis, Wisconsin U., Madison, 2015.
- [83] M. Aartsen *et al.*, “Energy Reconstruction Methods in the IceCube Neutrino Telescope,” *JINST*, vol. 9, p. P03009, 2014.
- [84] T. K. Gaisser, R. Engel, and E. Resconi, *Cosmic rays and particle physics*. Cambridge University Press, 2016.
- [85] CERN, “Cosmic rays: particles from outer space.” <https://home.cern/science/physics/cosmic-rays-particles-outer-space>.
- [86] A. Fedynitch, R. Engel, T. K. Gaisser, F. Riehn, and T. Stanev, “Calculation of conventional and prompt lepton fluxes at very high energy,” *EPJ Web Conf.*, vol. 99, p. 08001, 2015.
- [87] A. Fedynitch, J. B. Tjus, and P. Desiati, “Influence of hadronic interaction models and the cosmic ray spectrum on the high energy atmospheric muon and neutrino flux,” *Physical Review D*, vol. 86, no. 11, p. 114024, 2012.
- [88] P. Gondolo, G. Ingelman, and M. Thunman, “Charm production and high-energy atmospheric muon and neutrino fluxes,” *Astropart. Phys.*, vol. 5, pp. 309–332, 1996.
- [89] R. Engel, A. Fedynitch, T. Gaisser, F. Riehn, and T. Stanev, “Charm production in sibyll,” *EPJ Web of Conferences*, vol. 99, 02 2015.
- [90] J. R. Hoerandel, “On the knee in the energy spectrum of cosmic rays,” *Astropart. Phys.*, vol. 19, pp. 193–220, 2003.
- [91] T. K. Gaisser, “Spectrum of cosmic-ray nucleons, kaon production, and the atmospheric muon charge ratio,” *Astropart. Phys.*, vol. 35, pp. 801–806, 2012.
- [92] V. Zatsepin and N. Sokolskaya, “Three component model of cosmic ray spectra from 10 gev to 100 pev,” *Astronomy and Astrophysics*, vol. 458, 01 2006.
- [93] O. Adriani *et al.*, “Pamela measurements of cosmic-ray proton and helium spectra,” *Science*, vol. 332, no. 6025, pp. 69–72, 2011.
- [94] M. Takeda, N. Sakaki, K. Honda, M. Chikawa, M. Fukushima, N. Hayashida, N. Inoue, K. Kadota, F. Kakimoto, K. Kamata, *et al.*, “Energy determination in the akeno giant air shower array experiment,” *Astroparticle Physics*, vol. 19, no. 4, pp. 447–462, 2003.

- [95] M. Nagano, T. Hara, Y. Hatano, N. Hayashida, S. Kawaguchi, K. Kamata, T. Kifune, and Y. Mizumoto, “Energy spectrum of primary cosmic rays between 1014.5 and 1018 eV,” *Journal of Physics G: Nuclear Physics*, vol. 10, no. 9, p. 1295, 1984.
- [96] F. Arqueros *et al.*, “Energy spectrum and chemical composition of cosmic rays between 0.3-PeV and 10-PeV determined from the Cherenkov light and charged particle distributions in air showers,” *Astron. Astrophys.*, vol. 359, pp. 682–694, 2000.
- [97] D. Bird, S. Corbato, H. Dai, B. Dawson, J. Elbert, B. Emerson, K. Green, M. Huang, D. Kieda, M. Luo, *et al.*, “The cosmic-ray energy spectrum observed by the fly’s eye,” *The Astrophysical Journal*, vol. 424, pp. 491–502, 1994.
- [98] N. L. Grigorov, V. E. Nesterov, I. D. Rapoport, I. A. Savenko, and G. A. Skuridin, “Investigation of energy spectrum of primary cosmic particles with high and superhigh energies of space stations *proton*,” *Yad. Fiz.*, vol. 11, pp. 1058–1069, 1970. in Proceedings of the 12th International Conference on Cosmic Rays., Vol. 2 (Hobart, 1971) p. 206.
- [99] M. A. K. Glasmacher *et al.*, “The cosmic ray energy spectrum between 10^{14} -eV and 10^{16} -eV,” *Astropart. Phys.*, vol. 10, pp. 291–302, 1999.
- [100] R. U. Abbasi *et al.*, “First observation of the Greisen-Zatsepin-Kuzmin suppression,” *Phys. Rev. Lett.*, vol. 100, p. 101101, 2008.
- [101] K. Asakimori *et al.* in *Proceedings of 23rd International Cosmic Ray Conference*, p. 25, 1993.
- [102] K. Asakimori *et al.* in *Proceedings of 22nd International Cosmic Ray Conference*, p. 57 and 97, 1991.
- [103] W. D. Apel *et al.*, “Kneelike structure in the spectrum of the heavy component of cosmic rays observed with KASCADE-Grande,” *Phys. Rev. Lett.*, vol. 107, p. 171104, 2011.
- [104] T. Antoni *et al.*, “Kascade measurements of energy spectra for elemental groups of cosmic rays: Results and open problems,” *Astroparticle Physics*, vol. 24, no. 1, pp. 1–25, 2005.
- [105] T. Danilova in *Proceedings of 15th International Cosmic Ray Conference*, p. 129, 1977.
- [106] Y. Fomin *et al.* in *Proceedings of 22nd International Cosmic Ray Conference*, p. 85, 1991.
- [107] Y. Tsunesada, “Highlights from Telescope Array,” in *32nd International Cosmic Ray Conference*, 11 2011.

- [108] M. Amenomori *et al.*, “The All-particle spectrum of primary cosmic rays in the wide energy range from 10^{14} eV to 10^{17} eV observed with the Tibet-III air-shower array,” *Astrophys. J.*, vol. 678, pp. 1165–1179, 2008.
- [109] M. Amenomori *et al.*, “The Cosmic ray energy spectrum between $10^{14.5}$ -eV and $10^{16.3}$ -eV covering the ‘knee’ region,” *Astrophys. J.*, vol. 461, pp. 408–414, 1995.
- [110] F. Riehn, H. P. Dembinski, R. Engel, A. Fedynitch, T. K. Gaisser, and T. Stanev, “The hadronic interaction model SIBYLL 2.3c and Feynman scaling,” *PoS*, vol. ICRC2017, p. 301, 2018.
- [111] F. Riehn, R. Engel, A. Fedynitch, T. K. Gaisser, and T. Stanev, “A new version of the event generator Sibyll,” *PoS*, vol. ICRC2015, p. 558, 2016.
- [112] T. Pierog, I. Karpenko, J. Katzy, E. Yatsenko, and K. Werner, “EPOS LHC: Test of collective hadronization with data measured at the CERN Large Hadron Collider,” *Phys. Rev. C*, vol. 92, no. 3, p. 034906, 2015.
- [113] S. Ostapchenko, “Monte Carlo treatment of hadronic interactions in enhanced Pomeron scheme: I. QGSJET-II model,” *Phys. Rev. D*, vol. 83, p. 014018, 2011.
- [114] D. d’Enterria, R. Engel, T. Pierog, S. Ostapchenko, and K. Werner, “Constraints from the first LHC data on hadronic event generators for ultra-high energy cosmic-ray physics,” *Astropart. Phys.*, vol. 35, pp. 98–113, 2011.
- [115] Pierog, Tanguy, “Hadronic interactions and air showers: Where do we stand?,” *EPJ Web Conf.*, vol. 208, p. 02002, 2019.
- [116] S. Robbins, “Atmospheric Neutrino Predictions and the Influence of Hadron Production,” 2004. Presented on 22 Sep 2004.
- [117] G. D. Barr, T. K. Gaisser, S. Robbins, and T. Stanev, “Uncertainties in Atmospheric Neutrino Fluxes,” *Phys. Rev.*, vol. D74, p. 094009, 2006.
- [118] A. Fedynitch, H. P. Dembinski, R. Engel, T. Gaisser, F. Riehn, and T. Stanev, “A state-of-the-art calculation of atmospheric lepton fluxes,” in *Proceedings of 35th International Cosmic Ray Conference — PoS(ICRC2017)*, vol. 301, p. 1019, 2017.
- [119] J.-P. Yáñez, A. Fedynitch, and T. Montgomery, “Calibration of atmospheric neutrino flux calculations using cosmic muon flux and charge ratio measurements,” in *Proceedings of 36th International Cosmic Ray Conference — PoS(ICRC2019)*, vol. 358, p. 881, 2019.
- [120] G. L. W. H. Collin, *Neutrinos, neurons and neutron stars: applications of new statistical and analysis techniques to particle and astrophysics*. PhD thesis, MIT, 2018.

- [121] Jet Propulsion Laboratory , “AIRS/AMSU/HSB Version 6 Level 3 Product User Guide,” *Version 1.2*, November 2014.
- [122] A. Bhattacharya, R. Enberg, M. H. Reno, I. Sarcevic, and A. Stasto, “Perturbative charm production and the prompt atmospheric neutrino flux in light of RHIC and LHC,” *JHEP*, vol. 06, p. 110, 2015.
- [123] M. e. Aartsen, M. Ackermann, J. Adams, J. Aguilar, M. Ahlers, M. Ahrens, D. Altmann, T. Anderson, C. Argüelles, T. Arlen, *et al.*, “Observation of high-energy astrophysical neutrinos in three years of icecube data,” *Physical review letters*, vol. 113, no. 10, p. 101101, 2014.
- [124] R. Abbasi *et al.*, “The IceCube high-energy starting event sample: Description and flux characterization with 7.5 years of data,” 11 2020.
- [125] M. Aartsen, K. Abraham, M. Ackermann, J. Adams, J. Aguilar, M. Ahlers, M. Ahrens, D. Altmann, K. Andeen, T. Anderson, *et al.*, “Observation and characterization of a cosmic muon neutrino flux from the northern hemisphere using six years of icecube data,” *The Astrophysical Journal*, vol. 833, no. 1, p. 3, 2016.
- [126] A. Schneider, “Characterization of the Astrophysical Diffuse Neutrino Flux with IceCube High-Energy Starting Events,” vol. ICRC2019, p. 1004, 2020.
- [127] Stachurska, Juliana, “Icecube high energy starting events at 7.5 years - new measurements of flux and flavor,” vol. 207, p. 02005, 2019.
- [128] F. Halzen and D. Saltzberg, “Tau neutrino appearance with a 1000 megaparsec baseline,” *Phys. Rev. Lett.*, vol. 81, pp. 4305–4308, Nov 1998.
- [129] A. M. Dziewonski and D. L. Anderson, “Preliminary reference earth model,” *Physics of the Earth and Planetary Interiors*, vol. 25, no. 4, pp. 297–356, 1981.
- [130] M. G. Aartsen *et al.*, “Characterization of the Atmospheric Muon Flux in IceCube,” *Astropart. Phys.*, vol. 78, pp. 1–27, 2016.
- [131] D. Heck, G. Schatz, J. Knapp, T. Thouw, and J. Capdevielle, “CORSIKA: A Monte Carlo code to simulate extensive air showers,” tech. rep., 1998.
- [132] D. Heck and T. Pierog, “Extensive air shower simulation with CORSIKA: A users guide,” *Forschungszentrum Karlsruhe, Institut für Kernphysik*, 2000.
- [133] T. K. Gaisser, T. Stanev, and S. Tilav, “Cosmic Ray Energy Spectrum from Measurements of Air Showers,” *Front. Phys. (Beijing)*, vol. 8, pp. 748–758, 2013.
- [134] T. Gaisser, “Seasonal variation of atmospheric neutrinos in IceCube,” in *33rd International Cosmic Ray Conference*, p. 0492, 2013.

- [135] M. G. Aartsen *et al.*, “Efficient propagation of systematic uncertainties from calibration to analysis with the SnowStorm method in IceCube,” *JCAP*, vol. 10, p. 048, 2019.
- [136] U. S. Atmosphere, “National oceanic and atmospheric administration,” *National Aeronautics and Space Administration, United States Air Force, Washington, DC*, 1976.
- [137] R. Forsberg, A. V. Olesen, F. Ferraccioli, T. A. Jordan, and K. Matsuoka, “Airborne geophysical surveys of unexplored regions of Antarctica - results of the ESA PolarGap campaign,” in *AGU Fall Meeting Abstracts*, vol. 2016, pp. C52A–01, Dec. 2016.
- [138] R. Forsberg and T. Jordan, “Airborne ice penetrating radar and geophysics around south pole.” presented at IceCube Polar Science Workshop, 2017.
- [139] J. Koskinen, “Where is the bedrock?.” presented at IceCube Collaboration calibration call, 2017.
- [140] W. J. Hinze, “Bouguer reduction density, why 2.67?,” *GEOPHYSICS*, vol. 68, no. 5, pp. 1559–1560, 2003.
- [141] C. R. Bentley, B. R. Koci, L. J.-M. Augustin, R. J. Bolsey, J. A. Green, J. D. Kyne, D. A. Lebar, W. P. Mason, A. J. Shturmakov, H. F. Engelhardt, W. D. Harrison, M. H. Hecht, and V. Zagorodnov, *Ice Drilling and Coring*, ch. 4, pp. 221–308. John Wiley & Sons, Ltd, 2009.
- [142] P. Spector, J. Stone, D. Pollard, T. Hillebrand, C. Lewis, and J. Gombiner, “West antarctic sites for subglacial drilling to test for past ice-sheet collapse,” *The Cryosphere*, vol. 12, no. 8, pp. 2741–2757, 2018.
- [143] F. Garwood, “Fiducial limits for the poisson distribution,” *Biometrika*, vol. 28, no. 3/4, pp. 437–442, 1936.
- [144] V. Patil and H. Kulkarni, “Comparison of confidence intervals for the poisson mean: Some new aspects,” *Revstat - Statistical Journal*, vol. 10, pp. 211–227, 06 2012.
- [145] H. Sahai and A. Khurshid, “Confidence intervals for the mean of a poisson distribution: A review,” *Biometrical Journal*, vol. 35, no. 7, pp. 857–867, 1993.
- [146] C. A. Argüelles, A. Schneider, and T. Yuan, “A binned likelihood for stochastic models,” *JHEP*, vol. 06, p. 030, 2019.
- [147] M. E. Peskin and D. V. Schroeder, *An Introduction to quantum field theory*. Reading, USA: Addison-Wesley, 1995.
- [148] S. S. Wilks, “The Large-Sample Distribution of the Likelihood Ratio for Testing Composite Hypotheses,” *The Annals of Mathematical Statistics*, vol. 9, no. 1, pp. 60 – 62, 1938.

- [149] G. J. Feldman and R. D. Cousins, “A Unified approach to the classical statistical analysis of small signals,” *Phys. Rev. D*, vol. 57, pp. 3873–3889, 1998.
- [150] G. Cowan, K. Cranmer, E. Gross, and O. Vitells, “Asymptotic formulae for likelihood-based tests of new physics,” *Eur. Phys. J. C*, vol. 71, p. 1554, 2011. [Erratum: *Eur.Phys.J.C* 73, 2501 (2013)].
- [151] F. Feroz, M. P. Hobson, E. Cameron, and A. N. Pettitt, “Importance Nested Sampling and the MultiNest Algorithm,” *Open J. Astrophys.*, vol. 2, no. 1, p. 10, 2019.
- [152] Q. An *et al.*, “Measurement of the cosmic-ray proton spectrum from 40 GeV to 100 TeV with the DAMPE satellite,” *Sci. Adv.*, vol. 5, no. 9, p. eaax3793, 2019.
- [153] R. Alfaro *et al.*, “All-particle cosmic ray energy spectrum measured by the HAWC experiment from 10 to 500 TeV,” *Phys. Rev. D*, vol. 96, no. 12, p. 122001, 2017.
- [154] E. Atkin *et al.*, “First results of the cosmic ray NUCLEON experiment,” *JCAP*, vol. 07, p. 020, 2017.
- [155] M. G. Aartsen *et al.*, “Cosmic Ray Spectrum from 250 TeV to 10 PeV using IceTop,” *Phys. Rev. D*, vol. 102, p. 122001, 2020.
- [156] O. Adriani *et al.*, “Direct Measurement of the Cosmic-Ray Proton Spectrum from 50 GeV to 10 TeV with the Calorimetric Electron Telescope on the International Space Station,” *Phys. Rev. Lett.*, vol. 122, no. 18, p. 181102, 2019.
- [157] J. Evans, D. G. Gamez, S. D. Porzio, S. Söldner-Rembold, and S. Wren, “Uncertainties in Atmospheric Muon-Neutrino Fluxes Arising from Cosmic-Ray Primaries,” *Phys. Rev. D*, vol. 95, no. 2, p. 023012, 2017.
- [158] T. K. Gaisser, “The atmospheric neutrino flux,” in *Probing Particle Physics With Neutrino Telescopes*. (H. Carlos Perez De Los, ed.), ch. 3, World Scientific, 2020.
- [159] A. Aduszkiewicz *et al.*, “Measurements of π^\pm , K^\pm , p and \bar{p} spectra in proton-proton interactions at 20, 31, 40, 80 and 158 GeV/c with the NA61/SHINE spectrometer at the CERN SPS,” *Eur. Phys. J. C*, vol. 77, no. 10, p. 671, 2017.
- [160] F. Riehn, R. Engel, A. Fedynitch, T. K. Gaisser, and T. Stanev, “Hadronic interaction model Sibyll 2.3d and extensive air showers,” *Phys. Rev. D*, vol. 102, no. 6, p. 063002, 2020.
- [161] A. Hourlier, *Background Studies for Electron Antineutrino Oscillations Measurement at the Double Chooz Experiment*. PhD thesis, Paris U. VII, APC, 2016.